

**ANALYSIS AND DESIGN OF SPIRALLY WELDED THIN-WALLED STEEL
TAPERED CYLINDRICAL SHELLS UNDER BENDING WITH APPLICATION
TO WIND TURBINE TOWERS**

by

Abdullah Mahmoud

A dissertation submitted to Johns Hopkins University in conformity with the
requirements for the degree of Doctor of Philosophy

Baltimore, Maryland

October 2017

Abstract

An important obstacle restricting the growth of wind-generated energy is the production of taller towers for wind turbines that can harvest energy from the steadier, stronger winds at higher elevations. Currently, the need to transport wind turbine tower sections to the construction site constrains the diameter of the section, which then limits the height of the tower. This limitation can be avoided if the tower sections are made on-site, and one potential method for on-site manufacturing is automated spiral welding. This thesis, which focuses largely on computational modeling for design, is part of a larger research effort to advance the application of spirally welded tubes (SWTs) in wind tower structures. With the new manufacturing technique, a wider range of tower diameters and thicknesses, and potentially more optimal thin-walled sections can be employed. Thin-walled shells are one of the most advanced and efficient forms of large structures; however, their behavior can be unstable and extremely sensitive to imperfections. For decades, the structural design of such shell structures relied on elastic buckling “knockdown factors” obtained from experimental results, but with the expansion in the capabilities of computational modeling, today design is working to leverage the power of shell finite element models that are geometrically and materially nonlinear with imperfections included (i.e. “GMNIA” analysis models). This thesis explores the analysis and design of spirally welded tapered cylindrical steel shells and complements experimental results conducted as a companion to this effort within the larger SWT effort. The thesis includes an introduction and historical background on the development of research on thin shells; a summary of relevant experimental work completed in the literature and in the SWT project; careful examination of geometric imperfections in the world of shells in general and spirally welded shells in

particular; provides a practical finite element modeling protocol for predicting the flexural strength and collapse behavior of thin-walled spirally welded tapered steel tubes; validates the proposed modeling protocols for GMNIA models with SWT test results; extends the results to provide standard “reference resistance” curves that can be used for future GMNIA analyses by structural designers; and highlights the application to an archetype 3MW wind turbine tower using both classical and new analysis-based.

Readers:

Prof. Benjamin W. Schafer (advisor)

Prof. James K. Guest

Prof. Andrew T. Myers

Acknowledgements

As I write these words I go through lots of memories from the first day I arrived at Johns Hopkins University to the day of my defense, and I am still asking myself am I going to make it? It was a wonderful journey and I enjoyed every day of it. I got the chance to meet and work with some of the brightest, smartest, and most wonderful people I have ever met, to whom I will be always grateful.

Before everything I would like to dedicate this thesis to all my brave friends in Egypt who stood up against injustice and lost their lives or their freedom.

I would like to express my special appreciation and thanks to my advisor Prof. Ben Schafer for his continuous support during my Ph.D study, for his patience, motivation, and immense knowledge. His tremendous amount of knowledge and guidance helped me in all the time of research and writing of this thesis. I could not have imagined having a better advisor and mentor for my Ph.D study.

I would like to thank the SWT research team: Dr. Angelina Jay, Fariborz Mirzaie, Florian Roscheck, Eric Smith and special thanks to Prof. Andrew Myers for his help and guidance throughout my research and for serving on my proposal and thesis committee.

I would like to thank my fellow lab mates in TWS group: Dave Fratamico, Guanbo Bian, Hamid Fouroghi, Astrid Fischer, Fardad Haghpanah, Xi Zhou, Jean Batista Abreu and Jiazhen Leng for being friend and colleagues, for the stimulating discussions and invaluable feedback on my work, and for all the fun we have had in the last four years. It was fantastic working with you all.

A very special gratitude goes to Dr. Shahabeddin Torabian for his dedicated support, guidance, and mentorship along my research, thanks to you.

Also, I want to thank all my friends at the Civil Engineering department and the whole staff and faculty, specially prof. James Guest for being on my proposal committee and defense committee. I also want to thank you for your brilliant comments and suggestions, that enriched the work in this thesis.

I would like to thank the National Science Foundation for funding the spirally welded wind turbine towers research project.

I would like to thank my family: my parents and my brother and sister for supporting me throughout my study and my life in general. You have been an incredibly supporting team.

And finally, last but by no means least, to my wife Sarah, whom I believe more than a lifetime would be needed to thank you enough. For believing in me, for encouraging me, for supporting me in every step, I owe it all to you!

Co-Authorship

This dissertation contains material from four published manuscripts (Chapters 4-6).

Mahmoud, A., Torabian, S., Jay, A., Myers, A. T., Smith, E., Schafer, B. W. (2015) “*Modeling protocols for elastic buckling and collapse analysis of spirally welded circular hollow thin-walled sections*” Proceedings of the Annual Stability conference, SSRC’15, Nashville-Tennessee, USA.

Mahmoud, A., Torabian, S., Jay, A., Mirzaie, F., Myers, A. T., Smith, E., Schafer, B. W. (2016) “*Collapse Analyses on Spirally Welded Tapered Tubes using EC3 Generated Imperfections*” Proceedings of the Annual Stability conference, SSRC’16, Orlando-Florida, USA

Mahmoud, A. N., Mirzaie, F., Torabian, S., Jay, A., Myers, A. T., Smith, E., Schafer, B. W. (2016) “*Collapse Analysis of Spirally Welded Tapered Tubes under Flexural Moments using Measured and Generated Imperfections*” Proceedings of the 7th International Conference on Coupled Instabilities in Metal Structures. Baltimore-Maryland, USA.

Mahmoud, A., Torabian, S., Jay, A., Mirzaie, F., Myers, A. T., Smith, E., Schafer, B. W. (2017) “*Modeling the Flexural Collapse of Thin-Walled Spirally Welded Tapered Tubes*”, J. Structural Engineering (In print).



"In the name of God, the Most Gracious, the Most Merciful"

Table of Contents

Abstract	ii
Acknowledgements	iv
Co-Authorship	vi
List of Figures	xiii
List of Tables.....	xxiv
Chapter 1 Introduction.....	1
1.1 Shell structures	1
1.2 Wind Turbines	3
1.3 Motivation	7
1.4 Spirally welded wind turbines	8
1.5 Scope of this study	11
1.6 Thesis roadmap	12
Chapter 2 Shell Stability and Available Design Guides	14
2.1 Historical remarks.....	14
2.2 Stability analysis of shells	16
2.2.1 Linear stability theory of cylindrical shells – Donnell’s equations	18
2.2.2 Critical axial stress	21
2.2.2 Critical bending stress	23
2.2.3 Length factor in circular shells	23
2.2.4 Tapered cylindrical shells stability	25
2.3 Available design guides	25
2.3.1 American Institute for Steel Construction (AISC 360-10) and American Iron and Steel Institute (AISI S100-16).....	26
2.3.2 American Society of Mechanical Engineers (ASME STS-1 2011).....	26
2.3.3 American Petroleum Institute (API RP-2A).....	27

2.3.4 Recommended Practice for Compliance of Large Lan-based Wind Turbine Support Structures (ASCE/AWEA RP2011)	29
2.3.5 Eurocode 3 –Part 1-6: Strength and Stability of Shell Structures (BS EN 1993-1-6:2007)	31
2.3.6 Comparison between design guides	35
2.4 Summary and conclusions	36
Chapter 3 Existing Experimental Work	38
3.1 Introduction	38
3.2 Experimental work of thin-walled tubes	39
3.2.1 Thin-walled tubes under axial compression	39
3.2.2 Thin-walled tubes under flexural bending	41
3.3 SWT Project tests on spirally welded tapered tubes	46
3.3.1 Test Setup	49
3.3.2 Laser Scans	50
3.3.3 Test Results	53
3.3.4 Fatigue Tests	60
3.4 Summary and Conclusions	62
Chapter 4 Imperfections	65
4.1 Introduction	65
4.2 Eurocode fabrication tolerances	68
4.2.1 Out-of-roundness Tolerance	68
4.2.2 Dimple Tolerance	70
4.2.3 Accidental Eccentricity tolerance	72
4.3 Imperfections in Numerical Modeling	72
4.3.1 Measured Imperfections:	72
4.3.1.1 Laser scanner measurements of SWT specimens (SWT project)	74

4.3.1.2 Residual Stresses (SWT project)	80
4.3.2 Generated imperfections.....	83
4.3.3 SWT Project	84
4.3.3.1 1 st eigenmode-affine pattern	85
4.3.3.2 Weld Depression by (Rotter and Teng 1989).....	86
4.4 Summary and conclusions.....	90
Chapter 5 Mesh Sensitivity Analyses	92
5.1 Introduction	92
5.2 Part I: Linear Buckling Analyses.....	93
5.2.1 Parametric Model Geometry	95
5.2.2 Boundary Conditions	96
5.2.3 Sensitivity to shell element type	97
5.2.4 Sensitivity to element aspect ratio	101
5.2.5 Sensitivity to inclination angle of element	104
5.3 Part II: Validation of the meshing protocols for the nonlinear analysis	107
5.4 Testing the Effect of the Imperfections Pattern.....	112
5.5 Summary and Conclusions	116
Chapter 6 SWT Numerical Modeling.....	118
6.1 Introduction	118
6.2 Boundary conditions	120
6.3 Material properties	122
6.4 GMNIA models vs SWT tests results	126
6.4.1 GMNIA models with generated imperfections.....	127
6.4.1.1 1 st eigenmode-affine patterns.....	127
6.4.1.2 Weld depression.....	132

6.4.2 GMNIA models with measured imperfections.....	139
6.4.3 GMNIA models with measured imperfections and residual stresses	145
6.5 Commentary on nonlinear collapse analyses	152
Chapter 7 Reference Resistance Design of Spirally Welded Tubes	157
7.1 Introduction	157
7.2 Building RRD curves	160
7.2.1 An example from literature (Chen et al. 2008).....	161
7.3 RRD for SWT models.....	163
7.3.1 Geometry of Parametric Model with Spiral Weld Depression Imperfection	164
7.3.2 Imperfections	165
7.3.3 Imperfections according to EC3-1-6.....	166
7.3.4 1 st eigenmode-affine imperfections pattern.....	166
7.3.5 Weld Depression imperfections.....	168
7.3.6 Validation of the methodology of choosing the parametric model dimensions .	170
7.4 Fitting RRD parameters for SWT sections	173
7.5 Summary and Conclusions	174
Chapter 8 Design of Archetype 3 MW Wind Turbine Tower	176
8.1 Wind Turbines load cases	176
8.2 3 MW 140 m archetype spirally welded wind turbine towers.....	178
8.3 Tower geometry.....	180
8.4 Design of the sections using hand calculations	182
8.5 Design using GMNIA models	186
8.6 Linear elastic analysis of Full tower model.....	188
8.7 Summary and conclusions.....	189
Chapter 9 Summary, Conclusions and Future Work.....	191

9.1 Summary	191
9.2 Conclusions	192
9.3 Future Work.....	197
References.....	199
Appendix A.....	206
Appendix B	214
Appendix C	234
Appendix D.....	241
Appendix E	253
Curriculum Vitae	260

List of Figures

Figure 1.1 (a) Greek Chalcidian helmet (500 BC), and (b) Hadrian’s villa in Tivoli, Italy (100 AD).	1
Figure 1.2 Examples of modern applications of thin shells.	2
Figure 1.3 (a) The first automated wind turbine generator ⁵ , and (b) U.S. inventor Charles F. Brush in 1920.	4
Figure 1.4 NASA/DOE/DOI prototype wind turbines (Linscott, Perkins, and Dennett 1984).	4
Figure 1.5 U.S. installed capacity of wind power by state (AWEA 2017).	6
Figure 1.6 U.S. annual (by yearly quarters) and cumulative wind power capacity growth (AWEA 2017).	6
Figure 1.7 Existing wind turbine average heights, their capacities and cost of energy and desired heights and their estimated capacities if the transportation barrier is resolved (Cotrell et al. 2014).	7
Figure 1.8 Transportation of tower section under overhead obstruction (Jay 2017).	8
Figure 1.9 Current applications of spirally welded tubes.	9
Figure 1.10 Schematic of the spiral welding procedure to manufacture tapered tubes then these tubes are cut and welded together to build wind turbine tower.	10
Figure 1.11 a section of wind turbine tower and its bending moment distribution.	12
Figure 2.1 Chladni’s patterns of guitar plate (Altenbach and Eremeyev 2017).	15
Figure 2.2 Bifurcation types.	16
Figure 2.3 Typical bifurcation types for columns, plates, and shells.	17
Figure 2.4 Circular cylindrical shells with sign conventions (Singer, Arbocz and Weller 2002).	19
Figure 2.5 The effect of cylinder length on linear bifurcation stress (ECCS 2013).	25
Figure 2.6 EC3-1-6 design limit states and permitted methods for each limit state.	33
Figure 2.7 Comparison between normalized nominal flexural strength using different design guides for shelled structures.	36
Figure 3.1 Buckling of unstiffened cylindrical shell under uniform axial compression (a) Prismatic and (b) tapered (Horton et al. 1965)	41

Figure 3.2 Summary of experimental results from literature (by Harris et al. 1957) and traditional approaches for buckling design, using knockdown factors, of tubes under axial compression (Rotter 2011).....	41
Figure 3.3 Experimental results for 140 tests from 18 studies (see Table 1 and Table 2) on static, flexural buckling of hollow circular, unstiffened, non-pressurized steel sections. Pure bending tests, represented with hollow circles, include 4-pt bending tests and simple bending tests (the latter is defined as flexure achieved by applying end rotations). All spiral weld tests are loaded in pure bending and are depicted with gray markers. For all tests, marker size is related to specimen diameter through an inverse power relationship of 2.5 (Jay et al. 2016a).	45
Figure 3.4 Test setup for full-scale test of 65 kW wind turbine tower (Sim et al. 2014). .	46
Figure 3.5 Schematic of spirally welded tapered tube.....	47
Figure 3.6 Schematic showing the experimental set-up for large scale bending tests on tapered spirally welded tubes and a photo of the test rig with one specimen mounted on before testing (Jay et al. 2016b).....	50
Figure 3.7 (a) The laser scanner on the test rig, and (b) framing of laser scanner and its components.....	51
Figure 3.8 Scans of part of specimens under compression for seven of the nine specimens (a) during test (before buckling) and (b) at buckling (Jay 2017).....	52
Figure 3.9 The correction made to the SWT tests moment-rotation curves.	55
Figure 3.10 (a) Moment-rotation curves of the tested specimens.	55
Figure 3.10 (b-c) Moment-rotation curves of the tested specimens.	56
Figure 3.10 (d-e) Moment-rotation curves of the tested specimens.	57
Figure 3.11 Region of local buckling for each specimen after the first load drop (θt) and at the end of the test ($\theta final$) (Jay et al. 2016b).....	59
Figure 3.12 Photos of (a) fatigue specimen with strain gauge below the transverse weld and (b) the specimen in the hydraulic grips with both welds highlighted (Jay 2017).	60
Figure 3.13 Plot comparing all fatigue data with the EC3-1-9 S-N curve for DC = 102 (black line, outlying white-fill data point excluded). The purple line indicates the CAFL calculated from data (Jay 2017).....	62

Figure 3.14 SWT test results compared to normalized nominal flexural strength according to different design codes.	64
Figure 4.1 Equilibrium postbuckling paths (a) asymmetric, (b) symmetric stable, and (c) symmetric unstable (typical shells).....	65
Figure 4.2 Coiling SWT sections (Hanada et al. 1986).....	66
Figure 4.3 Measurements of diameters assessment of out-of-roundness.	69
Figure 4.4 Measurements of dimples imperfections.	70
Figure 4.5 One of the earliest initial imperfections measurements by (Arbocz et al. 1969).	73
Figure 4.6 The KTS laser scanner with a specimen mounted (photos provided by KTS).	75
Figure 4.7 (a-d): Specimens scanned geometry with amplified imperfections 10x (color bar is radial deviations in mm).	76
Figure 4.7(e-h) Specimens scanned geometry with amplified imperfections 10x (color bar is radial deviations in mm).	77
Figure 4.8 (a) Scan data for SW-145-0° showing deviations measured out-of-plane from the geometry of a perfect tapered tube. Positive deviations indicate imperfect geometry that is outside of the perfect tapered tube (Jay 2017).....	79
Figure 4.8 (b) Scan data for SW-350-240° showing deviations measured out-of-plane from the geometry of a perfect tapered tube. Positive deviations indicate imperfect geometry that is outside of the perfect tapered tube (Jay 2017).....	79
Figure 4.9 Membrane and bending residual stresses directions.....	81
Figure 4.10 Measured residual stresses from six trapezoidal plates and the red line indicate the median and the blue boxes indicates 25 th and 75 th percentiles of the data (Jay 2017).....	82
Figure 4.11 (a) Typical trapezoidal plate residual stress with areas of residual stresses pattern shown.....	83
Figure 4.11 (b) Pattern of residual stresses within the thickness of the plate in both meridional and circumferential directions.....	83
Figure 4.12 The first eigenmode of a tapered cylindrical moment under flexural.....	85
Figure 4.13 Specimen with weld depression along the spiral seam magnified 10x.....	87

Figure 4.14 weld depression profiles Rotter and Teng (1989) Type A and Type B.	89
Figure 4.15 Weld depression Type ‘A’ scaled to EC3-1-6 Classes B and C, and WTC used in GMNIA models.	89
Figure 5.1 Definition of reference points RP-1 and RP-2 used to apply boundary conditions through Multi-Point Constraint (MPC) of the nodes at each end of the tube.....	97
Figure 5.2(a-b) Mesh convergence for different shell elements types under axial compression.....	99
Figure 5.3(a-b) Mesh convergence for different shell elements types under pure bending.	100
Figure 5.4 Shell element aspect ratio in terms of a:b, where a is the meridional direction and b is the circumferential direction.....	102
Figure 5.5 Typical buckled shape of cylindrical shell with 1:1 mesh under (a) axial compression, and (b) bending.....	102
Figure 5.6 Mesh convergence for different element aspect ratios size with respect to element size in the meridional direction in terms of (Rt) under axial compression	103
Figure 5.7 Mesh convergence for different element aspect ratios size with respect to element size in the meridional direction in terms of (Rt) under pure bending	103
Figure 5.8 Helical mesh with different inclination angles θ : (a) 5°, (b) 15°, (c) 25°.....	105
Figure 5.9 Typical buckled shape of a tapered cylindrical mesh with helical mesh with angle θ under (a) & (c) bending and (b) & (d) axial compression.	105
Figure 5.10 Mesh convergence with the size of element in the meridional direction and 1:1 element aspect ratio for pure compression.	106
Figure 5.11 Mesh convergence with the size of element in the meridional direction and 1:1 element aspect ratio for pure bending.	106
Figure 5.12 Material properties of GMNIA models used in nonlinear mesh sensitivity analysis.	108
Figure 5.13(a-b) The effect of the element types for S4, S4R, S8R & S9R5 on the nonlinear models vs (a) number of Degrees of Freedom (b) size of mesh in Meridional direction.....	109

Figure 5.14 The effect of element aspect ratio on nonlinear models	110
Figure 5.15 the effect of the inclination angle of the mesh on nonlinear models.	110
Figure 5.16 Full mesh of typical model of helically meshed tapered tube following the mesh guidance and the predicted collapse shape under bending.....	112
Figure 5.17 (a-b) The effect of the element types for S4, S4R, S8R & S9R5 on the nonlinear models with interpolated imperfection pattern vs (a) number of Degrees of Freedom (b) size of mesh in Meridional direction.	114
Figure 5.18 The effect of element aspect ratio on nonlinear models with interpolated imperfections pattern	115
Figure 5.19 the effect of the inclination angle of the mesh on nonlinear models with interpolated imperfection pattern.....	115
Figure 6.1 (a) Test rig schematic (Jay et al. 2016b) and (b) Finite Element model of one of the specimens with test rig modeled.....	121
Figure 6.2 Deformed shape of SW-325-0° GMNIA model with scanned geometry after the first load drop for (a) with test rig modeled, and (b) equivalent boundary conditions model.....	122
Figure 6.3 Moment-rotation curve comparison of the GMNIA models for specimen SW- 325-0° with simplified boundary conditions and with the test rig included.	122
Figure 6.4 (a-b) Stress-Strain curves with True simplified curve used in numerical modeling.....	123
Figure 6.4 (c-h) Stress-Strain curves with True simplified curve used in numerical modeling.....	124
Figure 6.4 (i) Stress-Strain curves with true stress-strain curve points used in numerical modeling.....	125
Figure 6.5 (a-f) Moment-Rotation curves for GMNA and GMNIA-eigenmode models vs test results.	128
Figure 6.6 Deformed shape for all GMNIA-eigenmode models with EC3-1-6 Class C imperfections, and contour of von-Mises stress.	132
Figure 6.7 (a-d) Moment-Rotation curves for GMNA and GMNIA-weld depression models vs test results	133

Figure 6.7 (e-i) Moment-Rotation curves for GMNA and GMNIA-weld depression models vs test results.	134
Figure 6.8 (a-d) Moment-Rotation curves for GMNIA-weld depression models with EC3-1-6 Class C imperfections using “problematic” Riks solver and artificial damping solver as reported in section 6.4.1.2.....	135
Figure 6.8 (e-i) Moment-Rotation curves for GMNIA-weld depression models with EC3-1-6 Class C imperfections using “problematic” Riks solver and artificial damping solver as reported in section 6.4.1.2.....	136
Figure 6.9 Deformed shape for all GMNIA models with weld depression imperfections consistent with EC3-1-6 Class C with contour of von-Mises stress.....	139
Figure 6.10 Moment-rotation curves of specimen SW-325-0° GMNIA models with measured imperfections and different mesh sizes.	141
Figure 6.11 Moment-rotation curves of specimen SW-325-0° GMNIA models with measured imperfections and different orientations.....	142
Figure 6.12 (a-b) Moment-Rotation curves for GMNA and GMNIA-measured imperfections models vs test results	142
Figure 6.12 (c-h) Moment-Rotation curves for GMNA and GMNIA-measured imperfections models vs test results.	143
Figure 6.13 Deformed shape for all GMNIA models with measured imperfections, contour for von-Mises Stress.....	145
Figure 6.14 Deformed shape of perfect numerical model with only residual stresses applied to it scaled 500x.....	147
Figure 6.14 (d) Distributions for the bending stresses on a trapezoidal plate for the three cases.	147
Figure 6.15 (a-d) Moment-Rotation curves for GMNIA-measured imperfections models without residual stresses (MI), with original residual stresses (MI+RS) and inverted bending residual (MI+RS inverted) vs test results.	148
Figure 6.15 (e-h) Moment-Rotation curves for GMNIA-measured imperfections models without residual stresses (MI), with original residual stresses (MI+RS) and inverted bending residual (MI+RS inverted) vs test results.	149

Figure 6.16 Deformed shape for all GMNIA (MI+RS) at the end of the analysis, contour for Von-Mises Stress.....	152
Figure 6.17 Summary of the test-to-predicted moment ratio mean GMNA and GMNIA models with all imperfections patterns discussed in this chapter.	154
Figure 6.18 Summary of the test-to-predicted stiffness ratio mean GMNA and GMNIA models with all imperfections patterns discussed in this chapter.	155
Figure 7.1 Design by GMNIA analyses according to EC3-1-6 (ECCS 2013).	159
Figure 7.2 The processes of RRD method (Rotter 2016).	159
Figure 7.3 Typical shell strength curves.	161
Figure 7.4 RRD capacity curves built with the (α , β , and η) parameters computed by Chen et al. (2008) and SWT test results indicated.....	162
Figure 7.5 Spirally welded tube parametric model dimensions.	164
Figure 7.6 Typical imperfections from 1 st eigenmode-affine pattern.....	167
Figure 7.7 Capacity curve for GMNIA models with imperfections from 1 st eigenmode-affine pattern.....	167
Figure 7.8. (a) Typical spirally welded tube with scaled weld depression imperfection along spiral seam weld, and (b) weld depression profiles as recommended by EC3-1-6 using Type A weld profile proposed by Rotter and Teng (1989).....	168
Figure 7.9 Capacity curves of normalized flexural strength of GMNIA models of spirally welded tapered tubes in terms of relative slenderness.	169
Figure 7.10 Capacity curves of normalized flexural strength of GMNIA models of spirally welded tapered tubes in terms of relative strength.	170
Figure 7.11 Capacity curves in terms of relative slenderness of Set 2 of GMNIA models with imperfections consistent with EC3-1-6 quality classes and the closest curves of Set 1 of GMNIA models and test results.	172
Figure 7.12 Capacity curves in terms of relative strength of Set 2 of GMNIA models with imperfections consistent with EC3-1-6 quality classes and the closest curves of Set 1 of GMNIA models and test results.	172
Figure 7.13 RRD curve parameters (a) elastic imperfection reduction factor, and (b) plastic range factor.....	173

Figure 7.14 Capacity curves of SWT built with updated RRD parameters with SWT tests results against (a) relative slenderness, and (b) relative strength.	174
Figure 8.1 (a) Local coordinate system and operational forces directions, and (b) envelope of straining actions.	179
Figure 8.2 (a) SWT sections and elevations, (b) section transitions and location of flanges, and (c) slenderness ratio along the height.	181
Figure 8.3 The ratio of unfactored applied moment to nominal moment obtained from design guides and proposed RRD-SWT.	184
Figure 8.4 The ratio of compressive stress to allowable stress obtained from design guides and proposed RRD-SWT.	185
Figure 8.5 (a) Moment strength from GMNIA results vs applied moment, and nominal strengths calculated from EC3-1-6 and RRD Class, and (b) GMNIA von-Mises contour for each section.	187
Figure 8.6 LBA results for the full tower and the SWT models compared to critical moment from theoretical calculation and 1 st eigen-buckling mode for full tower model.	189
Figure 9.1 New fabrication method of SWT with staggered cross weld (provided by KTS).	197
Figure B.1: Material stress strain curve used for GMNIA models.	215
Figure B.2.a: Moment rotation curves of FE models for models with R/t=25	217
Figure B.2.b: Moment rotation curves of FE models for models with R/t=50.	217
Figure B.2.c: Moment rotation curves of FE models for models with R/t=75	218
Figure B.2.d: Moment rotation curves of FE models for models with R/t=100.	218
Figure B.2.e: Moment rotation curves of FE models for models with R/t=300	219
Figure B.2.f: Moment rotation curves of FE models for models with R/t=500.	219
Figure B.3.a: Failure modes of models with R/t =25 (a)VS1-GMNIA (b)VS-1 GNIA (c) VS2-GMNIA (d) VS2-GNIA and (e) VS0-GMNA	220
Figure B.3.b: Failure modes of models with R/t =50 (a)VS1-GMNIA (b)VS-1 GNIA (c) VS2-GMNIA (d) VS2-GNIA and (e) VS0-GMNA	221
Figure B.3.c: Failure modes of models with R/t =75 (a)VS1-GMNIA (b)VS-1 GNIA (c) VS2-GMNIA (d) VS2-GNIA and (e) VS0-GMNA	222

Figure B.3.d: Failure modes of models with $R/t = 100$ (a)VS1-GMNIA (b)VS-1 GNIA (c) VS2-GMNIA (d) VS2-GNIA and (e) VS0-GMNA	223
Figure B.3.e: Failure modes of models with $R/t = 300$ (a)VS1-GMNIA (b)VS-1 GNIA (c) VS2-GMNIA (d) VS2-GNIA and (e) VS0-GMNA	224
Figure B.3.f: Failure modes of models with $R/t = 500$ (a)VS1-GMNIA (b)VS-1 GNIA (c) VS2-GMNIA (d) VS2-GNIA and (e) VS0-GMNA	225
Figure C.1: Mesh sensitivity analysis for nonlinear collapse models with aspect ratio 1:2.	234
Figure C.2: Mesh sensitivity analysis for nonlinear collapse models with aspect ratio 1:1.	234
Figure C.3: Mesh sensitivity analysis for nonlinear collapse models with aspect ratio 2:1.	235
Figure C.4: Mesh sensitivity analysis for nonlinear collapse models for element S4R.	235
Figure C.5: Mesh sensitivity analysis for nonlinear collapse models for element S4.	236
Figure C.6: Mesh sensitivity analysis for nonlinear collapse models for element S8R.	236
Figure C.7: Mesh sensitivity analysis for nonlinear collapse models for element S9R5.	237
Figure C.8: Mesh sensitivity analysis for nonlinear collapse models for helical angle 0°	237
Figure C.9: Mesh sensitivity analysis for nonlinear collapse models for helical angle 5°	238
Figure C.10: Mesh sensitivity analysis for nonlinear collapse models for helical angle 10°	238
Figure C.11: Mesh sensitivity analysis for nonlinear collapse models for helical angle 15°	239
Figure C.12: Mesh sensitivity analysis for nonlinear collapse models for helical angle 25°	239
Figure D.1: GMNIA-WD moment-rotation curves for RRD curves for sections with $R/t=25$	241
Figure D.2: GMNIA-WD moment-rotation curves for RRD curves for sections with $R/t=50$	241

Figure D.3: GMNIA-WD moment-rotation curves for RRD curves for sections with R/t=75.....	242
Figure D.4: GMNIA-WD moment-rotation curves for RRD curves for sections with R/t=100.....	242
Figure D.5: GMNIA-WD moment-rotation curves for RRD curves for sections with R/t=125.....	243
Figure D.6: GMNIA-WD moment-rotation curves for RRD curves for sections with R/t=150.....	243
Figure D.7: GMNIA-WD moment-rotation curves for RRD curves for sections with R/t=175.....	244
Figure D.8: GMNIA-WD moment-rotation curves for RRD curves for sections with R/t=200.....	244
Figure D.9: GMNIA-WD moment-rotation curves for RRD curves for sections with R/t=250.....	245
Figure D.10: GMNIA-WD moment-rotation curves for RRD curves for sections with R/t=300.....	245
Figure D.11: GMNIA-WD moment-rotation curves for RRD curves for sections with R/t=350.....	246
Figure D.12: GMNIA-WD moment-rotation curves for RRD curves for sections with R/t=25.....	247
Figure D.13: GMNIA-WD moment-rotation curves for RRD curves for sections with R/t=50.....	247
Figure D.14: GMNIA-WD moment-rotation curves for RRD curves for sections with R/t=75.....	248
Figure D.15: GMNIA-WD moment-rotation curves for RRD curves for sections with R/t=100.....	248
Figure D.16: GMNIA-WD moment-rotation curves for RRD curves for sections with R/t=125.....	249
Figure D.17: GMNIA-WD moment-rotation curves for RRD curves for sections with R/t=150.....	249

Figure D.18: GMNIA-WD moment-rotation curves for RRD curves for sections with R/t=175.....	250
Figure D.19: GMNIA-WD moment-rotation curves for RRD curves for sections with R/t=200.....	250
Figure D.20: GMNIA-WD moment-rotation curves for RRD curves for sections with R/t=250.....	251
Figure D.21: GMNIA-WD moment-rotation curves for RRD curves for sections with R/t=300.....	251
Figure D.22: GMNIA-WD moment-rotation curves for RRD curves for sections with R/t=350.....	252
Figure E.1 The ratio of applied moment to nominal moments obtained from design guides and proposed RRD-SWT.	258
Figure E.2 The ratio of applied compressive stress to nominal compressive stress obtained from design guides and proposed RRD-SWT.....	259

List of Tables

Table 2.1 Values of fabrication quality parameter (CEN 2007)	35
Table 3.1 Summary of static flexural testing programs for tubes with no internal pressurization (Jay et al. 2016a)	43
Table 3.2 Summary of static flexural testing programs for spirally welded tubes with no internal pressurization (Jay et al. 2016a).....	44
Table 3.3 Measured dimensions, quality class and ultimate moment of the eight large- scale specimens (Jay et al. 2016b).	48
Table 3.4 Average yield and ultimate stress obtained from coupon tests.....	49
Table 3.5 Summary of the flexural buckling results for all specimens (Jay 2017).	58
Table 3.6 Fatigue test results (Jay 2017)	61
Table 4.1 Recommended values for out-of-roundness tolerance parameter (CEN 2007).69	
Table 4.2 Measurements required for different cases of initial dimple imperfections.....	71
Table 4.3 Recommended Values of $U_{0,max}$ as listed in EC3-1-6 Table 8.4.....	71
Table 4.4 Summary of measurements of the maximum geometric imperfections for imperfection categories and associated quality classes (QC) (Jay et al., 2016a)	78
Table 4.5 Magnitude of the maximum amplitude of imperfection considered in the GMNIA models with 1 st eigenmode-affine pattern imperfections for each specimen.	86
Table 4.6 Magnitude of the maximum imperfection considered in the GMNIA models with Type ‘A’ weld depression for each specimen.	88
Table 5.1: Boundary conditions applied at the reference points which control the nodes at the end of each end of the model, respectively. The X-Y-Z coordinate system is defined in Fig. 5.1. X means that the indicated degree of freedom is constrained....	97
Table 6.1 Comparison between ultimate moments from GMNA and GMNIA eigenmode nonlinear collapse models and large-scale tests.	130
Table 6.2 Comparison between stiffness from GMNA and GMNIA eigenmode nonlinear collapse models and large-scale tests.....	131
Table 6.3 Comparison between ultimate moments from GMNIA weld depression models and large-scale tests.	137

Table 6.4 Comparison between stiffness from GMNIA weld depression models and large-scale tests.....	138
Table 6.5 Comparison between GMNIA models with measured imperfections and large-scale tests.....	144
Table 6.6 Comparison between ultimate moment GMNIA models with measured imperfections and residual stresses and large-scale tests.....	150
Table 6.7 Comparison between stiffness of GMNIA models with measured imperfections and residual stresses and large-scale tests.....	151
Table 7.1 Values of recommended dimple imperfections amplitude parameter.	166
Table 9.1 Design load cases (IEC 61400-1:2005).....	177
Table 8.1 Summary of the sections geometry.....	180
Table 8.2 Intermediate flanges dimensions.....	181
Table B.1 Dimensions and details of VS1 and VS2 models.....	215
Table B.2 Dimensions and details of VS0 models.....	216
Table B.3 Theoretical critical bending moment and lowest eigenbuckling moment	216

Chapter 1

Introduction

1.1 Shell structures

Shell structures, as one of the most efficient forms of structures, are found everywhere around us from the body of your phone to airplanes and rockets, but shells are not a modern technology to humans. Millions of years ago humans realized the extraordinary strength of shell-like structures just from natural observations, turtle shells, crab shells, humans and animals' skulls and bones. Their need to create mobilized tools and shelter pushed to the establishment of the human made thick and thin shells. For thousands of years the concept of shell structures was present in almost every civilization, from simple tools such as helmets and pots to ships and domes, Fig. 1.1.



(a)



(b)

Figure 1.1 (a) Greek Chalcidian helmet (500 BC)¹, and (b) Hadrian's villa in Tivoli, Italy (100 AD)².

Domes were the dominant form of structural shells throughout history, landmarks such as Notre-Dame in Paris (1163 AD), St. Peter's Basilica in Rome (1506 AD), and Hagia Sofia

¹ <http://art.thewalters.org/detail/22640/chalcidian-type-helmet/> (accessed on 9/21/2017)

² <https://pixabay.com/en/villa-adriana-hadrian-s-villa-tivoli-2330590/> (accessed on 9/21/2017)

in Constantinople (360 AD) are some examples of domes structures that still exists. For centuries, the development in shells was based only on experiments and structural applications were limited to thick shells due to the complex nature and the catastrophic failure of thin shells. By the end of the 19th century, with the industrial revolution, the thin shell applications were rapidly growing, and researchers started to have deeper understanding for shell stability. From the early 20th century till today, the research on thin shells is motivated by the aerospace industry. Silos, tanks, chimneys, and wind turbines are some examples of thin shell steel structures in structural world, Fig. 1.2.



(a) Steel silos³



(b) Wind turbines⁴

Figure 1.2 Examples of modern applications of thin shells.

Thin shells vary in shape and features according to application to serve its purpose efficiently. Circular cylindrical steel shells are the most common shape of shells, they can efficiently withstand normal, shear and torsion stresses. Cylindrical steel shells are usually used for wind turbines, where the major loads are in the meridional (longitudinal) direction, or pressurized tanks and pipelines, where internal and external pressure are the major loads. Geometric aspects such as tapered cylindrical shells and additional features such as

³ <https://pixabay.com/en/silos-grain-storage-agriculture-1598168/> (accessed on 9/21/2017)

⁴ <https://pixabay.com/en/pinwheel-energy-eco-wind-power-sky-2202780/> (accessed on 9/21/2017)

intermediate stiffeners are design according to manufacturing and operational needs or for optimal design where the most efficient geometry should be chosen. In this thesis we are focused on spirally welded tapered cylindrical shells under bending moment as part of a project aiming to enable spiral welding technique in the manufacturing of taller wind turbine towers.

1.2 Wind Turbines

In 1888, American inventor Charles Brush built the first automatically operated windmills generator (wind turbine) producing 12 KW of direct current to power his mansion. For the next 20 years, the wind turbine provided his home continuously with electricity and never failed once (Richter 1996). The use of wind turbines was limited to charging batteries in remote areas that did not have access to the electric grid for most of the twentieth century. In 1941, American engineer Palmer Cosslett Putnam and S. Morgan Smith company built the world's first megawatt-size wind turbine. Smith-Putnam wind turbine provided 1.25 MW of power, it had a 2-blade 53-m rotor and supported by a 36-m steel lattice tower. Although it only operated for 1100 hours before a blade failed catastrophically, it was the largest built wind turbine in the world till 1979 (Burton, Jenkins, Sharpe, and Bossanyi 2011). In 1973 when the oil prices rocketed, wind energy research and development started growing rapidly, NASA, the U.S. Department of Energy and U.S. Department of Interior collaborated in 1975 to develop and test prototype wind turbines with generators starting from 100 KW to 7 MW, Fig. 1.4.

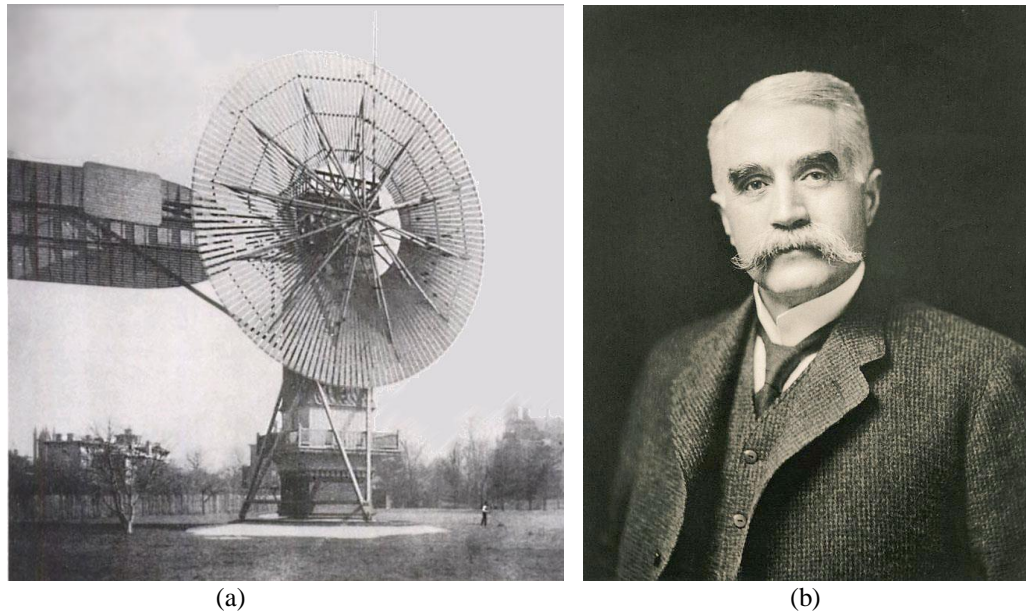


Figure 1.3 (a) The first automated wind turbine generator⁵, and (b) U.S. inventor Charles F. Brush in 1920⁵.

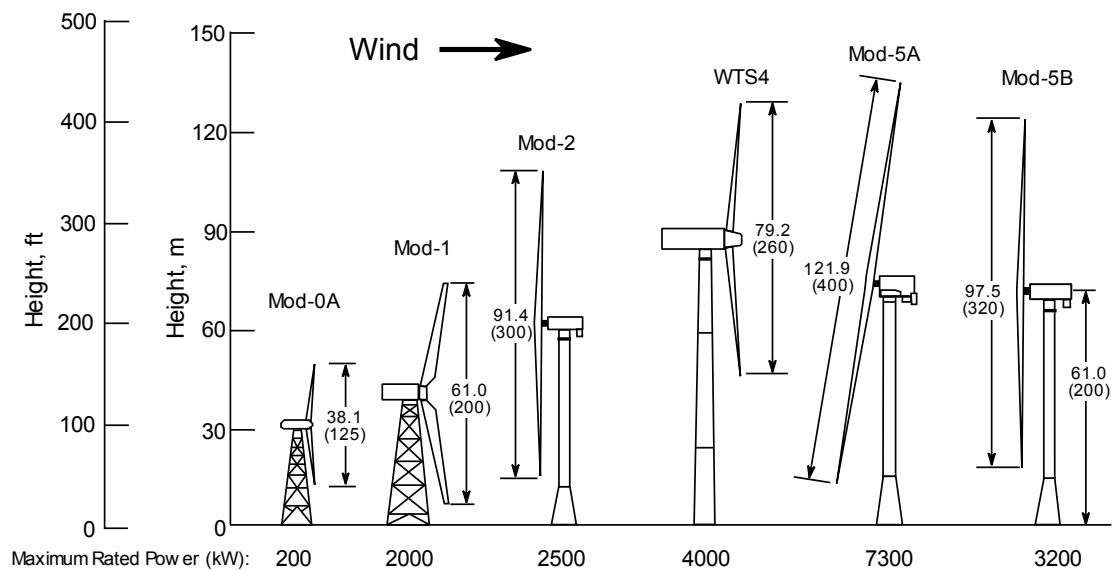


Figure 1.4 NASA/DOE/DOI prototype wind turbines (Linscott, Perkins, and Dennett 1984).

Although MOD-5A was designed to be the most powerful wind turbine it was never built, and the WTS-4 held the world record for the highest power output by generating 4 MW for

⁵ <http://omp.ohiolink.edu/Images/Bdg/Hist1MDS/> (accessed on 9/20/2017)

more than 20 years. The NASA/DOE/DOI project's main goals were to develop the technology and support the industry, however, in the 1980s the oil prices dropped and most of the manufacturers left the business (Linscott, Perkins, and Dennett 1984). Although, the pace of wind energy research slowed in the U.S., it continued to grow in Europe and the first offshore wind farm was constructed in 1991 in Denmark. The main motivation for the use of wind energy in the 1990s was the need of a clean source for electricity generation with low environmental impact to help mitigate climate change (Burton, Jenkins, Sharpe, and Bossanyi, 2011). In 2006, the oil prices jumped and again the interest in renewable energy increased. In the U.S. several laws were issued (the Energy Policy Act of 2005, the Energy Independence and Security Act of 2007, and the American Recovery and Reinvestment Act of 2009) aiming to increase electricity generated from renewable sources to 10% by 2012, and 25% by 2025. Due to the boost in wind generated energy the 2012 percentage was exceeded, 12.5% of the total electrical energy produced in that year was from renewable sources (Apt et al. 2013). The latest report issued by the U.S. Energy Information Administration, showed that renewable energy sources provided 19.35% of the total energy produced in 2017. Fig. 1.5 shows the existing wind energy capacity in each state in the U.S., and Fig 1.6 shows the growth in wind Energy in the U.S. from the early 2000s until the second quarter of 2017, these data is provided in a wind industry market report published by the American Wind Energy Association (AWEA).

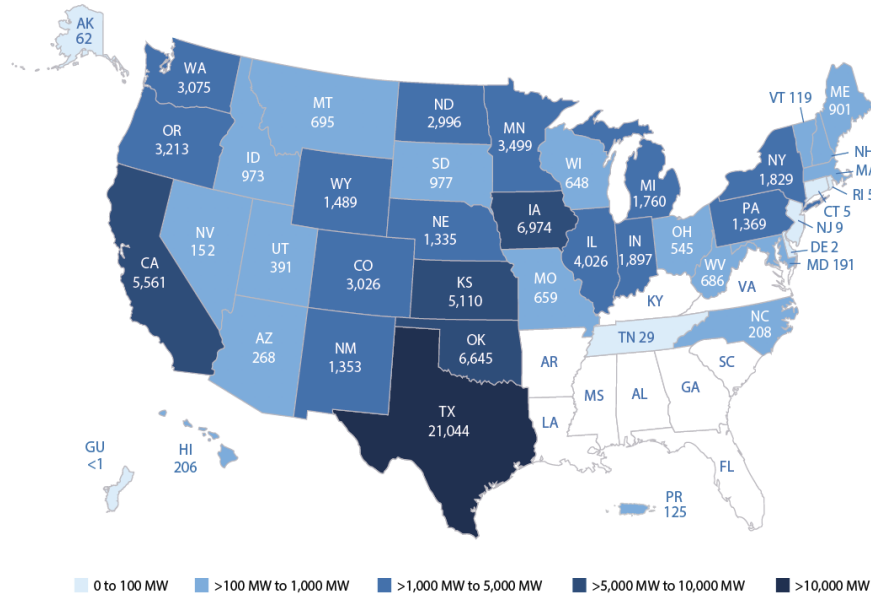


Figure 1.5 U.S. installed capacity of wind power by state (AWEA 2017).

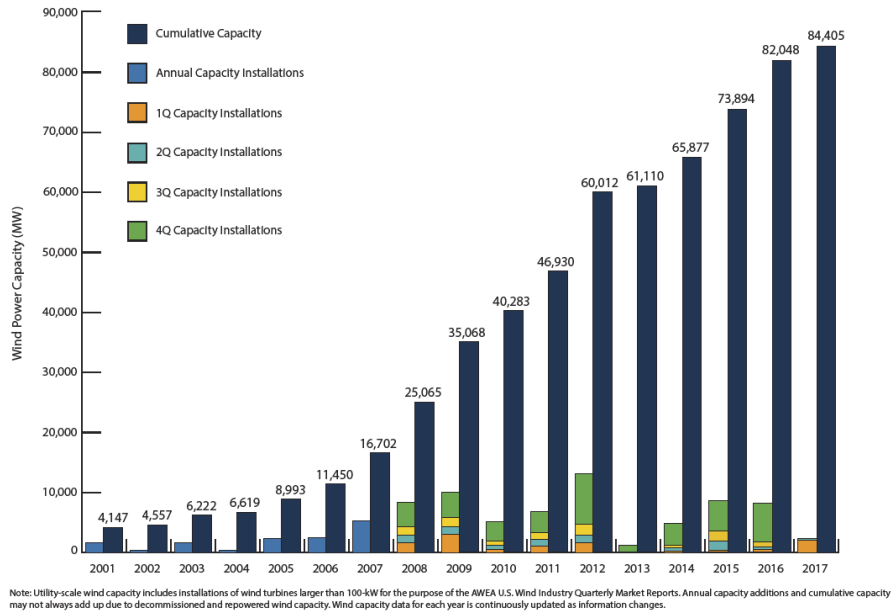


Figure 1.6 U.S. annual (by yearly quarters) and cumulative wind power capacity growth (AWEA 2017).

The power output of modern wind turbines is given by:

$$P = \frac{1}{2} C_p \rho A V^3$$

where ρ is the air density, C_p is the performance coefficient, A is the rotor swept area, and V is the velocity of wind. From this equation, wind generated power is controlled by these factors, since the air density is constant, and the performance coefficient has a theoretical maximum ($C_p \leq 0.593$) known as the Betz limit, the velocity of wind and the rotor swept area are the factors that can be controlled. The rotor swept area is controlled by the length of the blades and the velocity of the wind is controlled by the location of the wind turbine and its height, taller wind turbines get higher and steadier wind velocities. Wind turbines are usually built in open areas with high wind speeds.

1.3 Motivation

In 2014, National Renewable Energy Lab (NREL) published a technical report addressing transportation as one of the obstacles facing the growth of taller land based wind turbine towers. Taller wind turbines can harvest energy from the steadier, stronger winds at higher elevations with lower costs per energy unit, Fig. 1.7.

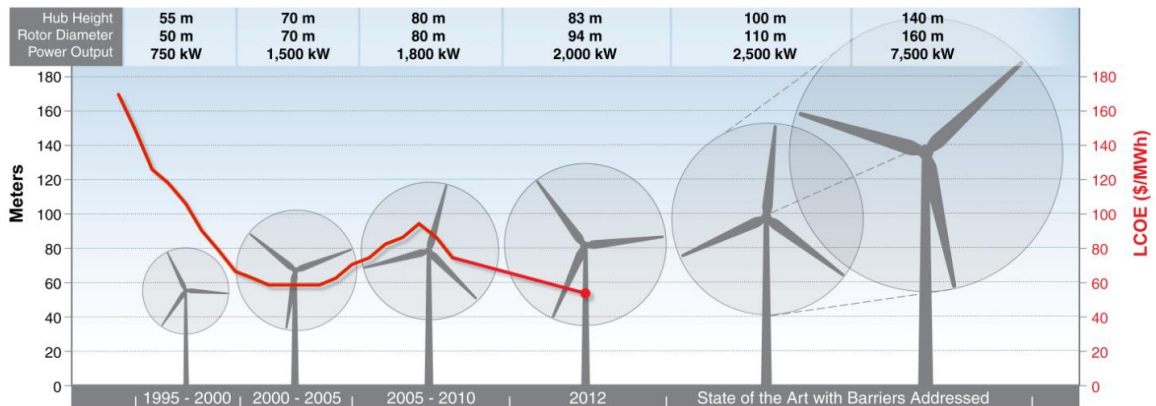


Figure 1.7 Existing wind turbine average heights, their capacities and cost of energy and desired heights and their estimated capacities if the transportation barrier is resolved (Cotrell et al. 2014).

Large diameters with lower section thicknesses (high slenderness) are most desired for optimal (most efficient) design of towers for taller wind turbines. Due to overhead

obstructions, the section that can be transported to construction site are currently limited to diameters of 4.3 m to 4.6 m, see Fig. 1.8.

Most existing wind towers are tubular and are manufactured by can-welding, wherein a steel plate is rolled and welded longitudinally into a can. These cans are then welded together circumferentially to form sections, which are transported to the wind farm where they are assembled into a full tower by bolting together thick flanges welded to the end of each section. The need to transport the section to the construction site constrains the diameter of the section, which then limits the height of the tower (Jay et al 2014). This limitation can be avoided if wind tower sections are made on-site, and one potential method for on-site manufacturing is automated spiral welding.

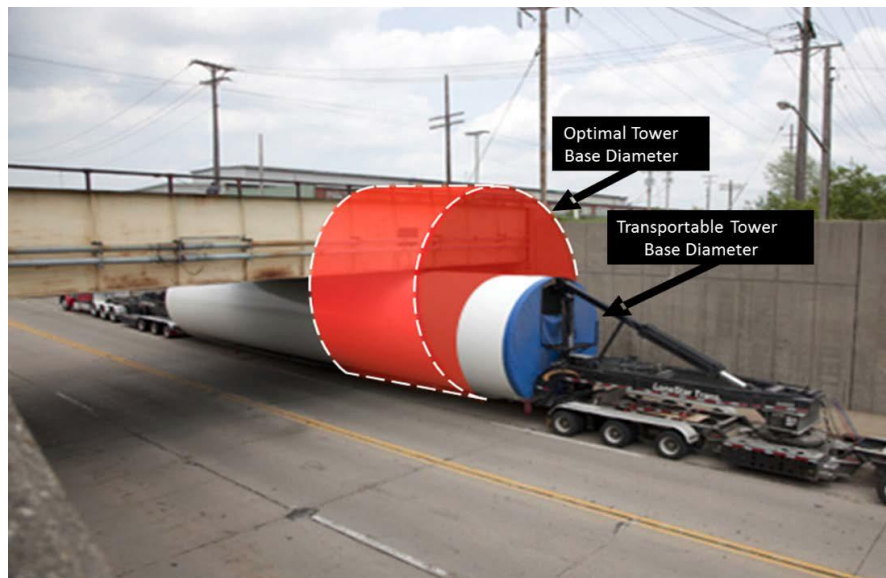


Figure 1.8 Transportation of tower section under overhead obstruction (Jay 2017).

1.4 Spirally welded wind turbines

Spiral welding technique had been used in on-site-manufacturing of light steel tubes since late 19th century. It is commonly used for manufacturing of sheet piles, silos, tanks, and

pipelines, Fig. 1.9. In this manufacturing process, constant-width plates are cut into trapezoids and then transported to the site where they are welded end-to-end along the short edge of the trapezoid, rolled, and then welded along the long edge of the trapezoid with a helical weld (Jay et al. 2016a), see Fig. 1.10.



(a) Pipelines⁶



(b) Sheet Piles⁷



(c) Steel Tanks⁸

Figure 1.9 Current applications of spirally welded tubes.

One of the major differences between current applications of spiral welding technique and for wind towers, that for current applications SW structures are mainly subjected to internal or external pressure, while wind turbines are subjected to nonuniform axial compressive stress due to axial compression and bending. The axial compressive forces are due to own weight of mechanical parts (rotor blades and hub), and structural components (tower and intermediate flange connections), and the flexural bending is due to large lateral forces

⁶ <http://www.turboair.com.au/products/ductwork/spiral-welded-pipe/> (accessed on 9/21/2017)

⁷ <https://foundationtechnology.com/services/helical-piers-anchors/> (accessed on 9/21/2017)

⁸ <http://upgrade-storage.com/construction-methods/the-spiral-method/> (accessed on 9/21/2017)

acting at the top of the tower. The normal stress due to axial compression is relatively negligible if compared to stresses due to flexural bending, hence, the wind turbines towers' design is usually controlled by the flexural strength (Jay et al. 2016a). The other major difference between SW wind turbines and current applications, that the process results in a tapered rather than a prismatic tube (necessitating two helical welds as shown in Fig. 1.10), and the cross-sectional slenderness for wind towers is expected to be much higher than most of these applications (i.e., with D/t ratios up to 500), for example for pipelines (i.e., with D/t ratios up to 150 (API 2004)). This process has not yet been used to manufacture utility-scale wind towers, and the impact of the imperfection pattern created by this process on the flexural behavior of such towers is a topic of active research by the authors (Jay et al. 2016a).

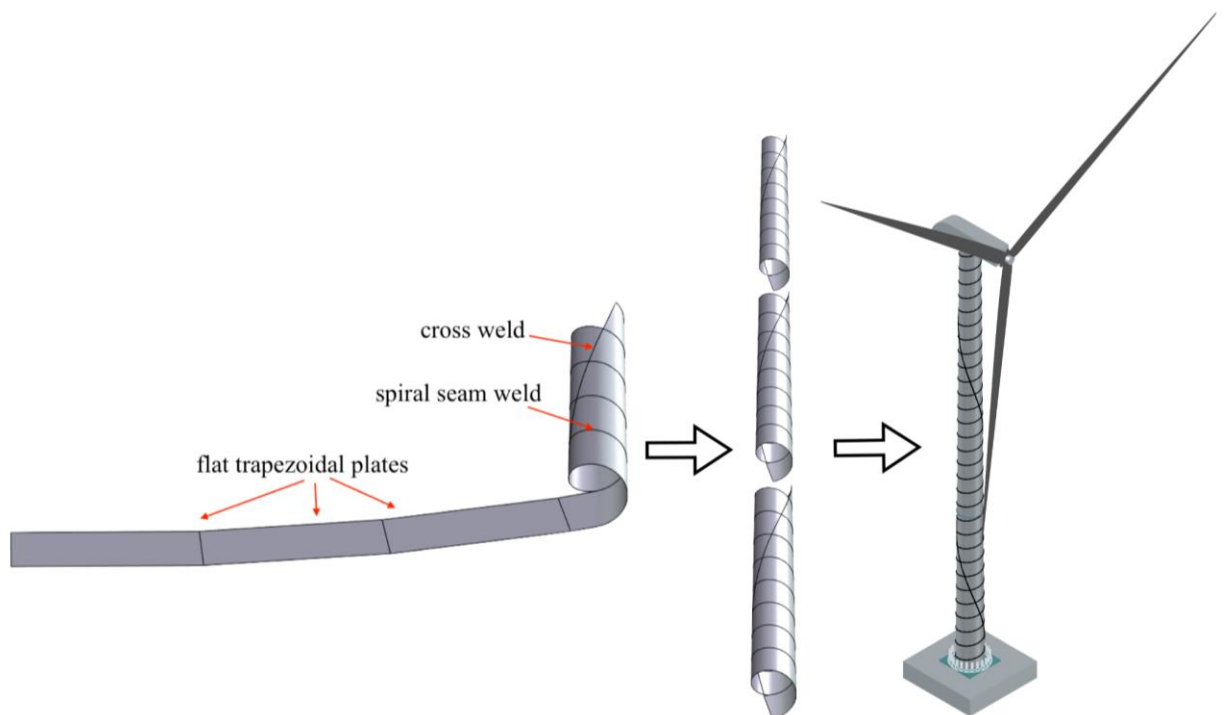


Figure 1.10 Schematic of the spiral welding procedure to manufacture tapered tubes then these tubes are cut and welded together to build wind turbine tower.

The idea of using spiral welding technique is proposed by Keystone Tower System KTS, which is only manufacturer planning to use this technique in wind industry, and a partner in this research project. From an analytical point of view, behavior of thin-walled cylindrical shells is relatively complex due to sensitivity of the response under axial compression to imperfections and residual stresses, and due to post-buckling behavior, which is typically unstable. This complexity increases for thin-walled tubes with other features such as; combined loading, section transitions, tapering, intermediate stiffeners, and openings. Since SW wind turbines is a state-of-the art technology there were no studies that covered high slenderness cylindrical shells with both tapering and spiral welds under flexural bending.

1.5 Scope of this study

This study is part of an ongoing research project that involves Johns Hopkins University, Northeastern University, and Keystone Tower Systems (KTS). The project aims to enable the spiral welding technique to be used in on-site-manufacturing of wind turbine towers. The main goal of this research project is to provide reliable numerical models to be used in design of mid-length spirally welded tapered cylindrical shells (SWT) under pure bending (and spirally welded wind turbines). Although, wind turbines are tall structures, intermediate flanges add much stiffness to original sections, restraining global ovalization modes and the tower acts as a series of mid-length SWT sections attached together where usually failure occurs due to local buckling. As mentioned before, the normal stress in wind turbine towers due to own weight is negligible if compared to normal stress due to bending, so this study is focused on SWT sections under pure bending. The numerical models are validated with the large-scale experimental results done by NEU research team

for nine spirally welded tapered specimens with high slenderness ratio ($D/t = 145$ to 350) under pure bending. The range of sections chosen in the numerical study are based on the tested specimens which intended to represent a scaled cut of a wind turbine tower with diameter and thickness $1/8^{\text{th}}$ the expected diameter and thickness of 140 m wind turbine (Jay et al. 2016b), see Fig. 1.11.



Figure 1.11 a section of wind turbine tower and its bending moment distribution.

1.6 Thesis roadmap

In this chapter, thesis starts with an introduction to the idea and the motivation for this research. Chapter Two covers a review on basic shell theory, and comparative study of available design guides for thin walled cylindrical shells and their limitations. Then Chapter Three presents a summary for available experiments from literature and SWT experiments conducted by NEU are provided, with detailed description and evaluation of SWT specimens. Then the next chapters focus on numerical modeling, since imperfections play a huge role in buckling and postbuckling behavior of circular shells, two approaches

for implementing material and geometric imperfections in numerical models are described and recommendation are provided in Chapter Four. From literature and early investigations, it was known that the irregularities due to helical mesh could affect the final results of numerical models, so Chapter Five describes a study that was conducted on the effect of mesh irregularities on linear and nonlinear collapse models and a meshing guidance was proposed to minimize its effect. Chapter Six covers Geometrically and Materially Nonlinear Analysis with Imperfections (GMNIA) models that were built using mesh guidance from Chapter Five and with imperfections implemented as described in Chapter Four to get estimation for the buckling strength and behavior of tested SWT specimens, the measured and generated imperfections are used and a comparison between GMNIA models with different approaches of imperfections implementation is discussed. In Chapter Seven, a new method for building shell strength curves using GMNIA models, that is referred to as Reference Resistance Design (RRD), is used to build strength curves for SWTs. Lastly in Chapter Eight, the design of archetype 3 MW 140 m tower is checked using existing and proposed design methods and a comparison between them is discussed. In Chapter Nine, thesis summary, conclusions and future work are presented.

Chapter 2

Shell Stability and Available Design Guides

2.1 Historical remarks⁹

Early in 17th century, the development of the first engineering theory was formulated by Daniel Bernoulli and Leonhard Euler, the beam theory. Their formulation included all elements needed: kinematics, reactions to loading, and equilibrium based on balancing forces and moments. Although, the beam theory was approximate, and its application bounds not clear, it made the analytical solutions available (Altenbach and Eremeyev 2017). The first recorded investigation of plates or shells was by the German physicist and musician Ernest Chladni, when he studied the vibration patterns (deflections) of the guitar backplate in his 1787 book “Discoveries in The Theory of Sound”, Fig. 2.1. The first theory for the analysis of thin plates was established by the French physicist and mathematician Sophie Germain and was corrected by Joseph Lagrange and published in 1821 the first closed equation for a thin plate;

$$N^2 \left(\frac{\partial^4 z}{\partial x^4} + \frac{\partial^4 z}{\partial x^2 \partial y^2} + \frac{\partial^4 z}{\partial y^4} \right) + \frac{\partial^2 z}{\partial t^2} = 0$$

The elastic solution of the Germain’s equation and the meaning of the parameter N were established by Claude-Louis Navier in 1826 along with the bending stiffness. In 1850, Gustav Kirchhoff presented the first complete plate theory with few assumptions and approximations that allowed reducing three-dimensional equations into two-dimensional equations. Later in 1906 Kirchhoff’s theory was analyzed by English mathematician

⁹ The historical remarks are based on CISM-course: “Shell-Like Structures: Advanced Theories and Applications” published by CISM International Centre for Mechanical Sciences.

Augustus E. H. Love to form the first shell theory, the Kirchhoff-Love shell theory. In 1910, Theodore von Kármán suggested that deflections can be huge compared to small shell thickness and could cause nonlinear strains, this nonlinear shell theory was in high demand in the aerospace industry. The earliest studies on the behavior of thin-walled cylindrical shells under bending were by von Kármán in 1911 and Brazier 1927, aimed to explain why classical linear beam theory was not able to capture the ovalization phenomenon in longer cylinders (Rotter et al. 2014). At this point three major failure modes in thin-shell cylinders were distinguished: local bifurcation buckling, ovalization, and material plasticity.

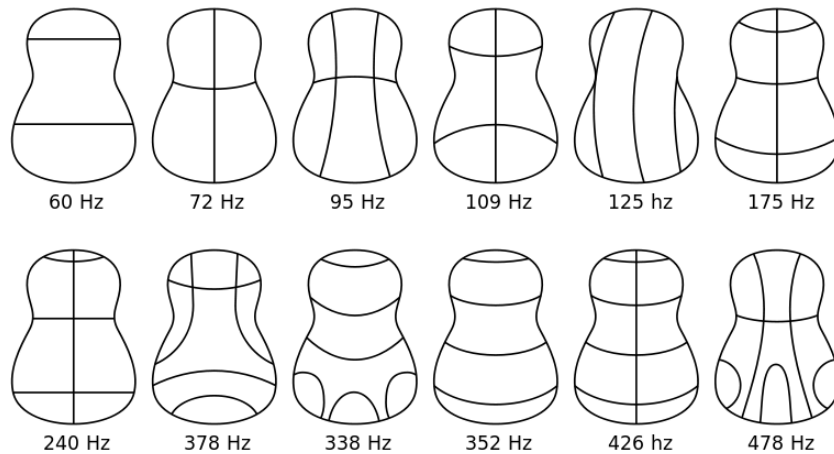


Figure 2.1 Chladni's patterns of guitar plate (Altenbach and Eremeyev 2017).

Lloyd Hamilton Donnell came up with the idea of using external skin as a structural member and formulated his equations based on surface kinematic equations, in 1933. Donnell's equations are still used in their simplified form, these equations provide accurate solution for cylindrical shells displacement components in the circumferential coordinates (Singer, Arbocz and Weller 2002).

2.2 Stability analysis of shells

There are two major ways where a shell become unstable;

- 1- Snap-through buckling: while increasing the load, the structure's geometry changes and the overall stiffness of the structure decreases, until the load reaches the snap-through load at this point the structure suddenly buckles and become unstable (ECCS 2013).
- 2- Bifurcation buckling: happens when two or more secondary equilibrium paths pass through the same point with primary path. Once the structure reaches the bifurcation point it may shift suddenly from the stable primary path to one of the secondary paths, the postbuckling behavior is either stable or unstable depending on the secondary path. After bifurcation a new pattern of deformations start to form in which what is referred to as the buckling mode (ECCS 2013), there are three different types of bifurcation: (a) asymmetric, (b) stable symmetric, and (c) unstable symmetric bifurcation, Fig. 2.2.

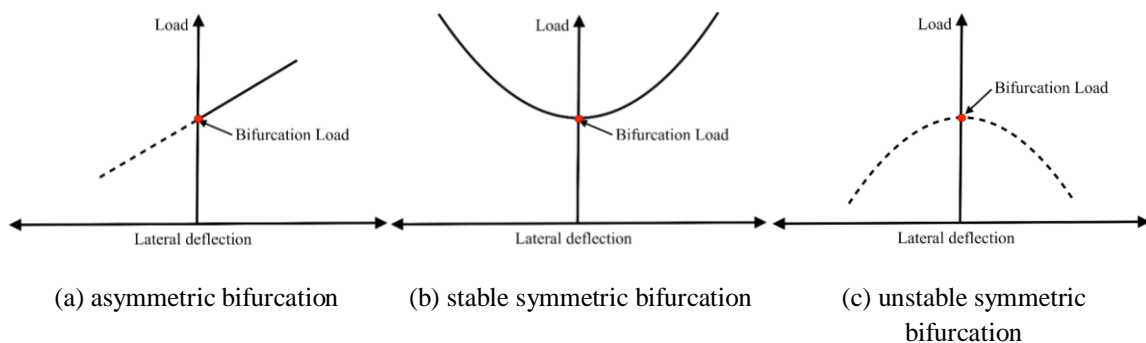


Figure 2.2 Bifurcation types.

For columns and beams the stability problem is a one-dimensional problem as the bending is assumed to take place in one plane only, so the deflections and bending moments are

function in one independent variable. Most columns and beams have neutral stability response for small deflections. The buckling of plates and shells is more complicated as it involves bending in two planes and consequently the deflections and bending moments are functions of two independent variables. Postbuckling behavior of plates is much more complicated than columns and beams. Buckling in columns and beams is considered a failure where the member cannot bear additional axial load after reaching the buckling load, while in plates and shells after reaching critical load the member can bear taking more axial load. The main difference between thin plates and thin shells that thin shells are assumed to have initial curvature in the unstressed state while thin plates are assumed to be flat in the unstressed state, this curvature has significant effect on the membrane behavior of the surface. The membrane stresses at the shell wall controls stability of shells, while the bending stresses have minimal effect on the shell stability. In contrast to columns, beams, and plates, which have stable symmetric bifurcation, shells usually have unstable symmetric bifurcation, see Fig. 2.3. For axially compressed shells in specific the asymmetric bifurcation may be encountered, due to the sensitivity to imperfections the post-buckling path could be stable or unstable depending on the direction the buckling wave form (ECCS 2013).

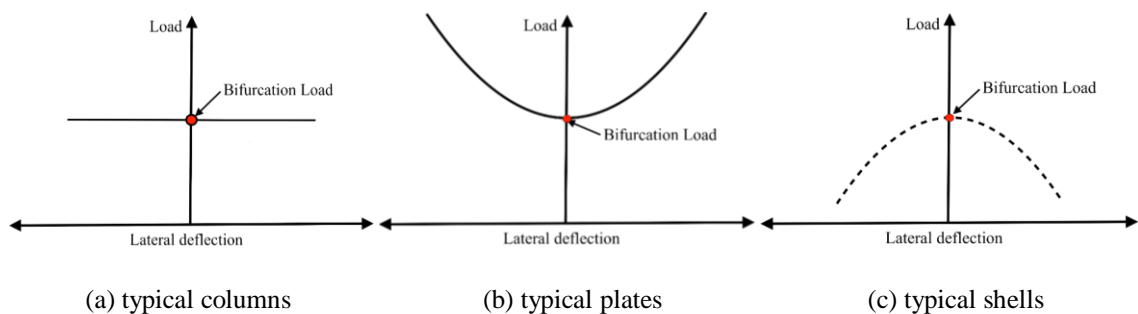


Figure 2.3 Typical bifurcation types for columns, plates, and shells.

2.2.1 Linear stability theory of cylindrical shells – Donnell's equations¹⁰

Circular cylindrical shells are much simpler than shells of general shape and they are used to illustrate different types of instabilities that can occur (Singer, Arbocz and Weller 2002). In this a brief description for the derivation of stability equations for a cylindrical shell using Donnell's equations. The Donnell's equations are relatively uncomplicated, and they are proved to provide shell theory, they give accurate results for cylindrical shells buckling problems. Donnell equations are based on both small and large-deformation relationships already obtained for thin plates (Chajes 1974). In deriving the shell equations Donnell made the following assumptions:

- 1- Thickness of shell is much smaller compared to dimensions of shell.
- 2- Lateral deflections are small compared to shell thickness.
- 3- The material of the shell is homogenous, isotropic, and obeys Hooke's law.
- 4- Lines normal to the middle surface before bending remain straight and normal during bending.
- 5- The shell is initially a perfect cylinder and no eccentricity considered.

For a medium length prismatic cylindrical shell with radius R , length L , and thickness h , see Fig. 2.4, the stability equations are derived using Young's modulus E and Poisson's ratio μ , as follows:

¹⁰ This section is based on literature but the equations derivation and their description are mainly adopted from "Principles of Structural Stability Theory" by Alexander Chajes (1974).

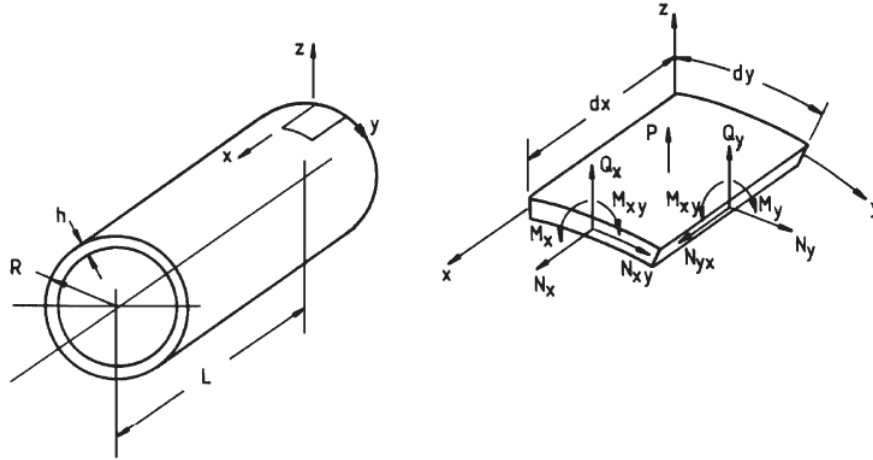


Figure 2.4 Circular cylindrical shells with sign conventions (Singer, Arboez and Weller 2002).

- The in-plane (x and y-direction) equilibrium equations are:

$$N_{x,x} + N_{xy,y} = 0 \quad (2.1a)$$

$$N_{xy,x} + N_{y,y} = 0 \quad (2.1b)$$

- The out-of-plane (z-direction) equilibrium equation is:

$$M_{x,xx} - 2M_{xy,xy} + M_{y,yy} + \frac{1}{R}N_y + N_x w_{,xx} + 2N_{xy}w_{,xy} + N_y w_{,yy} = 0 \quad (2.2)$$

- Force-Deformation relations:

$$\begin{aligned} u &= u_0 + u_b & \epsilon_x &= \epsilon_{x0} + \epsilon_{xb} \\ v &= v_0 + v_b & \epsilon_y &= \epsilon_{y0} + \epsilon_{yb} \\ w &= w_0 & \gamma_{xy} &= \gamma_{xy0} + \gamma_{xyb} \end{aligned} \quad (2.3)$$

Where at middle surface the displacements are termed (u_0, v_0, w_0) and the strains:

$$\begin{aligned} \epsilon_{x0} &= u_{0,x} \\ \epsilon_{y0} &= v_{0,y} - w/R \\ \gamma_{xy0} &= u_{0,y} + v_{0,x} \end{aligned} \quad (2.4)$$

and $(u_0, v_b, \epsilon_{xb}, \epsilon_{yb}$ and $\gamma_{xyb})$ are the bending terms for displacements and strains and they are neglected.

- The moment-curvature relations:

$$\begin{aligned} M_x &= -D(w_{,xx} + \mu w_{,yy}) \\ M_y &= -D(w_{,yy} + \mu w_{,xx}) \\ M_{xy} &= D\left(\frac{1-\mu}{2}\right)w_{,xy} \end{aligned} \quad (2.5)$$

where D is the bending stiffness parameter:

$$D = \frac{Eh^3}{(1-\mu^2)} \quad (2.6)$$

- Using constitutive equations, the total forces at the middle surface:

$$\begin{aligned} N_x &= \sigma_{x0}h + P_x = C(\epsilon_{x0} + \mu\epsilon_{y0}) + P_x \\ N_y &= \sigma_{y0}h + P_y = C(\epsilon_{y0} + \mu\epsilon_{x0}) + P_y \\ N_{xy} &= \tau_{xy0}h + S_{xy} = C\left(\frac{1-\mu}{2}\right)\gamma_{xy0} + S_{xy} \end{aligned} \quad (2.7)$$

where C is the extensional stiffness parameter:

$$C = \frac{Eh}{(1-\mu^2)} \quad (2.8)$$

- Substituting in equilibrium equations:

$$u_{,xx} + \frac{1-\mu}{2}u_{,yy} + \frac{1+\mu}{2}v_{,xy} - \frac{\mu}{R}w_{,x} = 0 \quad (2.9)$$

$$v_{,yy} + \frac{1-\mu}{2}v_{,xx} + \frac{1+\mu}{2}u_{,xy} - \frac{1}{R}w_{,y} = 0 \quad (2.10)$$

$$\begin{aligned} -D(w_{,xxxx} + 2w_{,xxyy} + w_{,yyyy}) + P_x w_{,xx} + P_y w_{,yy} + \frac{P_y}{R} + \frac{C}{R}\left(v_{,y} - \frac{w}{R} + \mu v_{,y}\right) + \\ S_{xy} w_{,xy} = 0 \end{aligned} \quad (2.11)$$

- Donnell reduced Eq. (2.9-2.11) from three variables to single equation in one variable w as follows:

$$D\nabla^3 w - \nabla^4 (P_x w_{,xx} + P_y w_{,yy} + 2S_{xy} w_{,xy}) + \frac{Eh}{R^2} w_{,xxxx} = 0 \quad (2.12)$$

2.2.2 Critical axial stress

For a simply supported cylinder under pure axial compression ($P_y = S_{xy} = 0$), Eq. (2.12) can be rewritten:

$$D\nabla^3 w - \sigma_x h \nabla^4 w_{,xx} + \frac{Eh}{R^2} w_{,xxxx} = 0 \quad (2.13)$$

The boundary conditions for simply supported cylindrical shell are

$$w = w_{,xx} = 0 \quad \text{at } x = 0 \text{ and } x = L$$

Displacement function can be considered

$$w = w_0 \sin \frac{m\pi x}{L} \sin \frac{n\pi y}{\pi R}$$

where m is the number of half-waves in meridional direction, and n is the number of half-waves in circumferential direction. For simplicity it can be rewritten

$$w = w_0 \sin \frac{m\pi x}{L} \sin \frac{\beta\pi y}{L} \quad (2.14)$$

$$\beta = \frac{nL}{\pi R}$$

By substituting Eq. (2.14) in Eq. (2.13)

$$D \left(\frac{\pi}{L}\right)^8 (m^2 + \beta^2)^4 - \sigma_x h \left(\frac{\pi}{L}\right)^6 m^2 (m^2 + \beta^2)^2 + \frac{Eh}{R^2} \left(\frac{\pi}{L}\right)^4 m^4 = 0 \quad (2.15)$$

If a parameter Z (Batdorf dimensionless length parameter) is used as a measure relating length to radius and thickness is considered

$$Z = \frac{L^2}{Rh} \sqrt{1 - \mu^2} \quad (2.16a)$$

and buckling stress coefficient

$$k_x = \frac{\sigma_x h L^2}{D \pi^2} \quad (2.16b)$$

Using the two parameters (Z, k_x) and dividing Eq. (2.7) by $D \left(\frac{\pi}{L}\right)^8$

$$(m^2 + \beta^2)^4 - k_x m^2 (m^2 + \beta^2)^2 + \frac{12m^4 Z^2}{\pi^4} = 0 \quad (2.17)$$

Solving Eq. (2.17)

$$k_x = \frac{(m^2 + \beta^2)^2}{m^2} + \frac{12m^2 Z^2}{\pi^4 (m^2 + \beta^2)^2} \quad (2.18)$$

$$\rho = \frac{(m^2 + \beta^2)^2}{m^2} \quad (2.19)$$

$$k_x = \rho + \frac{12Z^2}{\pi^4 \rho} \quad (2.20)$$

Minimum value of k_x is obtained by solving $\frac{\partial k_x}{\partial \rho} = 0$

$$\rho = \sqrt{\frac{12Z^2}{\pi^4}} \quad (2.21)$$

Substituting Eq. (2.21) in Eq. (2.20)

$$k_x = \frac{4\sqrt{3}}{\pi^2} Z \quad (2.22)$$

The classical elastic critical stress

$$\sigma_{cr} = \frac{1}{\sqrt{3(1-\mu^2)}} \frac{Eh}{R} = 0.605 \frac{Eh}{R} \quad (2.23)$$

2.2.2 Critical bending stress

In 1932, Flügge studied the relation between critical buckling stress for cylindrical shells under bending and axial compression for a specific radius-to-thickness and half-wavelength, his study found that ($\sigma_{cr-bending} = 1.3\sigma_{cr-axial}$) and this ratio was quoted by Timoshenko in his book “Theory of Elastic Stability” which was published in the same year 1932 without considering the specific conditions in Flügge’s study. For three decades, it was used as rule that the critical stress due to bending is 30% higher than critical stress due to axial compression, until 1961 when Seide and Weingarten showed that for a simply supported cylinder under bending with relatively short length and assuming simple linear pre-buckling membrane stress state and small deflection theory; the critical stress for bending is equal to critical stress under axial compression ($\sigma_{cr-bending} = \sigma_{cr-axial}$). However, experimental work showed that critical stress due to buckling of cylinders under bending can exceed critical stress under axial compression, some assume this is due to less sensitivity of cylinders under bending to imperfections. It is also observed that the critical stress ratio for bending to that for axial compression decreases for higher R/t (Singer, Arbocz and Weller 2002, Rotter et al. 2014). The circumferential influence would seem to matter a lot if the buckling half-wavelength in the circumferential direction exceeds (πR).

2.2.3 Length factor in circular shells

The previous expression for critical compressive stress is not valid for cylinders of any length, by substituting Eq. (2.19) in Eq. (2.21) and solving the equation for β

$$\beta = \left[\frac{\sqrt[4]{12Z^2}}{\pi} m - m^2 \right] \quad (2.24)$$

It is found that Z , which is the parameter representing the relation between length, radius and thickness, cannot be less than 2.85 unless β is imaginary or $m < 1$ where both conditions are unrealistic. The expression in Eq. (2.23) is only valid for $Z > 2.85$, for $Z < 2.85$ the critical stress coefficient can be determined by setting $m = 1$ and $\beta = 0$

$$k_x = 1 + \frac{12Z^2}{\pi^4} \quad (2.25)$$

Then the critical stress can be calculated as

$$\sigma_{cr} = k_x \frac{D\pi^2}{hL^2} \quad (2.26)$$

For long narrow cylindrical shells the critical circumferential mode decreases until it reaches a single half-wave around the circumference, at this point Euler column buckling failure could occur before local buckling failure, so both modes should be checked. Short and wide cylinders behave like plates that are supported along the loaded edges and they buckle into a single half-wave in the meridional direction (Chajes 1974, Rotter et al. 2016 and ECCS 2013). Fig. 2.5 for the relation between length L in terms of non-dimensional length factor $(\omega = \frac{\sqrt{Z}}{\sqrt[4]{1-\mu^2}} = \frac{L}{\sqrt{rt}})$, where r is the radius and t is the thickness, and the normalized critical stress for short, medium, and long cylinders.

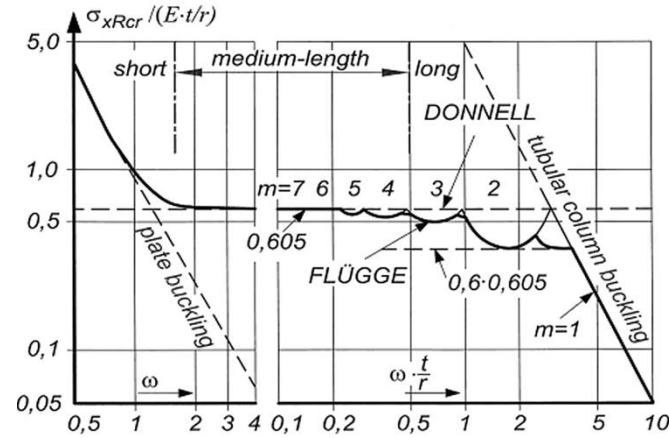


Figure 2.5 The effect of cylinder length on linear bifurcation stress (ECCS 2013).

For infinitely long cylinders under bending when ovalization mode is the critical mode, modified Brazier moment is more accurate for predicting critical moment.

$$M_{Braz} = 0.987 \left(\frac{ERh^2}{\sqrt{1-\mu^2}} \right) \quad (2.27)$$

$$M_{Braz-modified} = 0.94M_{Braz} \quad (2.28)$$

2.2.4 Tapered cylindrical shells stability

In 1956 Seide proved that a small modification to the critical axial load of prismatic cylindrical shell can yield to accurate prediction of the minimum critical axial compressive load of conical (tapered) shell. The critical stress equation is modified to be

$$\sigma_{cr} = \frac{E t \cos(\alpha)}{R_{min} \sqrt{3(1-\mu^2)}} \quad (2.29)$$

where α is the tapering angle and R_{min} is the minimum radius of a tapered cylindrical shell.

2.3 Available design guides

Thin-walled structures, in both forms plates and shells, are generally the most advanced form of structures. For decades design guides that are applicable to thin-walled shells were

based on critical buckling knockdown factors obtained from test results for similar shells under similar loading conditions. In the last decades with the advancement and availability of feasible numerical modeling tools design guides started adopting design using numerical modeling. Examples of design guides for circular cylindrical shells under flexural bending are provided in this section. Typically, the normal stress due to bending is calculated ($\sigma_x = \pm \frac{M}{S}$), and the elastic section modulus for prismatic section is ($S = \pi r^2 t$).

2.3.1 American Institute for Steel Construction (AISC 360-10) and American Iron and Steel Institute (AISI S100-16)

The AISC explicitly limit their provisions for design of round HSS to sections with diameter-to-thickness ratio less than $0.45 E/F_y$, this ratio is usually exceeded in thin-walled shells including wind turbine towers. The AISI limit is very close to that of the AISC, the design is not applicable to extremely thin tubes which are governed by elastic local buckling (sections with diameter-to-thickness greater than $0.441 E/F_y$).

2.3.2 American Society of Mechanical Engineers (ASME STS-1 2011)

For many years the capacity equations for design of steel stacks by ASME were used in United States for design of wind turbine towers. Thin-walled stacks are closest structure form to wind turbine towers (Agbayani et al. 2011). The ASME design formulas for nominal bending strength for local buckling limit state are:

$$M_n = S_{bl} S \quad (2.30)$$

$$S_{bl} = \frac{F_y(1-0.3K_s)Y}{(F.S.)} \quad \text{when} \quad \frac{10F_y}{E} < \frac{t}{D} \leq \frac{2.8F_y}{E} \quad (2.31a)$$

$$S_{bl} = \frac{EtY}{4D(F.S.)} \quad \text{when} \quad \frac{2.8F_y}{E} < \frac{t}{D} \quad (2.31b)$$

Where the slenderness factor K_s is computed:

$$K_s = \left(\frac{10F_y/E - t/D}{7.2F_y/E} \right)^2 \quad (2.32a)$$

$$\text{and} \quad Y = 1 \quad \text{when} \quad \frac{L_e}{R} \leq 60 \text{ and } F_y \leq 50 \text{ ksi} \quad (2.32b)$$

$$Y = \frac{21,600}{18,000 + \left(\frac{L_e}{R}\right)^2} \text{ when } \frac{L_e}{R} > 60 \text{ and } F_y \leq 50 \text{ ksi} \quad (2.32c)$$

Steel stacks rarely fail in the plastic zone $\left(\frac{t}{D} \leq \frac{10F_y}{E}\right)$, so the ASME design guide provided expressions in the elastic and inelastic buckling but ignored the plastic zone (Sim et al. 2014).

2.3.3 American Petroleum Institute (API RP-2A)

The API Recommended Practice for Planning, Designing, and Constructing Fixed Offshore Platforms limits the design of circular shells to sections with diameter-to-thickness ratio less than 300. The nominal bending stress is computed as follows:

$$F_b = 0.75 F_y \quad \text{for} \quad \frac{D}{t} \leq \frac{10,340}{F_y} \quad (2.33)$$

$$F_b = \left[0.84 - 1.74 \frac{F_y D}{Et} \right] F_y \quad \text{for} \quad \frac{10,340}{F_y} < \frac{D}{t} \leq \frac{20,680}{F_y} \quad (2.34)$$

$$F_b = \left[0.72 - 0.58 \frac{F_y D}{Et} \right] F_y \quad \text{for} \quad \frac{20,680}{F_y} < \frac{D}{t} \leq 300 \quad (2.35)$$

For sections with diameter-to-thickness ratio higher than 300 the API refers to Bulletin on Stability Design of Cylindrical Shells (API Bull. 2U). In this code the buckling capacities

are based on linear bifurcation analyses reduced by capacity reduction factors to account for the imperfections, geometrical nonlinearity and boundary conditions, a plasticity reduction factor to count for the material nonlinearity and residual stresses. The nominal buckling stresses are assumed the same for cylinders subjected to axial compression or bending, and is computed as follows:

a. Elastic buckling stresses:

$$F_{xeL} = \alpha_{xL} \sigma_{xeL} = \alpha_{xL} C_x 2E \left(\frac{t}{D} \right) \quad (2.36)$$

$$\alpha_{xL} = \begin{cases} 0.207 & D/t \geq 1242 \\ \frac{169\bar{c}}{195 + 0.5(D/t)} < 0.9 & D/t < 1242 \end{cases} \quad (2.37)$$

$$\bar{c} = \begin{cases} 2.64 & M_x \leq 1.5 \\ \frac{3.13}{M_x^{0.42}} & 1.5 < M_x \leq 15 \\ 1 & 15 < M_x \end{cases} \quad (2.38)$$

Where $C_x = 0.605$ for $\frac{D}{t} > 300$ (2.39)

and the length parameter $M_x = \frac{L_r}{\sqrt{Rt}}$

L_r = distance between stiffening rings in the meridional direction.

b. Inelastic buckling stresses is computed as the smaller of ηF_{xeL} and F_{xcL}

$$F_{xcL} = \begin{cases} \frac{233F_y}{166 + 0.5(D/t)} \leq F_y & D/t < 600 \\ 0.5F_y & D/t \geq 600 \end{cases} \quad (2.40)$$

Plasticity reduction factor should be applied such as

$$F_{xcL} = \eta F_{xeL} \quad (2.41)$$

$$\eta = \begin{cases} 1 & \Delta \leq 0.55 \\ \frac{0.45}{\Delta} + 0.18 & 0.55 < \Delta \leq 1.6 \\ \frac{1.31}{1 + 1.15\Delta} & 1.6 < \Delta \leq 6.25 \\ \frac{1}{\Delta} & \Delta > 6.25 \end{cases} \quad (2.42)$$

where

$$\Delta = \frac{F_{xeL}}{F_y} \quad (2.43)$$

2.3.4 Recommended Practice for Compliance of Large Lan-based Wind Turbine Support Structures (ASCE/AWEA RP2011)

The AWEA provisions is the first specialized design guide for the design procedures of wind energy in the United States. The design guide provides recommendations for design of wind turbine supporting structures where no maximum diameter-to-thickness ratio (λ_{max}) is not specified but stated that it is rare to find this ratio exceeding 330 in most of practical tube towers.

$$f_u = \frac{P_u}{A} + \frac{M_u}{S} \leq \phi_c F_n \quad (2.44)$$

Where (ϕ_c) is factor of safety, and (F_n) is the nominal compressive strength and it should be the lowest value of obtained from limit states (yielding, flexural buckling or local buckling).

$$F_n = F_{cr} \text{ and } \phi_c = 0.90$$

(F_{cr}) is calculated as the smaller of:

$$F_{cr} = F_y \quad \text{For } \lambda \leq 0.11 \frac{E}{F_y} \quad (2.45)$$

or F_{cr} due to flexural buckling calculated with stepped column procedures

$$F_{cr} = QF_y \quad \text{For } 0.11 \frac{E}{F_y} < \lambda \leq 0.357 \frac{E}{F_y} \quad (2.46)$$

where
$$Q = 0.038 \frac{E}{F_y(D/t)} + \frac{2}{3}$$

$$F_{cr} = 0.276 \frac{E}{(D/t)} \quad \text{For } 0.357 \frac{E}{F_y} < \lambda \leq \lambda_{max} \quad (2.47)$$

2.3.5 Eurocode 3 –Part 1-6: Strength and Stability of Shell Structures (BS EN 1993-1-6:2007)

EC3-1-6 was the first code to introduce detailed guidelines for design using numerical analysis in addition to traditional stress design using calculation. The design of shell structures in EC3-1-6 is grouped into four limit states (Plastic limit state, cyclic plasticity limit state, buckling limit state, and fatigue limit state), for every limit state EC3-1-6 permits using finite element models or stress analysis in design, see Fig 2.6. Global numerical analyses vary in complexity from LA to GMNIA where these acronyms are described in EC3-1-6 as follows¹¹:

- *LA: Linear elastic shell Analysis*

The linearity of the theory results from the assumptions of a linear elastic material law and the linear small deflection theory. Small deflection theory implies that the assumed geometry remains that of the undeformed structure.

- *LBA: Linear Buckling Analysis or Linear elastic Bifurcation Analysis*

This linear bifurcation analysis obtains the lowest eigenvalue at which the shell may buckle into a different deformation mode, assuming no change of geometry, no change in the direction of action of the loads, and no material degradation. Imperfections of all kinds are ignored. This analysis provides the elastic critical buckling resistance.

- *MNA: Materially Non-Linear Analysis*

The result of an MNA analysis gives the plastic limit load and provides the plastic reference resistance ratio.

¹¹ The global numerical analyses' acronym description is quoted from Eurocode 3 BS EN 1993-1-6:2007 (CEN 2007).

- *GNA: Geometrically Nonlinear Analysis*

Where compression or shear stresses are predominant in some part of the shell, a GNA analysis delivers the elastic buckling load of the perfect structure, including changes in geometry, that may be of assistance in checking the limit state LS3

- *GMNA: Geometrically and Materially Nonlinear Analysis*

The result of a GMNA analysis gives the geometrically nonlinear plastic limit load of the perfect structure and the plastic strain increment, that may be used for checking the limit states LS1 and LS2.

Where compression or shear stresses are predominant in some part of the shell, a GMNA analysis gives the elasto-plastic buckling load of the perfect structure, that may be of assistance in checking the limit state LS3.

- *GNIA: Geometrically Nonlinear elastic Analysis with Imperfections included*

A GNIA analysis is used in cases where compression or shear stresses dominate in the shell. It delivers elastic buckling loads of the imperfect structure, that may be of assistance in checking the limit state LS3.

- *GMNIA: Geometrically and Materially Nonlinear Analysis with Imperfections included*

A GMNIA analysis is used in cases where compression or shear stresses are dominant in the shell. It delivers elasto-plastic buckling loads for the "real" imperfect structure, that may be used for checking the limit state LS3.

Plastic Limit State (LS1)	<ul style="list-style-type: none"> • Stress design • Design by global numerical MNA or GMNA analysis
Cyclic Plasticity Limit State (LS2)	<ul style="list-style-type: none"> • Stress design • Design by global numerical MNA or GMNA analysis • Direct design
Buckling Limit State (LS3)	<ul style="list-style-type: none"> • Stress design • Design by global numerical MNA or LBA analysis • Design by global numerical GMNIA analysis
Fatigue Limit State (LS4)	<ul style="list-style-type: none"> • Stress design • Design by global numerical LA or GNA analysis

Figure 2.6 EC3-1-6 design limit states and permitted methods for each limit state.

A detailed description of design using global numerical analyses and discussion in Chapter 6 of this thesis. Stress design for buckling limit state (LS3) summarized here to compare EC3-1-6 to other codes.

The meridional design buckling stress $\sigma_{X,Rd} = \frac{\sigma_{X,Rk}}{\gamma_{MI}}$ (2.48)

The meridional characteristic buckling stress $\sigma_{X,Rk} = \chi_X f_{yk}$ (2.49)

Where the partial factor γ_{MI} is recommended to be greater than or equal to 1.10 and the buckling reduction factor χ_X should be determined from these functions:

$$\chi = 1 \quad \text{when } \lambda \leq \lambda_0 \quad (2.50)$$

$$\chi = 1 - \beta \left(\frac{\lambda - \lambda_0}{\lambda_p - \lambda_0} \right)^\eta \quad \text{when } \lambda_0 < \lambda < \lambda_p \quad (2.51)$$

$$\chi = \frac{\alpha}{\lambda^2} \quad \text{when } \lambda_p \leq \lambda \quad (2.52)$$

where the relative slenderness $\left(\lambda = \sqrt{\frac{f_{yk}}{\sigma_{X,Rcr}}}\right)$, $(\sigma_{X,Rcr})$ is the meridional elastic critical buckling stress, the plastic limit slenderness $\left(\lambda_p = \sqrt{\frac{\alpha}{1-\beta}}\right)$, (α) is the elastic imperfection reduction factor, (η) is the interaction component, (β) is the plastic range factor, and (λ_0) is the squash limit relative slenderness. The meridional buckling parameters and critical meridional buckling stresses are obtained from EC3-1-6 Annex D.

- Critical meridional buckling stress (as derived in Eq. 2.23 sec. 2.2.1):

$$\sigma_{X,Rcr} = 0.605EC_x \frac{t}{r} \quad (2.53)$$

The length of the shell segment is characterized by the length parameter $\left(\omega = \frac{\ell}{\sqrt{rt}}\right)$

Where the factor (C_x) is calculated for short cylinders:

$$C_x = 1.36 - \frac{1.83}{\omega} + \frac{2.07}{\omega^2} \quad \text{when } \omega \leq 1.7 \quad (2.54)$$

for medium length cylinders: $C_x = 1.0 \quad \text{when } 1.7 \leq \omega \leq 0.5 \frac{r}{t} \quad (2.55)$

for long cylinders $C_x = C_{x,N}$

and $(C_{x,N})$ is the greater of
$$C_{x,N} = \begin{cases} 0.60 \\ 1 + \frac{0.2}{C_{x,b}} \left[1 - 2\omega \frac{t}{r}\right] \end{cases} \quad (2.56)$$

and $(C_{x,b})$ is parameter depending on boundary conditions and obtained from Table D.1 in (CEN 2007).

- Meridional buckling parameters:

$$\lambda_0 = 0.20 \qquad \beta = 0.60 \qquad \eta = 1.0$$

The meridional elastic imperfection reduction factor is obtained by:

$$\alpha_X = \frac{0.62}{1+1.92(\Delta w_k/t)^{1.44}} \qquad (2.57)$$

$$\Delta w_k = \frac{1}{Q} \sqrt{\frac{r}{t}} \cdot t \qquad (2.58)$$

where (Δw_k) is the characteristic imperfections amplitude and (Q) is the meridional compression fabrication quality parameter.

Table 2.1 Values of fabrication quality parameter (CEN 2007)

Fabrication tolerance quality class	Q
Class A	40
Class B	25
Class C	16

2.3.6 Comparison between design guides

To compare the codes described in the previous sections, design curves are built for prismatic circular cylindrical shells using yielding stress ($F_y = 450\text{MPa}$) and elastic modulus ($E = 200\text{GPa}$), assumed the boundary conditions are hinged at both ends and the length of the cylindrical shells is chosen to be four times the diameter. Fig. 2.7 shows the nominal design curves in terms of the normalized bending strength versus the diameter-to-thickness ratio. The EC3-1-6 for Class A, B and C shows consistency in strength reduction with lower quality class and the gap between curves increases as the slenderness ratio

increases (as the imperfections gets more deleterious in more slender sections), and vice versa. The ASME and AWEA design curves are more conservative in the elastic buckling zone of the curves, since they are not based on quality class for safety considerations they approach the EC3-1-6 Class C curve (worst acceptable tolerance).

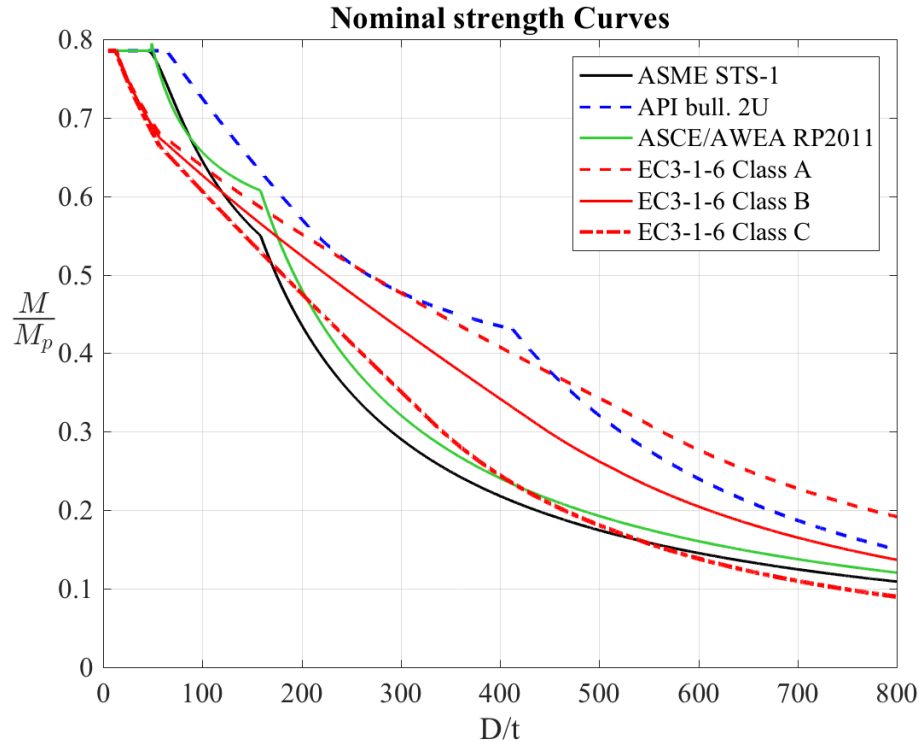


Figure 2.7 Comparison between normalized nominal flexural strength using different design guides for shelled structures.

2.4 Summary and conclusions

This chapter is divided into two parts: 1- Mechanical design of shells, and 2- Available design codes. In the first part, a summary was provided for the historical development of the linear elastic shell stability theory and a summary of classical solution using Donnell's equations to solve for the critical buckling stress of a typical shell was provided. Application of the shell theory for cylindrical shells under axial compression and bending

and the argument in literature on the differences in critical stresses under bending and compression was discussed. The effect of the length on the transition of the bifurcation buckling modes is described, however, the scope of this study is for medium length cylindrical shell where the local buckling bifurcation is more dominant. The transition from prismatic to tapered (conical) cylindrical shells was also described.

The design for bending capacity of cylindrical shell using three design guides from United States and Eurocode 3 (EC3-1-6), where all these guides are based on knockdown factor obtained from experimental data, are summarized and a comparison between the design curves for buckling due to bending are provided. It was found that the U.S. design guides are generally more conservative and less detailed if compared to EC3-1-6, which is more descriptive and specific fabrication tolerances are provided to assess shells and assign quality class for the shell, where for each quality class there is a specific curve, we believe that this design method is generally more efficient.

Chapter 3

Existing Experimental Work

3.1 Introduction

Thin shell structures are one of the most advanced and efficient form of structures; however, they are also one of the most complicated form due to their extreme sensitivity to imperfections and unstable post-buckling behavior (Singer, Arbocz & Weller 2002). For decades experiments were conducted to examine factors affecting buckling and postbuckling behavior of cylindrical shells (tubes) under external pressure, internal pressure, axial compression, flexural bending, and torsion (for example: Hoff et al. 1965, Seide 1961 and Schmidt et al. 1994), and some of the experimental investigations were focused on the effects of boundary conditions and special geometrical features such as: openings, thickness transitions or stiffeners (for example: Almroth 1965 and Chen et al. 2011), however, most of the research on thin-walled tubes had been focused on aerospace applications and were conducted on shells under uniform axial compression and external pressure. Even with the advancement of the computational (numerical) solid mechanics modeling, experimental work is still necessary to provide better understanding of the buckling and postbuckling behavior of a specific shell structure and provide benchmark reference for numerical modeling verification. Validation of numerical modeling with experimental work improves the reliability of the numerical models. Past research on tapered (or conical) shells with small tapering (conical) angle (similar to SWT pursued herein) typically followed an assumption of an equivalent theoretical section, where the relation of the tapered section to that equivalent section dependent on the loading. Tapered shells under flexural bending are more complicated as the stresses are variable

circumferentially across the cross section and longitudinally along the meridional axis with variable radius. Since the strength of thin shells is dependent on the location of the worst imperfection within the specimen it is harder to make this prediction for a cylindrical shell under bending with nonuniform compressive stress and it gets more complex when the shell is tapered, the imperfections sensitivity is related to radius-to-thickness ratio, so it is expected for a tapered shell to have severe imperfections at bigger diameters, while it is also known that the normal stress is higher at the near the smaller end for an axially compressed tapered cylindrical shell. These complications in addition to imperfection patterns due to fabrication necessitate doing more experimental work to study the buckling behavior and get better understanding of the postbuckling behavior and have a reference for the verification of GMNIA models.

3.2 Experimental work of thin-walled tubes

3.2.1 Thin-walled tubes under axial compression

The earliest shell buckling tests under axial compression were conducted around 1850 by Fairbairn and Hodgkinson for the Britannia and Conway Tubular Bridge (Timoshenko 1953). Decades later, in the 1920s, with the expansion in the aircraft industry researchers conducted more tests on thin-walled tubes. In the structural world, the studies range from thick-walled shells for columns and posts under pure axial compression to thin-walled slender shells for silos and tanks under combined loading of internal or external pressure and axial compression. However, most of the early tests were focused on shells under external pressure to determine the strength of cylindrical vessels under external pressure (Singer, Arbocz, and Weller 2002). In the late fifties and early sixties with the development

of theoretical solutions, researchers started testing tapered tubes under uniform axial compression to study their stability and some studies compared the buckling and post-buckling behavior of tapered thin-walled tubes to prismatic cylindrical tubes (for example Horton et al. 1965), see Fig. 3.1. From early studies, it was recognized that the behavior of tapered tubes is more complicated than prismatic tubes. The buckling behavior of tapered tubes depends on the type of loading and the taper ratio, and by balancing the location of high membrane stresses and highest effective radius-to-thickness ratio, the prominent buckling deformation and location of initiation of buckling could be determined (Singer, Arbocz, and Weller 2002). Typically, the testing procedure for unpressurized specimens under axial compression is to apply axial deformation and study the buckling and post buckling behavior in terms of load deformation curves. Due to the complicated behavior and extreme sensitivity of shell structures, the design recommendations in literature and design codes until the early 2000's were based on lower bound modification to the elastic buckling load obtained from test results, see Fig. 3.2 (Rotter 2011). For specimens under axial compression the stress is theoretically assumed to be uniform.

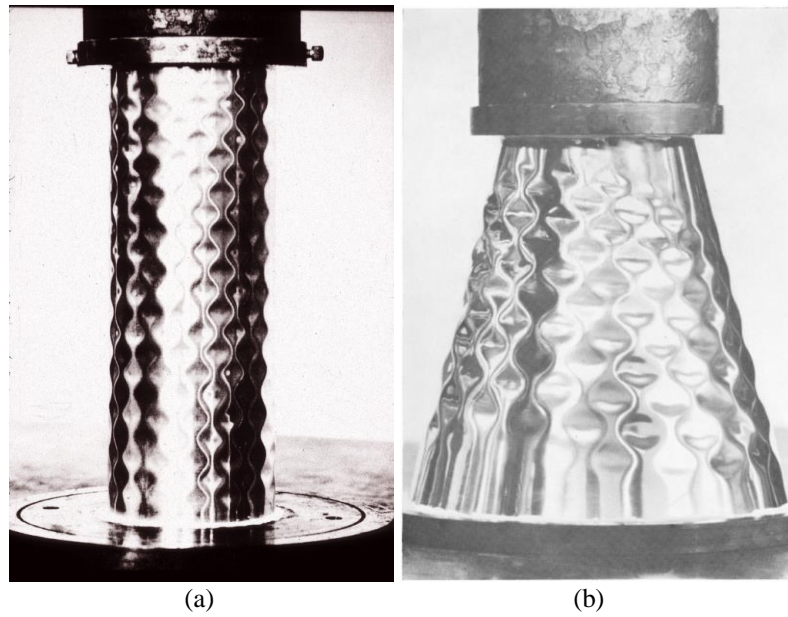


Figure 3.1 Buckling of unstiffened cylindrical shell under uniform axial compression (a) Prismatic and (b) tapered (Horton et al. 1965)

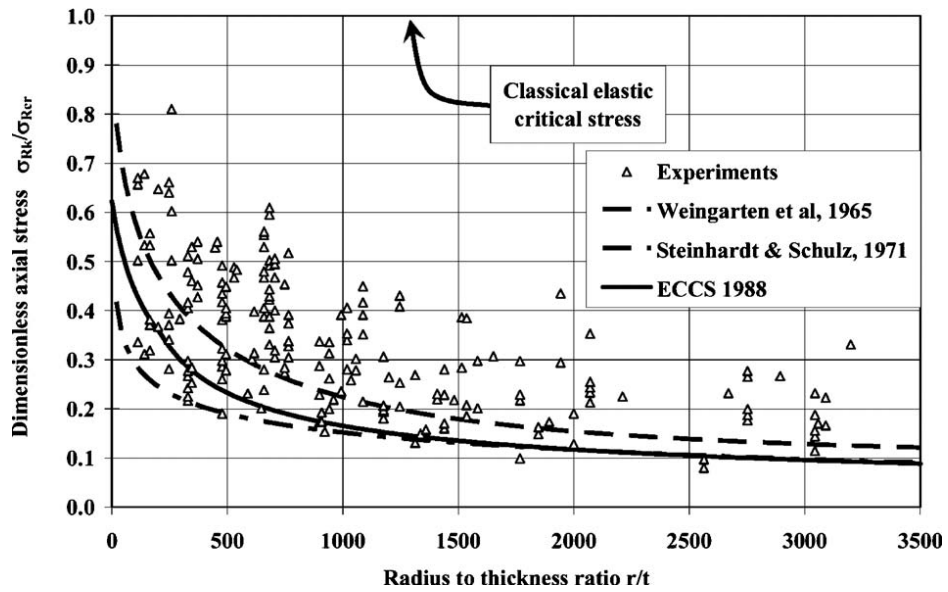


Figure 3.2 Summary of experimental results from literature (by Harris et al. 1957) and traditional approaches for buckling design, using knockdown factors, of tubes under axial compression (Rotter 2011).

3.2.2 Thin-walled tubes under flexural bending

Experimental research on tubes under flexural bending began around 1850s but extensive experimental studies did not start until early 1930s by Donnell and Lundquist where they

observed buckling failure was similar to buckling observed in shells under axial compression (Singer, Arbocz and Weller 2002). For long specimens, as defined in Chapter 2, where the cylinders get flattened due to curvature, ovalization of the cross section causes the specimens to lose flexural rigidity, and bifurcation-type buckling failure is observed, for medium length specimens usually local buckling is observed. Local buckling slenderness is defined in literature by $\left(\lambda^2 = (D/t) \left(\frac{F_y}{E}\right)\right)$, where D is the diameter, t is the shell thickness, F_y is the yield strength and E is the Young's modulus. In the SWT project we (Jay et al (2016a)) summarized 123 tests from 16 studies on cylindrical shell specimens under pure static bending (pure flexural or cantilever bending) with no internal pressure, see Table 3.1. the specimens' diameter-to-thickness ratio (D/t) ranges from 16 to 800 and buckling slenderness (λ^2) ranges from 0.04-1.02. The specimens were tested using three loading protocols; simple bend (where the load was applied using rotations at the ends of the specimens), cantilever and 4-pt bending.

Table 3.1 Summary of static flexural testing programs for tubes with no internal pressurization (Jay et al. 2016a)

Reference	No. of tests	D/t	λ^2	L/D	D (mm)	F_y (MPa)	Loading
Seide (1965)	6	800	1.06-1.42	0.5-1.0	406	273-367	Simple bend
Schilling (1965)	10	34-137	0.06-0.17	-	89-125	245-394	-
Jirsa (1972)	3	46-78	0.08-0.15	5.4-6.7	273-508	343-383	4-pt bend
Sherman (1976)	7	35-111	0.05-0.16	-	273	287-421	4-pt bend, cantilever
Korol (1978)	10	29-80	0.04-0.14	1.5-8.0	114-508	298-376	4-pt bend
Stephens (1982)	2	298-444	0.56-0.67	1.0	1523-1529	306-376	4-pt bend
Sherman (1984)	5	24-75	0.05-0.12	4.0-4.5	457-610	309-401	4-pt bend
Sherman (1987)	21	23-90	0.05-0.19	3.6-10.8	457-610	294-434	4-pt bend, cantilever
Steinmann (1989)	3	42-64	0.07-0.09	-	168	286-387	-
Elchalakani (2002)	12	36-122	0.07-0.26	3.6-6.9	87-110	365-412	Simple bend
Jiao (2004)	12	16-48	0.10-0.31	5.3-12.6	32-76	1284-1398	4-pt bend, simple bend
Kiymaz (2005)	6	46-145	0.14-0.27	2.3-4.8	103-220	337-602	4-pt bend
Poonaya (2009)	6	21-43	0.04-0.07	-	47-75	206-354	Simple bend
Dimopoulos (2012)	6	100	0.13	6.5	400	270	Cantilever
Guo (2013)	13	75-300	0.08-0.30	4.0-7.5	150-600	190	4-pt bend, cantilever
Sim (2014)	1	333	0.45	11.0	2000	270	Cantilever

Two of the recent experimental work on spirally welded tubes under pure bending are summarized in Table 3.2 shows two of recent experimental work with total of 17 tests. These spirally welded specimens were all prismatic and the diameter-to-thickness ratio (D/t) ranges from 49 to 121, and buckling slenderness (λ^2) ranges from 0.13 to 0.29.

Table 3.2 Summary of static flexural testing programs for spirally welded tubes with no internal pressurization (Jay et al. 2016a)

Reference	No. of tests	D/t	λ^2	L/D	D (mm)	F_y (MPa)	Loading
Zimmerman (2004)	2	49-81	0.13-0.20	4.2	762	483-552	Simple bend
Puppeke (2014)	15	65-121	0.14-0.29	7.6	1065-1071	340-570	4-pt bend

The results of the 140 tests from 18 studies are summarized on Fig. 3.3, with design curves built using AISC and EC3-1-6 design guidelines according to the three fabrication quality classes A, B and C. The curves are built using yield stress ($F_y = 345 \text{ MPa}$) and the ultimate moment is normalized to the plastic moment, and the diameter-to-thickness ratio and buckling slenderness on the horizontal axes. Most of the tests lies in the range of slenderness that is lower than conventional wind turbine towers range and since the spirally welded wind turbine towers range of slenderness is wider.

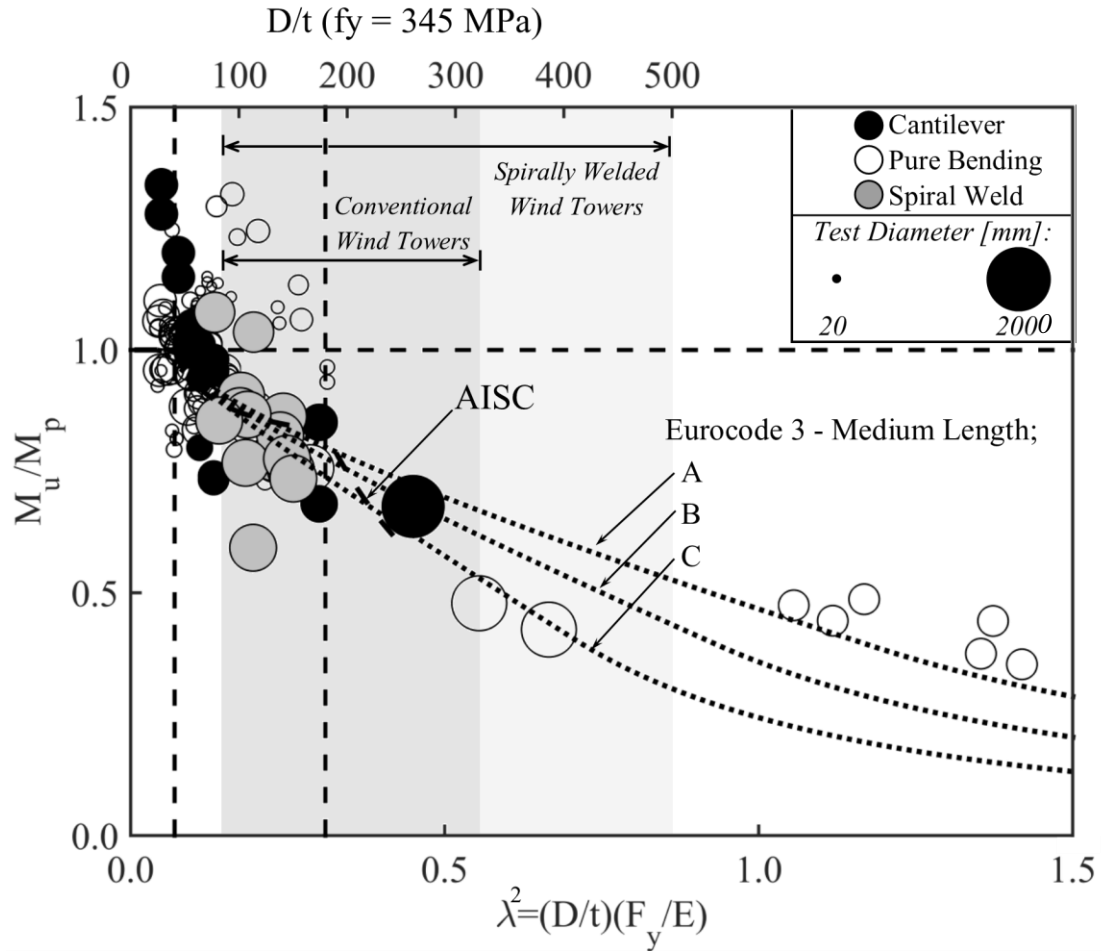


Figure 3.3 Experimental results for 140 tests from 18 studies (see Table 1 and Table 2) on static, flexural buckling of hollow circular, unstiffened, non-pressurized steel sections. Pure bending tests, represented with hollow circles, include 4-pt bending tests and simple bending tests (the latter is defined as flexure achieved by applying end rotations). All spiral weld tests are loaded in pure bending and are depicted with gray markers. For all tests, marker size is related to specimen diameter through an inverse power relationship of 2.5 (Jay et al. 2016a).

One of the tests reported in Table 3.1, Sim et al. (2014), was conducted on a full-scale wind turbine tower (21.9 m long) composed of three segments with tapered connections and stiffeners under bending, representing a 65-kW wind turbine tower and compared the results to available design codes in U.S. and numerical models.



Figure 3.4 Test setup for full-scale test of 65 kW wind turbine tower (Sim et al. 2014).

3.3 SWT Project tests on spirally welded tapered tubes

Given the novelty of the tapered spiral welding process and the lack of application-specific research for wind towers, large-scale tests and complementary parametric numerical analyses (finite element analyses (FEA)) are important endeavors for the development of analysis-based design methods for spirally welded wind turbine towers. For a tapered tube, the main geometric features are the maximum diameter D_{max} , minimum diameter D_{min} , the specimen's length L , and thickness t (or thicknesses if the tube is built from several plates with varied thicknesses), as shown in Fig. 3.5. For spirally welded tapered tubes (SWT), fabrication process is based on rolling and spirally welding flat steel trapezoidal sheets or plates with constant width. The plates or sheets are cut into specific trapezoidal shapes and welded together into segmental curves before feeding to the rolling and welding machine. SWTs have special geometric features; the helical angle of the spiral seam welds θ_i depends on the plates' orientation which is controlled by the plate width w , and the

number and location of the cross welds depends on the maximum length of the plates, see Fig. 3.5.

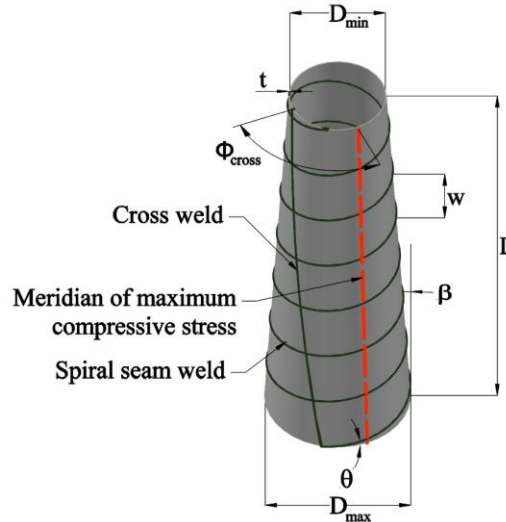


Figure 3.5 Schematic of spirally welded tapered tube.

A series of nine large-scale SWT specimens were manufactured by Keystone Tower Systems KTS using a spiral welding process, and tested for flexural capacity by NEU research team. Each SWT specimen was manufactured with constant width plates ($w = 305$ mm) and various diameters and thicknesses. Table 3.3 lists dimensions of the nine specimens. The length of the specimens was between 3.36 m and 3.43 m, the thicknesses ranges from 2.95 mm to 6.2 mm, the maximum diameters range from 761 mm to 1067 mm and minimum diameters range from 681 to 970. The specimens' maximum diameter-to-thickness ratio ranges from 144 to 353, while the minimum diameter-to-thickness ratio ranges from 133 to 321, the maximum buckling slenderness ranges from 0.29 to 0.83 and the minimum buckling slenderness 0.27 to 0.76. The helical angle at the maximum diameter ranges from 5.2° to 7.3° , the tapering angle ranges from 0.60° to 0.86° . Since, imperfections pattern is a concern it is important to record the location of cross-to-spiral

weld connections with respect to the maximum meridian of compressive stress at the small diameter Φ_{cross} . Two groups of the specimens (SW-325 and SW-350) each was designed to have three specimens with the same dimensions but with the cross weld placed at three different orientations ($\Phi_{cross} = 0^\circ, 120^\circ$ and 240°) to study the effect of the cross-to-spiral weld connections with respect to the meridian of the maximum compressive stress. The naming convention of each specimen (e.g., SW-325-120°) designates the welding process (e.g., SW = spirally welded), the maximum diameter-to-thickness ratio D_{max}/t rounded to the nearest five (e.g., $D_{max}/t = 325$), and the orientation of the cross weld with respect to the meridian of maximum compressive stress (e.g., $\Phi_{cross} = 120^\circ$).

Table 3.3 Measured dimensions, quality class and ultimate moment of the eight large-scale specimens (Jay et al. 2016b).

Specimen	D_{max} (mm)	D_{min} (mm)	t (mm)	L (m)	$\frac{D_{max}}{t}$	$\frac{D_{min}}{t}$	λ_{max}^2	λ_{min}^2	Φ_{cross}	θ	β
SW-230-0°	761	681	3.30	3.43	231	206	0.56	0.50	0°	7.3°	0.67°
SW-145-0°	895	825	6.2	3.38	144	133	0.29	0.27	0°	6.2°	0.60°
SW-305-0°	897	812	2.95	3.38	304	275	0.77	0.70	0°	6.2°	0.72°
SW-325-0°	956	859	2.95	3.40	324	291	0.70	0.63	0°	5.8°	0.82°
SW-325-120°	953	870	2.95	3.39	323	295	0.74	0.68	120°	5.8°	0.70°
SW-325-240°	965	867	2.97	3.36	325	292	0.76	0.68	240°	5.8°	0.84°
SW-350-0°	1048	970	3.02	3.37	347	321	0.81	0.75	0°	5.3°	0.66°
SW-350-120°	1054	962	3.00	3.37	351	321	0.83	0.76	120°	5.3°	0.78°
SW-350-240°	1067	966	3.02	3.36	353	320	0.82	0.74	240°	5.2°	0.86°

Three coupons were taken from each specimen for tension tests (full results described in chapter 6) to obtain material properties. The average yield and ultimate stresses from the coupon tests for the nine specimens are reported in Table 3.4. It should be mentioned here that each of these specimens was fabricated from several plates where the material properties and plate thicknesses varied, the measurements of the dimensions and the material properties reported in Table 3.3 and Table 3.4, are an average of several measurements or tests.

Table 3.4 Average yield and ultimate stress obtained from coupon tests.

Specimen	f_y (MPa)	f_u (MPa)
SW-230-0°	489	533
SW-145-0°	406	462
SW-305-0°	505	583
SW-325-0°	434	509
SW-325-120°	460	527
SW-325-240°	467	523
SW-350-0°	465	535
SW-350-120°	473	549
SW-350-240°	464	535

3.3.1 Test Setup

The test rig is designed to apply pure bending to each specimen, see Fig. 3.6. It is composed of two actuators placed 2.4 meters apart, each with a capacity of 965 kN in tension and 1,468 kN in compression. The specimens are welded to end plates before mounting them on the rig, and the end plates are connected to the crossbeams by tensioned high strength bolts which are, in turn, connected to the actuators and pins. The crossbeams rotate about pins placed at either end; the larger end is free to move longitudinally, applying equal bending moments at both ends of the specimen. One of the actuators retracts and the other expands to apply rotation at both ends, the testing protocol intends to keep the moment constant at both ends of the tube.

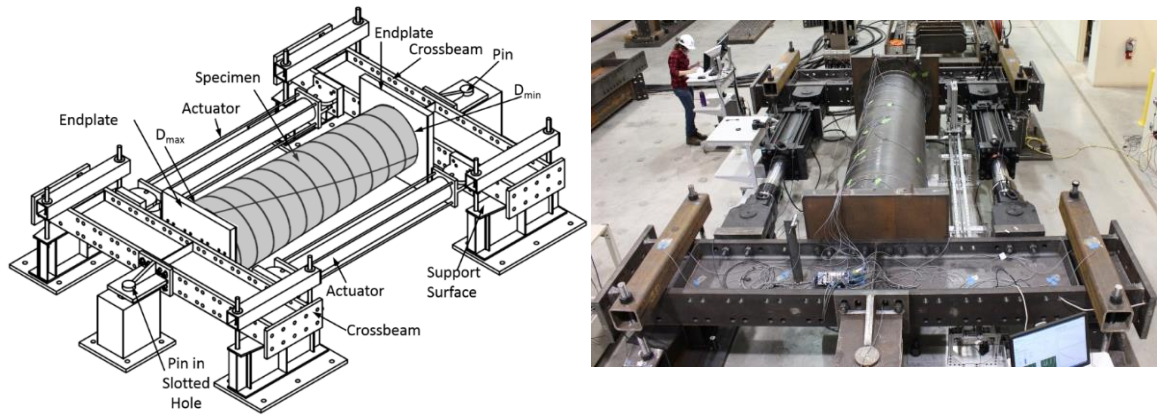


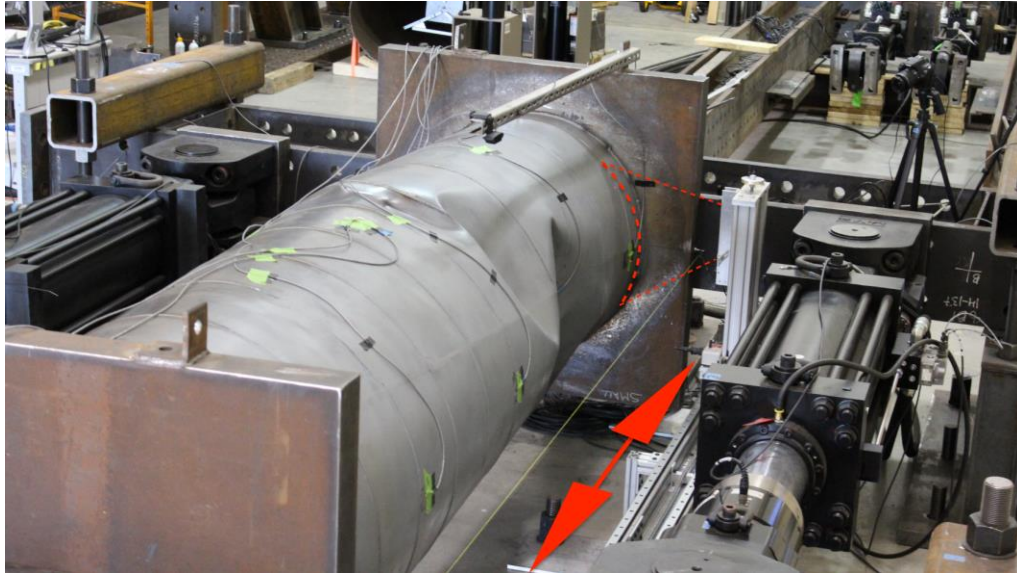
Figure 3.6 Schematic showing the experimental set-up for large scale bending tests on tapered spirally welded tubes and a photo of the test rig with one specimen mounted on before testing (Jay et al. 2016b).

3.3.2 Laser Scans

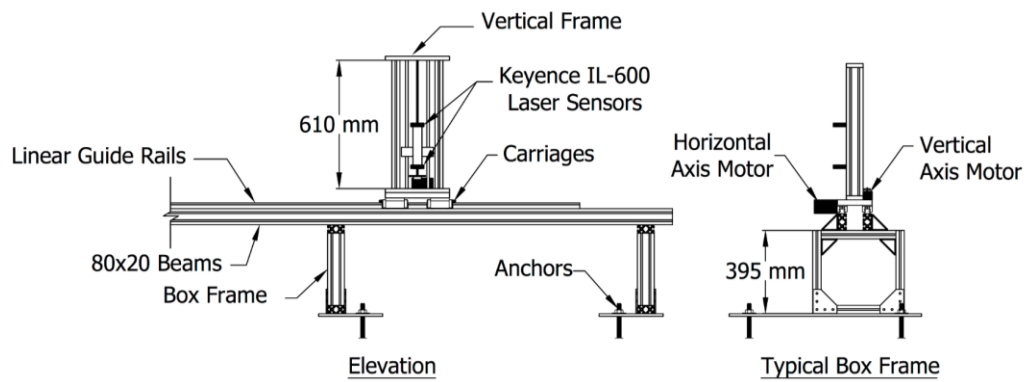
Before testing, specimen dimensions were measured, and each specimen was assigned to a specific quality class according to EC3-1-6 manufacturing tolerances (see Chapter 4 and Jay (2017) for further details). A laser scanner was built by the JHU team and mounted on the test rig to scan the development of buckling of the specimen during testing, while the loading is paused, Fig. 3.7 (a). The main purpose of these scans is to study the effect of initial imperfections on the development of buckling (Mirzaie et al. 2017).

The laser scanner consists of two (Keyence IL-600) laser sensors placed 300 mm apart fixed on a vertical frame and connected to a vertical axis electric motor that moves the scanners vertically to scan 24 inches of the compression side of the specimens. The vertical frame was placed on four carriages that move horizontally on two linear guide rails. The carriages are connected to a horizontal axis motor that moves the carriages on the guide rails. The linear guide rails are attached to two beams, these beams are placed on 4 box frames and connected to base plates and fixed to the lab floors with steel anchors, see Fig. 3.7 (b). For a single scan to be done, while the loading was paused, the laser scanners did

a set of measures moving from the bigger diameter side to the smaller diameter side of the specimen then the laser sensors move one step vertically and goes back to the bigger diameter side.



(a)



(b)

Figure 3.7 (a) The laser scanner on the test rig, and (b) framing of laser scanner and its components.

Fig. 3.8 shows the scans conducted on seven of the nine specimens during test before and after buckling, where the ratio to the ultimate moment observed in test M_t is displayed to indicate the load stage being shown.

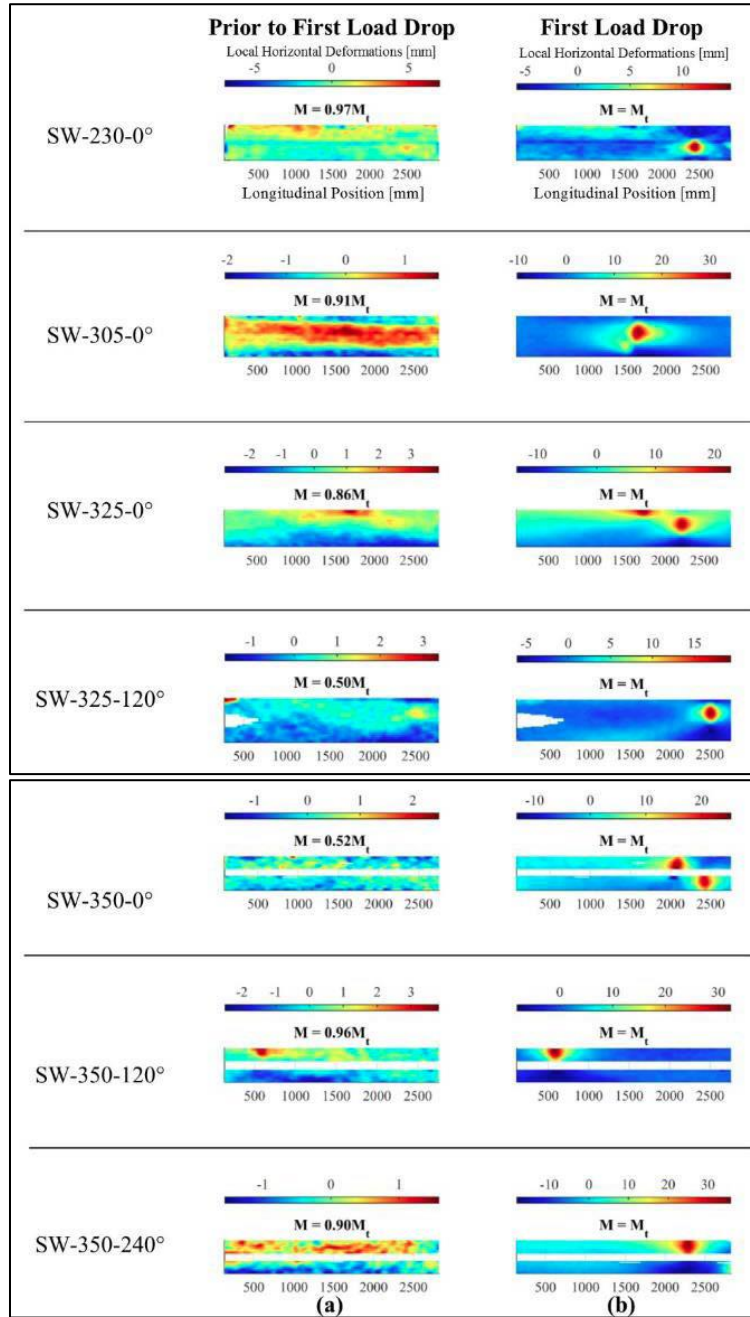


Figure 3.8 Scans of part of specimens under compression for seven of the nine specimens (a) during test (before buckling) and (b) at buckling (Jay 2017).

3.3.3 Test Results

Rotations in the tests are measured at the actuator locations and are corrected to account for flexibility in the test rig using local measurements made by linear voltage displacement transducers mounted at the endplates, the stiffness K_{FE} , is the secant bending stiffness of the models, with K_{test} , the measured stiffness of the tested specimens, calculated over a range between 40% and 60% of the ultimate bending capacity, see Fig. 3.9. A single value for the rig flexibility is calculated and applied across all tests, calculated as the average difference between applied (actuator) and local (voltage transducer) measurements per unit applied moment. Also, to reduce the effect of initial effects in the rig at the start of loading, data below 40% of the ultimate bending capacity are replaced by a line with slope equal to the measured stiffness. Note that the rotation measurements presented in Jay et al. (2016b) are reported without these alterations. Fig. 3.10 (a-e) shows the moment rotation curves for the nine tested SWT specimens.

Table 3.5 shows the main failure characteristics, the rotation angle at the peak load (buckling) θ_t , the diameter-to-thickness ratio at the location of the local buckling $(D/t)_t$, the circumferential angle from the meridian of the maximum compression stress ϕ_t , and the location of the buckling from the maximum diameter $(x/L)_t$. The test-to-predicted ratio of the ultimate moment from the test to the yield moment (M_t/M_y) , shows that the ultimate moment of all the specimens except SW-145-0° ranges from 60% to 76% of the yield moment. The stockiest specimen, SW-145-0°, nearly reached the yielding moment. As reported in Table 3.5, the EC3-1-6 design moments for quality Class B and Class C calculated using stress design method, $M_{EN,B}$ and $M_{EN,C}$ shows underestimation of strength

by 16% to 43% for Class B and 31% to 79% for Class C, excluding specimen SW-230-0°. (Specimen SW-230-0° was the first specimen fabricated by KTS and from the measurements of the imperfections it did not meet the tolerance of EC3-1-6 quality Class C, so it was assigned worse than C (WTC)). Note, the test of specimen SW-325-240° ended due to fracture on a spiral seam weld on the tension side of the bending and the moment measured at the time of fracture is reported as a lower bound of the ultimate moment, see Jay et al. (2016b) for more details. In most specimens after the first load drop (buckling), the specimen gained some stiffness postbuckling and the response continues until another load drop which is accompanied with the formation of a second buckling shape. For specimens SW-325 and SW-350, shown in Fig. 3.8 (d) and (e) respectively, the strength increased when the cross weld was placed further away from the maximum compressive stress meridian. Although there are differences in the dimensions and the quality class measurements, the strength of the specimens with the same diameter-to-thickness ratio, consistently increased when the cross weld was placed at ($\phi_{cross} = 120^\circ$ and 240°) if compared to ($\phi_{cross} = 0^\circ$) from the meridian of the maximum compressive stress.

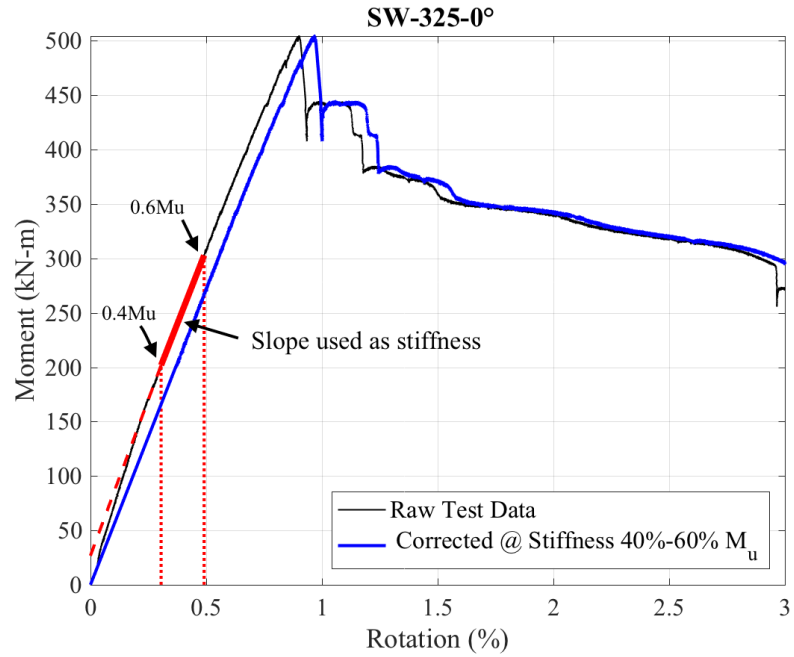


Figure 3.9 The correction made to the SWT tests moment-rotation curves.

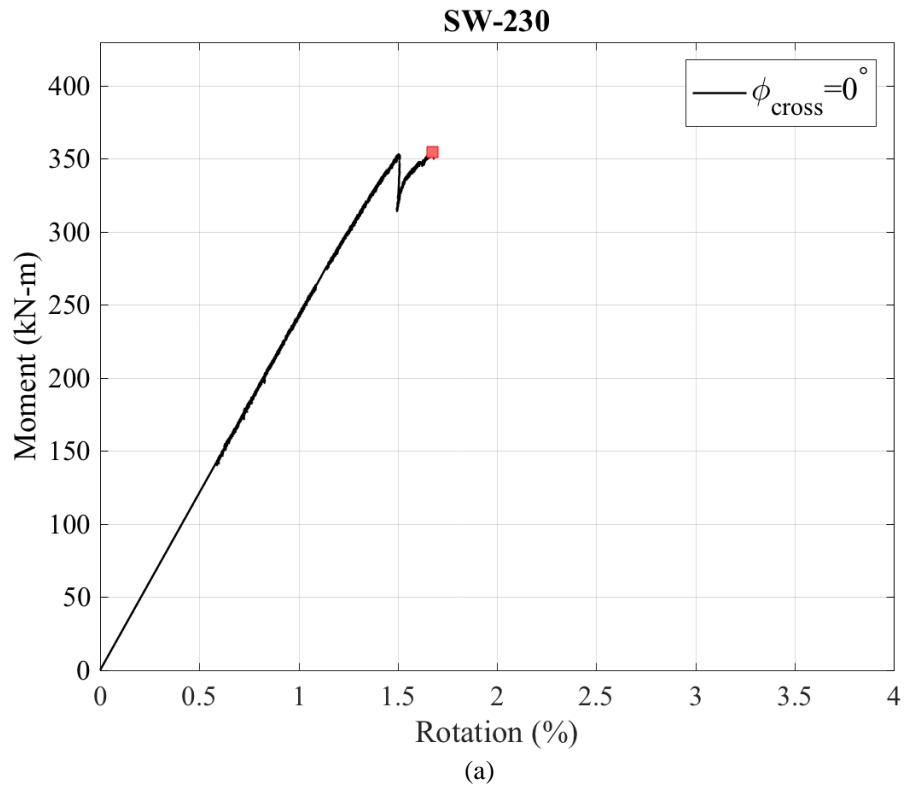


Figure 3.10 (a) Moment-rotation curves of the tested specimens.

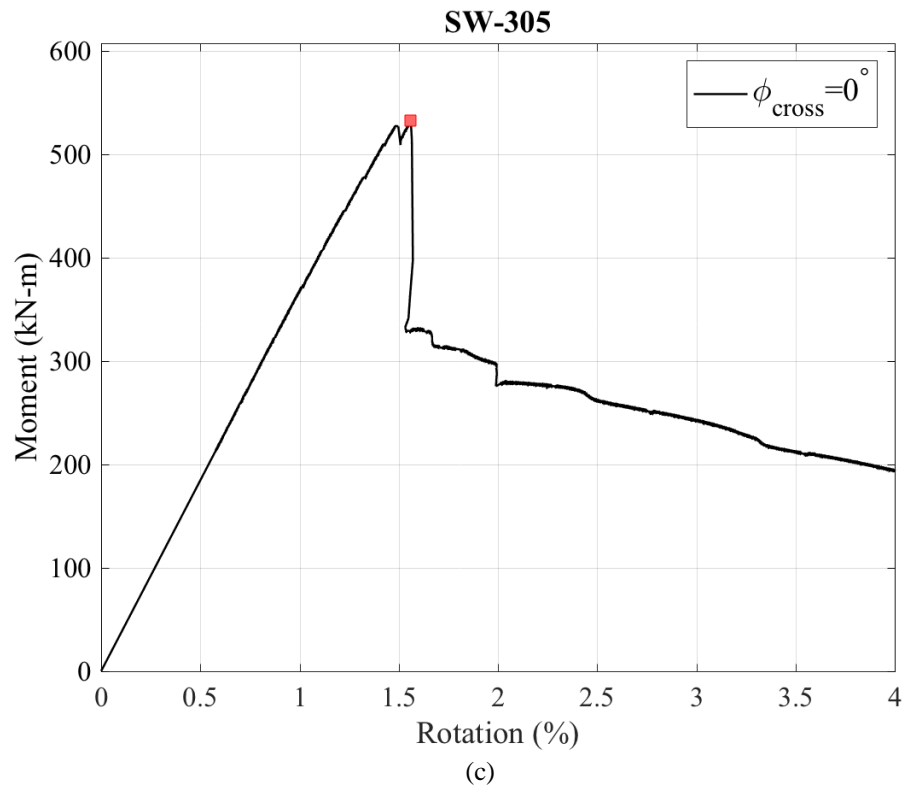
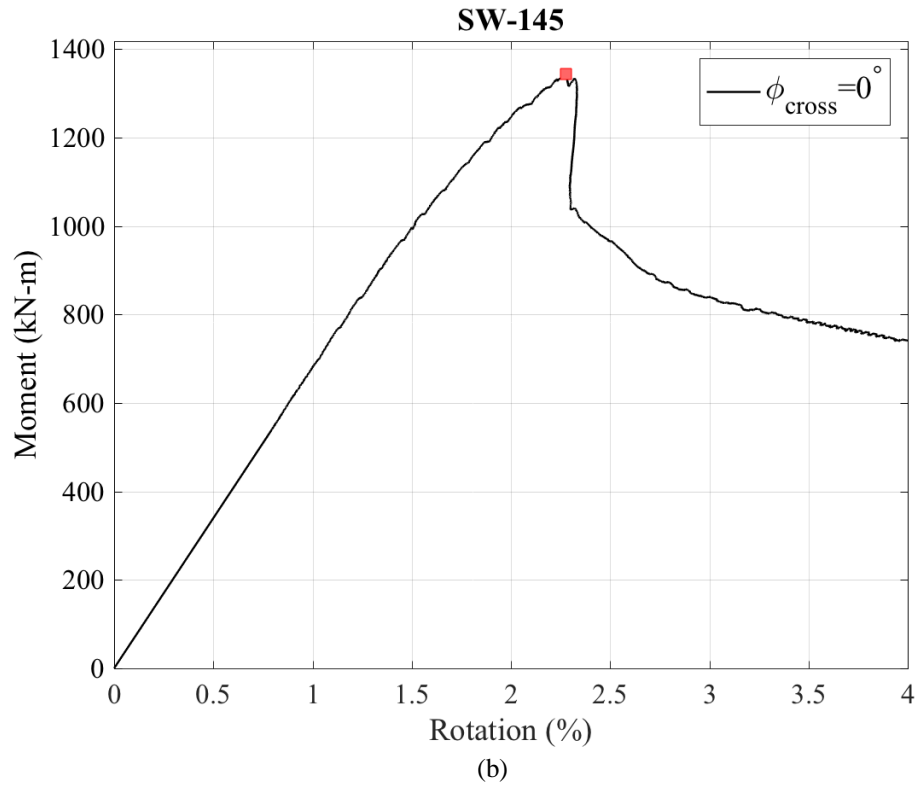


Figure 3.10 (b-c) Moment-rotation curves of the tested specimens.

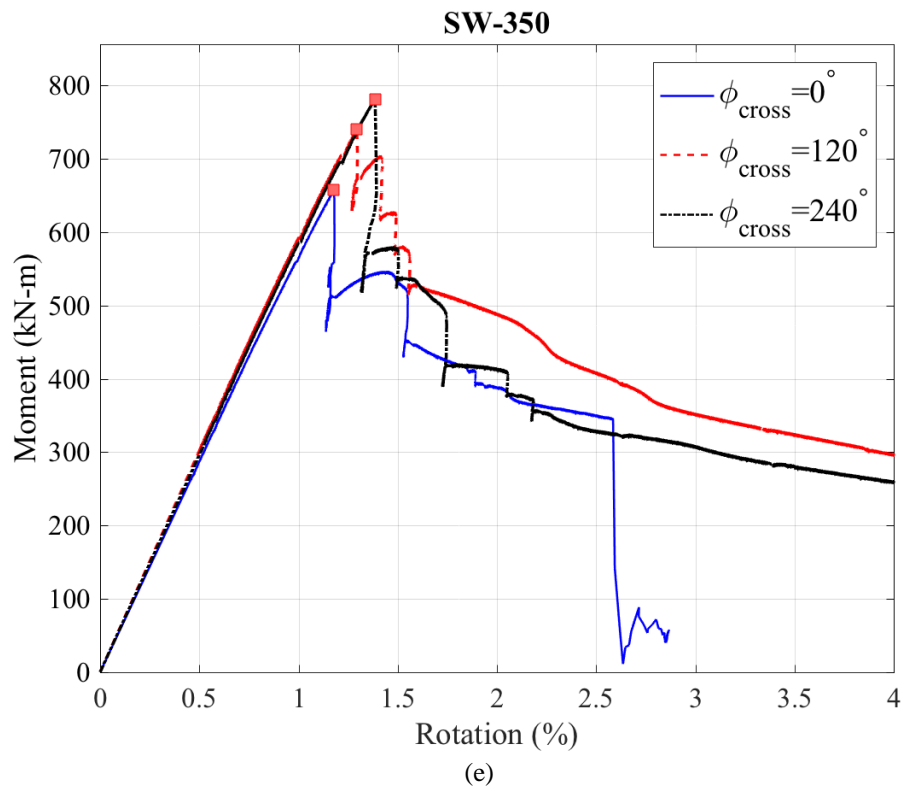
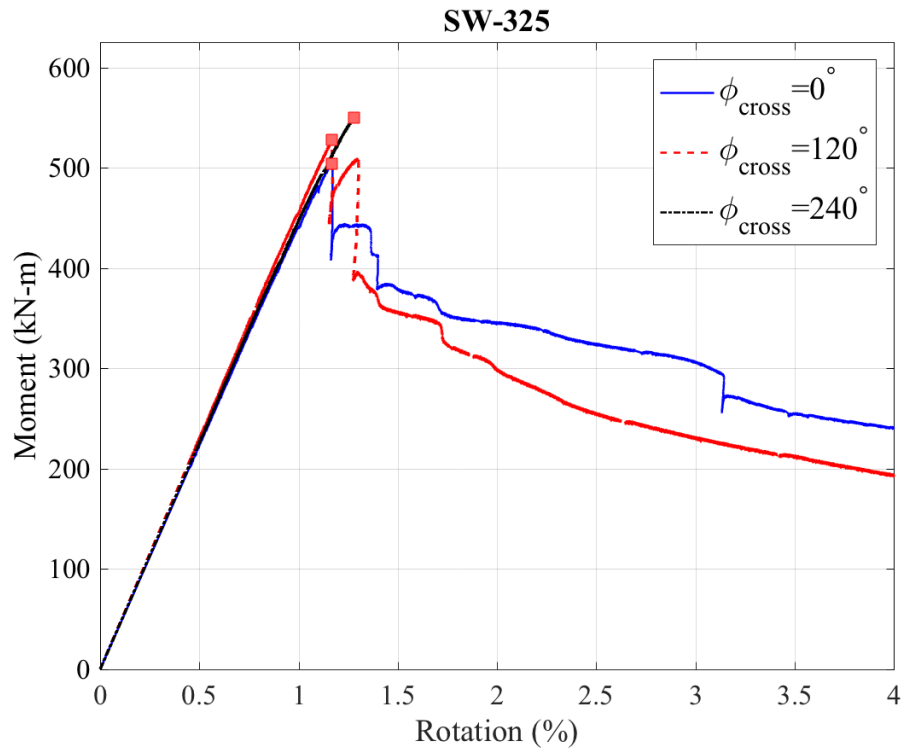


Figure 3.10 (d-e) Moment-rotation curves of the tested specimens.

Table 3.5 Summary of the flexural buckling results for all specimens (Jay 2017).

Specimen	At peak (1 st buckling)		Local Buckling Location			Test-to-predicted		
	M_t (kN-m)	θ_t (rad)	$\left(\frac{D}{t}\right)_t$	ϕ_t	$\left(\frac{x}{L}\right)_t$	$\frac{M_t}{M_y}$	$\frac{M_t}{M_{EN,B}}$	$\frac{M_t}{M_{EN,C}}$
SW-230-0°	350	0.015	209	-3°	0.82	0.60	0.90	0.99
SW-145-0°	1343	0.022	138	-15°	0.57	1.02	1.26	1.31
SW-305-0°	526	0.011	286	3°	0.58	0.69	1.22	1.46
SW-325-0°	502	0.011	294	2°	0.75	0.69	1.16	1.37
SW-325-120°	523	0.011	297	6°	0.84	0.66	1.16	1.39
SW-325-240°*	≥553	≥0.012	-	-	-	≥0.68	≥1.20	≥1.44
SW-350-0°	656	0.011	331	11°	0.71	0.64	1.20	1.50
SW-350-120°	737	0.012	312	12°	0.26	0.72	1.37	1.73
SW-350-240°	778	0.013	323	5°	0.77	0.76	1.43	1.79

*Specimen SW-325-240° failed due to weld fracture before buckling.

Figure 3.11 provides illustrated figures of the unwrapped geometry of each of eight of the specimens with the local buckling location and the layout of the spiral and cross welds. The buckling occurred in the location closer to the smaller diameter of the specimens in almost all the specimens (except SW-350-120°), this is consistent with theoretical solution of critical stresses, where higher stresses are expected to be closer to the smaller end of the tapered tube. However, the buckling of specimen SW-350-120° occurred closer to the bigger diameter likely due to the pattern of imperfections and the worst imperfection occurring near the meridian of the maximum compressive stress at the large diameter end. Nearly all the local buckling waves developed at weld locations and likely initiated from a weld imperfection this is consistent with past work (for example Yu et al. 2012) and stresses the importance of studying weld imperfections. When the cross weld was placed near the location of the meridian of the maximum compressive stress the buckling was triggered from the connection between the spiral seam and cross welds.

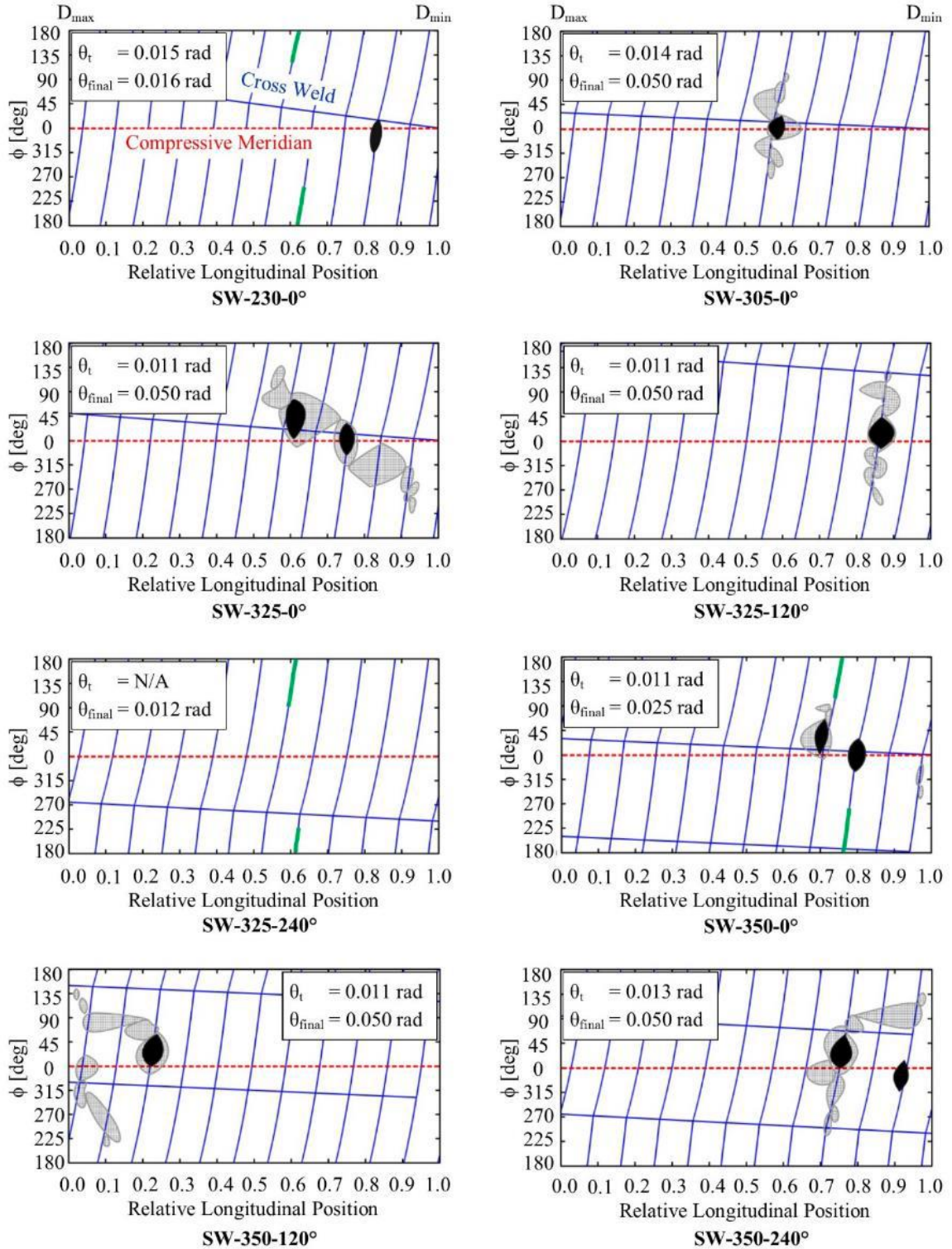


Figure 3.11 Region of local buckling for each specimen after the first load drop (θ_t) and at the end of the test (θ_{final}) (Jay et al. 2016b).

3.3.4 Fatigue Tests

Fatigue can be a critical limit state for structures that endure cycles of loading. Wind turbines are subjected to cycles of dynamic loading along their operation life time. At connections stress concentrations occur, for spirally welded structures all the weld connections are suspected to have potentially poor fatigue performance, especially the cross and spiral seam weld connections. As part of our SWT project, Jay (2017) conducted eleven tests to verify the fatigue design strength for the intersection of two complete joint penetration welds. The tests were designed to develop a fatigue detail category for the intersecting weld connections in full scale spirally welded tubes, see Fig. 3.12.

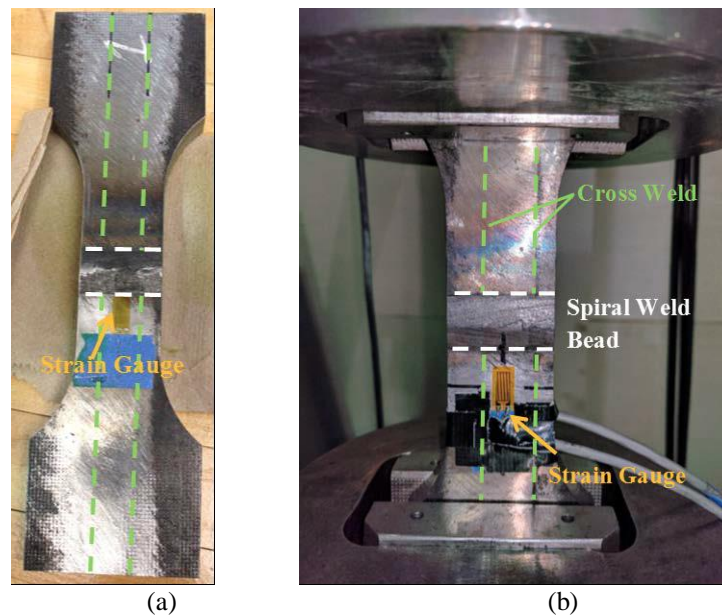


Figure 3.12 Photos of (a) fatigue specimen with strain gauge below the transverse weld and (b) the specimen in the hydraulic grips with both welds highlighted (Jay 2017).

The fatigue strength curves are identified by the detail category, representing the value of the fatigue strength at 2 million cycles in N/mm^2 , and constant amplitude factor limit (CAFL) which is the value of fatigue strength at 5 million cycles of constant amplitude loading. The fixation of the number of cycles when calculating the CAFL for all detail

categories in EC3-1-6, is not realistic but beneficial for damage sum computations, other codes such as AISC uses number of cycles ranging from 1.8 million to 22 million cycles according to the detail category. (ECCS 2011). The test results are summarized in Table 3.6 and plotted in Fig. 3.13. Experimentally the fatigue strength is not significantly affected by the intersecting weld connections and the results yielded to detail category (DC=102) per EC3-1-9 (Eurocode 3 EN 1993-1-9:2005). The test results also suggest a CAFL of 180 MPa, which is much higher than what the EC3-1-9 suggests (73 MPa) and this limit is placed at $N = 5 \times 10^6$ cycles. However, because the specimens were cut from flat plates welded together, and other differences with respect to spirally welded tubes Jay (2017) recommended using at least (DC=90) as single double sided CJP butt weld for intersecting weld connections.

Table 3.6 Fatigue test results (Jay 2017)

Specimen	S (MPa)	N	f (Hz)
1	194	$5 \times 10^{6+}$	4.00
2	241	$1 \times 10^{7+}$	4.00
3	383	1.38×10^5	0.75
4	383	3.52×10^3	0.60
5	300	1.75×10^5	1.25
6	300	2.75×10^5	1.25
7	250	4.01×10^5	1.50
8	250	4.83×10^5	1.50
9	200	$5 \times 10^{6+}$	2.00
10	300	2.72×10^5	1.00
11	300	3.02×10^5	1.00

+Test ended without failure detected (Test run out)

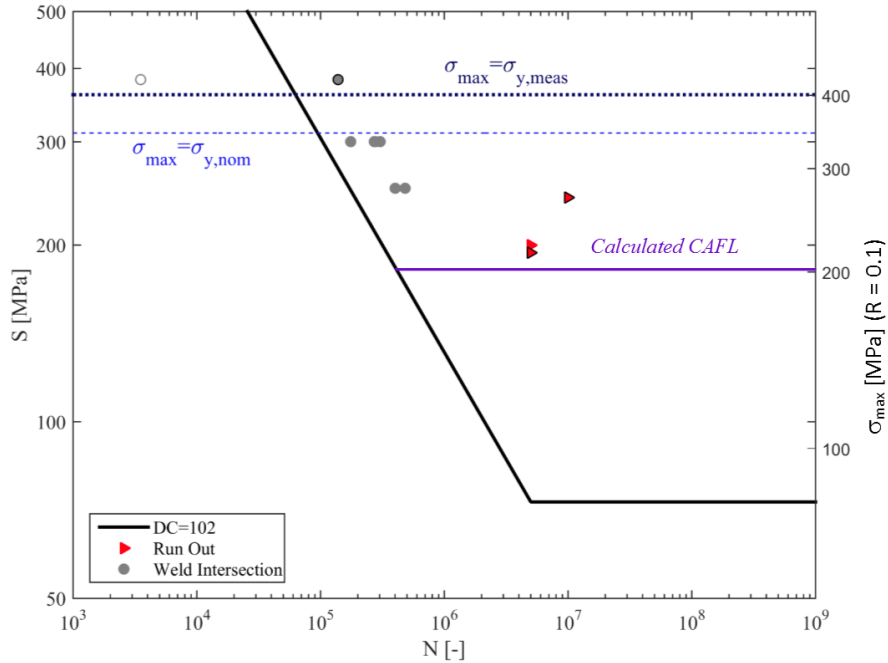


Figure 3.13 Plot comparing all fatigue data with the EC3-1-9 S-N curve for DC = 102 (black line, outlying white-fill data point excluded). The purple line indicates the CAFL calculated from data (Jay 2017).

3.4 Summary and Conclusions

A summary of the experimental work done for cylindrical shells under axial compression and bending from literature was provided. Nine large-scale slender SWT specimens were tested to predict their flexural buckling strength. The specimens were manufactured by KTS and tested by NEU research team under pure bending and results were described in detail. The test was intended to mimic a scaled cut of a wind turbine tower with almost equal moments at both ends, accordingly, the test rig was designed to mimic the boundary conditions and equal moments were applied at both ends of specimens. The SWT specimens ranged in diameter-to-thickness ratio from 145 to 350, with six of the specimens intended to study the effect of the cross-weld location with respect to the meridian of the maximum compressive stress. The SWT specimens were scanned using high resolution laser scanner before testing and a quality class according to EC3-1-6 tolerances was

assigned for each specimen. Another laser scanner was mounted on the test rig to track the initiation and development of buckling during test. Fatigue tests were conducted on eleven specimens with cross-to-spiral seam full penetration weld, to assign a detail category to be used in design for fatigue strength.

The buckling in seven of the nine tests occurred at location closer to the smaller end of the SWT specimens, which agrees with theoretical solutions, in the other two specimens the test ended due to fracture in spiral seam weld in the tension side and the other buckled at location closer to larger end of the specimen. Although the cross-to-spiral seam weld connections did not show a drastic effect on the ultimate strength of SWT specimens if compared to design moments for Class C per EC3-1-6 stress design method, see Fig. 3.14. The six specimens (SW-325 and SW-350) which were intended to study the effect of the cross-weld location with respect to meridian of maximum compressive stress, it was noted that when the cross weld was placed at angles ($120^\circ - 240^\circ$) from the meridian of the maximum compressive stress the strength of the specimens with same diameter-to-thickness ratio increased. The stockiest section (SW-145) showed less sensitivity to imperfections and almost reached the yielding moment capacity. The buckling was initiated at locations following weld imperfections and the pattern of the buckling waves seems to follow the helical orientation of the plates. Fatigue tests showed that the calculated detail category and CAFL recommended by EC3-1-9 for intersecting welds, is much lower than detail category and CAFL obtained from tests, and Jay (2017) recommended using at least DC=90 (as single double sided CJP butt weld).

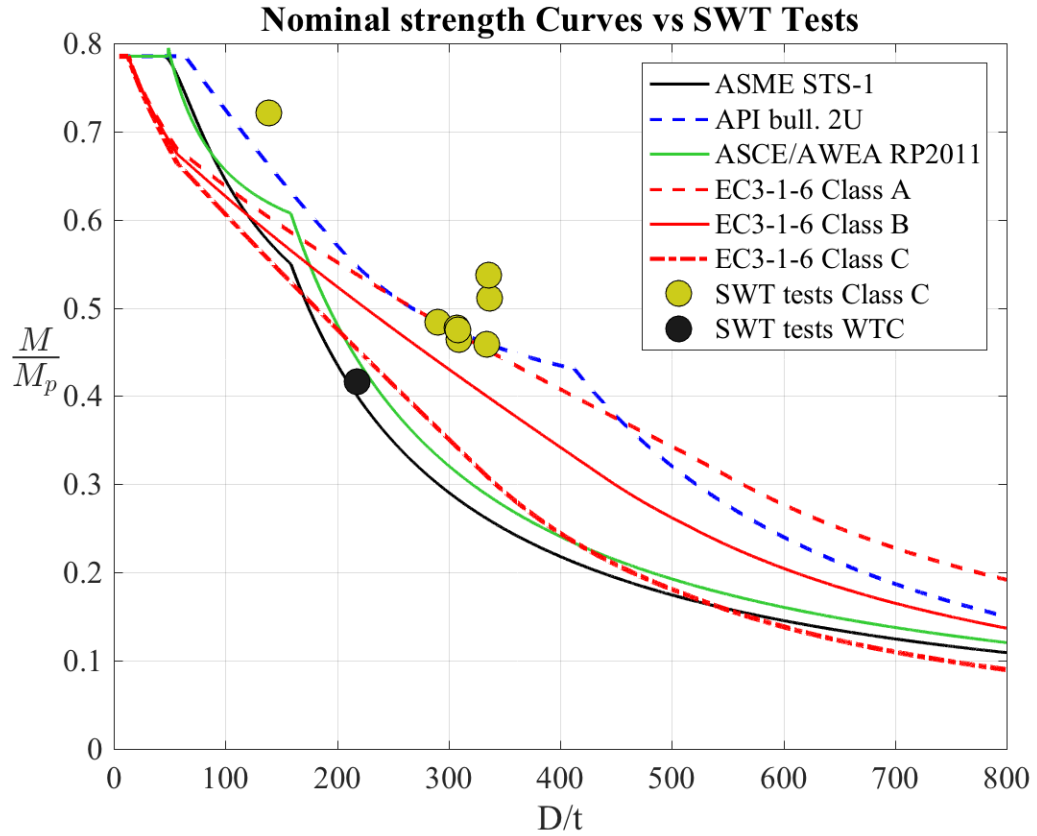


Figure 3.14 SWT test results compared to normalized nominal flexural strength according to different design codes.

Chapter 4

Imperfections

4.1 Introduction

The prediction of the strength of cylindrical shell structures is a complicated process as many factors influence the strength of such structures. One of the most important factors in reducing buckling strength of shell structures is the initial geometric imperfections caused by the manufacturing, transportation, and construction processes. Slender cylindrical shells under compression are known to be extremely sensitive to even the smallest imperfections. The imperfections pattern, magnitude and location on the shell with respect to compressive membrane stresses, all play a big role in severing the shell's strength. For shell buckling problems, different imperfection patterns can also show different unstable post-buckling paths (ECCS 2013), see Fig. 4.1.

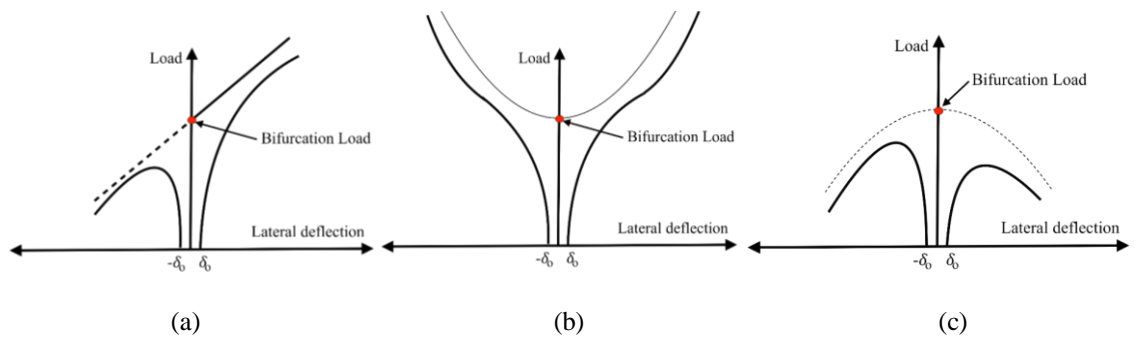


Figure 4.1 Equilibrium postbuckling paths (a) asymmetric, (b) symmetric stable, and (c) symmetric unstable (typical shells).

For spirally welded tubes, imperfections can be caused by welding, rolling and cutting during fabrication (see Fig. 4.2) or other causes such as transportation or erection. Imperfections can be mainly categorized into two groups; material and geometric

imperfections. Material imperfections largely include residual stresses caused by rolling of plates and welding. Geometrical imperfections are defined as any physical deviations in geometry in the radial direction from the nominal perfect geometry of the shell. For slender shells geometric imperfections generally have a more severe effect on their buckling strength.

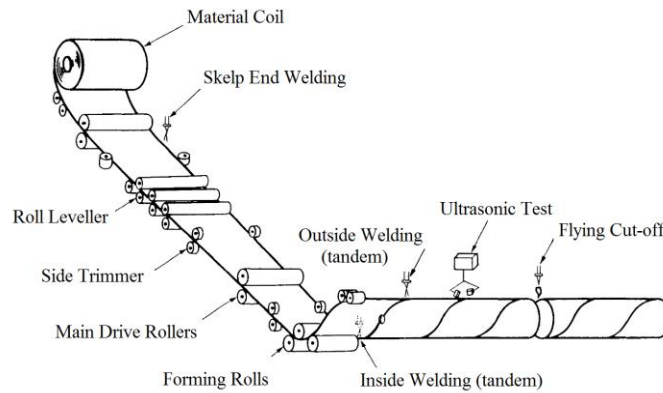


Figure 4.2 Coiling SWT sections (Hanada et al. 1986).

To have a good prediction of strength and post buckling behavior of shell structures, imperfections should be quantified and included in the calculations. Extensive studies were conducted on imperfection sensitivity and post-buckling behavior of elastic shells under axial compression and flexural moment such as (Berry et al. 2000, Hutchinson et al. 1971, Fajuyitan et al. 2015), another track of research was focused on representing imperfections by harmonic analysis or empirical equations (Pircher et al. 2000, Teng et al. 2005, Sadowski et al. 2014). Some studies compared different types of implementation of imperfections such as (Jansseune et al. 2016). Specifically, for the imperfections in spirally welded tubes some of the recent studies are (Nasim et al. 2014, Aslani et al. 2015, van Es et al. 2015, Jay et al. 2016b).

A new and robust design approach to predict buckling and ultimate strength of shells is to include the real imperfections in nonlinear analyses of shell numerical models, Eurocode 3 Part 1-6 (EC3-1-6) calls this (Geometrical and Material Non-linear Analysis with Imperfections (GMNIA) models). This design approach is being adopted or permitted to be used by many specifications and guides, such as (EC3-1-6, AWEA/ASCE RP 2011, ABS 2004, IEC 61400-1, and API 2U). Specifications and guides usually require quality evaluation to be done for the shell structure by inspecting different types of geometric imperfections, then a quality index (or quality class) should be assigned to the shell. API 2U and EC3-1-6 are examples of codes that specify exact tolerances measurement that should be conducted on fabricated shelled structure. In EC3-1-6 these measurements are for: out-of-roundness, dimples, and accidental eccentricity or thickness transition, and according to these measurements the shell is assigned one quality class of three (Class A (Excellent), Class B (High), and Class C (Normal)). In API the measurements are for: maximum difference in cross section diameters, location deviation from straight line along the meridian, and local deviation from true circle, and according to these measurements the reduction factors used in design of buckling strengths change. The AWEA/ASCE RP 2011 recommends incorporating fabrication tolerances, explicitly or by reference, in structural design drawings and must be explicitly on shop, assembly or fabrication drawings. In case these tolerances are not shown, the fabricator should coordinate with engineer and turbine and/or tower manufacturer to determine the required fabrication tolerances. These tolerances should be inspected by QA/QC (Quality Assurance and Quality Control) during fabrication, transportation and erection. The classical approach of design is still adopted in some codes for example ABS 2004 and IEC 61400-1, with recognition that the buckling

and ultimate strength are highly dependent on the amplitude and shape of imperfections, lower bound knockdown factors proposed in literature and based on experimental data is used to allow for shape imperfections. The design of slender shells based on lower-bound knockdown factors, is the most conservative but the least efficient design, it underestimates the buckling strength of higher quality shells. On the other hand, relating the design to the quality of the shell is much more efficient. In this study, we decided to use EC3-1-6 for deeper investigation.

4.2 Eurocode fabrication tolerances

For the buckling limit state (LS3) specified in the EC3-1-6, specific tolerances were set by EC3-1-6 for assigning fabrication quality class to a cylindrical shell. Three measurements are necessary for assigning a fabrication quality class for cylindrical shell. These measurements are; out-of-roundness, dimple and accidental eccentricity, these tolerances limits are measured according to functions in terms of geometry of the shell and it only focus on the amplitude of imperfection.

4.2.1 Out-of-roundness Tolerance

This measurement counts for section deviations from the perfect circular shape in terms of the maximum and minimum diameters of the imperfect section. This type of imperfections has not been widely studied for different load cases, however it is known to be more deleterious for tubes under external pressure than tubes under axial compression. The way the EC3-1-6 defined the imperfection is intended for shells with small diameters and the recommended values for out-of-roundness tolerance parameter $U_{r,max}$ listed in Table 8.1 in EC3-1-6 are intended to avoid occurrence of severe flattened (or low curvature) areas,

which may cause the shell to lose much of its strength (ECCS 2013). The parameter U_r is computed as the ratio between the maximum difference between diameters at a specific section to the nominal diameter at the same section. Fig. 4.3 shows typical measuring criteria for diameters of circular section to evaluate out-of-roundness. Fig. 4.3 (a) shows what is called flattening out-of-roundness which looks more like ovalization of circular section, is standard as the measures are all passing through the center point of the nominal section, while in Fig. 4.3 (b) the measurement is not as clear how to measure the diameters for unsymmetrical section but the EC3-1-6 specifies that D_{max} shall be the maximum distance between two point and in both cases “appropriate number of diameters should be measured to identify the maximum and minimum values”.

$$U_r = \frac{D_{max} - D_{min}}{D_{nom}} \quad (4.1)$$

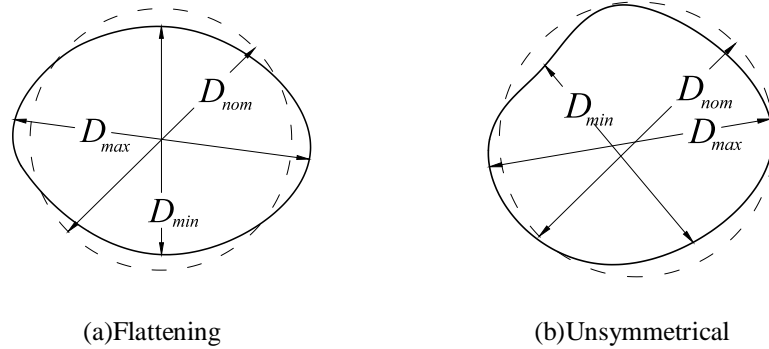


Figure 4.3 Measurements of diameters assessment of out-of-roundness.

Table 4.1 Recommended values for out-of-roundness tolerance parameter (CEN 2007)

Fabrication tolerance quality class	Diameter range	$D \leq 0.5m$	$0.5m < D < 1.25m$	$D \geq 1.25m$
	Description	Recommended value of $U_{r,max}$		
Class A	Excellent	0.014	$0.007 + 0.0093(1.25 - D)$	0.007
Class B	High	0.020	$0.010 + 0.0133(1.25 - D)$	0.010
Class C	Normal	0.030	$0.015 + 0.0200(1.25 - D)$	0.015

4.2.2 Dimple Tolerance

For shells under compressive stresses, initial dimple imperfections could be the most severe form of imperfections to the buckling strength of the shell. Shell sensitivity to dimples vary according to dimple shape and depth of the dimple. The measurement is done using a gauge length (l_g) and maximum dimple depth (Δw_0) which is measured in the inside direction of the tube, see Fig. 4.4. A survey should be conducted over the whole surface of the shell using a set of gauge lengths (l_{gx} or $l_{g\theta}$ or l_{gw}), the gauge length is chosen according to the type of stresses at the location of the dimple as summarized in Table 4.2. The direction of the measurement and the presence of weld within the dimple requires extra measurements. The tolerance is measured by the parameter U_0 which is the ratio of the maximum dimple depth to the adjacent gauge length and should be compared to dimple tolerance parameter $U_{0,max}$ for each quality class, where the recommended values provided by EC3-1-6 are listed in Table 4.3.

$$U_0 = \frac{\Delta w_0}{l_{gi}} \leq U_{0,max} \quad (4.2)$$

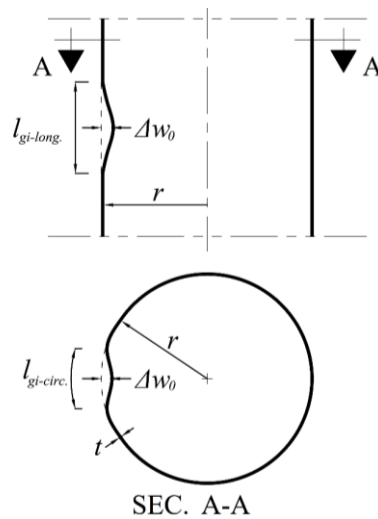


Figure 4.4 Measurements of dimples imperfections.

Table 4.2 Measurements required for different cases of initial dimple imperfections

Stress	Measurement Direction	Weld presence at the dimple	Gauge length (l_{gi})	Maximum Dimple Depth (Δw_{0i})
Meridional Compressive	Longitudinal	No	l_{gx}	Δw_{0x}
		Yes	l_{gx} or l_{gw}	Δw_{0x} or Δw_{0w}
	Circumferential	No	l_{gx}	Δw_{0x}
		Yes	l_{gx} or $l_{g\theta}$ or l_{gw}	Δw_{0x} or $\Delta w_{0\theta}$ or Δw_{0w}
Circumferential Compressive or Shear	Longitudinal	No	l_{gx}	Δw_{0x}
		Yes	l_{gx}	Δw_{0x}
	Circumferential	No	$l_{g\theta}$	$\Delta w_{0\theta}$
		Yes	l_{gx} or $l_{g\theta}$ or l_{gw}	Δw_{0x} or $\Delta w_{0\theta}$ or Δw_{0w}

where the gauge length is

$$l_{gx} = 4\sqrt{Rt}$$

$$l_{gw} = 25t \leq 500mm \quad \text{for sections with variable thickness } t = t_{min}$$

$$l_{g\theta} = 2.3\sqrt[4]{l^2Rt} \leq R$$

Table 4.3 Recommended Values of $U_{0,max}$ as listed in EC3-1-6 Table 8.4.

Fabrication tolerance quality class	Description	Recommended value of $U_{0,max}$
Class A	Excellent	0.006
Class B	High	0.010
Class C	Normal	0.016

Still some issues arise here as we deal with tapered section with variable radius along the length (meridional axis) of the structure as how to calculate l_{gx} and $l_{g\theta}$? And for sections under non-uniform compressive stress (for example under flexural moment or combined axial compression and moment), what if the worst dimple is located at lower compressive stress then other dimples?

4.2.3 Accidental Eccentricity tolerance

Accidental (unintentional) eccentricity or sometimes referred to as plates misfits, this tolerance is specific for shelled structures build from sheets or plates jointed together. The imperfection counts for misalignment of plates' centerlines at the joints between plates, this misalignment could be accidental or intended in design. Intended plate offset could be more desired for practical or aesthetic reasons specifically for shells with variable thicknesses. For SWTs the plate misfits or thickness transitions do not occur at a single cross section, but it follows the helical orientation of the plate. However, according to several studies it is believed the accidental eccentricity do not have radical effect on shell strength as dimple imperfections although it is believed to cause more damage when accidental eccentricity is accompanied with dimples (ECCS 2013, Rotter and Teng 1989). For the scope of this study the accidental eccentricity was not considered.

4.3 Imperfections in Numerical Modeling

As discussed previously imperfections play an important role when predicting buckling strength and post buckling behavior. Proper implementation of imperfections in a finite element model is crucial for good modeling. There are two major philosophies for implementing imperfections: realistic (measured) and generated imperfections.

4.3.1 Measured Imperfections:

Almost 50 years ago, aerospace researchers realized the importance of initial geometric imperfections and started measuring them in thin-walled shells. Arbocz (1968) and Koiter (1963) were among the earliest to measure real imperfections and study their effect on

buckling behavior of thin-walled shells, see Fig. 4.5. Koiter assumed an imperfection pattern and magnitude and proved its effect on buckling strength numerically. Hundreds of researchers came after measuring imperfections and recording buckling and post-buckling behavior, then came the idea of storing all available data of measured imperfections in an imperfection data bank to relate fabrication technique to patterns of imperfections (Arbocz et al. 1979, De Vries 2009).

The traditional method for measuring imperfections was using LVDTs around the shell and moving the specimen or the LVDTs either around or along the meridional axis. These measurements then represented by set of Fourier coefficients for half-wave sine, half-wave cosine or full wave representation (Sadowski et al. 2015). With the advancement in technology it became more feasible to use high-resolution laser scanner to scan the full geometry. Laser scanners are more accurate for detecting minor imperfections, which may affect the strength of thin-walled shells (Sadowski et al. 2014, Jay et al. 2016b).

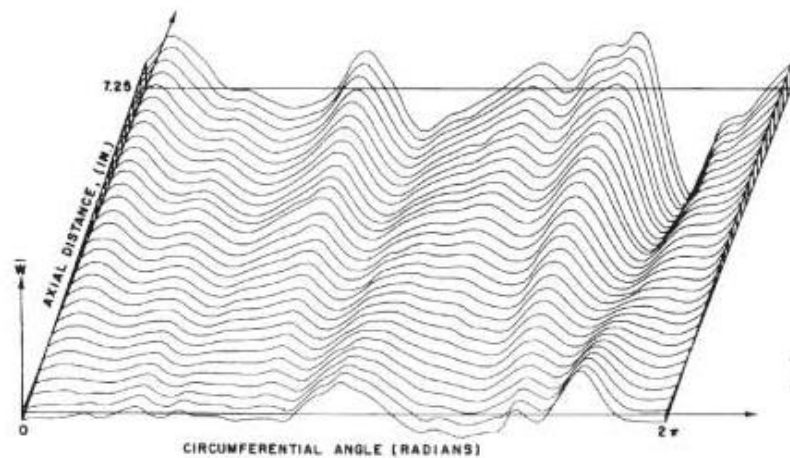


Figure 4.5 One of the earliest initial imperfections measurements by (Arbocz et al. 1969).

4.3.1.1 Laser scanner measurements of SWT specimens (SWT project)

Before testing, the nine SWT specimens were scanned at KTS fabrication facility then shipped. The point cloud resulted from measurements is the base for building the geometry of the numerical models. The measurements were performed by placing the specimen on a revolving rig and having the laser scanner move in the meridional direction, as shown in Fig. 4.6. The specimens were mounted on the scanner rig and fixed with two clamps at both ends of the specimen. Fig. 4.6 (a) shows the 3-point clamping of the ends of one of the specimens on the scanner rig. This method of supporting the specimens was problematic, as the deformation caused by the heavy weight of the specimens influenced the imperfections specially in the circumferential direction. The imperfections in the longitudinal directions were less influenced by the clamping, as the wavelengths of the clamping-induced imperfections were much longer than dimples' gauge lengths (dimples are the most severe form of imperfections for medium-length cylindrical shells under compressive stress). The scanned geometry for 8 of the specimens is shown in Fig. 4.7 (a-h). These figures show the initial imperfections (i.e. radial deviations from the perfect geometry) scaled 10x for eight of the nine specimens, specimen SW-230-0° was scanned in full. The effect of the clamps can be seen on all specimens near the ends, on early specimens (SW-145-0° and SW-305-0°) the effect of the clamps was noticeably affecting the measurements, see Fig. 4.7 (a-b). For later specimens, the clamping fixture was modified from 3-point clamps to 5-point clamps at the ends of the specimens, to decrease that effect, see Fig. 4.7 (c-h). Although the scans are made after the weld beads were flattened, the spiral seam and cross welds imperfections can be observed in the scans, see Fig. 4.7 (a-h). However, the spiral seam welds imperfections are more obvious (even

without scaling the imperfections) as the fabrication technique is to weld the flat plates together into segmental curves before feeding them to the rolling machines which also weld them spirally, see Fig. 1.10.

A report is made for each specimen that measures the tolerances and assign a quality class according to EC3-1-6 recommendations, where the out-of-roundness and the dimples are measured in both the circumferential and longitudinal directions, see Table 4.4.

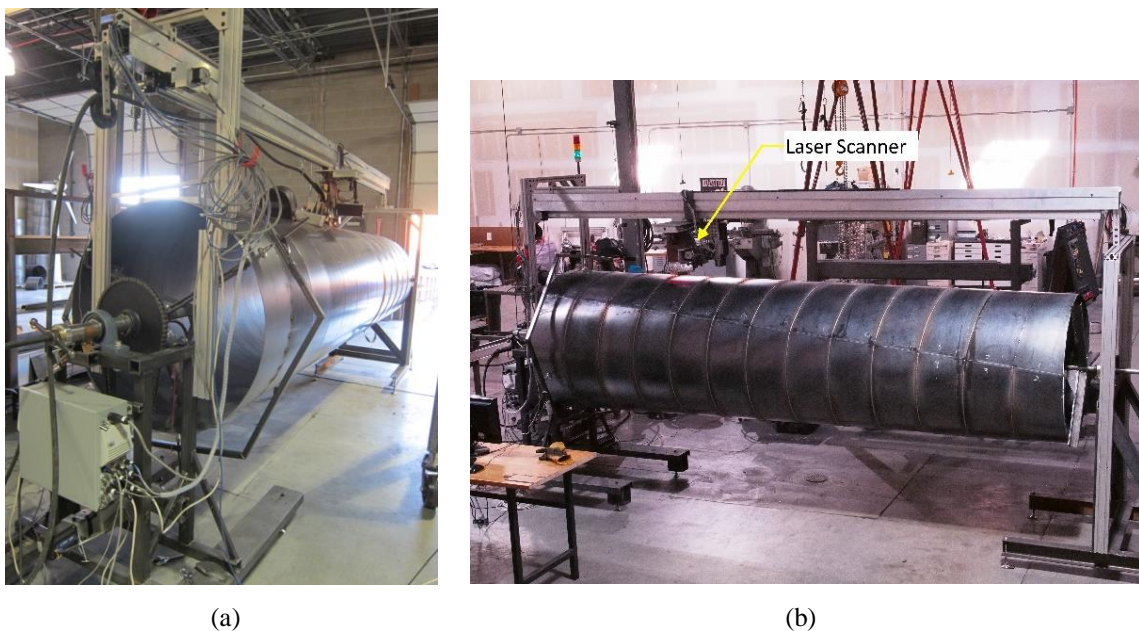


Figure 4.6 The KTS laser scanner with a specimen mounted (photos provided by KTS).

The deviations at the spiral seam and cross weld joints are severe and predicted to cause weak locations where buckling is expected to be triggered. For that reason, the location of the cross weld relative to the maximum meridional compressive stress was focused on while testing. Except for SW-145-0°, the worst circumferential and longitudinal dimples were adjacent to the cross welds, see Fig. 4.8 (b), and the worst weld dimple was located on the cross weld, see Fig. 4.8 (a) and (b) (for full reports refer to Jay 2017). Further

investigation was done by Mirzaie et al. (2017) on the relation between imperfections, buckling and post-buckling behavior of specimens.

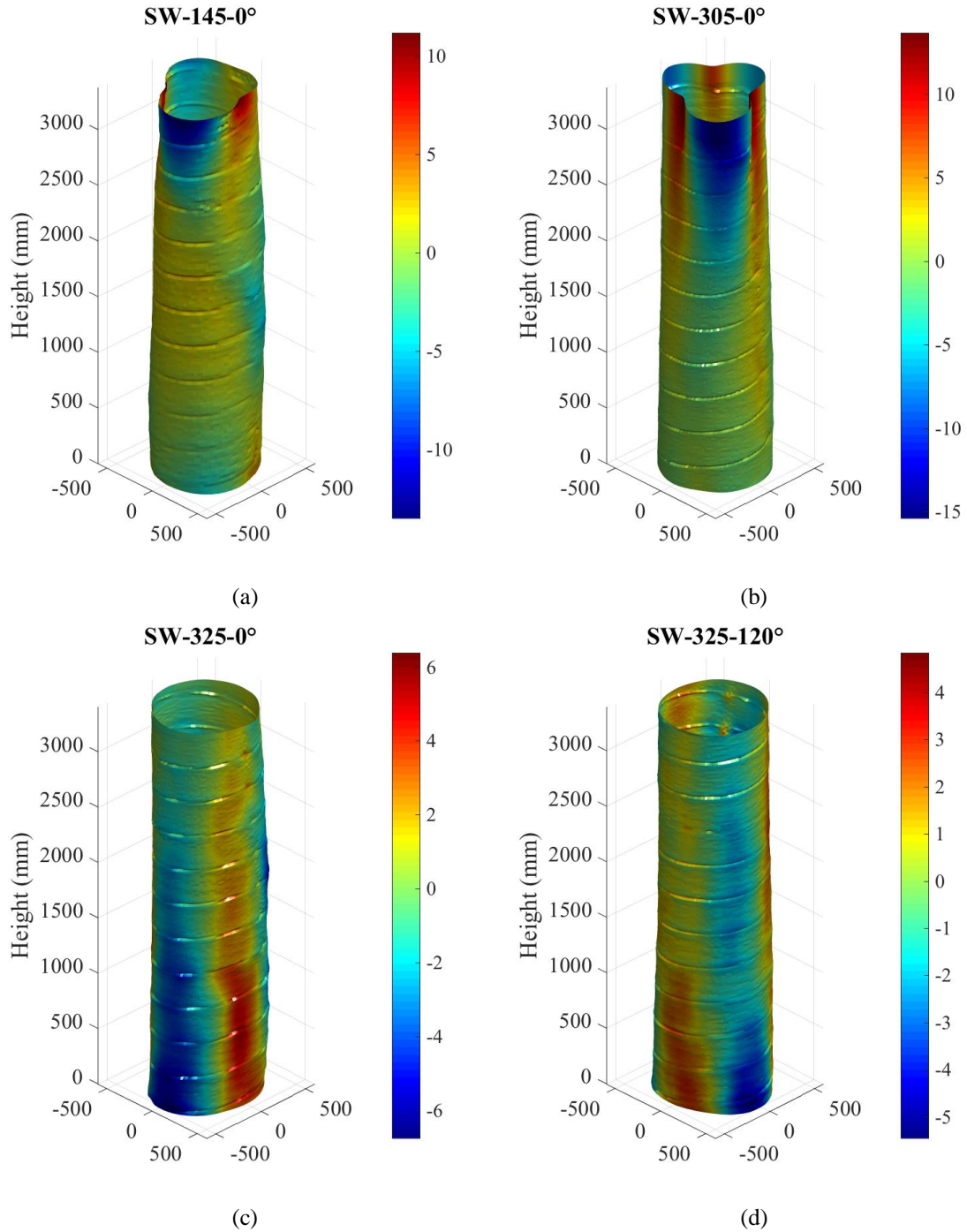


Figure 4.7 (a-d): Specimens scanned geometry with amplified imperfections 10x (color bar is radial deviations in mm).

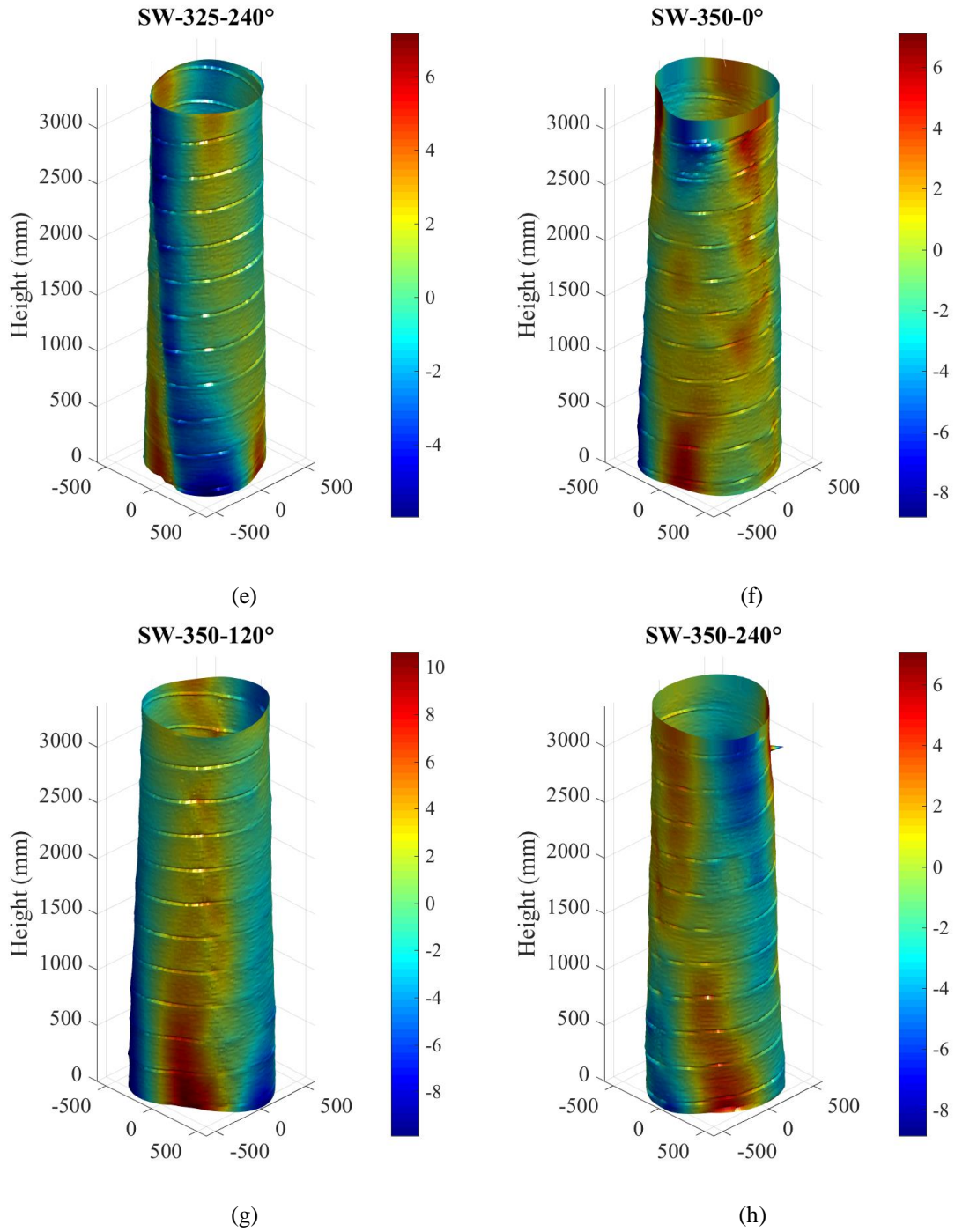


Figure 4.7(e-h) Specimens scanned geometry with amplified imperfections 10x (color bar is radial deviations in mm).

Table 4.4 summarizes the imperfection measurements for dimples in the circumferential and longitudinal directions and weld dimple imperfections as defined in EN 1993 1-6. The weld dimples are restricted to locations where the gauge length overlaps with a weld and

are measured with a smaller gauge length ($l_{gw} = 25t$) than that for the non-weld dimples ($l_{gx} = 4\sqrt{Rt}$), as prescribed in EN 1993 1-6. The length of the lines shown in Fig. 4.8 (a) and (b) at each maximum dimple location shows the gauge length to-scale as defined by EC3-1-6 for that cross-section and dimple type. EC3-1-6 also provides the corresponding Quality Class for each imperfection category individually and for all imperfections collectively (i.e., the worst Quality Class of all imperfection categories). All the specimens were classified as Class C, except SW-230-0° was classified as worse than Class C (WTC). Specimens SW-145-0°, SW-350-120° and SW-350-240° were classified as Class C according to one tolerance measurement only. Fig. 4.5 (a) and (b) shows an example of detailed analysis of the scans of two of the specimens.

Table 4.4 Summary of measurements of the maximum geometric imperfections for imperfection categories and associated quality classes (QC) (Jay et al., 2016a)

Specimen	EN 1993 1-6 Dimple Imperfections									Spec. Quality Class
	Weld Dimple			Longitudinal Dimple			Circumferential Dimple			
	Δw_0 [mm]	l_{gw} [mm]	QC	Δw_0 [mm]	l_{gx} [mm]	QC	Δw_0 [mm]	l_{gx} [mm]	QC	
SW-230-0°	1.7	83	WTC	1.8	137	C	1.6	137	C	WTC
SW-145-0°	1.5	155	B	2.0	203	B	2.7	203	C	C
SW-305-0°	1.1	74	C	0.9	140	B	2.0	139	C	C
SW-325-0°	1.0	74	C	1.1	145	B	2.1	146	C	C
SW-325-120°	0.9	74	C	0.8	146	A	2.2	144	C	C
SW-325-240°	0.8	74	C	0.6	146	A	2.2	149	C	C
SW-350-0°	1.0	76	C	1.6	154	C	2.2	158	C	C
SW-350-120°	1.1	75	C	0.8	158	A	1.4	158	B	C
SW-350-240°	1.0	76	C	0.8	160	A	1.4	158	B	C

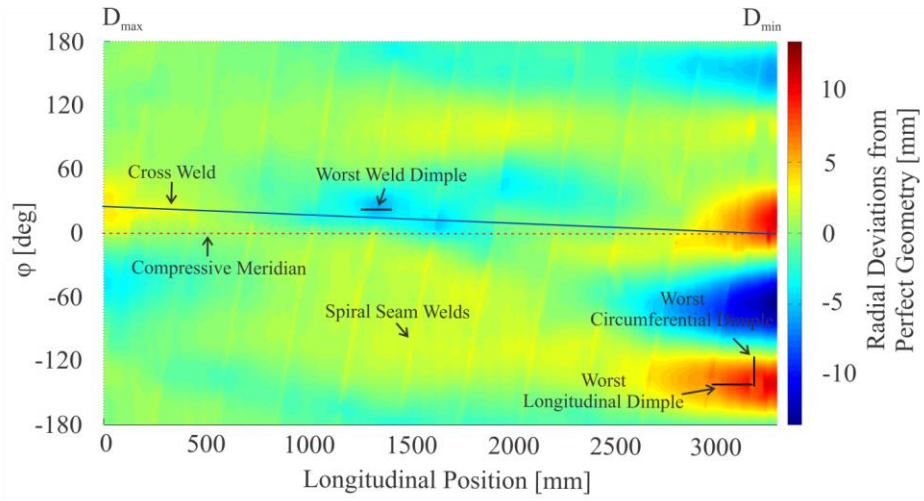


Figure 4.8 (a) Scan data for SW-145-0° showing deviations measured out-of-plane from the geometry of a perfect tapered tube. Positive deviations indicate imperfect geometry that is outside of the perfect tapered tube (Jay 2017)

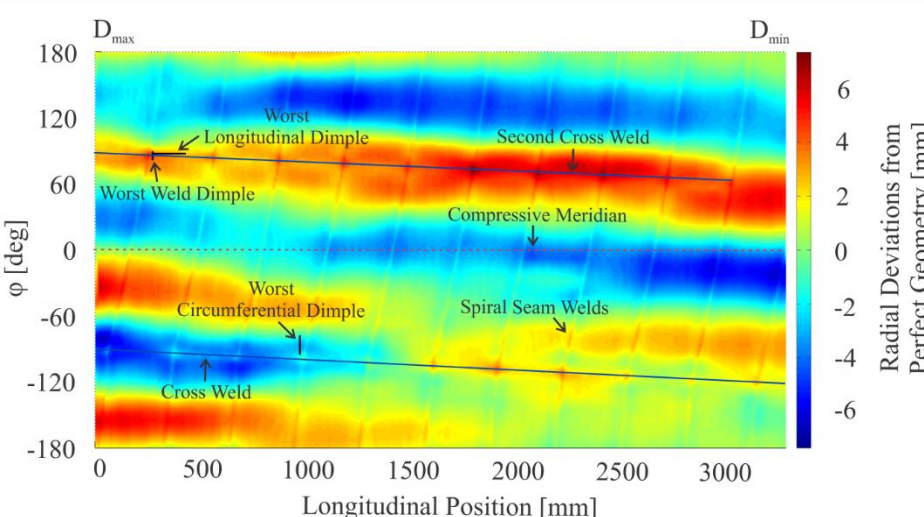


Figure 4.8 (b) Scan data for SW-350-240° showing deviations measured out-of-plane from the geometry of a perfect tapered tube. Positive deviations indicate imperfect geometry that is outside of the perfect tapered tube (Jay 2017).

It is worth mentioning that the measurements and reports were made before shipping the specimens to the lab and before placing the specimens on the testing rig, also parts from the ends of the specimens were cut at the lab to fit into the test rig, so there was more than one chance that more imperfections were induced during these processes. It is harder to predict the worst imperfection as the specimens were tested under flexural bending, so the

axial compressive stress distribution was not uniform, and the worst dimple imperfection could be in a lower stress zone than another dimple that is located at higher compressive stress.

4.3.1.2 Residual Stresses (SWT project)

For a thin-shelled structure, material non-linearities, such as residual stresses, are expected to influence the buckling strength and behavior (Singer et al. 2002, Vasilis et al. 2015). However, it is generally believed the loss of strength is primarily attributed to geometrical imperfections (ECCS 2013)

“A few studies of the development and consequences of residual stresses in cylindrical shells have been conducted (Guggenberger 1996; Rotter 1996; Holst et al. 1999, 2000). These generally lead to the conclusion that a consistent residual stress (one that satisfies equilibrium and can be present in the shell in its final imperfect geometrical form and does not increase the amplitude of the geometric imperfection when the shell is unloaded) is usually slightly beneficial, in that it increases the buckling resistance of the imperfect shell. Some earlier studies (Bornscheuer et al, 1983) reached a different conclusion but were conducted without using a consistent residual field.” (ECCS 2013)

In SWTs residual stresses potentially develop due to two main reasons, misfit and welding of plates. Misfit of plates during rolling as plates cannot be rolled to the exact radius as designed and the rolling process causes some waviness in the plate (Jay 2017) this type of residual stresses is believed to cause bending residual stresses within the thickness of the plate, see Fig. 4.9 (b). During the manufacturing process, the rolling machine control the radius to be as it was originally designed and deform the rolled plate elastically to force the plates' edges to align, according to the manufacturing process this type of imperfections is highly variable (Jay 2017, Arif 2012). Welding residual stresses on the other hand are more

uniform and predictable for a specific type of weld and they are believed to be the major cause of membrane stresses, see Fig. 4.9 (a). Jay (2017) measured residual stresses from large scale spirally welded tapered specimens and provided data and distributions within a typical rolled trapezoidal plate from the measurements (refer to Jay 2017 for the full details).

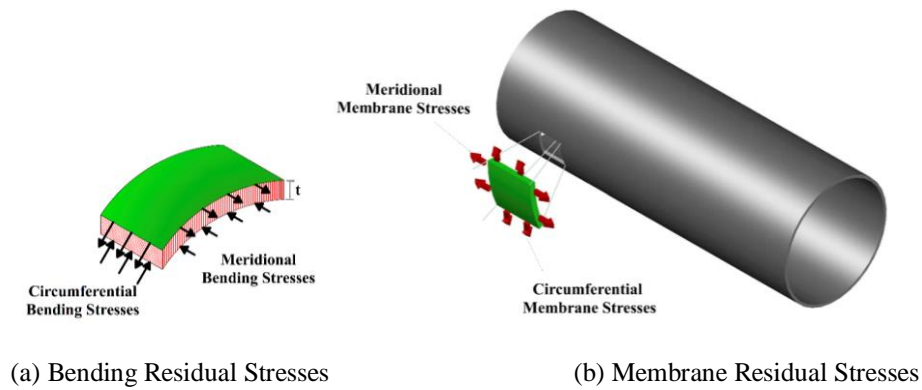
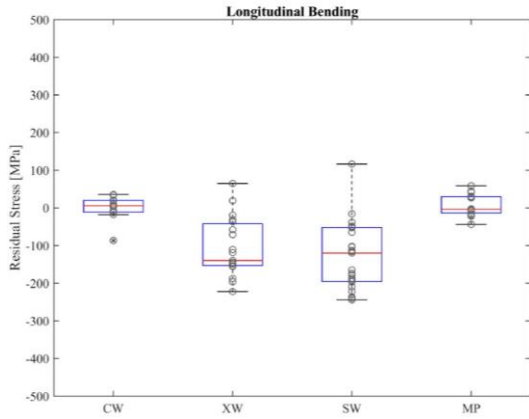
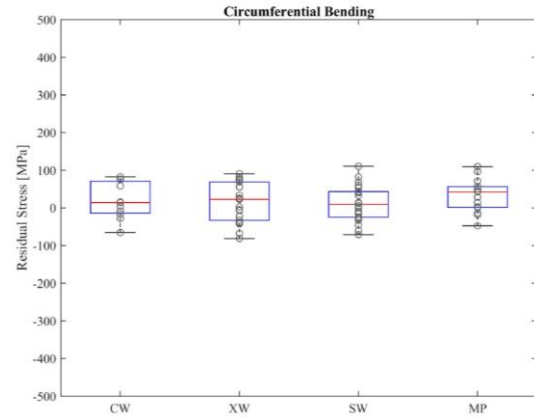


Figure 4.9 Membrane and bending residual stresses directions

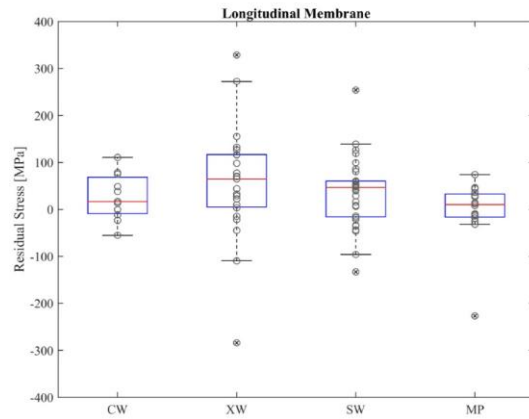
Fig. 4.10 shows a summary of the measured residual stresses for plates cut from six specimens. The abbreviations in Fig. 4.10 are described as: “CW” indicates residual stresses measurements at points near cross welds, “XW” indicates residual stresses measurements at points near cross-to-spiral weld connections, “SW” indicates residual stresses measurements at points near spiral seam weld, and “MP” indicates residual stresses measurements taken at points near the mid-plate.



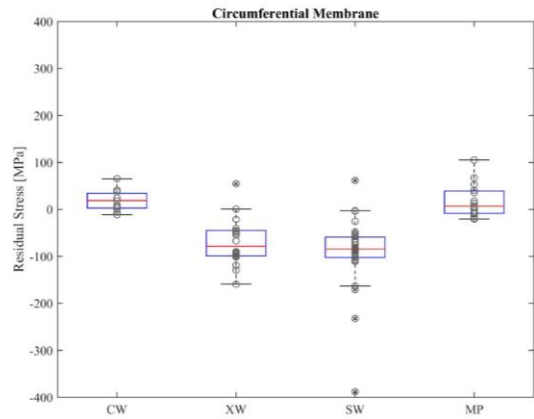
(a) Longitudinal (Meridional) bending



(b) Circumferential Bending



(c) Longitudinal (Meridional) membrane



(d) Circumferential membrane

Figure 4.10 Measured residual stresses from six trapezoidal plates and the red line indicate the median and the blue boxes indicates 25th and 75th percentiles of the data (Jay 2017).

Jay also provided an equivalent stresses pattern within a trapezoidal plate from the measurements that she proved it agrees with literature to be implemented in finite element models. The names of the areas within a trapezoidal plate as reported by Jay and its corresponding areas is shown in Fig. 4.11 (a). Fig. 4.11 (b) shows the typical distributions of bending and membrane residual stresses on both directions for various areas within the trapezoidal plate.

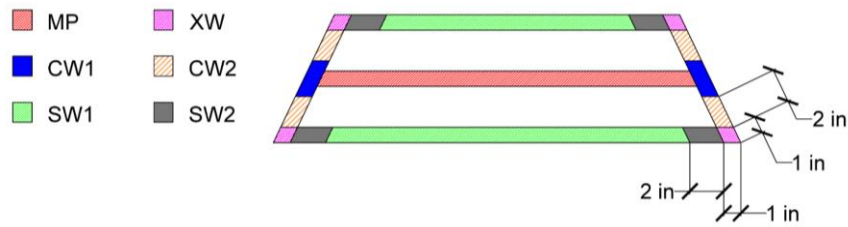


Figure 4.11 (a) Typical trapezoidal plate residual stress with areas of residual stresses pattern shown.

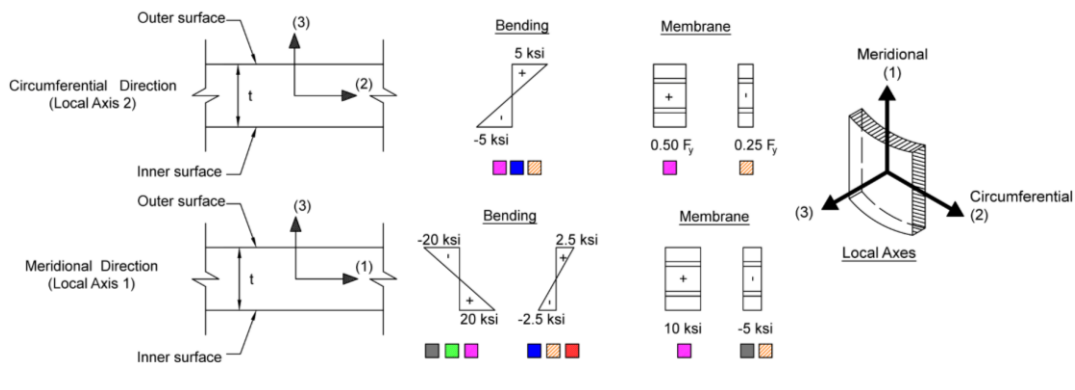


Figure 4.11 (b) Pattern of residual stresses within the thickness of the plate in both meridional and circumferential directions.

4.3.2 Generated imperfections

In design, actual imperfections are unknown, so analytically engineers generate an artificial imperfection, which they assume it is equivalent to the real imperfections. The nature of this generated imperfection varies from simplified, mathematical, construction-focused, statistical ...etc. The simplest approach for adding imperfection is to add little amount of lateral load to an axially compressed member to count for its out-of-straightness. Using 1st eigenmode as an imperfection pattern is an example of mathematical approaches for implementing imperfections. For generated imperfections, a lower-bound strength can be obtained by using the worst imperfection pattern. Using a numerical model with the perfect geometry (referred to in EC3-1-6 language as GMNA i.e. without imperfections, refer to Chapter 2) results in an upper bound, although, determining the worst imperfection pattern

is not a trivial process. To get a reasonable prediction of strength between the upper- and lower-bounds, many studies proposed methods for implementing imperfections either by “equivalent” or “worst shape” imperfections (Rotter 2004, Schmidt 2000, Jamal et al. 2003). Typically, these studies focused on shells under uniform axial compression. For welded shells, many studies focused on localized imperfections specifically patterned welds (Rotter and Teng 1989, Pircher et al. 2001, Hubner et al. 2006) as weld in these shells cause large imperfections. For shells under flexural bending the imperfections pattern should be implemented carefully to make sure the locations where compressive stresses are high are considered, as imperfections at these locations are most severe to the strength of the shell.

EC3-1-6 recommends using a simplified imperfection shape such as 1st eigenmode-affine imperfection pattern (obtained from linear buckling analysis (LBA) of the perfect model) or an equivalent imperfection pattern that is based on reasonable assumptions and affects the perfect geometry in an unfavorable way (CEN 2007, sec. 8.7.2). A recent study compared using different analytical method for generating imperfections such as linear and non-linear bifurcation buckling, weld depression profiles and post-buckling deformed shape and found that the imperfections pattern and magnitude choice by a designer or researcher can have a significant effect on the strength (up to 20%) of the GMNIA models (Jansseune et al. 2016).

4.3.3 SWT Project

For SWT project geometric imperfections are modeled for each specimen following two patterns of generated imperfections. The first pattern is based on the language in EC3-1-6

which recommends the use of an eigenmode-affine pattern unless a different unfavorable pattern can be justified (CEN 2007); in this case, the first eigenmode under pure bending, see Fig. 4.12 for an example, is selected. The second pattern is a “weld depression” imperfection which is modeled here along the spiral seam weld, see Fig. 4.13. As a baseline, a GMNA, or geometric and material nonlinear analysis model without imperfections, is considered for comparison.

4.3.3.1 1st eigenmode-affine pattern

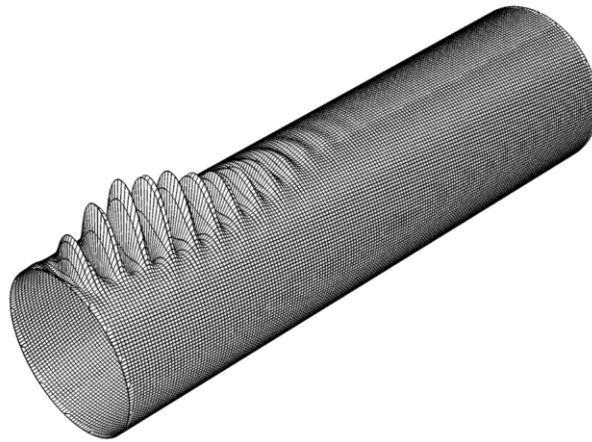


Figure 4.12 The first eigenmode of a tapered cylindrical member under flexural.

A set of 27 GMNIA models, i.e., geometric and material nonlinear analyses with imperfections, was created for SWT models. Three imperfection magnitudes with the eigenmode-affine imperfections are considered. For the eigenmode-affine imperfections the maximum imperfection magnitude is scaled to be consistent with the thresholds of the three fabrication tolerance quality classes in EC3-1-6 (A, B, C) for ‘dimple’ imperfections. The magnitude of the imperfection associated with these thresholds ($\Delta w_{0,eq1}$) is calculated per EC3-1-6 based on the gauge length (l_g) and the dimple magnitude parameter (U_{n1}), where $\Delta w_{0,eq1} = U_{n1} l_g$ and U_{n1} is defined for each fabrication tolerance quality class in

Table 8.1 in EC3-1-6 (CEN 2007). The gauge length, l_g , is equal to $l_{gx} = 4\sqrt{R_{avg}t}$, where l_{gx} is the gauge length in the meridional direction at locations not coincident with weld lines. Numerical values of $\Delta w_{0,eq1}$ and $\Delta w_{0,eq1}/t$ are provided for each specimen considered here in Table 4.4. The ratio of $\Delta w_{0,eq1}/t$ varies from 0.42 to 1.30 across all specimens and fabrication tolerance quality classes. It is noted that the half-wavelength of the first eigenmode in the meridional direction for the geometries considered here ranges between $2.0\sqrt{R_{avg}t}$ and $2.5\sqrt{R_{avg}t}$, which is comparable to theoretical prediction of half-wavelength for prismatic tubes under pure bending $\lambda = 2.44\sqrt{Rt}$ (Calladine 1983). Also, the gauge lengths are chosen to be greater than the theoretical half-wavelength, to capture the range of half-wavelengths where the dimple imperfections are more critical (when it matches or exceeds the eigenmode-affine pattern).

Table 4.5 Magnitude of the maximum amplitude of imperfection considered in the GMNIA models with 1st eigenmode-affine pattern imperfections for each specimen.

Specimen	Eigenmode Pattern					
	$\Delta w_{0,eq1}$ (mm)			$\Delta w_{0,eq1}/t$		
	Imperfection Classes in EC3-1-6			Imperfection Classes in EC3-1-6		
	A	B	C	A	B	C
SW-230-0°	1.38	2.21	3.45	0.42	0.67	1.04
SW-145-0°	2.07	3.30	5.16	0.33	0.53	0.83
SW-305-0°	1.42	2.27	3.55	0.48	0.77	1.20
SW-325-0°	1.46	2.34	3.66	0.50	0.79	1.24
SW-325-120°	1.47	2.34	3.66	0.50	0.80	1.24
SW-325-240°	1.48	2.36	3.69	0.50	0.79	1.24
SW-350-0°	1.56	2.50	3.90	0.52	0.83	1.29
SW-350-120°	1.55	2.49	3.89	0.52	0.83	1.30
SW-350-240°	1.57	2.51	3.92	0.52	0.83	1.30

4.3.3.2 Weld Depression by (Rotter and Teng 1989)

For each SWT specimen, a profile of weld induced geometrical imperfections is considered, this profile is referred to as weld depression. The profile used here is weld

depression profile suggested by Rotter and Teng (1989), where they suggested two general weld profiles Type ‘A’ to consider for full bending capacity and in Type ‘B’ which assumes no bending stiffness at the weld. Eq. 4.3 is the general weld depression profile equation where, δ_o is the amplitude of the imperfection profile, λ is the theoretical half-wavelength, x_w is the centerline of the spiral seam weld and ζ is the parameter for the weld stiffness and is taken as ($\zeta = 1.0$) for Type ‘A’ and ($\zeta = 0$) for Type ‘B’, see Fig. 4.14. The Type ‘A’ profile is chosen here as it has been shown to be more realistic and to have a more severe effect on reducing strength (Sadowski et. al 2015, Jansseune et al. 2016, Pircher et al. 2001). Three different magnitudes δ_o for the Type ‘A’ weld depression profile, were considered.

The gauge length used in calculating the amplitude of weld depression is $l_{gw} = \min(25t, 500mm)$ and the amplitude of the weld depressions is ($\delta_o = U_{n1}l_{gw}$), which are provided in Table 4.6.

$$\delta(x) = \delta_o e^{-\frac{\pi}{\lambda}(x-x_w)} \left[\cos\left(\frac{\pi}{\lambda}|x - x_w|\right) + \zeta \sin\left(\frac{\pi}{\lambda}|x - x_w|\right) \right] \quad (4.3)$$

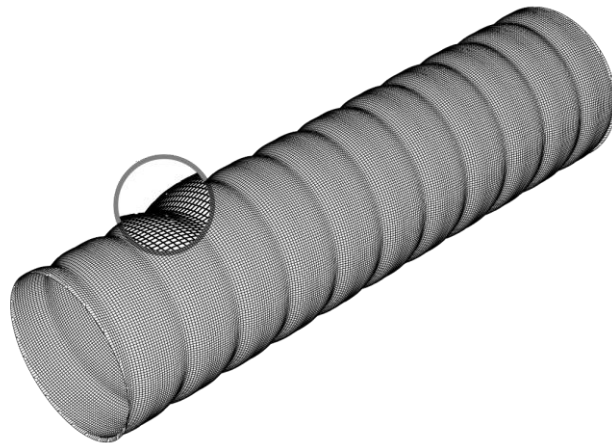


Figure 4.13 Specimen with weld depression along the spiral seam magnified 10x

The amplitudes are calculated according to corresponding to thresholds of imperfection magnitude for Class B and C in EC3-1-6 and a third magnitude that is worse than Class C (WTC) where the amplitude of the imperfection profile was taken the value as the thickness ($\delta_o = t$), see Fig. 4.12. Numerical values of δ_o are provided in Table 4.6. To have a proper representation of the weld depression a fine mesh is used ($0.25\sqrt{R_{avg}t}$) as recommended by Rotter and Teng (1989).

Table 4.6 Magnitude of the maximum imperfection considered in the GMNIA models with Type ‘A’ weld depression for each specimen.

Specimen	Weld Depression Pattern		
	δ_o (mm)		
	EC3-1-6 Class B ($\frac{\delta_o}{t} = 0.4$)	EC3-1-6 Class C ($\frac{\delta_o}{t} = 0.6$)	WTC ($\frac{\delta_o}{t} = 1$)
SW-230-0°	1.32	2.06	3.3
SW-145-0°	2.48	3.87	6.2
SW-305-0°	1.18	1.84	2.9
SW-325-0°	1.18	1.84	2.9
SW-325-120°	1.18	1.84	2.9
SW-325-240°	1.19	1.86	3.0
SW-350-0°	1.21	1.89	3.0
SW-350-120°	1.20	1.87	3.0
SW-350-240°	1.21	1.89	3.0

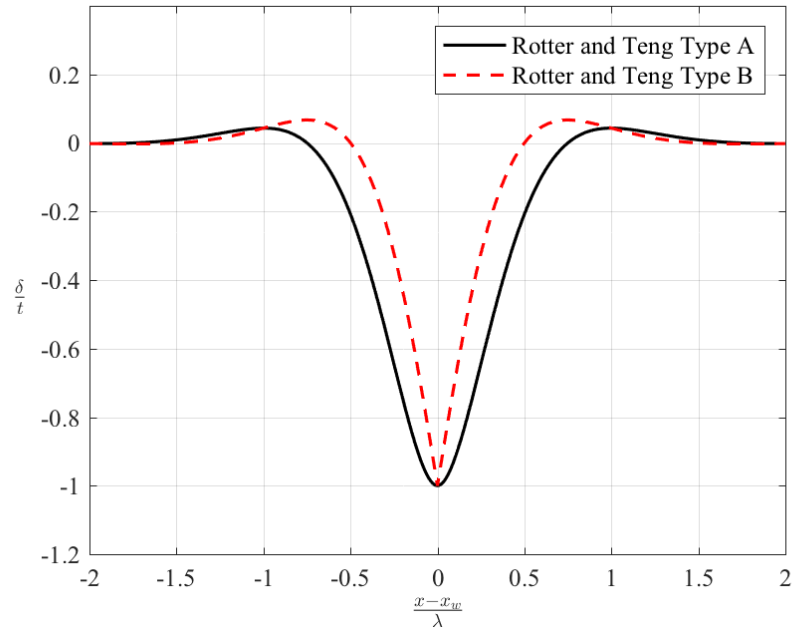


Figure 4.14 weld depression profiles Rotter and Teng (1989) Type A and Type B.

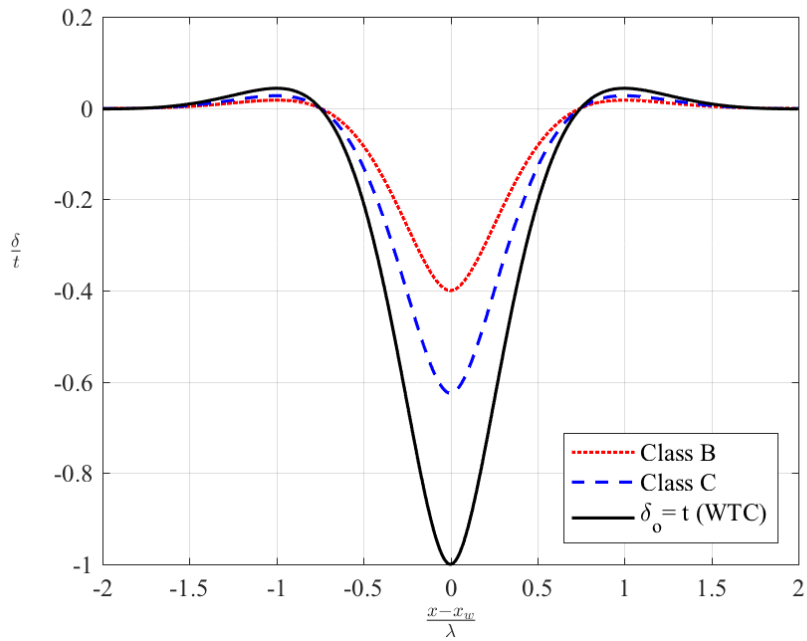


Figure 4.15 Weld depression Type 'A' scaled to EC3-1-6 Classes B and C, and WTC used in GMNIA models.

4.4 Summary and conclusions

In this chapter imperfections were discussed, as one of the most important factors controlling the buckling strength and postbuckling behavior of shells. The design methodology of specifications and guides that relates the design to the shell quality and others that use lower-bound knockdown factors was briefly described in the beginning of the chapter. Then a summary was provided for the evaluation of the quality of shells for out-of-roundness and local dimples tolerances per EC3-1-6. For SWT specimens, the imperfections of the nine specimens was measured using high resolution laser scanner by KTS, and a report was prepared for each specimen describing its quality class according to EC3-1-6 tolerances measurements and a commentary on the observations from these scans to the relation of the worst imperfection and the weld. Measured residual stresses are then briefly described and the equivalent distribution was provided. The two major approaches for implementation of imperfections in numerical GMNIA models were described. The first approach where the real imperfections from scanned geometry of SWT specimens was used to build the GMNIA models. The other approach is the generated equivalent imperfection pattern, two patterns were described: 1st eigenmode-affine pattern and weld depression. The amplitudes used in the generated imperfections were adopted from EC3-1-6, with one modification in the weld depression models, where instead of Class A we chose to consider a WTC where the amplitude of the imperfection profile was equal to thickness of SWT specimen.

For shells under bending, imperfections only matter in the compression side of the cross sections, but the buckling could be triggered by an imperfection that is less severe than the worst imperfection, if the compressive stress was higher at the less severe imperfection.

Imperfections due to dimples usually control the design of circular shells under compressive stress (where failure occurs due to local buckling modes). There is no clear way on how to measure tolerances on tapered sections or sections with thickness transitions, for the scope of this study (SWT project), thicknesses were constant and average radius was used for the gauge lengths. Patterns and amplitudes of generated imperfections should be carefully chosen to get a good prediction of the shell strength. High resolution scanners can be used in measuring real imperfections for quality evaluation, however, the preloading scanning process should be carefully designed in the future to not affect the measurements. The scans of eight of the SWT specimens will be implemented in numerical models and used for further investigation of the relation of imperfections and stresses to buckling in future.

Chapter 5

Mesh Sensitivity Analyses

5.1 Introduction

In research the number of tests conducted on a specific structure under specific type of loading is limited by mainly three factors: costs, time, and capacity of testing facility. With the advancement in computational processing and the availability of feasible numerical analyses tools (via Finite Element Analyses FEA), numerical modeling can potentially overcome most of the experimental limitations. Typically, for most of research programs, the numerical modeling is performed and verified against available experimental results. Then, based on the reliability of the models, the research can be expanded to larger scales (that cannot be tested) or by applying loads that are beyond the capacities of the loading jacks in lab. It is very important to include all possible aspects to mimic to the highest details the test conditions, and to validate the model results with the test results to get the reliable model. The geometry of a numerical model of a structure should represent all influential aspects of the structure's geometry. For modeling thin-walled tubes, shell elements are a reasonable choice for the finite element model, so long as through-thickness deformations and tri-axial stress distribution are not significant. Meshing SWT models, while considering the welds, is challenging due to the preference of a non-orthogonal mesh. Recently, a study has been performed on the mesh geometry using different layouts such as single helix partition, distorted mesh, double helix partition, and inclined irregular mesh to optimize the mesh geometry for spirally welded tubes (Sadowski et al. 2014). The main challenges are to orient the mesh in a way that is compatible with the spiral and cross weld

locations and to provide a proper mesh for the ends. To establish a modeling protocol that should be used for nonlinear collapse analyses of SWT GMNIA models, the mesh and elements features and irregularities is studied in this chapter.

5.2 Part I: Linear Buckling Analyses

To study the effect of mesh geometry and provide a base-line meshing protocol, a series of parametric eigen-buckling studies including both buckling loads (axial compression and pure bending) and shapes was performed and compared against the theoretical elastic critical compressive axial load and bending moment for pure compression and pure bending. Theoretical equations for critical normal stress, bending and axial load are provided in Eq. 5.1 to 5.3 (Seide 1956), and the theoretical buckling half-wavelength for prismatic tubes under bending is provided in Eq. 5.4 (Calladine 1983) and under axial load in Eq. 5.5 (Seide 1961).

$$\sigma_{cr-th} = \frac{E t \cos(\beta)}{r_{min} \sqrt{3(1-\nu^2)}} \quad (5.1)$$

$$M_{cr-th} = \pi r_{min}^2 t \sigma_{cr-th} \quad (5.2)$$

$$P_{cr-th} = 2\pi r_{min} t \sigma_{cr-th} \quad (5.3)$$

$$\lambda_{bending} = \frac{\pi \sqrt{rt}}{\sqrt[4]{3(1-\nu^2)}} \approx 2.44 \sqrt{rt} \quad (5.4)$$

$$\lambda_{compression} = \frac{\pi \sqrt{rt}}{\sqrt[4]{12(1-\nu^2)}} \approx 1.72 \sqrt{rt} \quad (5.5)$$

σ_{cr-th} is the theoretical critical compressive buckling stress, r_{min} is the minimum radius of the tapered cone, r the radius at mid height of the tapered shell, E is the Young's

modulus, ν is the Poisson's ratio, t is the thickness of the cylinder, which is assumed to be constant along the length, β is the angle of tapering, which is zero for prismatic tubes (see Fig. 3.5), M_{cr-th} is the theoretical elastic buckling moment, and P_{cr-th} is the theoretical elastic buckling load.

These classical equations were updated and reformulated in EC3-1-6 Annex D for buckling design for cylindrical sections with varied diameter where effective dimensions are considered, by introducing a factor C_x to count for the length of the shells and the changes in modes from local buckling to ovalization in longer sections introducing length parameter $\omega = L_e/\sqrt{r_e t}$, where L_e is the effective length ($L_e = L/\cos(\beta)$), r_e is the effective radius and it is taken ($r_e = r/\cos(\beta)$), the effective critical stress can be then considered as

$$\sigma_{cr-th} = \frac{EtC_x}{r_e\sqrt{3(1-\nu^2)}} \quad (5.6)$$

$$M_{cr-th} = \pi r_e^2 t \sigma_{cr-th} \quad (5.7)$$

$$P_{cr-th} = 2\pi r_e t \sigma_{cr-th} \quad (5.8)$$

where C_x is computed as follows:

$$C_x = 1.36 - \frac{1.83}{\omega} + \frac{2.07}{\omega^2} \quad \text{when} \quad \omega \leq 1.7 \quad (5.9)$$

$$C_x = 1 \quad \text{when} \quad 1.7 \leq \omega \leq 0.5 \frac{r_e}{t} \quad (5.10)$$

$$C_x = \max \left\{ \begin{array}{l} 0.6 \\ 1 + \frac{0.2}{C_{xb}} \left(1 - 2\omega \frac{r_e}{t} \right) \end{array} \right. \quad \text{when} \quad 0.5 \frac{r_e}{t} < \omega \quad (5.11)$$

and C_{xb} is a factor based on boundary conditions.

5.2.1 Parametric Model Geometry

The model geometry chosen for the parametric study on the mesh effects is a section with a maximum diameter of 1.07 m and minimum diameter of 0.98 m, a thickness of 3.05 mm ($D_{max}/t = 350$ and $D_{min}/t = 320$) and a height of 3.43 m. This geometry represents a scaled model of a segment of wind tower almost 1:8 of the base diameter of 140m wind turbine tower and is similar to the SWT test specimens. The predominant loading at the bottom of a wind tower is bending, distributed approximately linearly, with the maximum at the bottom of the tower and near zero bending. Presuming the length of the modeled segment considered here is small compared to the total length of the tower, a uniform moment distribution is a reasonable approximation to the loading expected in a wind tower.

The geometry of tapered spirally welded cylinders was built with an initial Matlab code that was created by KTS for manufacturing, and then this code was modified by JHU research team to be used in creation of models with helical mesh geometry and include imperfections and another custom code was created that generates input files for commercial finite element program ABAQUS. The Matlab code generates quadrilateral shell elements with desired mesh size, aspect ratio, and angle of inclination applicable to different shell element types (4 to 9 node quadrilateral shell elements).

5.2.2 Boundary Conditions

The boundary conditions of the numerical models are selected to be consistent with those for the SWT experiments, which as mentioned previously will be used to validate the nonlinear modeling protocol described in the following section. Two reference points were created at the center of both ends of the tube to define loads and boundary conditions. A beam-type multi-point constraint (MPC) connects the reference points (shown as RP-1 and RP-2 in Fig. 5.1 and Table 5.1) to the end nodes of the models. This type of constraint prevents any relative deformation between the reference point and the end nodes of the model, thereby restricting ovalization of the ends, and permits all end nodes along with the reference point to collectively displace or rotate in any direction. The boundary conditions applied to these two reference points are defined in Table 5.1 and Fig. 5.1. The applied boundary conditions allow flexural end rotations at both end, restrict in-plane displacements across the member (i.e., in the X or Y directions) at both ends, restrict meridional (longitudinal) displacements (i.e., in the Z direction) at the small diameter end (RP-2), allow meridional displacement at the large diameter end (RP-1), and restrict torsional rotations at both ends. Flexural loading is considered with two equal end moments (M_x) are applied to both ends, while axial compressive loading is considered with an axial load (P_z) applied to the small diameter end (RP-2), see Fig. 5.1.

Table 5.1: Boundary conditions applied at the reference points which control the nodes at the end of each end of the model, respectively. The X-Y-Z coordinate system is defined in Fig. 5.1. X means that the indicated degree of freedom is constrained.

Reference Point Name	Location	Displacement			Rotation		
		X	Y	Z	X	Y	Z
RP-1	Large diameter end	×	×				×
RP-2	Small diameter end	×	×	×			×

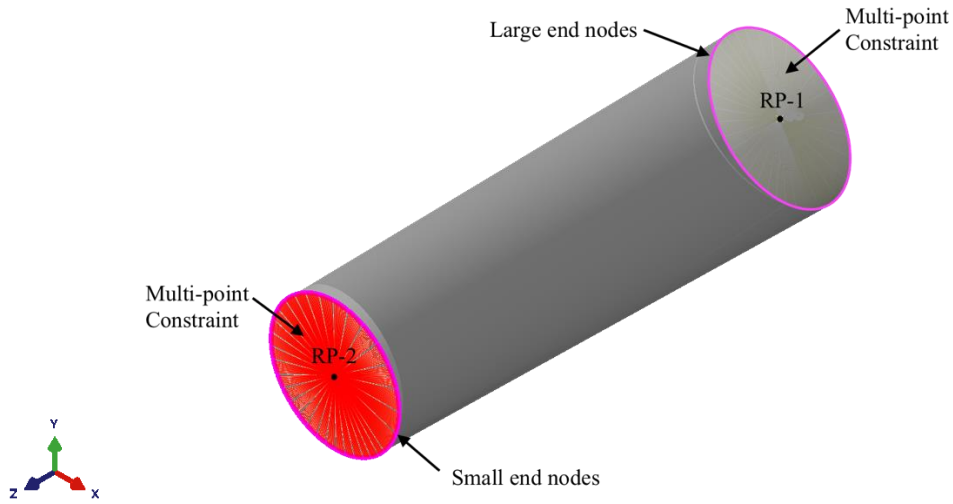


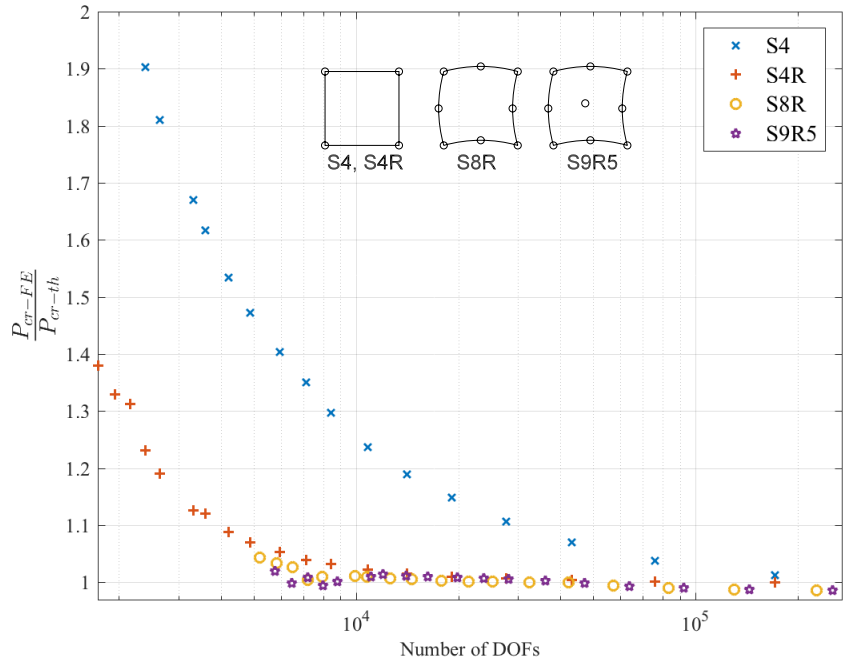
Figure 5.1 Definition of reference points RP-1 and RP-2 used to apply boundary conditions through Multi-Point Constraint (MPC) of the nodes at each end of the tube.

5.2.3 Sensitivity to shell element type

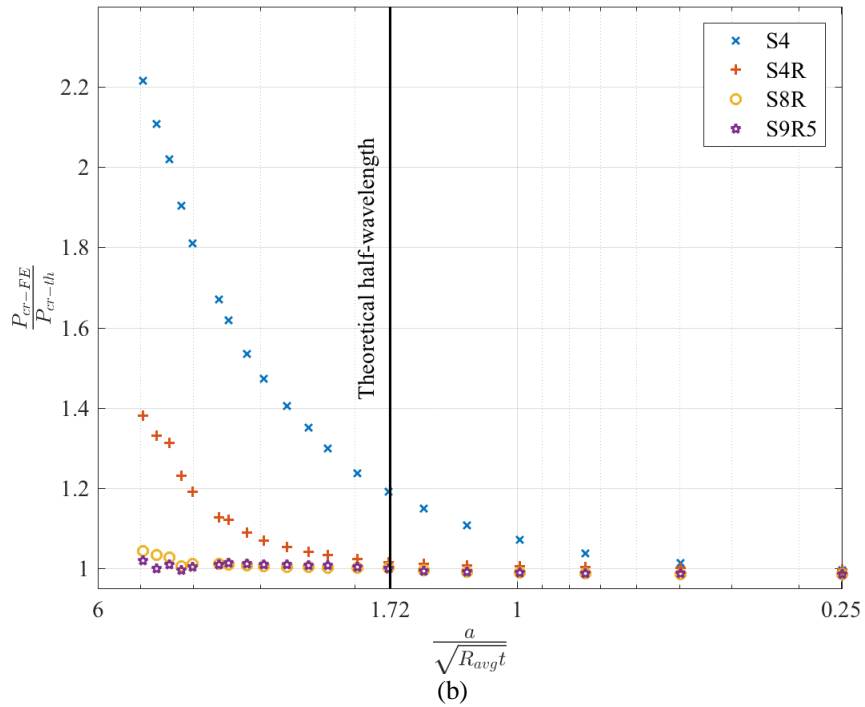
Four types of ABAQUS shell elements (S4, S4R, S8R, and S9R5) are considered to study the effect of element type on the elastic buckling of model geometry described previously under both axial load and bending moment (Simulia 2014). For this study, the element aspect ratio is fixed at 1:1, and the angle of inclination is zero (i.e., the mesh is a regular structured mesh oriented with respect to the meridional and circumferential directions of the tube).

The results of the linear buckling analyses are shown in Fig. 5.2. The critical loads are normalized by the associated critical loads (see Eq. 5.7-5.8) for axial compression (Fig. 5.2

(a) and (b)) and for bending (Fig. 5.3 (a) and (b)) and are plotted against number of degrees of freedom (Fig. 5.2 (a) and 5.3 (a)) and number of elements (Fig. 5.2 (b) and 5.3 (b)) to indicate convergence characteristics. For the case of axial compression, the S4 has the slowest rate of convergence, and the S4R element with reduced integration and hourglass control converges much faster. The thin shell quadratic elements, S8 and S9R5, converge at approximately the same rate as the S4R, but converge to a different axial critical load that is approximately 2% lower than the theoretical buckling load. The mode shape at the converged critical load is indistinguishable among the four element types. It is important to note that the quadratic elements are thin shell elements while the S4R only enforces Kirchoff constraints through a penalty. However, since the studied shell is thin, it is not surprising that the quadratic elements perform well. For the case of pure bending, the S4 element again exhibits poor convergence. The results show that the S4R, S8R, and S9R5 elements eventually converge, with the S9R5 showing the fastest rate of convergence. Based on convergence with respect to the number of degrees of freedom, the S4R converges faster than the S8R and nearly as fast as the S9R5. The one drawback to the S4R is its overly stiff response for very coarse meshes, otherwise it provides a robust solution. Given the element formulation, agreement with theoretical solutions, and the reasonable speed of convergence, the S4R is selected for further study. The S4R is easier to code from a meshing perspective as it is available using the ABAQUS graphical user interface unlike the S9R5. Theoretically, the S4R is a more robust element, with an ability to handle a larger range of D/t , as well as finite strains (Simulia 2014).

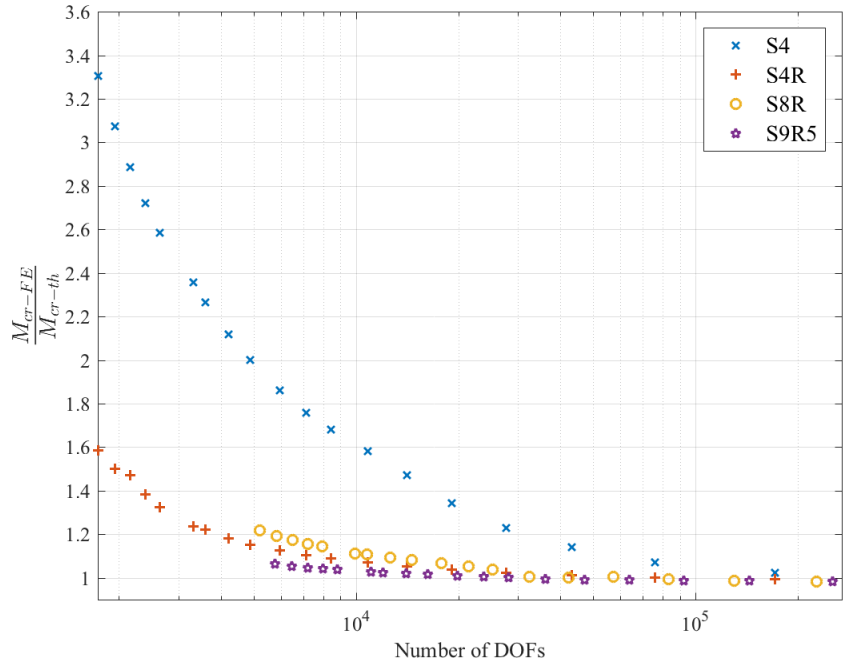


(a)

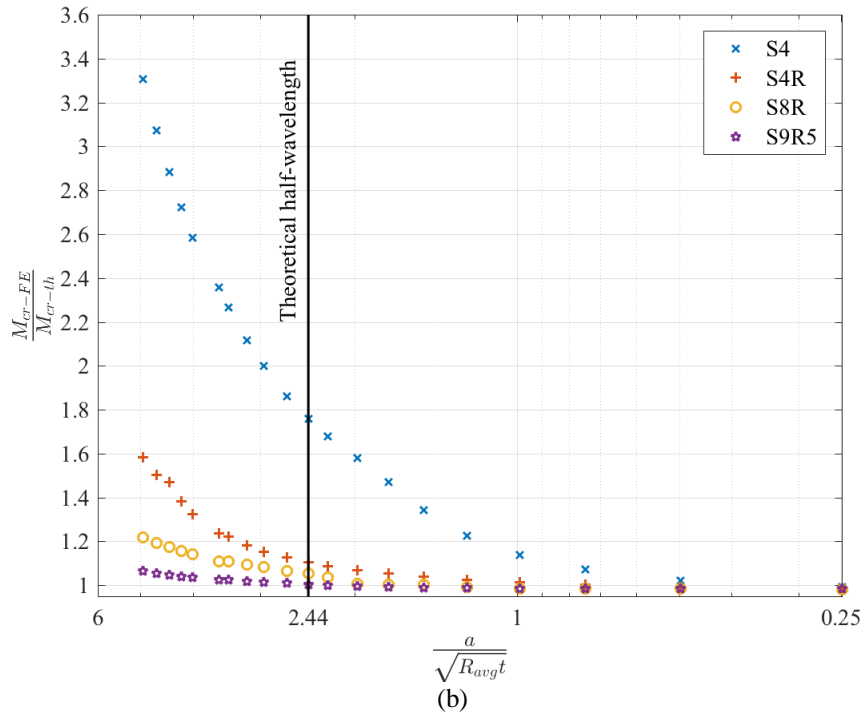


(b)

Figure 5.2(a-b) Mesh convergence for different shell elements types under axial compression



(a)



(b)

Figure 5.3(a-b) Mesh convergence for different shell elements types under pure bending.

5.2.4 Sensitivity to element aspect ratio

Three element aspect ratios ($1:1$, $1:2$, and $2:1$; where the first number represents the meridional direction and the second number represents the circumferential direction, see Fig. 5.4) are considered to study the effect of element aspect ratio on the elastic buckling of the model geometry described previously (sec. 5.2.1) under both axial load and bending moment. All models considered in this particular study are meshed with the S4R shell element, without inclination.

The results of the linear buckling analyses are shown in Fig. 5.6 and 5.7. The critical loads are normalized by the associated critical loads (see Eq. 5.7 and 5.8) for axial compression (Fig. 5.6) and bending (Fig. 5.7). Results are plotted against the mesh size in terms of a/\sqrt{Rt} , where a is the dimension in the meridional direction of the model, R is the tube mean radius, and t is the tube thickness. The results, indicate, as expected, that, for an accurate model, the mesh size should be less than the theoretical buckled half-wavelength. Although the convergence of the models with element with $1:2$ aspect ratios is much faster in the meridional direction, even for meshes coarser than theoretical half-wavelengths for both axial compression and bending, it is shown that for a finer mesh size (less than $1.00\sqrt{Rt}$) the effect of the aspect ratio decreases for both cases of loading and all of the considered aspect ratios give reasonable results. As such, an aspect ratio of $1:1$ combined with a maximum element size of $1.00\sqrt{Rt}$ has been recommended

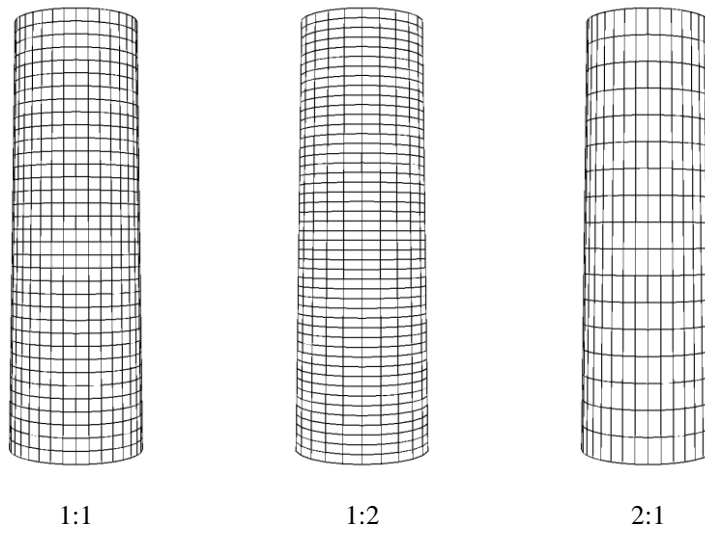


Figure 5.4 Shell element aspect ratio in terms of $a:b$, where a is the meridional direction and b is the circumferential direction.

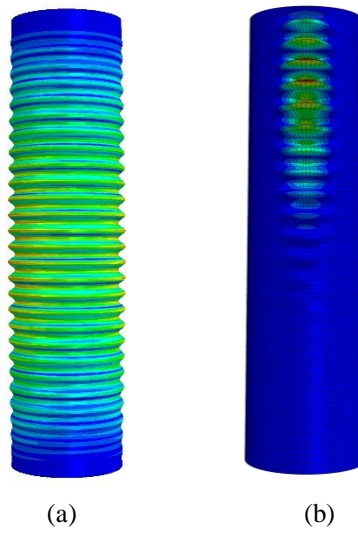


Figure 5.5 Typical buckled shape of cylindrical shell with $1:1$ mesh under (a) axial compression, and (b) bending.

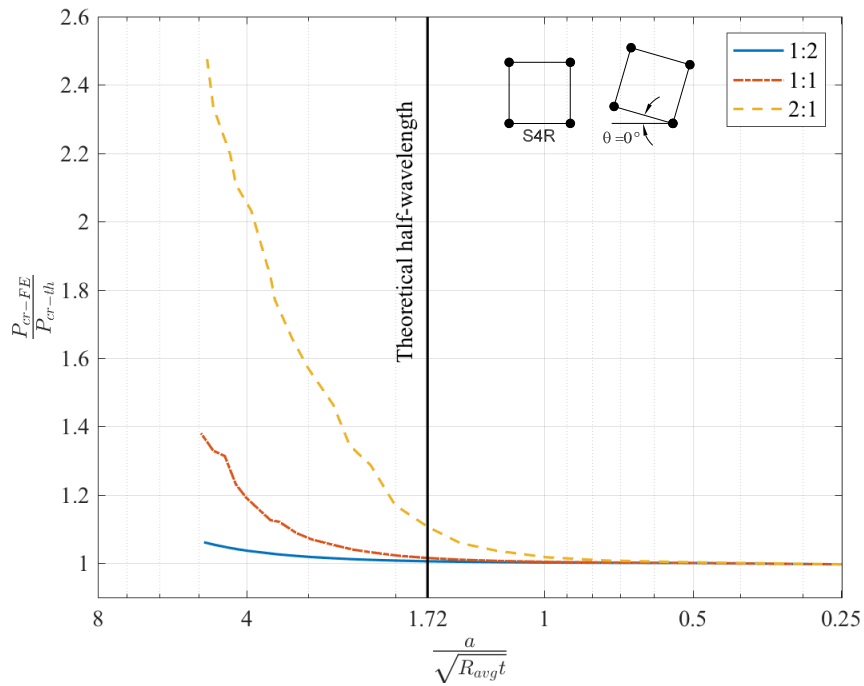


Figure 5.6 Mesh convergence for different element aspect ratios size with respect to element size in the meridional direction in terms of (\sqrt{Rt}) under axial compression

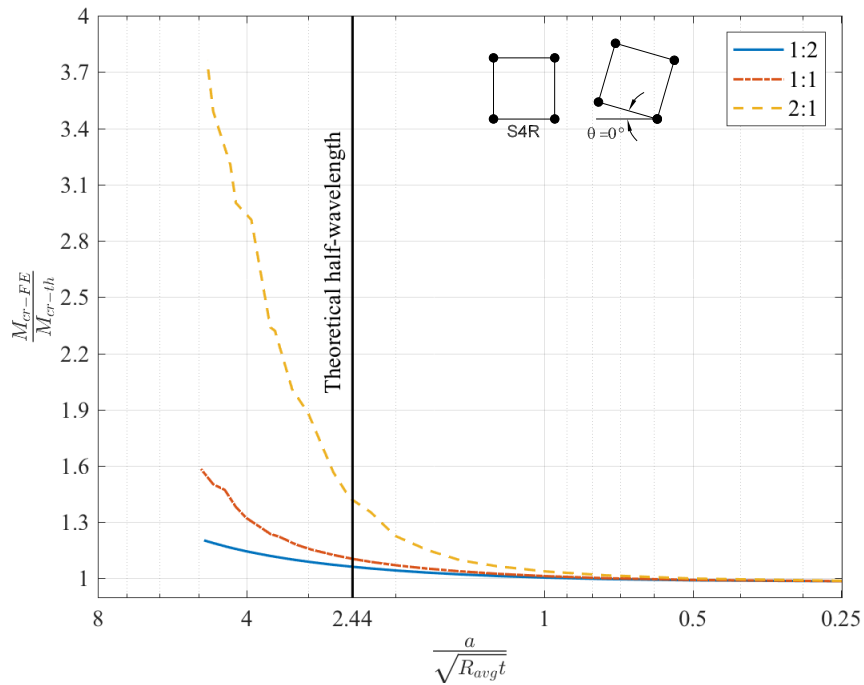


Figure 5.7 Mesh convergence for different element aspect ratios size with respect to element size in the meridional direction in terms of (\sqrt{Rt}) under pure bending

5.2.5 Sensitivity to inclination angle of element

The S4R element inclination angles ($\theta = 0^\circ, 5^\circ, 10^\circ, 15^\circ$ and 25° , where θ is defined in Fig. 5.8) are considered to study the effect of element orientation on the elastic buckling of the model geometry described previously under both axial load (Fig. 5.10) and bending moment (Fig. 5.11). All models considered in this particular study are meshed with the S4R shell element with a 1:1 aspect ratio.

There are modeling advantages to aligning the inclination of the elements with respect to the inclination of the spiral welds. Note, for wind towers made from spiral welding, the inclination angle of the spiral welds is expected to be less than 15° . Since element inclination angles greater than zero are no longer aligned with the meridional and circumferential directions of the tube, some care must be taken when meshing the ends of the tubes. For this study, the ends are meshed using quadrilaterals, which, depending on the inclination angle, can be distorted with angles far from 90° , see Fig. 5.8. As mentioned before, the boundary conditions are modeled in a way that constrains the end nodes to remain in a circle, and, as a result, it is not expected that these mesh irregularities at the ends are strongly influential. Fig. 5.9 shows the typical buckled shape of the 1st eigenmode for a tapered cylindrical shell models with helical mesh under axial compression and bending, the buckled shape seems to be inclined at an angle that is almost equal to the helical angle of the mesh, see Fig. 5.8 (b) and Fig. 5.9 (d).

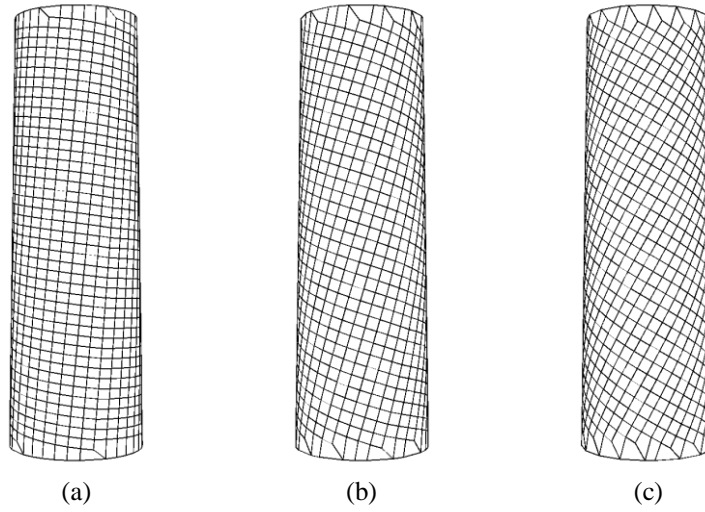


Figure 5.8 Helical mesh with different inclination angles θ : (a) 5° , (b) 15° , (c) 25° .

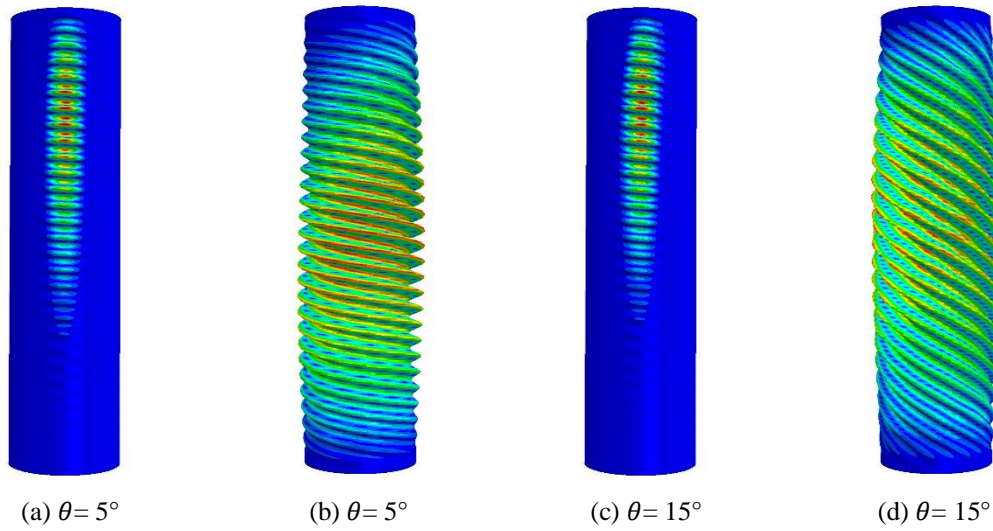


Figure 5.9 Typical buckled shape of a tapered cylindrical mesh with helical mesh with angle θ under (a) & (c) bending and (b) & (d) axial compression.

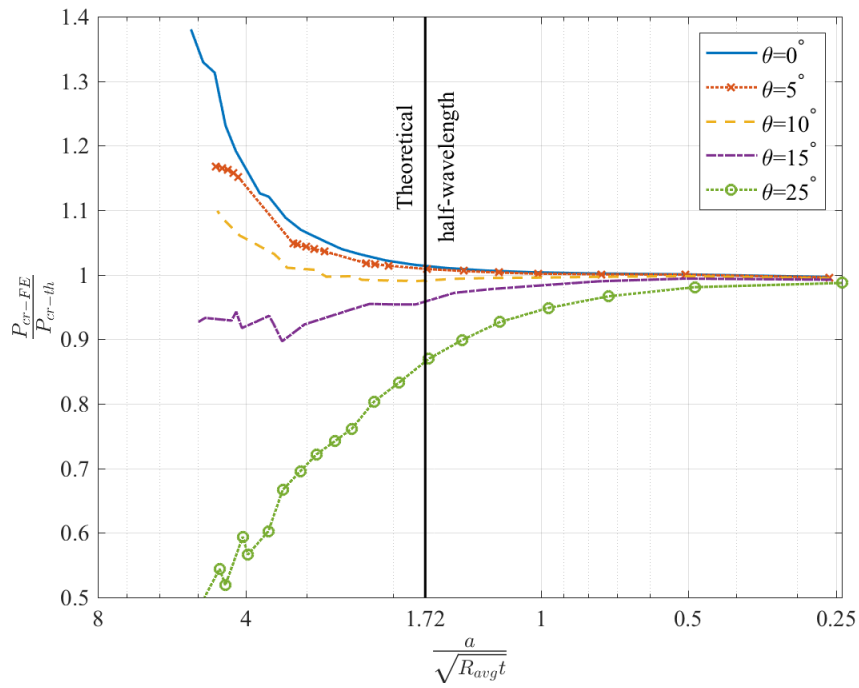


Figure 5.10 Mesh convergence with the size of element in the meridional direction and $1:1$ element aspect ratio for pure compression.

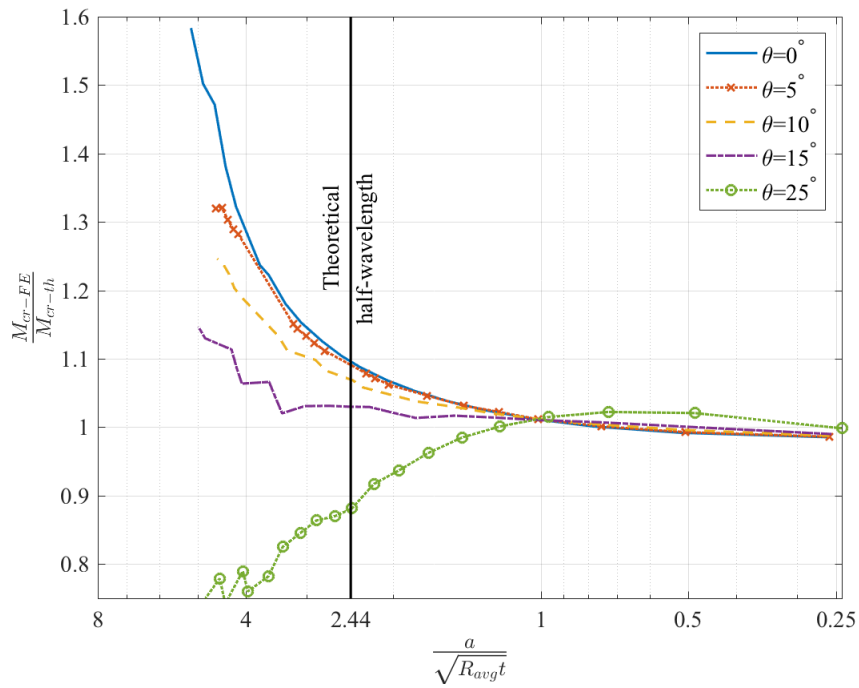


Figure 5.11 Mesh convergence with the size of element in the meridional direction and $1:1$ element aspect ratio for pure bending.

The results in Fig. 5.10 and 5.11 show that the large inclination angles can dramatically reduce the mesh performance for loading in both axial compression and in pure bending. Small inclination angles (0° - 10°) show better convergence rates even for mesh size equal to $1.00\sqrt{Rt}$. As the angle of inclination increases from 10° to 30° , it is required to refine the mesh to almost $0.10\sqrt{Rt}$ to achieve convergence. One would expect higher stiffness and critical loads when using coarser meshes, but due to numerical issues, which were observed similarly by Sadowski et al. (2013), coarser meshes with inclination increased angles between 10° and 30° underestimate the critical loads. It is also noted that the convergence rate is better in pure bending than in axial compression. Accordingly, the maximum mesh size is suggested to be limited to ensure the convergence of the numerical models. For angles of inclination between 0° and 10° , the mesh size should be less than $0.50\sqrt{Rt}$ to ensure convergence for all loading conditions. As such, in this study, the mesh size is $\leq 0.50\sqrt{Rt}$.

For future research the source of this error should be formally addressed, and sensitivity of other possible elements should be determined (for example: Bathe's MITC4 in ADINA).

5.3 Part II: Validation of the meshing protocols for the nonlinear analysis

The meshing protocols from the linear buckling analyses must be validated for the nonlinear analysis models. This section only studies the mesh sensitivity of GMNIA models under pure bending, to prepare for the SWT GMNIA models. Using 1st eigenmode-affine pattern as imperfections and scaled to quality Class B, the same parametric model described in section 5.2.1 of this Chapter, is validated for the nonlinear analysis. First for

each model, nominal perfect geometry was subjected to LBA analysis was done to get the 1st eigenmode and then the deviation from the nominal geometry was scaled such that the amplitude of the buckled shape deviation meets Class B recommended amplitude in EC3-1-6 (as described in Chapter 4). Fig. 5.13 to 5.15 summarize the results of this study. The material model used is the true stress-strain curve model from one of the tested specimens (specifically SW-325-120°) which represents a realistic behavior of the specimens.

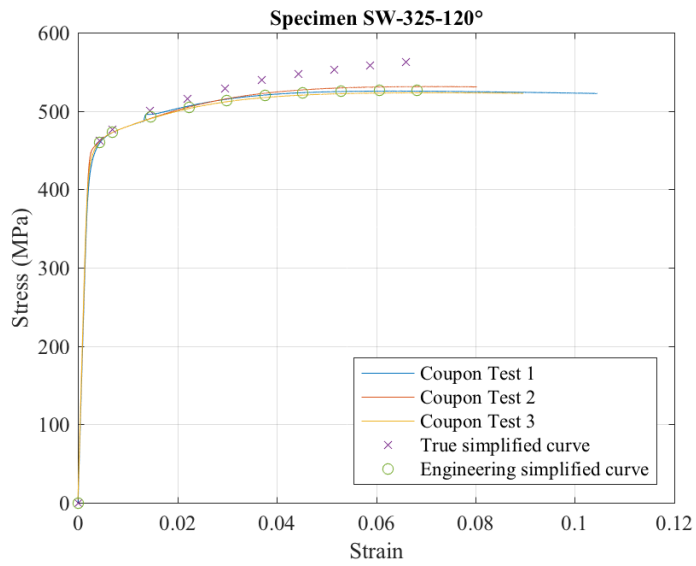
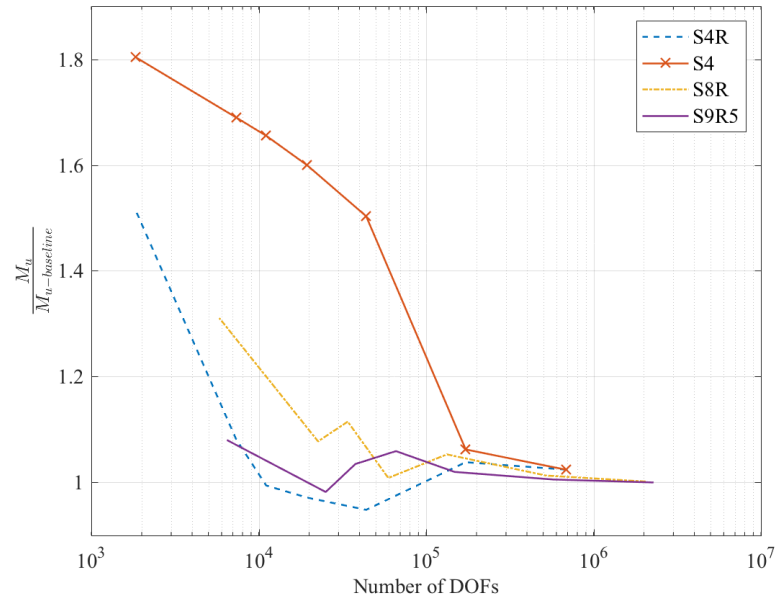
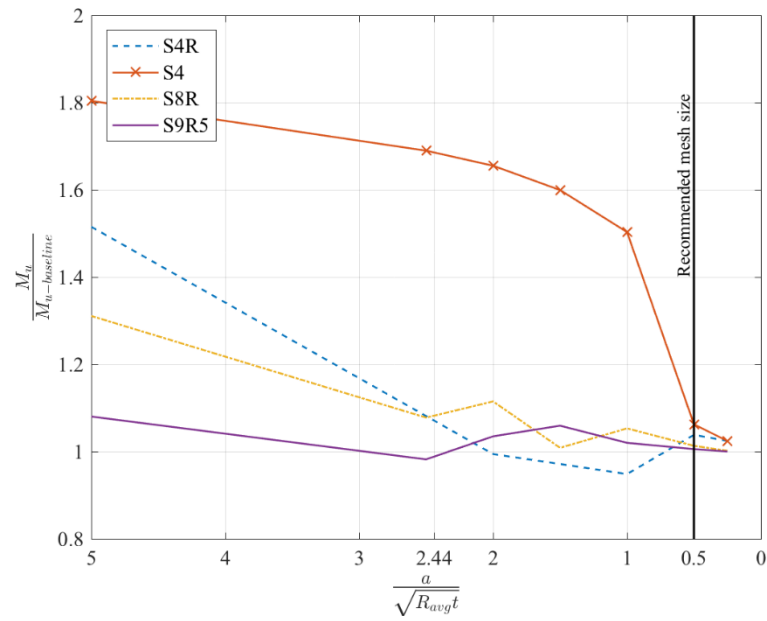


Figure 5.12 Material properties of GMNIA models used in nonlinear mesh sensitivity analysis.



(a)



(b)

Figure 5.13(a-b) The effect of the element types for S4, S4R, S8R & S9R5 on the nonlinear models vs (a) number of Degrees of Freedom (b) size of mesh in Meridional direction.

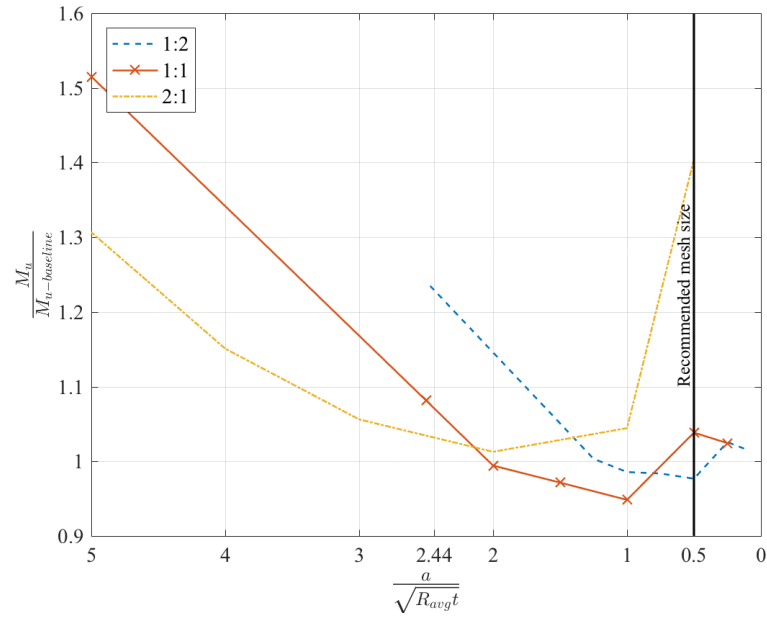


Figure 5.14 The effect of element aspect ratio on nonlinear models

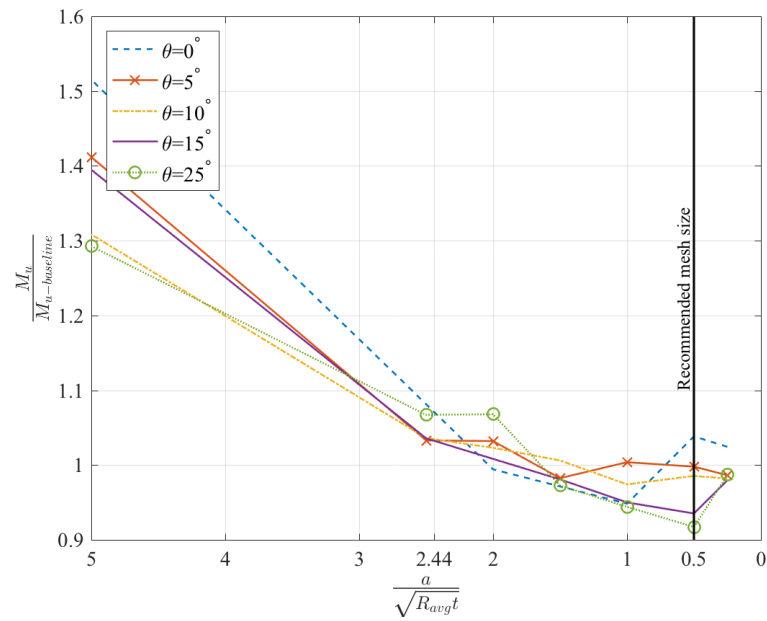


Figure 5.15 the effect of the inclination angle of the mesh on nonlinear models.

Without test, a fine mesh with S9R5, the best performing element in elastic buckling, was selected to be our baseline model for comparison.

Fig. 5.13 (a) and (b) shows the ratio of the ultimate flexural capacity for different sizes of different shell element types (S4, S4R, S8R and S9R5) to the ultimate flexural capacity of our chosen baseline model which is the model with finest mesh of the S9R5 ($M_u/M_{u_baseline}$). The elements have 1:1 aspect ratio and 0° helical angle. S4R, S8R and S9R5 showed a reasonable convergence as the mesh size decreases; however, the S4 is highly influenced by the mesh size. As in the elastic buckling studies, the S4R element and the quadratic S9R5 element are found to be adequate in comparison with benchmarks.

Fig. 5.14 shows the effect of the aspect ratio of the elements in circumferential direction to the meridional direction (see Fig. 5.4) on the ratio of the ultimate flexural capacity of each model to the ultimate flexural capacity of the base model ($M_u/M_{u_baseline}$) for different sizes of S4R element with 0° helical angle. Aspect ratios of 1:2 show the fastest convergence, but note it can still be more difficult to create the geometry in the spirally meshed models. In comparison, and aspect ratio of 2:1 shows inconsistent behavior, while a 1:1 geometry is both easy to create and collapse results are reasonable.

Fig. 5.13 shows the mesh size vs the ratio of ultimate flexural capacity of the models with mesh inclination angles (0°, 5°, 10°, 15° and 25°) to the ultimate flexural capacity of the model with finest mesh of the S9R5 ($M_u/M_{u_baseline}$).

The meshing protocol established in sec 5.2 of this Chapter is valid for the nonlinear collapse analysis for GMNIA models, using S4R shell elements with a mesh size less than or equal to $0.5\sqrt{Rt}$ as shown in Fig. 5.16.



Figure 5.16 Full mesh of typical model of helically meshed tapered tube following the mesh guidance and the predicted collapse shape under bending.

5.4 Testing the Effect of the Imperfections Pattern

In section 5.3, we ran the same model twice first LBA with the perfect model to get the 1st eigenmode, then that buckled shape was scaled and used as an imperfection pattern for the GMNIA models. To be consistent and prove the reliability of the mesh sensitivity analysis for the nonlinear collapse models, we repeated the same study but with the same imperfection pattern among all the models.

A single profile of imperfections was used, specifically the 1st eigenmode of the baseline model used in section 5.3, the models were created with different mesh sizes and orientations, and the deviations of the perfect geometry were interpolated to the same imperfect shape as the baseline model. For the coarser meshes the imperfect shape was less smooth, pixelated, and in some of the models missing parts of the imperfection profile. However, as shown in Fig. 5.17 to Fig. 5.19, the results of the mesh sensitivity to the

element type, aspect ratio and helical angle are somehow consistent with the original study and the differences on the finer mesh side are negligible. The results are represented the same way as in section 5.3, the ultimate moment is normalized to the ultimate moment of baseline model ($M_u/M_{u_baseline}$) which in this case again is the S9R5 model with the finest mesh and it is the same model we used for the imperfection pattern. It is noticed here that the moment ratio ($M_u/M_{u_baseline}$) is always over 1 for the coarser meshes, that means that with the same imperfection pattern the convergence of the solution is normal from the over stiff coarser mesh to the correct fine mesh.

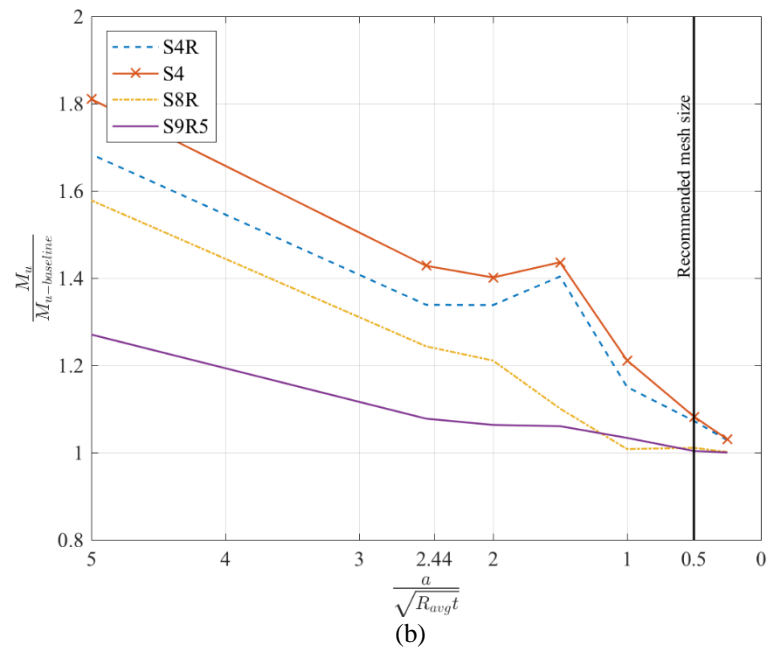
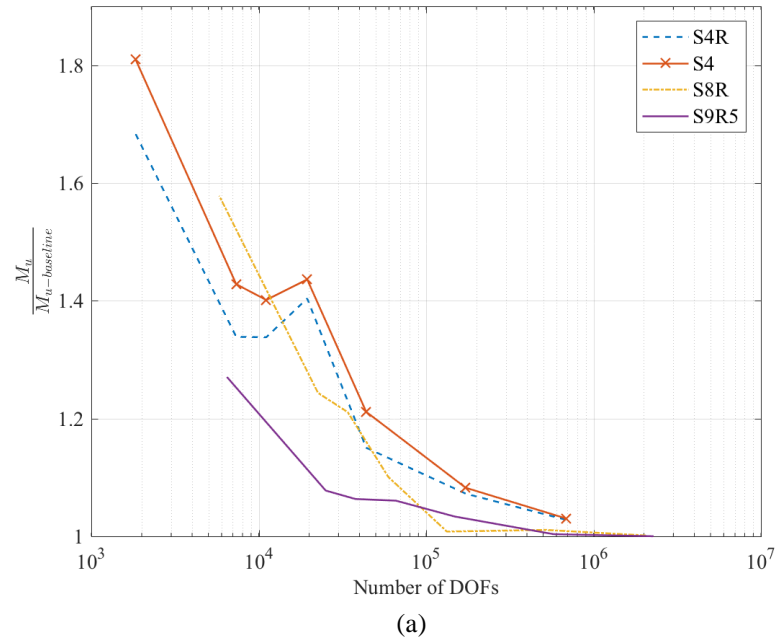


Figure 5.17 (a-b) The effect of the element types for S4, S4R, S8R & S9R5 on the nonlinear models with interpolated imperfection pattern vs (a) number of Degrees of Freedom (b) size of mesh in Meridional direction.

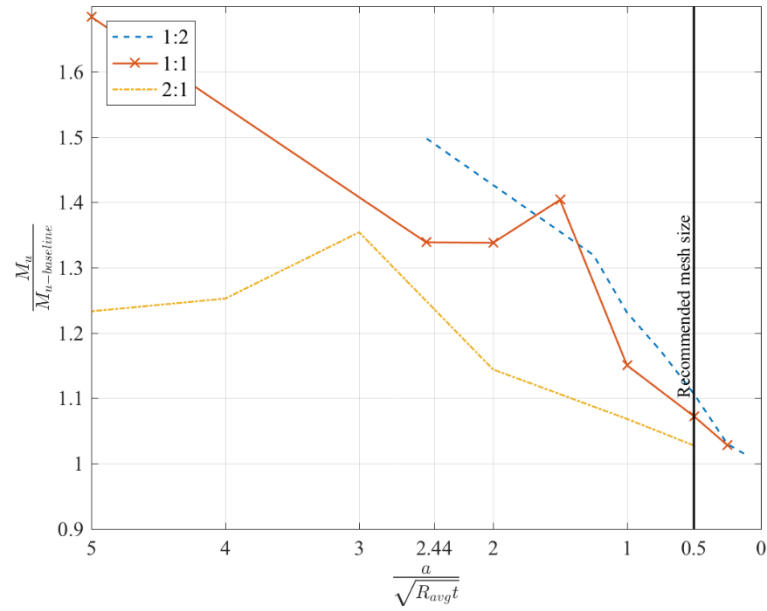


Figure 5.18 The effect of element aspect ratio on nonlinear models with interpolated imperfections pattern

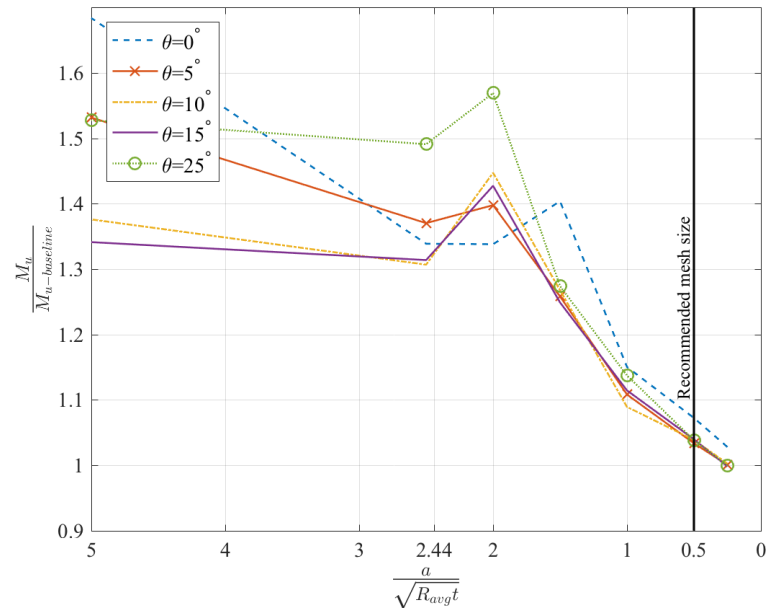


Figure 5.19 the effect of the inclination angle of the mesh on nonlinear models with interpolated imperfection pattern.

5.5 Summary and Conclusions

In this chapter, a modeling protocol, based on nonlinear collapse shell finite element models that include geometric imperfections, has been proposed for modeling thin-walled spirally welded tapered tubes that can potentially be used as steel wind turbine towers. The overall modeling protocol is developed employing two series of shell finite element analyses: first, a series of linear buckling analyses, designed to understand the effects of meshing characteristics on model performance and, second, a series of nonlinear collapse models with imperfections to understand the effects of imperfection modeling on model performance. The series of linear buckling analyses consider the effects of shell element type, element aspect ratio, element angle of inclination, and mesh density on models loaded in pure bending. The geometry of the models ($D = 1070$ mm, $t = 3.05$ mm, $\beta = 0.75^\circ$) is similar to the SWT tests.

The analyses demonstrate that, for mesh inclination angles less than 10° , a model meshed with the S4R element with a 1:1 aspect ratio provided satisfactory performance if the mesh size is limited to $0.5\sqrt{R_{avg}t}$. For inclination angles larger than 10° , a finer mesh ($\leq 0.25\sqrt{R_{avg}t}$) is needed for satisfactory performance. Although the error resulting from the models with helical angles larger than 10° is out of the scope of SWT project, the error resulting from the mesh layout should be investigated in the future for ABAQUS and other finite element software packages. The modeling protocol is valid for nonlinear collapse analyses such as GMNIA models. The modeling protocol has been intentionally constructed to be convenient for designers to use, with meshing characteristics that are

easily obtained in commercial finite element software such as ABAQUS and imperfection patterns, which are easily obtained and modeled.

The modeling protocol will be used in following building GMNIA models in Chapter 6, Chapter 7 and Chapter 8.

Chapter 6

SWT Numerical Modeling

6.1 Introduction

In the last few decades numerical modeling has become more affordable and available for designers. Numerical modeling for predicting the strength of shells is potentially the most convenient and powerful tool for design, especially when the shell geometry is unique or other special features exist. However, creating a reliable numerical model of a shell structure is not a straight forward process as many factors can significantly change the results: boundary conditions, loading, imperfections, details such as openings, stiffeners, and attachments (stairs, pipe supports, vents ...etc.). As introduced in Chapter 4 and Chapter 5, EC3-1-6 was the first structural code to give a detailed description for the design of shelled structures using numerical modeling for predicting the strength. To create a reliable numerical model, it should be as much detailed as possible (inclusion of imperfections, material nonlinearities and all influential geometrical features), and it must be verified with test results or well verified calculations.

In this chapter, Geometrically and Materially Nonlinear Analysis with Imperfections (GMNIA) models are created for predicting the strength of each of the SWT-project tested specimens, as GMNIA models are the most complicated and detailed numerical models and if verified they could potentially be used in design of SWT sections. Also, the reliability of the GMNIA models is tested and verified, for potential expansion in SWT research project where the GMNIA models could be used for some issues that cannot be studied experimentally such as: modeling the full-scale wind turbine tower with real load

cases, or if the manufacturer decided to change the geometry for a better quality. However, the GMNIA models were created according to some assumptions that simplify the real SWT specimens geometry and the material properties.

The Design using GMNIA as EC3-1-6 specified, requires several analyses with less details to act as an upper bound to GMNIA models results. For each geometry, several models were created that varies in complexity and features, they are listed as follows:

1. LBA models: Linear Buckling Analyses are performed using the perfect geometry with nominal dimensions to get reference critical buckling and 1st eigenmode-affine patterns to use as an imperfection pattern.
2. GMNA models: Geometric and Material Nonlinear Analyses using the perfect geometry with nominal dimensions for computing the upper bound of the nonlinear analyses using the perfect nominal geometry of specimens.
3. GMNIA models: Geometric and Material Nonlinear Analyses with Imperfections included, to estimate the strength of SWT specimens. Four sets of models according to the imperfections considered:
 - a. GMNIA-MI: created using real scans (Measured Imperfections).
 - b. GMNIA-MI-RS: created using measured imperfections and estimated residual stresses.
 - c. GMNIA eigenmode: 1st eigenmode-affine imperfection pattern.
 - d. GMNIA-WD: Weld Depression Type 'A' according to Rotter and Teng (1989)

For each of the GMNIA models the effect of the imperfection pattern and amplitude should be tested to ensure these imperfections in these models severe the strength.

The meshing protocol, developed in Chapter 5, is carefully used in creating SWT models and imperfections are introduced in the models as described in Chapter 4. The nonlinear collapse analyses of loaded shells were performed using ABAQUS built-in Riks solver. Riks solver is efficient in predicting the buckling and post buckling paths, however in the cases where there is bifurcation, the step size becomes critical as it might skip the bifurcation point (Doerich 2007). To overcome this problem one solution is to make sure the step size is small; however, this approach will increase the computing time and does not guarantee accuracy. Another solution is to identify a load that is very close to the bifurcation load and restart the analysis with extremely small step-size from this load (ECCS 2013). The bifurcation point is easier to track in stockier shells, in the SWT GMNIA models, the only model that approached the yielding moment (plasticity) with was the one with the smallest diameter-to-thickness ratio SW-145-0°, the buckling behavior of the other eight specimens was more challenging to track and required several trials with the step size.

6.2 Boundary conditions

The boundary conditions considered herein aim to mimic the SWT specimens in the test rig at NEU. Fig. 6.1 shows a model built with detailed end plates, cross beams and pins. The detailed model has a close approximation to the boundary conditions as the test rig: the cross beams and pins are restrained from movement in Y-direction at the same locations of the supports in the test rig. The pins at the small end are restrained from movement in

the X and Z-directions but free to rotate around the Y-axis, while the slotted-pin at the large end of the specimen is restrained from displacement in the X-direction but free to rotate around the Y-axis.

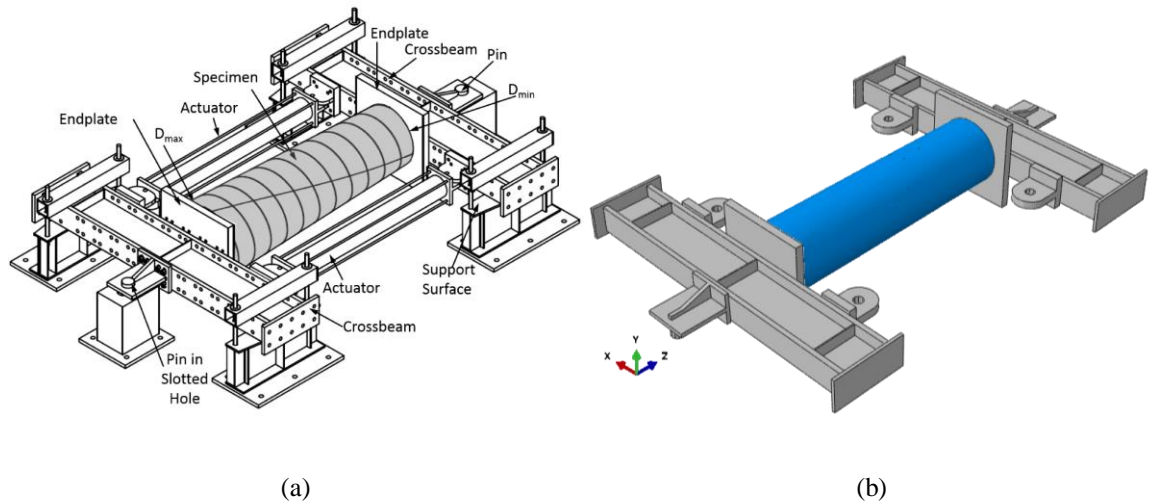


Figure 6.1 (a) Test rig schematic (Jay et al. 2016b) and (b) Finite Element model of one of the specimens with test rig modeled

In this model loading was applied, as in SWT test, by inducing displacements at the same connection between the actuators and cross beams. On one side the displacement increased to mimic the actuator expanding and the other side the displacement is decreased to simulate the actuator retraction resulting in end rotations on the specimen. The model with detailed end boundary conditions was compared to an equivalent (simplified) model with equivalent constraints: a multi-point beam constraint was created at the specimen ends that connects the nodes at each end to a reference point at the centers of the end cross sections (Simulating the constraint of the extremely thick endplates). In the simplified model, the loads and boundary conditions are applied at the reference points. Fig. 6.2 (a) and (b) show the deformed shape of SWT model for SW-325-0° with both the test rig modeled and with the equivalent (simplified) boundary conditions and loading. The moment-rotation curves for the two models, is showed in Fig. 6.3. The simplified models proved to have good

results and saves much of time required for the analysis. All nonlinear collapse finite element models are created with equivalent boundary conditions.

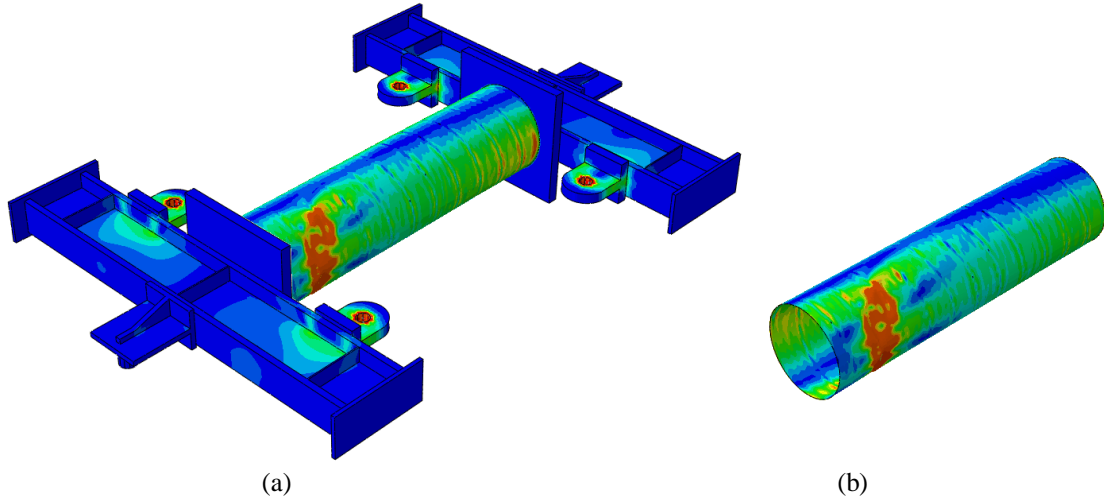


Figure 6.2 Deformed shape of SW-325-0° GMNIA model with scanned geometry after the first load drop for (a) with test rig modeled, and (b) equivalent boundary conditions model.

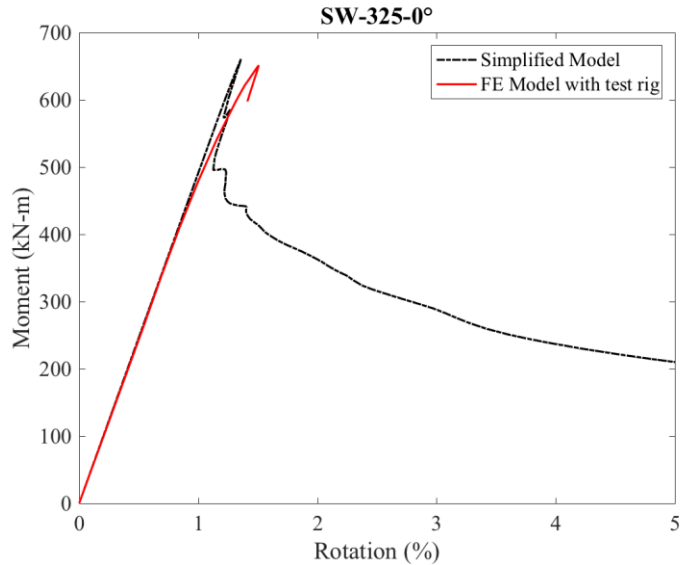


Figure 6.3 Moment-rotation curve comparison of the GMNIA models for specimen SW-325-0° with simplified boundary conditions and with the test rig included.

6.3 Material properties

The material properties employed in the models herein are based on real coupon test results from coupons taken from SWT specimens. Since SWT specimens are assembled from

many flat plates material variation can be great; however, for small specimens, plates are usually from the same batch. Ultimately, results from averages of three coupons were employed. The coupon tests were conducted by the NEU research team and data was processed by JHU research team. Engineering stress-strain curves are built from averaging three coupon tension tests taken from each specimen. It is assumed Young's Modulus ($E = 200 \text{ GPa}$) and Poisson's ratio ($\nu = 0.3$). The yield strength is based on the engineering stress-strain curves using the 0.2% offset, and the selected points were chosen to represent main features of the curves (averaged total elongation, yielding plateau ...etc.). Fig. 6.4 (a-i) shows the coupon test results with the simplified engineering stress-strain curve points and the corresponding estimated true stress-strain curve points as required by large deformation analysis in ABAQUS.

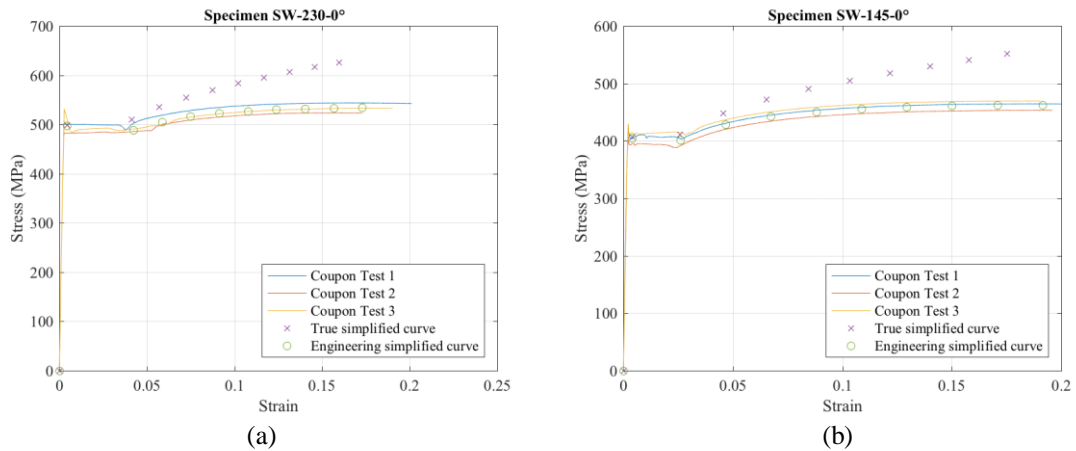
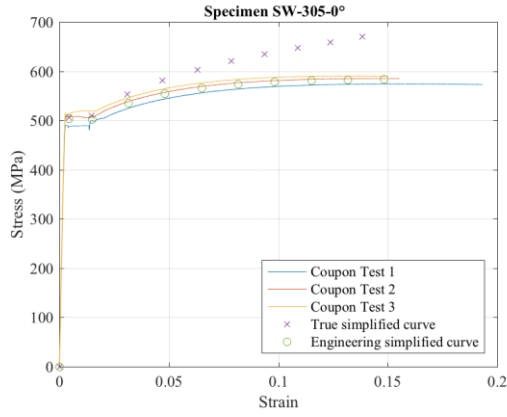
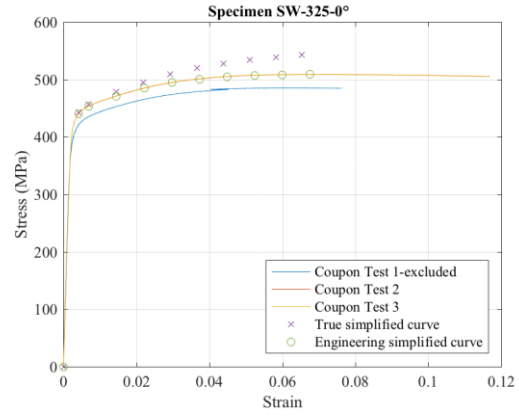


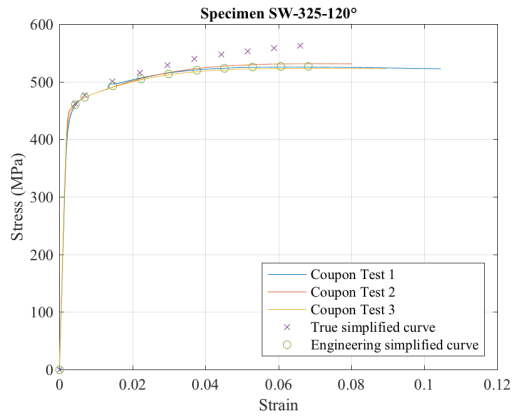
Figure 6.4 (a-b) Stress-Strain curves with True simplified curve used in numerical modeling.



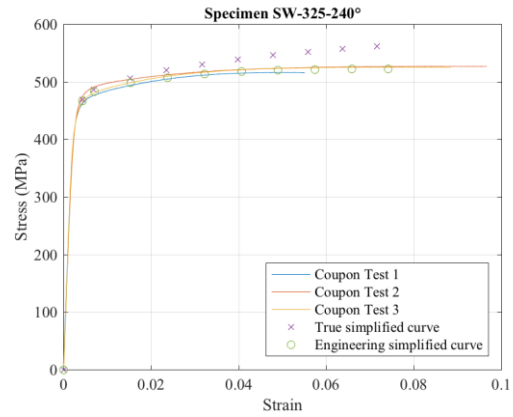
(c)



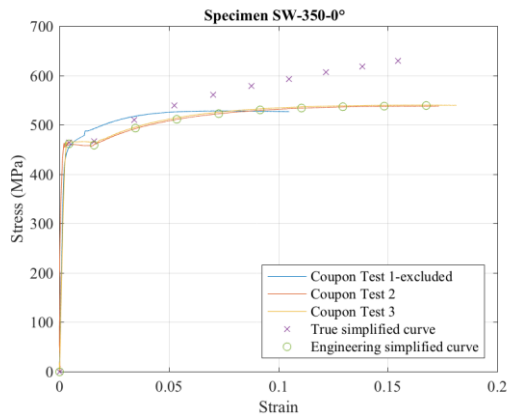
(d)



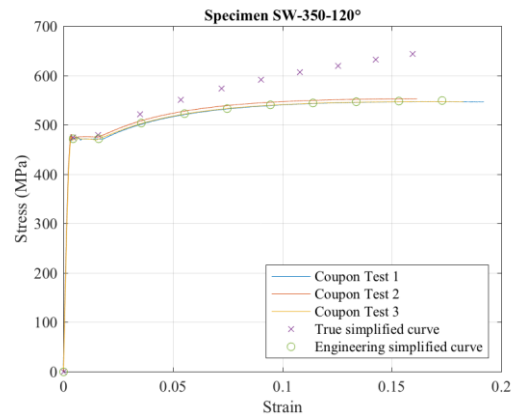
(e)



(f)

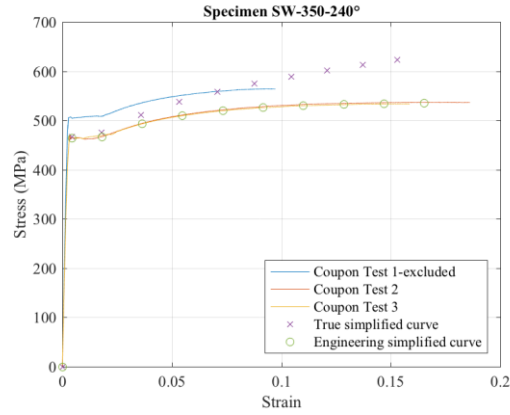


(g)



(h)

Figure 6.4 (c-h) Stress-Strain curves with True simplified curve used in numerical modeling.



(i)

Figure 6.4 (i) Stress-Strain curves with true stress-strain curve points used in numerical modeling.

Two coupon tests one from SW-350-0° coupons and the other from SW-350-240° coupons showed clear difference in behavior and higher yielding stress than the other two coupons from the same specimens, so they were excluded, see Fig. 6.4 (g) and (i). True stress-strain curves are built for each model from average engineering stress-strain curve and used in GMNIA and GMNA models, where

$$\sigma_{true} = \sigma_{eng}(1 + \varepsilon_{eng}) \quad (6.1)$$

and

$$\varepsilon_{true} = \ln(1 + \varepsilon_{eng}) \quad (6.2)$$

As described in ABAQUS manual:

“Most materials that exhibit ductile behavior (large inelastic strains) yield at stress levels that are orders of magnitude less than the elastic modulus of the material, which implies that the relevant stress and strain measures are “true” stress (Cauchy stress) and logarithmic strain. Material data for all of these models should, therefore, be given in these measures.” (Simulia 2014)

6.4 GMNIA models vs SWT tests results

The shell finite element models were created using the meshing protocols established in Chapter 5 and implemented imperfections as described in detail in Chapter 4 and herein; the comparison between SWT GMNIA models and SWT tests provided herein, is mainly focused on the stiffness and the strength of the specimens as represented by moment-rotation curves. The moment is the constant moment applied at both ends of SWT specimens during test, or the constant moment applied at the center points of the end cross sections of the SWT models. The rotation is the sum of rotations at both ends of the SWT specimens, measured in test by the displacements of the end plate, or the sum of the rotations of the cross sections at both ends of SWT models.

The measured imperfections for specimen SW-230-0° indicate that this specimen would be classified as worse than Class C and for specimen SW-325-240° the test ended due to fracture of the spiral seam weld before a load drop due to buckling was observed.

Stiffness is defined here as the bending moment in the specimen or model divided by the sum of the rotations at each end of the specimen or model. In comparing the numerical results to the experimental results, it should be noted that the raw experimental deflections were corrected based on the tangent stiffness between 40 and 60% of the ultimate bending capacity; this correction contributes to the numerical model slightly under-predicting the stiffness.

6.4.1 GMNIA models with generated imperfections

6.4.1.1 1st eigenmode-affine patterns

This section covers the work on GMNIA models created with imperfections based on 1st eigenmode-affine pattern. Tables 6-1 provides the results for the ultimate moments, M_{u-FE} , from the GMNA and GMNIA models and the ratio between the ultimate moment observed in the tests to the ultimate moment in the finite element models, M_{u_test}/M_{u_FE} , for the GMNIA models.

Fig. 6.5 (a-f) shows the responses for the moment-rotation curves for the nine specimens, with the moment and moment normalized to the plastic moment on the vertical axis and rotation in radian percentage on horizontal axis. The load drops on the curves represent formation of a new buckling wave in the test or in the models. The figures provide a useful comparison of the collapse behavior of the models and tests. Although the post-buckling behavior of the tested specimens and the models is not expected to match, as the equivalent imperfection pattern adopted in the models is not necessarily realistic, it is observed that the number of load drops in the models and tests are similar, though differing in the magnitude of the decrease in capacity. The post-buckling load drops in the models tend to be more regular in size, shape, and frequency than observed in the test, see Fig. 6.5 (d) for specimen SW-325-0° response. In the tests, the first load drops tended to be larger than the secondary load drops, while, in the models, the load drops are more consistent in size throughout the loading.

Note the difference between the buckling behavior of specimen SW-145-0° in both test and models compared to the other eight models, the smooth profile of the moment-rotation

curves due is to the low slenderness of that specimen and the fact it exhibits primarily yielding, not buckling, phenomenon.

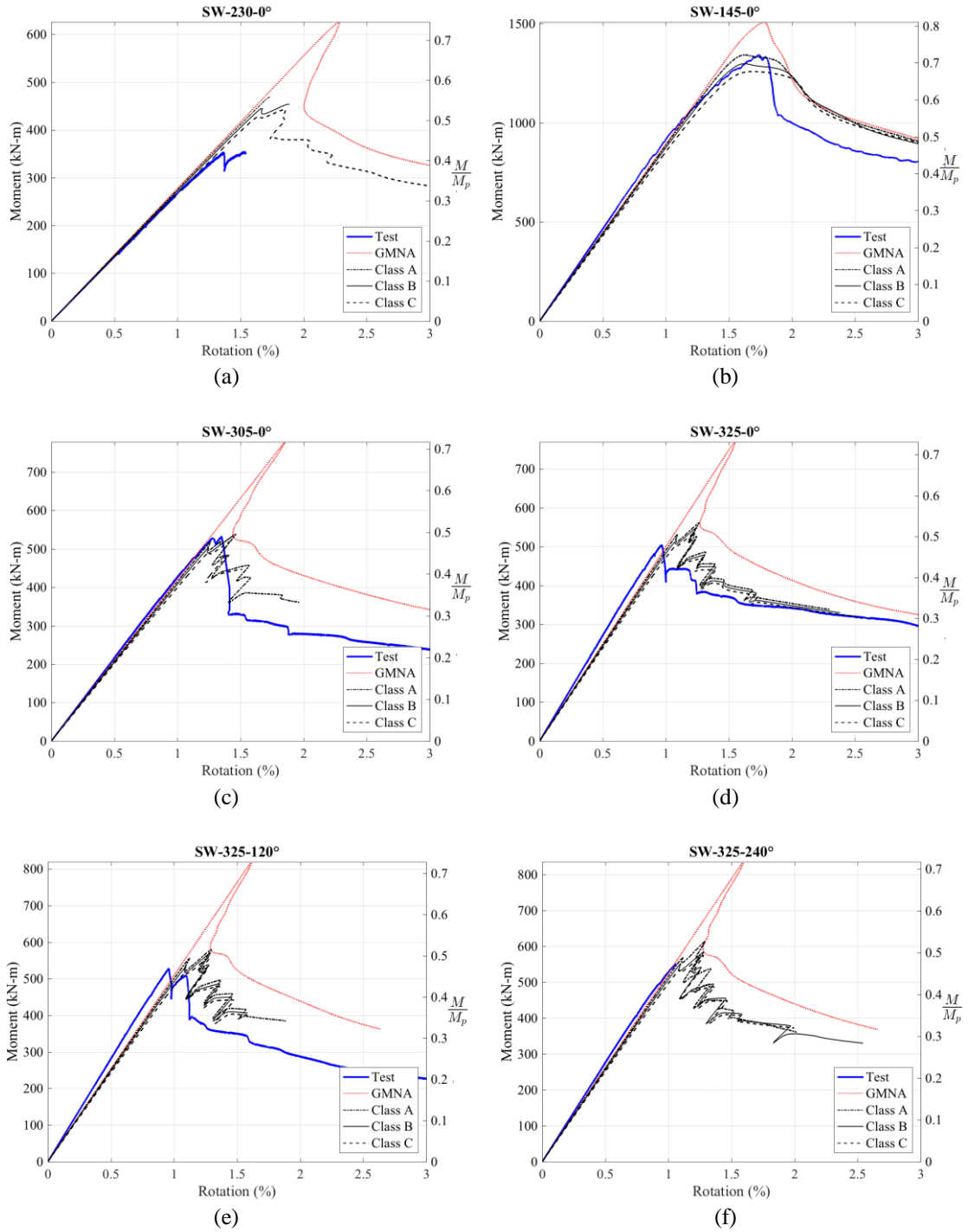


Figure 6.5 (a-f) Moment-Rotation curves for GMNA and GMNIA-eigenmode models vs test results.

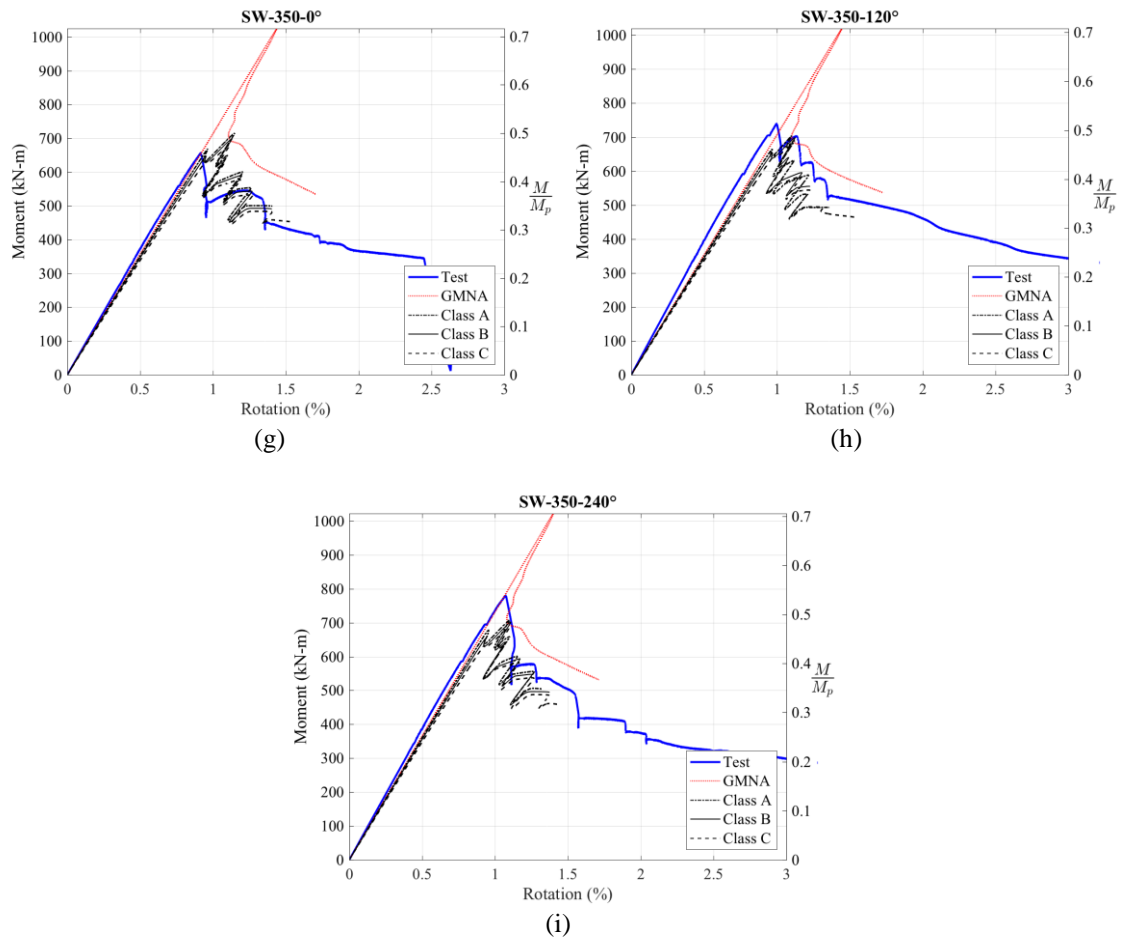


Figure 6.5 (g-i) Moment-Rotation curves for GMNA and GMNIA-eigenmode models vs test results.

For all models, except SW-230-0° and SW-325-120°, the GMNIA models show agreement between test results and models in terms of moments and stiffness for the three Classes magnitudes with a maximum test-to-predicted ratio of M_{u_test}/M_{u_FE} equal to 1.13, a minimum ratio of 0.89. The mean of the test-to-predicted ratios for each of the three imperfection classes ranges between 0.98-1.02 and the standard deviation is 8%.

For SW-230-0° the strength predicted by the GMNIA models for this specimen is 26-33% larger than the strength measured during the test. Although specimen SW-325-120° showed weld fracture before buckling the results of the models are very close to test results.

As expected, increasing the magnitude of the imperfection consistently decreases the predicted bending capacity in the numerical models; however, the differences in strengths between classes for this pattern of imperfections are small or negligible (as in SW-350-120° Class A and B for example).

Table 6.1 Comparison between ultimate moments from GMNA and GMNIA eigenmode nonlinear collapse models and large-scale tests.

Specimen	M_{u-test} (kN-m)	M_{u-FE} (kN-m)				Moment ratio (M_{u-test}/M_{u-FE})			
		GMNA	GMNIA			GMNA	GMNIA		
			EC3-1-6 Classes				EC3-1-6 Classes		
			A	B	C		A	B	C
SW-230-0° *	350	626	469	454	443	0.56	0.75	0.77	0.79
SW-145-0°	1343	1509	1343	1299	1260	0.89	1.00	1.03	1.07
SW-305-0°	526	778	538	532	519	0.68	0.98	0.99	1.01
SW-325-0°	502	769	562	550	538	0.65	0.89	0.91	0.93
SW-325-120°	523	819	580	571	560	0.64	0.90	0.92	0.93
SW-325-240° *	≥553	835	614	585	574	≥0.66	≥0.90	≥0.95	≥0.96
SW-350-0°	656	1025	715	700	681	0.64	0.92	0.94	0.96
SW-350-120°	737	1020	704	699	681	0.72	1.05	1.05	1.08
SW-350-240°	778	1022	708	702	688	0.76	1.10	1.11	1.13
Mean						0.71	0.98	0.99	1.02
Standard deviation						0.09	0.08	0.08	0.08

*Specimens SW-230-0° and SW-325-240° are excluded from the mean and standard deviation calculations

Table 6.2 provides the test-to-predicted stiffness ratio K_{test}/K_{FE} of the eigenmode imperfection models, excluding the GMNA models. Results vary between a minimum of 1.04 and a maximum of 1.15, with seven of the nine models being more flexible than the corresponding test for all three fabrication tolerance quality classes.

Table 6.2 Comparison between stiffness from GMNA and GMNIA eigenmode nonlinear collapse models and large-scale tests.

Specimen	K_{test} (kN-m/rad)	K_{FE} (kN-m/rad)				Stiffness ratio (K_{test}/K_{FE})			
		GMNA	GMNIA			GMNA	GMNIA		
			EC3-1-6 Classes				EC3-1-6 Classes		
			A	B	C		A	B	C
SW-230-0°	271	371	276	273	269	0.73	0.98	0.99	1.01
SW-145-0°	918	1146	888	878	861	0.80	1.03	1.04	1.07
SW-305-0°	433	569	418	413	405	0.76	1.04	1.05	1.07
SW-325-0°	546	674	495	489	480	0.81	1.10	1.12	1.14
SW-325-120°	565	688	505	499	489	0.82	1.12	1.13	1.16
SW-325-240°	556	709	521	515	505	0.78	1.07	1.08	1.10
SW-350-0°	752	966	706	697	682	0.78	1.07	1.08	1.10
SW-350-120°	780	957	700	691	677	0.81	1.11	1.13	1.15
SW-350-240°	769	990	724	715	701	0.78	1.06	1.08	1.10
Mean						0.79	1.07	1.08	1.10
Standard deviation						0.03	0.04	0.05	0.05

Fig.6.5 (a-i) shows the deformed shape of each of the GMNIA models at the end of the analyses with 1st eigenmode-affine pattern scaled to be consistent with EC3-1-6 class C. Since the collapse deformation is driven by the amplitude of the imperfections and for the three classes the shape of the imperfection was the same but scaled to different classes, the deformed shape is almost the same for the three classes at the end of the run. The deformed shape in this GMNIA group is not comparable to the buckled shape observed in the experiments as the imperfections pattern is numerically generated.

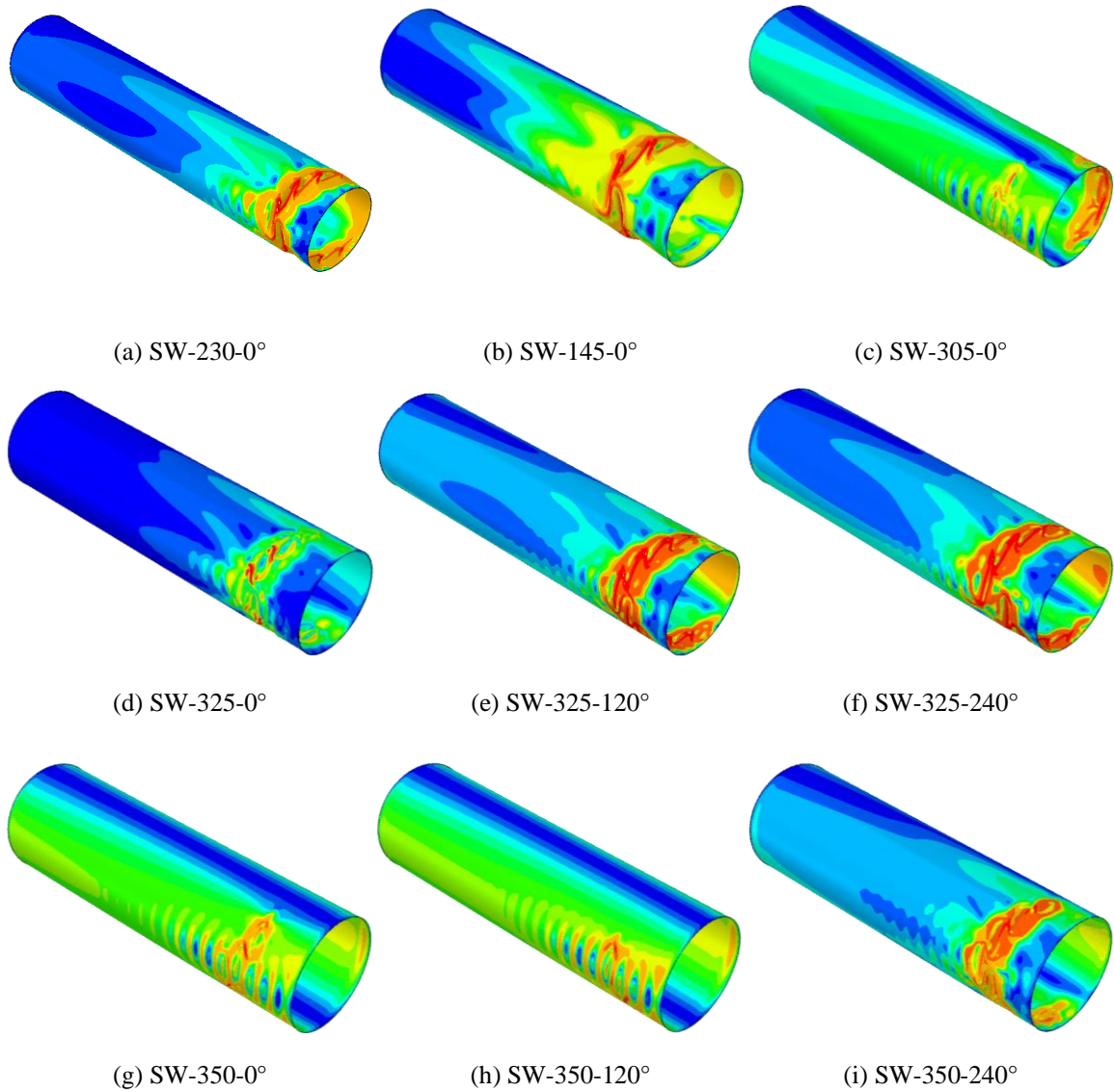


Figure 6.6 Deformed shape for all GMNIA-eigenmode models with EC3-1-6 Class C imperfections, and contour of von-Mises stress.

6.4.1.2 Weld depression

GMNIA models with an imperfection shape following the weld depression and imperfection magnitude were also created as described in Chapter 4 and meshed following protocols established in Chapter 5. To have a smooth representation of the weld depression profile, the mesh used in this part of the study was finer than what was recommended in the meshing protocol chapter ($0.25\sqrt{R_{avg}t}$). Three imperfection amplitudes used here:

($\delta_o=0.4t$, $\delta_o=0.6t$ and $\delta_o=t$) as described in detail in Chapter 5, to represent Class B and Class C in EC3-1-6, and WTC (worse than C) respectively.

Fig. 6.7 shows the moment-rotation curves for all GMNIA models with weld depression imperfections vs test results, the GMNA models are also included for reference. In some of the models the solver could not shift from the pre-buckling to the post-buckling, the solver goes back on the same path of the elastic loading.

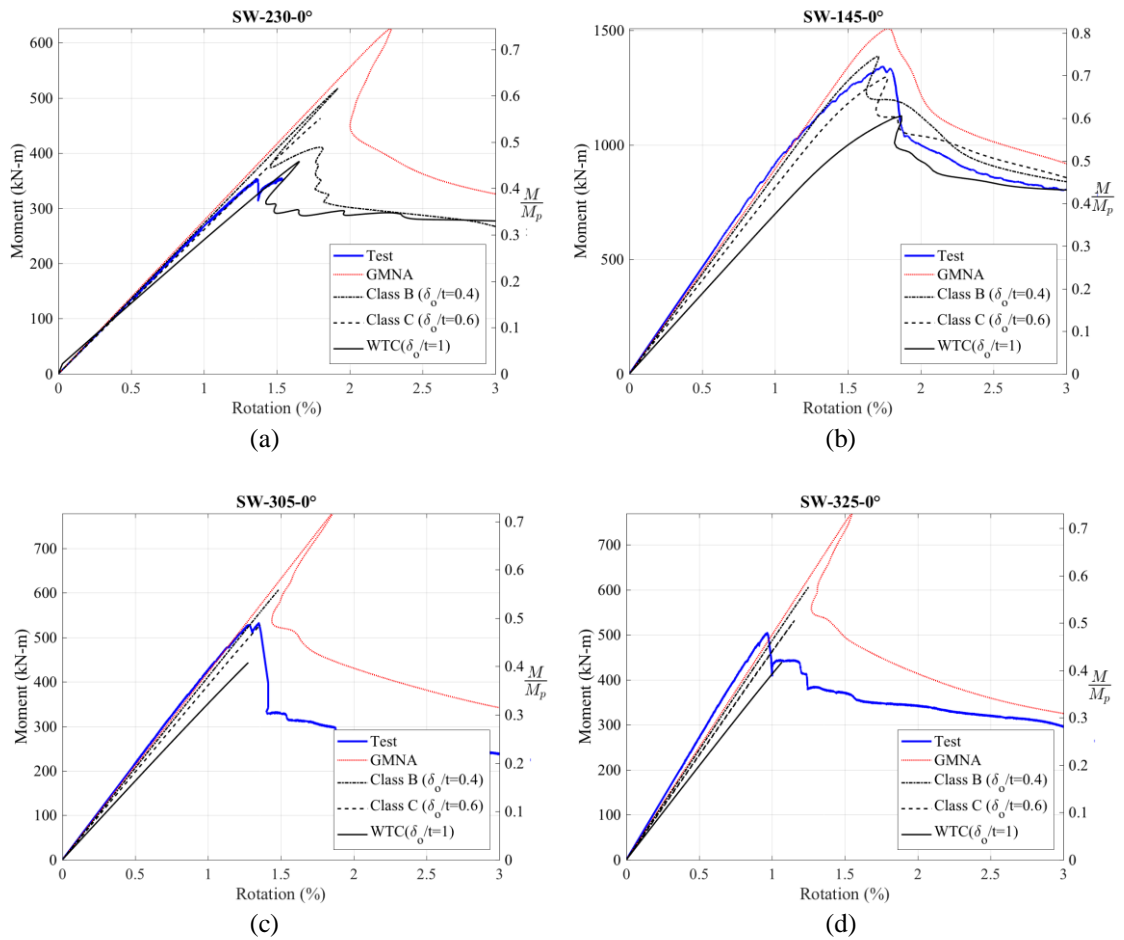


Figure 6.7 (a-d) Moment-Rotation curves for GMNA and GMNIA-weld depression models vs test results

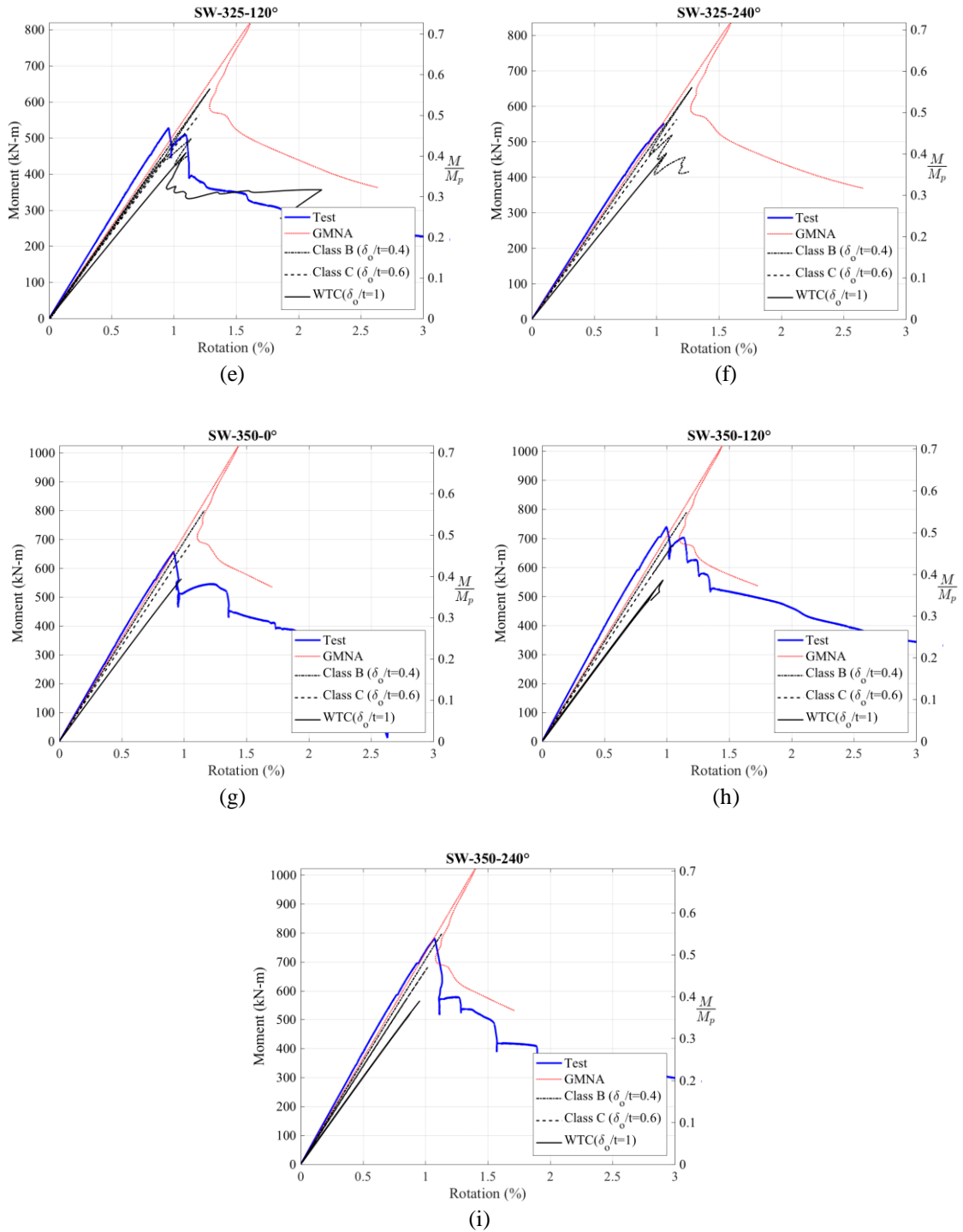


Figure 6.7 (e-i) Moment-Rotation curves for GMNA and GMNIA-weld depression models vs test results.

To be confident in our results we tested running nonlinear collapse analysis using “Artificial Damping” solver for GMNIA models with weld depression imperfections

consistent with EC3-1-6 Class C and the results in terms of strength and stiffness were almost the same, see Fig. 6.8. The presented plots in Fig. 6.7 and Tables 6.3 and 6.4, are for GMNIA models results from analyses using Riks solver.

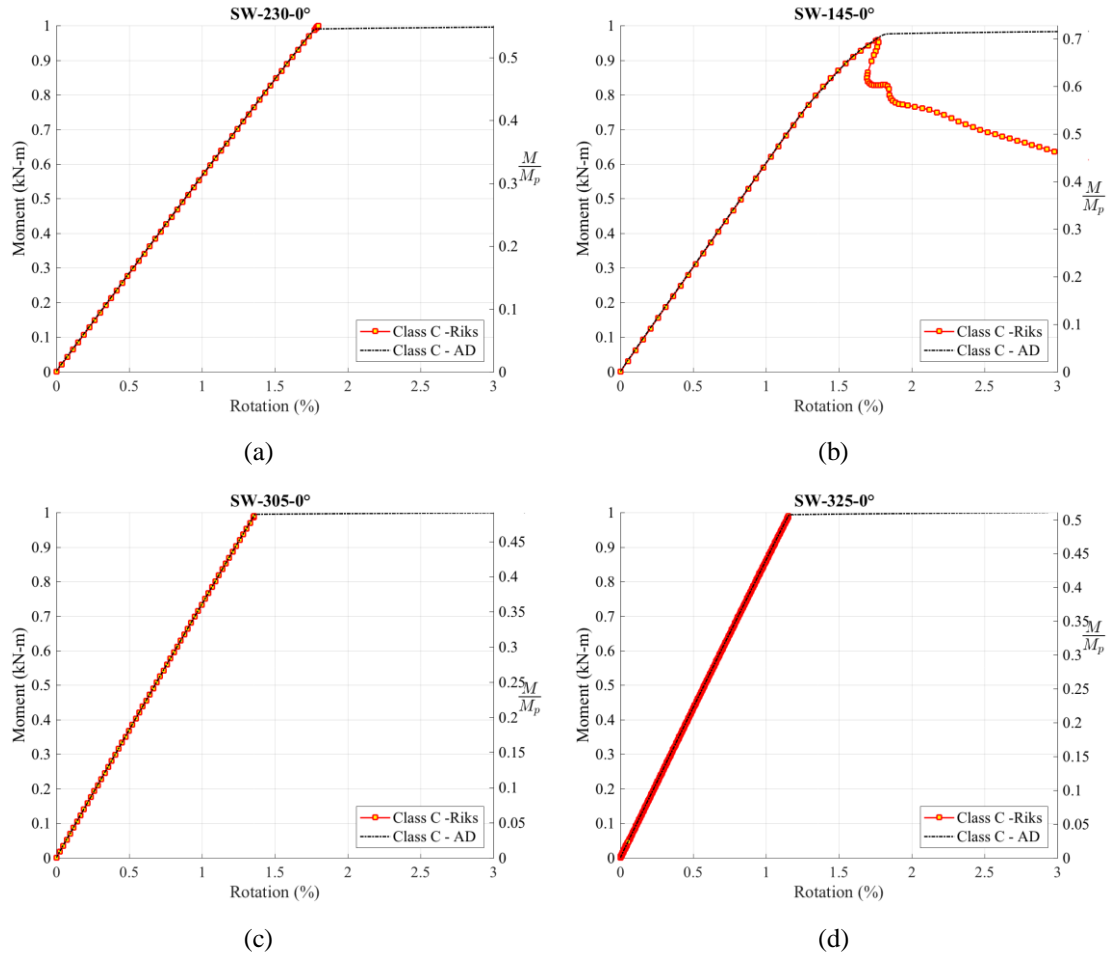


Figure 6.8 (a-d) Moment-Rotation curves for GMNIA-weld depression models with EC3-1-6 Class C imperfections using “problematic” Riks solver and artificial damping solver as reported in section 6.4.1.2.

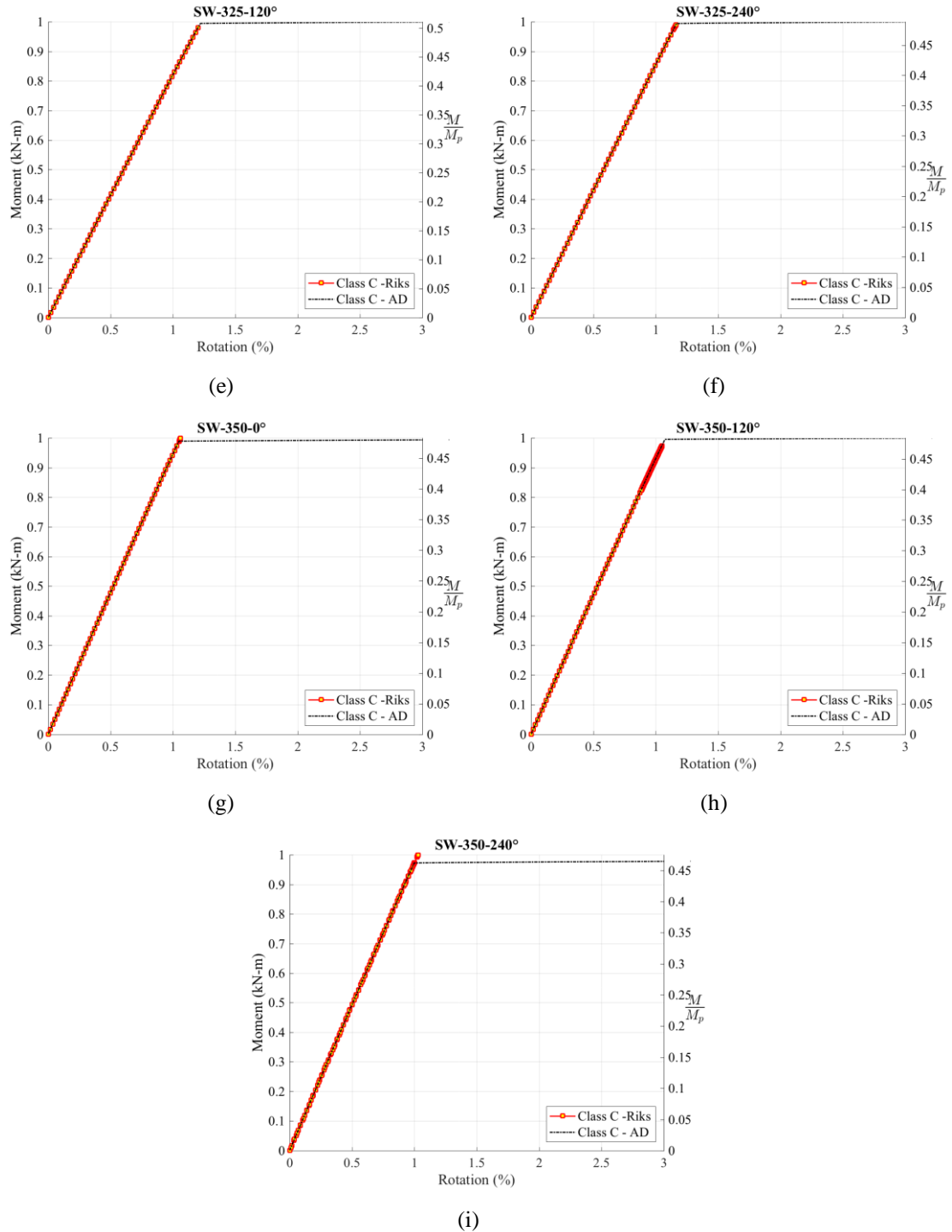


Figure 6.8 (e-i) Moment-Rotation curves for GMNIA-weld depression models with EC3-1-6 Class C imperfections using “problematic” Riks solver and artificial damping solver as reported in section 6.4.1.2.

Table 6.3 provides the comparison between the ultimate moment of the tests and GMNIA models with weld depression imperfections. Excluding specimen SW-230-0°, the moment

ratio (M_{u_test}/M_{u_FE}) ranges from 0.82 to 1.38 for the three classes but for Class C the range is between 0.91 and 1.15. The mean of the moment ratio excluding specimens SW-230-0° and SW-325-240°, ranges from 0.89 and 1.22, the standard deviation ranges from 0.07 to 0.09. For Class C the mean is 1.0, and standard deviation is 0.08. The differences in strengths between the three Classes are more distinct, indicating that the selected imperfection pattern is indeed detrimental to the predicted strength.

Table 6.3 Comparison between ultimate moments from GMNIA weld depression models and large-scale tests.

Specimen	M_{u_test} (kN-m)	M_{u_FE} (kN-m)			Moment ratio (M_{u_test}/M_{u_FE})		
		GMNIA		GMNIA	GMNIA		GMNIA
		EC3-1-6 Classes		WTC	EC3-1-6 Classes		WTC
		B	C		B	C	
		($\delta_o/t=0.4$)	($\delta_o/t=0.6$)	($\delta_o/t=1$)	($\delta_o/t=0.4$)	($\delta_o/t=0.6$)	($\delta_o/t=1$)
SW-230-0°	350	517	461	385	0.68	0.76	0.91
SW-145-0°	1343	1388	1355	1127	0.97	0.99	1.19
SW-305-0°	526	607	534	443	0.87	0.99	1.19
SW-325-0°	502	606	538	439	0.83	0.93	1.14
SW-325-120°	523	637	575	459	0.82	0.91	1.14
SW-325-240°	≥553	653	569	456	≥0.85	≥0.97	≥1.21
SW-350-0°	656	801	687	564	0.82	0.96	1.16
SW-350-120°	737	790	697	556	0.93	1.06	1.33
SW-350-240°	778	798	674	565	0.97	1.15	1.38
Mean*					0.89	1.00	1.22
Standard deviation*					0.07	0.08	0.09

*Specimens SW-230-0° and SW-325-240° are excluded from the mean and standard deviation calculations

The model results are sensitive to the imperfection pattern and magnitude; for the weld depression imperfection when the magnitude is consistent with Class B the GMNIA models results are almost 25% higher than SWT tests results for all the specimens except specimens SW-145-0°, SW-350-120° and SW-350-240°. These three specimens were classified as Class C according to one tolerance measurement only (check Table 4.4 in Chapter 4), their results are closer to Class B. For larger imperfections, the peak strength is reduced by 40% or more. The weld depression imperfections are more physically

realistic, and the strength results are more sensitive to this type of imperfections than the 1st eigenmode-affine patterns. Table 6.4 shows that for the test-to-predicted stiffness of the weld depression imperfection models, the ratio varies between 0.99 and 1.33. The mean of the test-to-predicted stiffness ratios varies from 1.08-1.27, and the standard deviation ranges from 5-6%.

Table 6.4 Comparison between stiffness from GMNIA weld depression models and large-scale tests.

Specimen	K_{test} (kN-m/rad)	K_{FE} (kN-m/rad)			Stiffness ratio (K_{test}/K_{FE})		
		GMNIA		GMNIA	GMNIA		GMNIA
		EC3-1-6 Classes		WTC	EC3-1-6 Classes		WTC
		B	C	($\delta_o/t=1$)	B	C	($\delta_o/t=1$)
		($\delta_o/t=0.4$)	($\delta_o/t=0.6$)		($\delta_o/t=0.4$)	($\delta_o/t=0.6$)	
SW-230-0°	271	273	262	236	0.99	1.03	1.15
SW-145-0°	918	871	817	701	1.05	1.12	1.31
SW-305-0°	433	413	395	355	1.05	1.10	1.22
SW-325-0°	546	489	467	419	1.12	1.17	1.30
SW-325-120°	565	498	476	427	1.13	1.19	1.32
SW-325-240°	556	514	491	440	1.08	1.13	1.26
SW-350-0°	752	696	663	590	1.08	1.13	1.28
SW-350-120°	780	690	658	587	1.13	1.19	1.33
SW-350-240°	769	713	680	606	1.08	1.13	1.27
Mean					1.08	1.13	1.27
Standard deviation					0.05	0.05	0.06

Fig. 6.9 (a-i) shows the deformed shape at the end of the analysis using the for each of the GMNIA models with weld depression imperfections consistent with EC3-1-6 Class C, these models are analyzed using “Artificial Damping” solver. The buckled shape in these models is more realistic, the pattern of the buckling waves along the spiral seam weld is what was observed in the experiments although the pattern of the weld depression imperfections is numerically generated.

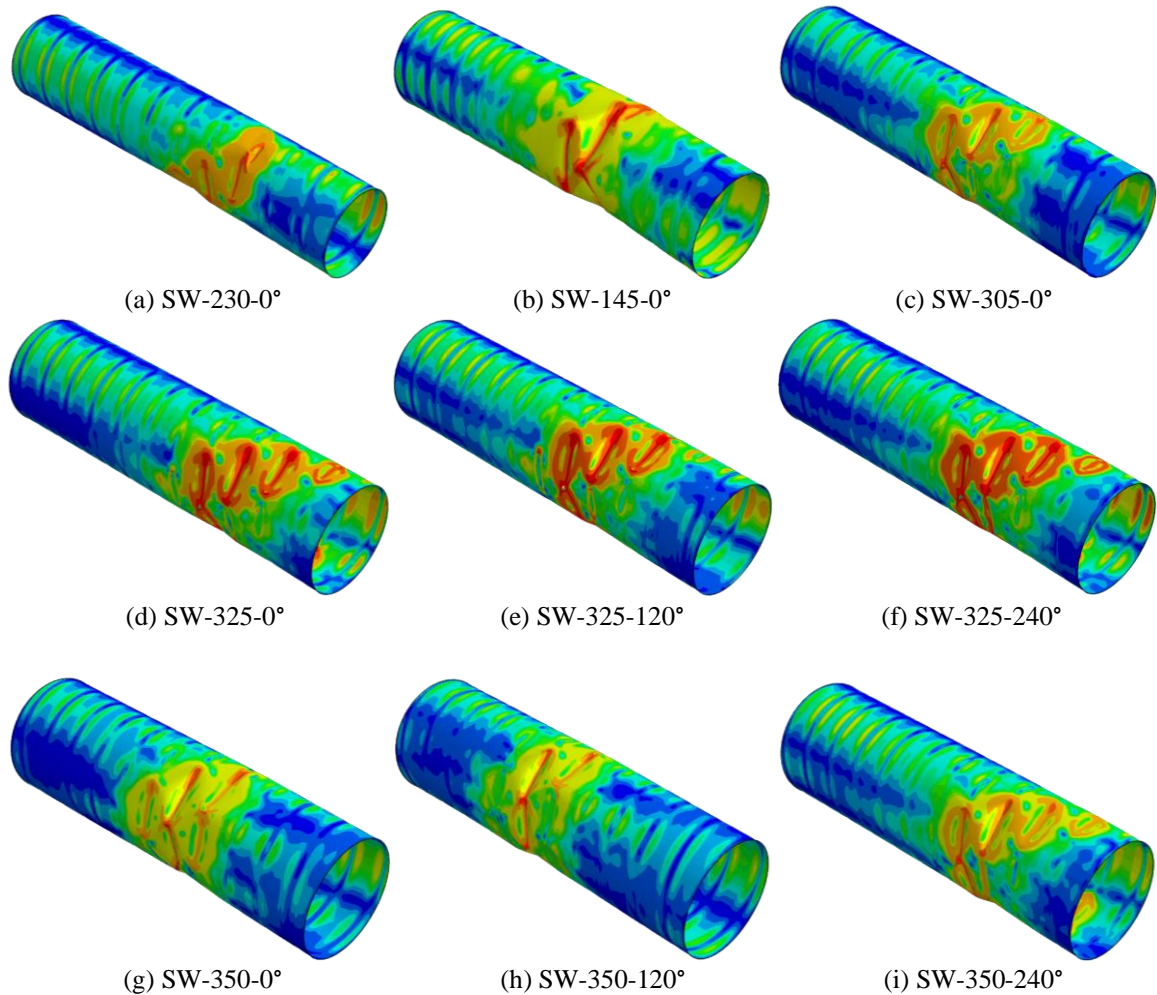


Figure 6.9 Deformed shape for all GMNIA models with weld depression imperfections consistent with EC3-1-6 Class C with contour of von-Mises stress.

6.4.2 GMNIA models with measured imperfections

The scanned geometry of the manufactured SWT specimens prior to shipping and welding on end plates, is used here in building the imperfect geometry of the GMNIA models. Full scans for 8 out of 9 specimens were provided by KTS, only specimen SW-230-0° was not scanned in full. A point cloud was provided by KTS for each of the specimens using a high-resolution scanner. Although as mentioned in Chapter 3, the scanned geometries were influenced by the way the specimens were clamped to the revolving motor on the scanner rig, and the new imperfections that could have been induced during transportation and

mounting on the test rig, the scans provided very good and consistent presentation to the local weld induced imperfections, from which the buckling was triggered as observed in most of the tests.

Special precautions were considered for the GMNIA models created with the scanned geometry:

- 1- The geometry of the GMNIA models is built using a finer mesh than what was recommended in Chapter 5, as it was mentioned before as the slenderness ratio of the shelled structures increases the sensitivity to the smallest imperfections increases. Sometimes the coarser mesh of the model misses a sharp dent from the scanned point cloud which leads to a change in the buckling and post-buckling behavior. Fig. 6.10 shows a comparative study of three models with different mesh sizes, regular mesh ($1.0\sqrt{R_{avg}t}$), fine mesh ($0.5\sqrt{R_{avg}t}$), and extra fine mesh ($0.25\sqrt{R_{avg}t}$), for GMNIA models of specimen SW-325-0°, shows that the strength, stiffness, and the buckling location is highly affected by the mesh size.
- 2- The specimens were scanned before they were shipped to the testing facility, also it was cut from both ends before the specimen was mounted to the test rig and welded to the end plates. During each of these processes new imperfections were induced.
- 3- The orientation of the specimens, and the models, is more critical in case of applying nonuniform axial compressive stress, as the buckling and post buckling behavior depends on the location of the imperfection that triggers the buckling with respect to the meridian of maximum compressive stress. A test was conducted on one SWT model with scanned geometry and two orientations, and the differences in strength was

not that significant. Fig. 6.11 shows GMNIA models of specimen SW-325-0° with two orientations, one of them is the exact orientation as test and the other is a random orientation. The model with the exact orientation is more accurate in getting the buckled shape, however, getting the exact orientation is an exhausting process (because the specimens were scanned before being shipped to NEU where they cut parts from the ends and weld it to the end plates, during these processes new imperfections are induced that are not recorded), and the difference in the results in terms of strength and stiffness is not significant.

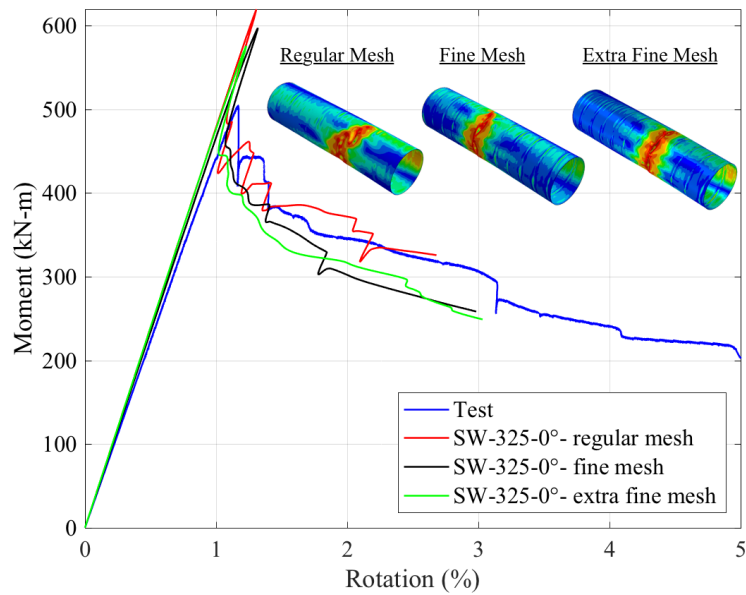


Figure 6.10 Moment-rotation curves of specimen SW-325-0° GMNIA models with measured imperfections and different mesh sizes.

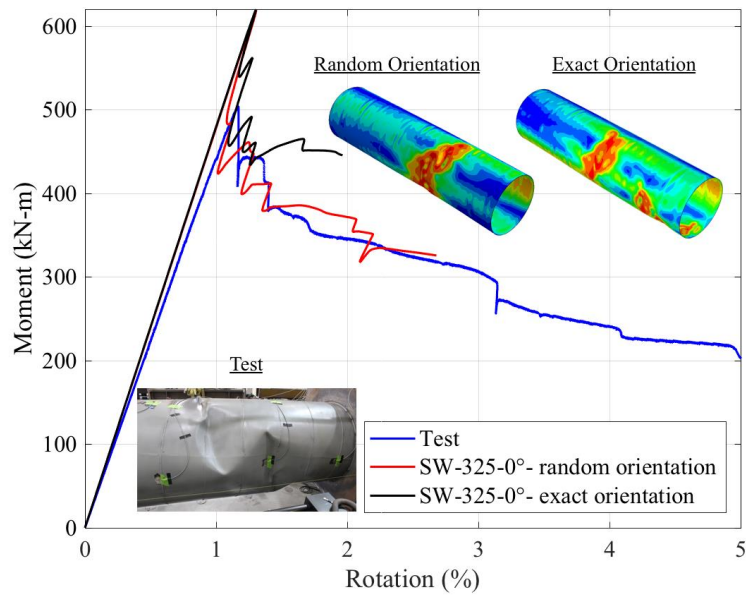


Figure 6.11 Moment-rotation curves of specimen SW-325-0° GMNIA models with measured imperfections and different orientations.

Fig. 6.12 (a-h) provides the moment-rotation curves of the models with the GMNA and GMNIA models with real measured imperfections. It is noticeable that the post-buckling behavior could be compared to post buckling behavior observed in the experiments in terms of number of load drops accompanied by the buckling waves developed are similar to tests in most of the GMNIA models with measured imperfections.

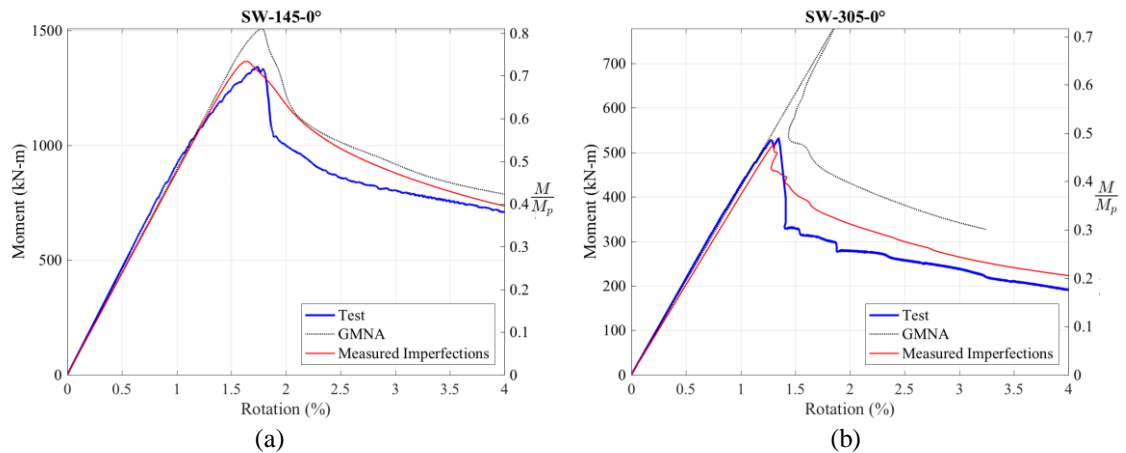


Figure 6.12 (a-b) Moment-Rotation curves for GMNA and GMNIA-measured imperfections models vs test results

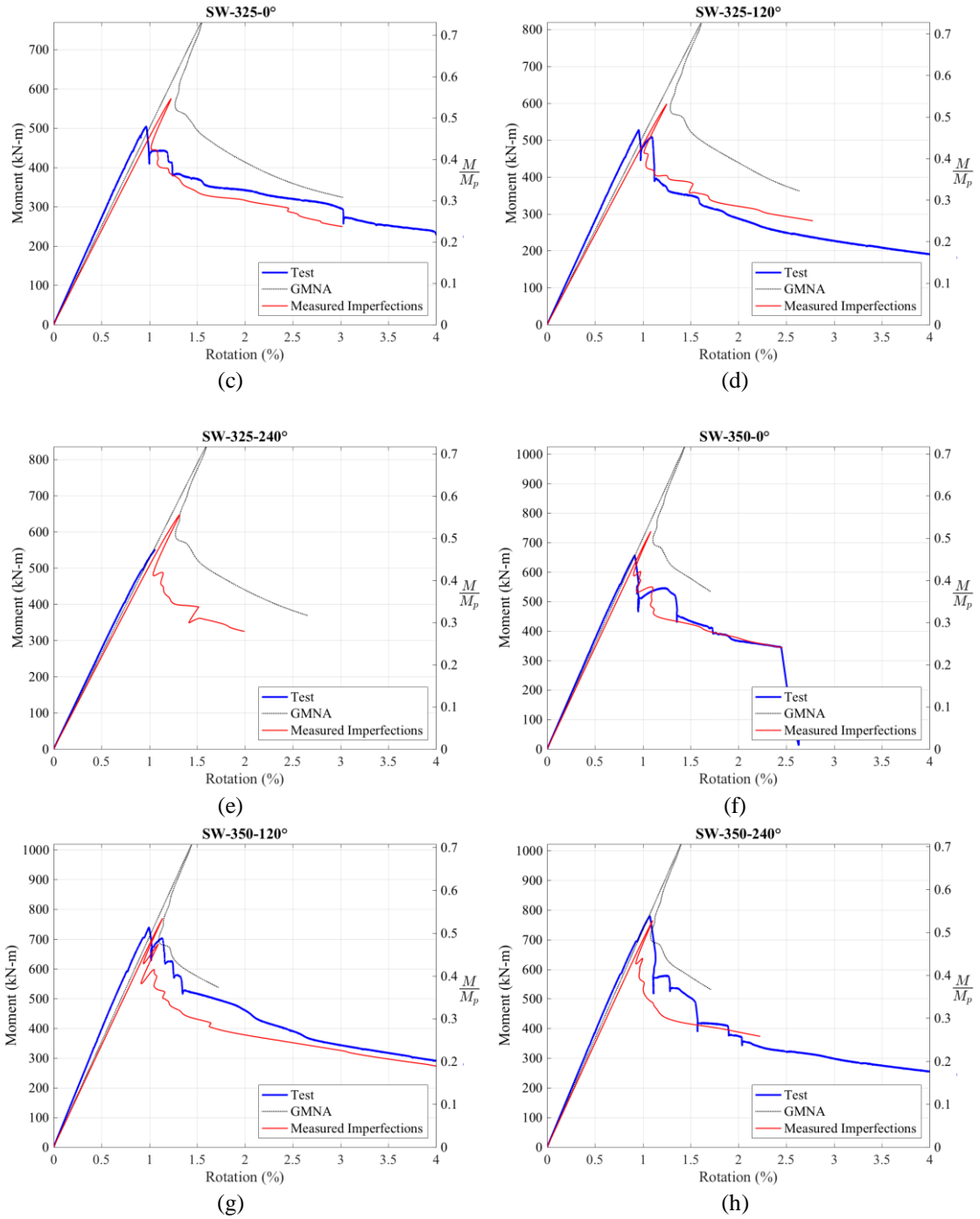


Figure 6.12 (c-h) Moment-Rotation curves for GMNA and GMNIA-measured imperfections models vs test results.

After several trials with the models we selected the extra fine mesh size ($0.25\sqrt{R_{avg}t}$), to balance between accurately capturing the scanned imperfections and saving the time consumed in computation. Table 6.5 summarizes the results from GMNIA models with

measured imperfections and the comparison to test results, the test-to-model moment ratio ranges from 0.87 to 1.02 with a mean and standard deviation of 0.94 and 7% respectively. The test-to-model stiffness ratio ranges from 1.04 to 1.16 with a mean and standard deviation of 1.10 and 4% respectively. The deformed shape at the end of the analysis of each of the GMNIA models is shown in Fig. 6.13 (a-h).

Table 6.5 Comparison between GMNIA models with measured imperfections and large-scale tests.

Specimen	M_{u-test} (kN-m)	Measured Imperfections M_{u-FE} (kN-m)	Moment Ratio (M_{u-test}/M_{u-FE})	K_{test} (kN-m/rad)	Measured Imperfections K_{FE} (kN-m/rad)	Stiffness Ratio (K_{test}/K_{FE})
SW-145-0°	1343	1366	0.98	918	884	1.04
SW-305-0°	526	518	1.02	433	404	1.07
SW-325-0°	502	576	0.87	546	479	1.14
SW-325-120°	523	598	0.87	565	489	1.16
SW-325-240°	≥553	647	≥0.85	556	507	1.10
SW-350-0°	656	738	0.89	752	688	1.09
SW-350-120°	737	770	0.96	780	684	1.14
SW-350-240°	778	763	1.02	769	702	1.10
Mean			0.94*			1.10
Standard deviation			0.07*			0.04

*Specimen SW-325-240° is excluded from the mean and standard deviation calculations of the moment ratio.

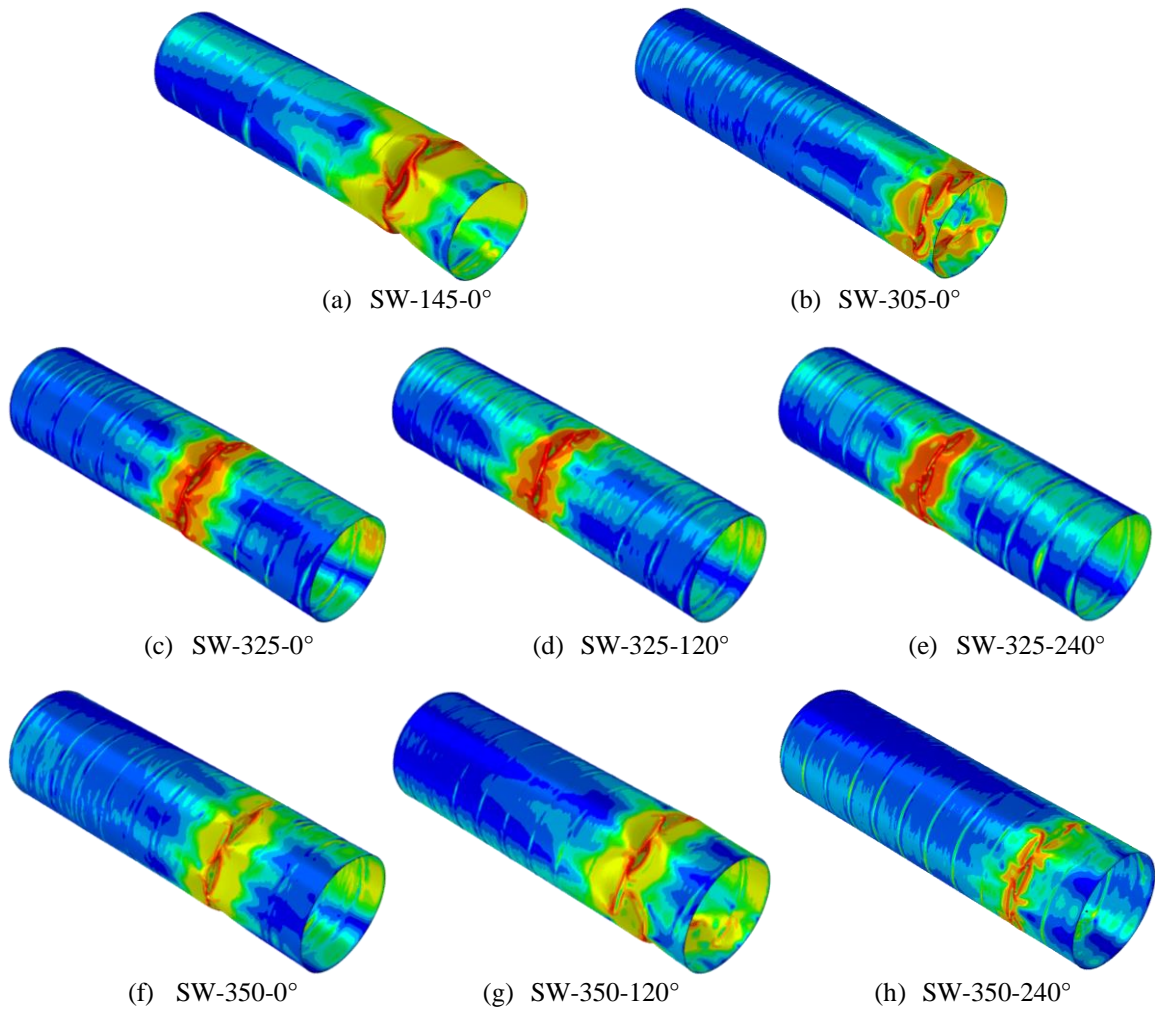


Figure 6.13 Deformed shape for all GMNIA models with measured imperfections, contour for von-Mises Stress.

6.4.3 GMNIA models with measured imperfections and residual stresses

Initial stresses were implemented in models with scanned geometry to study the effect of residual stresses on the strength. The residual stress patterns used did not satisfy equilibrium of the unloaded shell (but we allow the shell to come into equilibrium before loading) which is a known problem in literature. Some studies suggested adding a set of residual strains at the weld areas to satisfy equilibrium in what is referred to as “consistent residual stress field” (Holst et al. 2000, Rotter et al. 1996). A consistent residual stress field

is the stress that satisfies equilibrium and can be kept its value in the final imperfect geometrical form of the shell and does not increase the amplitude of the geometric imperfections in the unloaded shell. This inclusion of residual stresses was believed to be slightly beneficial to the strength of the shell model; however, there is an ongoing argument about whether it causes to increase or decrease the buckling strength (ECCS 2013).

We decided to add residual stresses according to SWT-project residual stresses measurements conducted by NEU team, and described in Chapter 4, without going any deeper into the implementation of the residual strains but we do let the model equilibrate. Fig. 6.14 (a) shows the deformed shape of the nominal perfect geometry after applying residual stresses, the deformed shape in this case shows the mirrored shape of the weld imperfections from the scanned data. Fig. 6.14 (b-c) shows two trials where a modification was made to the bending residual stresses where the bending stresses were inverted through the thickness. The first trial was to invert all the meridional bending stress, the deformed shape matched the weld depression observed in the scanned geometry along the spiral seam weld but did not match the observed imperfections around the cross weld, see Fig. 6.14 (b). The second trial the meridional bending residual stress only was inverted through the thickness, this geometry matches what was observed in the scans around the welds in both cross and spiral seam weld, see Fig. 6.14 (c).

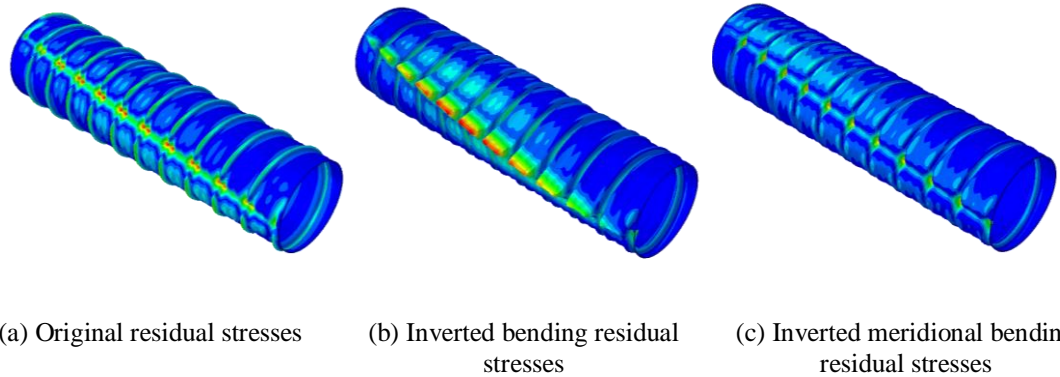


Figure 6.14 Deformed shape of perfect numerical model with only residual stresses applied to it scaled 500x.

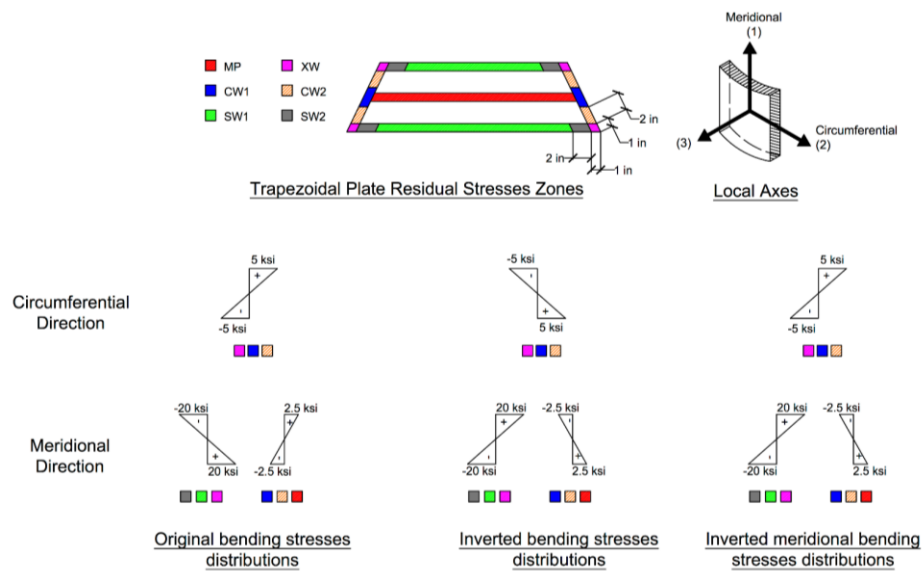


Figure 6.14 (d) Distributions for the bending stresses on a trapezoidal plate for the three cases.

To study the effects of the residual stresses on the buckling behavior of spirally welded tapered tubes, two cases were considered: residual stresses patterns as provided originally by Jay (2017) and the same pattern with inverted bending stress in the meridional direction at the spiral seam weld. Residual stresses are added to the models with scanned geometry for eight specimens. Fig. 6.15 (a-h) shows the moment rotation curves of the models with measured imperfections only (MI), models with measured imperfections and original residual stresses (MI+RS), and models with measured imperfections and residual stresses

with inverted bending stresses along the spiral seam weld (MI+RS inv.). In all of the models except SW-325-240°, the inclusion of the residual stresses did not change the post-buckling behavior compared to the (MI) models. That proves the assumption discussed in literature that the geometric imperfections are more dominant in slender shell buckling strength and behavior.

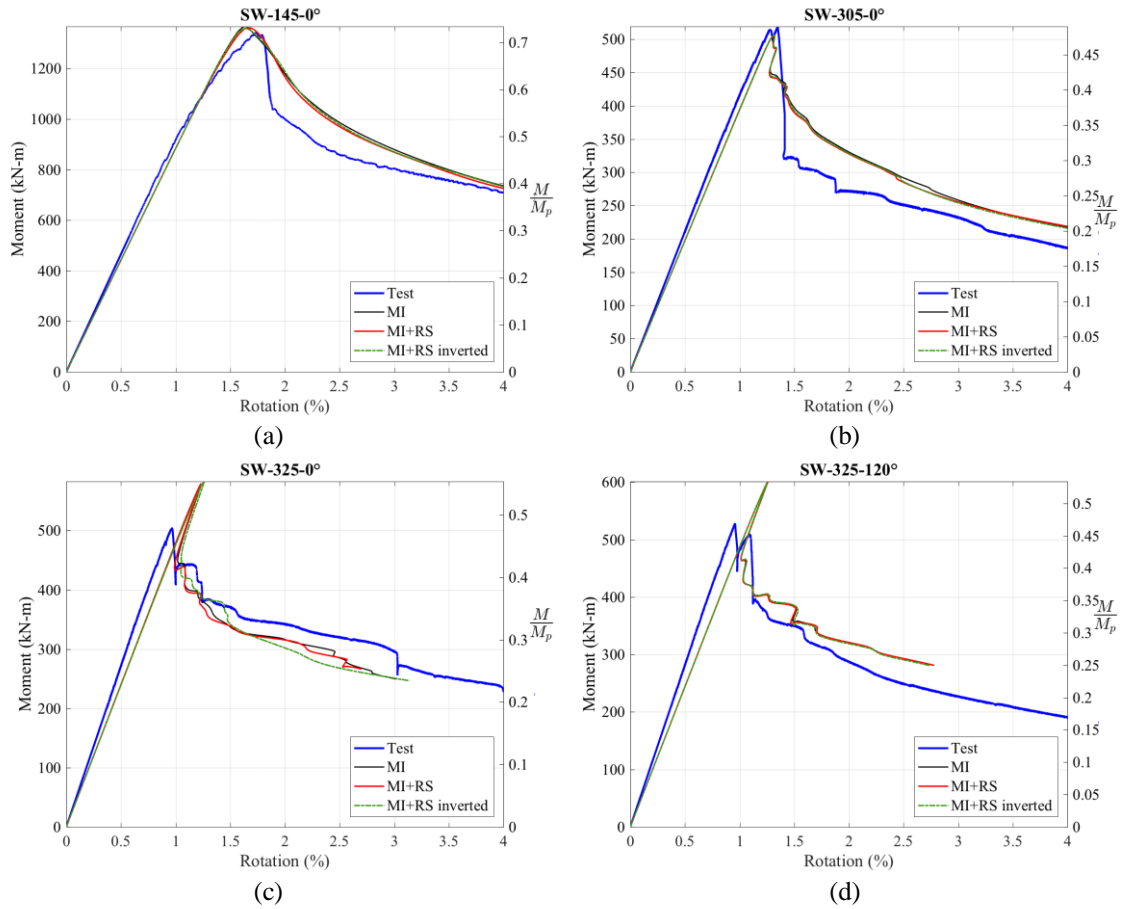


Figure 6.15 (a-d) Moment-Rotation curves for GMNIA-measured imperfections models without residual stresses (MI), with original residual stresses (MI+RS) and inverted bending residual (MI+RS inverted) vs test results.

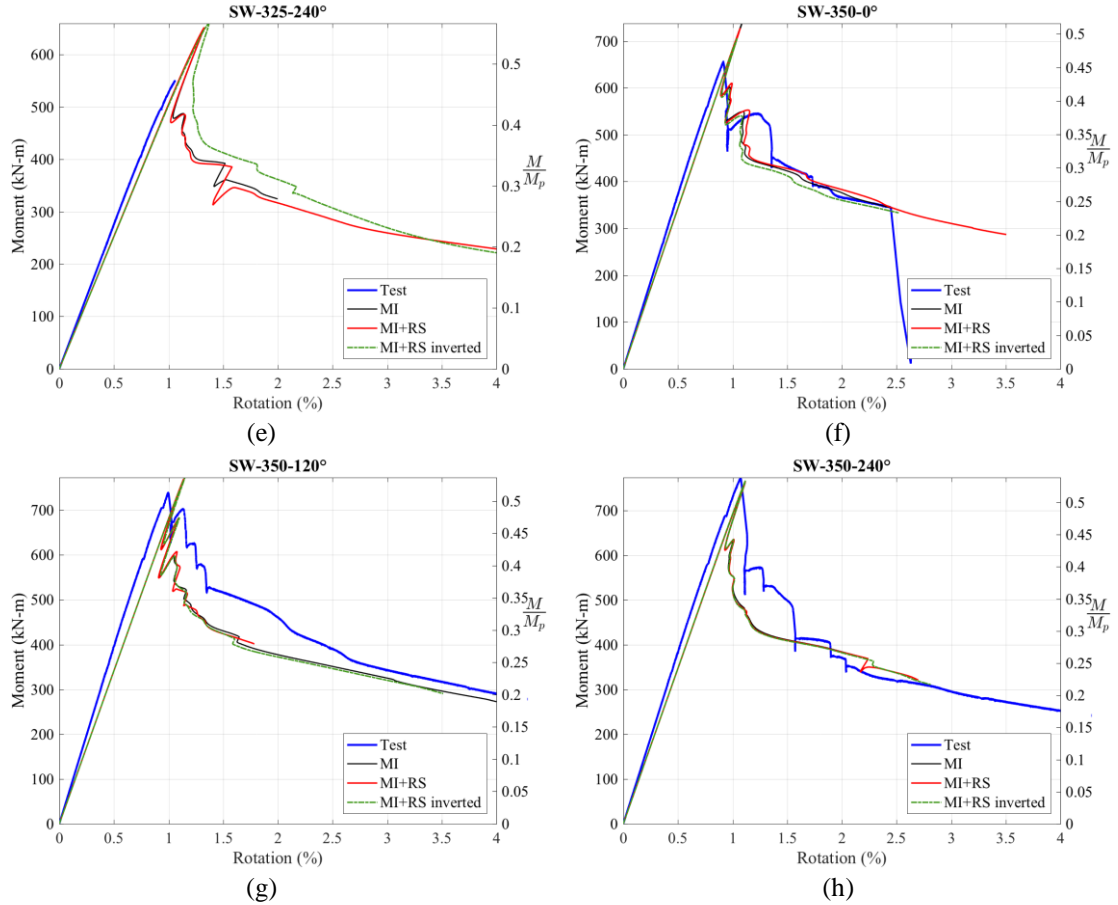


Figure 6.15 (e-h) Moment-Rotation curves for GMNIA-measured imperfections models without residual stresses (MI), with original residual stresses (MI+RS) and inverted bending residual (MI+RS inverted) vs test results.

Table 6.6 shows the ultimate moments of the (MI+RS and MI+RS inv.) GMNIA models are compared with ultimate moment from tests and ultimate moment of (MI) GMNIA models. Excluding specimen SW-325-240°, the test-to-model moment ratio (M_{u-test}/M_{u-FE}) ranges from 0.85 to 1.02 with mean of 0.94 and standard deviation 6% for the (MI+RS) GMNIA models, while it ranges from 0.86 to 1.01 with mean of 0.95 and standard deviation 6% for (MI+RS inv.) GMNIA models. The moment ratio of the GMNIA models without residual stresses (MI) to the models with residual stresses (M_{u-MI}/M_{u-FE}) for (MI+RS) GMNIA models ranges from 0.99 to 1.01 with mean of 1.0 and standard deviation

1%, while it ranges from 0.98 to 1.04 with mean 1.0 and standard deviation 2% for the (MI+RS inv.) GMNIA models.

Table 6.6 Comparison between ultimate moment GMNIA models with measured imperfections and residual stresses and large-scale tests.

Specimen	<i>Test</i>	<i>MI</i>	MI +RS			MI+RS inv.		
	M_{u-test}	M_{uMI}	M_{uRS}	$\frac{M_{uMI}}{M_{uRS}}$	$\frac{M_{u-test}}{M_{uRS}}$	$M_{uRS\ inv.}$	$\frac{M_{u-test}}{M_{uRS\ inv.}}$	$\frac{M_{uMI}}{M_{uRS\ inv.}}$
	(kN-m)	(kN-m)	(kN-m)			(kN-m)		
SW-145-0°	1343	1366	1361	1.00	0.99	1358	0.99	1.01
SW-305-0°	526	518	518	1.00	1.02	519	1.01	1.00
SW-325-0°	502	576	579	0.99	0.87	583	0.86	0.99
SW-325-120°	523	598	601	0.99	0.87	599	0.87	1.00
SW-325-240°	≥553	647	652	0.99	≥0.85	660	≥0.84	0.98
SW-350-0°	656	738	728	1.01	0.90	706	0.93	1.04
SW-350-120°	737	770	770	1.00	0.96	773	0.95	1.00
SW-350-240°	778	763	771	0.99	1.01	774	1.01	0.99
Mean				1.00	0.94*		0.95*	1.00
Standard deviation				0.01	0.06*		0.06*	0.02

*Specimen SW-325-240° is excluded from the mean and standard deviation calculations

Table 6.7 shows the summary of the results in terms of stiffness. The GMNIA models with residual stresses (MI+RS and MI+RS inv.) are compared to tests stiffness and GMNIA models without residual stresses (MI). The test-to-models stiffness ratio (K_{test}/K_{FE}) ranges from 1.04 to 1.16 with mean of 1.10 and standard deviation of 4% for both the (MI+RS) and (MI+RS inv.) GMNIA models, while the ratio of the models without residual stresses to those with residual stresses (K_{MI}/K_{FE}) ranges from 0.997 to 1.001 with mean 1.0 and standard deviation of 0.2% for (MI+RS) GMNIA models, while for the (MI+RS inv.) GMNIA models it ranges from 0.998 to 1.001 with the mean of 1.00 and standard deviation 0.2%.

Table 6.7 Comparison between stiffness of GMNIA models with measured imperfections and residual stresses and large-scale tests.

Specimen	K_{test} (kN-m/rad)	K_{MI} (kN-m/rad)	K_{FE} (kN-m/rad)		(K_{test}/K_{FE})		(K_{MI}/K_{FE})	
			MI+RS	MI+RS inv.	MI+RS	MI+RS inv.	MI+RS	MI+RS inv.
SW-145-0°	918	884	884	884	1.04	1.04	0.999	1.000
SW-305-0°	433	404	405	405	1.07	1.07	0.998	0.998
SW-325-0°	546	479	480	479	1.14	1.14	0.997	0.999
SW-325-120°	565	489	489	488	1.16	1.16	1.000	1.001
SW-325-240°	556	507	507	506	1.10	1.10	1.001	1.003
SW-350-0°	752	688	687	689	1.10	1.09	1.001	0.999
SW-350-120°	780	684	684	684	1.14	1.14	1.000	1.000
SW-350-240°	769	702	701	702	1.10	1.10	1.001	0.999
Mean					1.10	1.10	1.00	1.00
Standard deviation					0.04	0.04	0.002	0.002

The inclusion of residual stresses slightly fluctuated between slightly increasing or decreasing the strength of the models (MI+RS and MI+RS inv. compared to MI models). However, it is found that the effect of the residual stresses in most of the models is negligible compared to (MI) models, the change in strength never exceeded 0.3%. Comparing both (MI+RS) and (MI+RS inv.) models, the effect of the directions of the meridional bending is undistinguished. The deformed shape of all GMNIA (MI+RS) models are shown in Fig. 6.16.

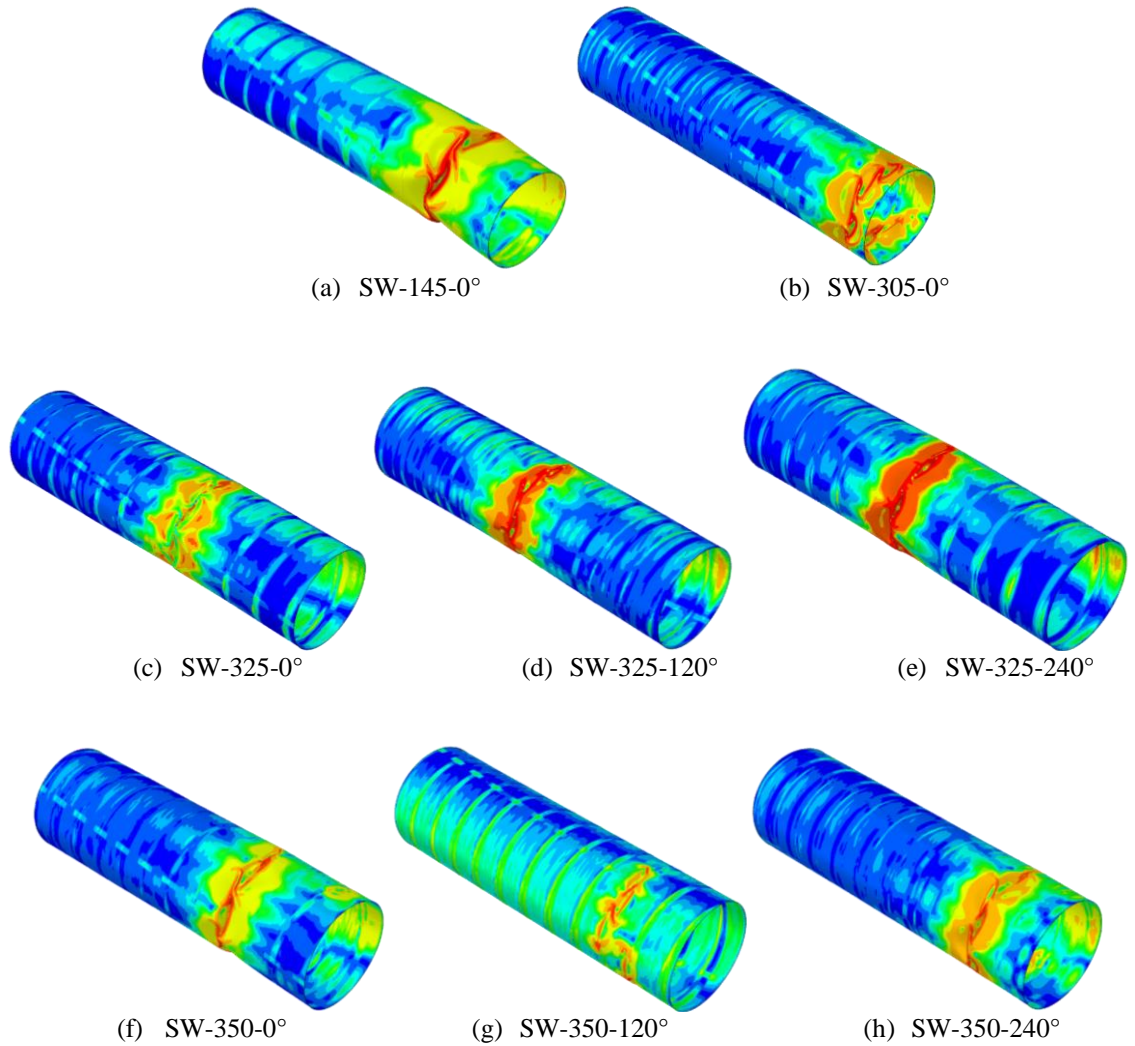


Figure 6.16 Deformed shape for all GMNIA (MI+RS) at the end of the analysis, contour for Von-Mises Stress.

6.5 Commentary on nonlinear collapse analyses

The modeling protocol, proposed in Chapter 5, is validated by comparing modeling results with measurements from a series of nine large-scale flexural tests, recently completed by (Jay et al. 2016b), on thin-walled spirally welded tapered tubes (SWT-project). The second series of analyses follows the procedures in EC3-1-6 (CEN 2007) for design based on geometric and material nonlinear analysis including imperfections (GMNIA).

Despite the variation, the agreement between the model predictions and test results is reasonable for all GMNIA models with both generated and measured imperfections. Fig. 6.17 shows the mean and standard deviation of the test-to-predicted moment ratio across the seven out of nine specimens (only seven of the nine tests are included in these statistics because specimen SW-230-0° was classified as worse than Class C and the tests of specimen SW-325-120° ended due to fracture on a spiral seam weld). The mean ranges between 0.89 and 1.22 and the standard deviation ranges from 6% to 9%. For the GMNIA models with generated imperfections consistent with Class C imperfection in EC3-1-6 the mean was almost 1.0 and the standard deviation 8%. The nonlinear collapse models with eigenmode-affine imperfections showed relatively little change in strength with changing quality class than those with weld depression based imperfections, although models with weld depression imperfections worked reasonably for larger imperfection magnitudes. As the maximum diameter to thickness ratio studied here is 350, the nonlinear collapse models failed due to elastic-plastic buckling and for this reason showed less sensitivity to imperfection pattern (at least in the models with eigenmode-affine pattern). For the GMNIA models with measured imperfections, with or without residual stresses, the mean for the test-to-predicted moment ratio was 0.94 and the standard deviation ranges from 6% to 7%. The inclusion of residual stresses caused negligible effects in all forms.

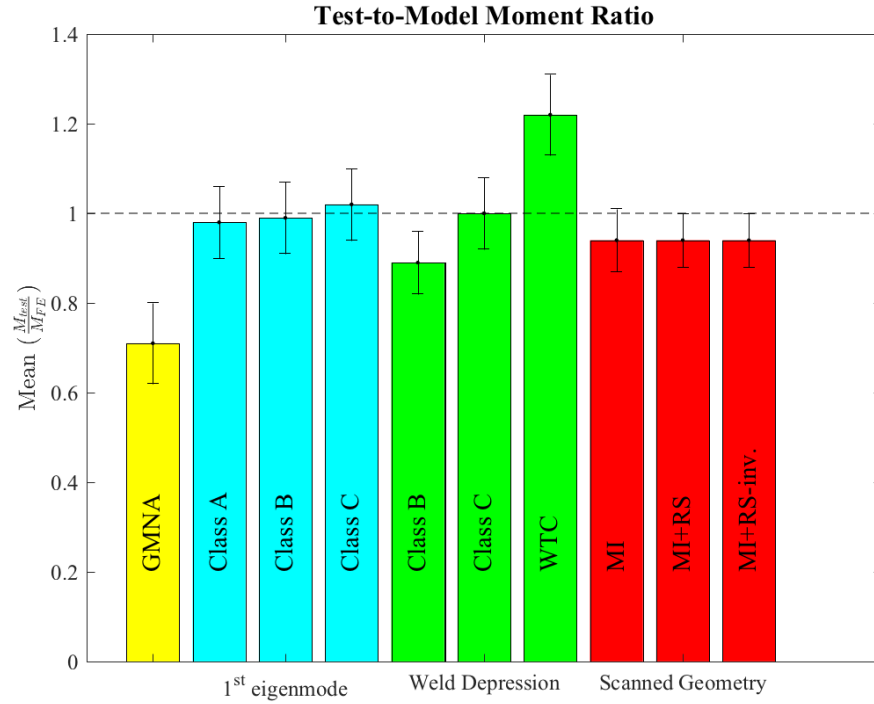


Figure 6.17 Summary of the test-to-predicted moment ratio mean GMNA and GMNIA models with all imperfections patterns discussed in this chapter.

Fig. 6.18 shows the summary of the mean of test-to-predicted stiffness ratios for the nine specimens GMNIA models with both generated and measured imperfections the mean ranges from 1.07 to 1.27 and the standard deviation ranged from 4% to 6%. For the models with generated imperfections consistent with EC3-1-6 Class C, the mean test-to-predicted moment ration ranges from 1.10 to 1.13, and the standard deviation ranges from 5% to 6%. For the measured imperfection, with or without residual stresses, the mean was 1.10 and the standard deviation was 4%. Only the GMNA models were stiffer than the tests, it was expected that the numerical models are going to be under-predicting the stiffness since the tests stiffness were corrected based on the tangent stiffness between 40 and 60% of the ultimate bending capacity to remove the effect of the test rig stiffness.

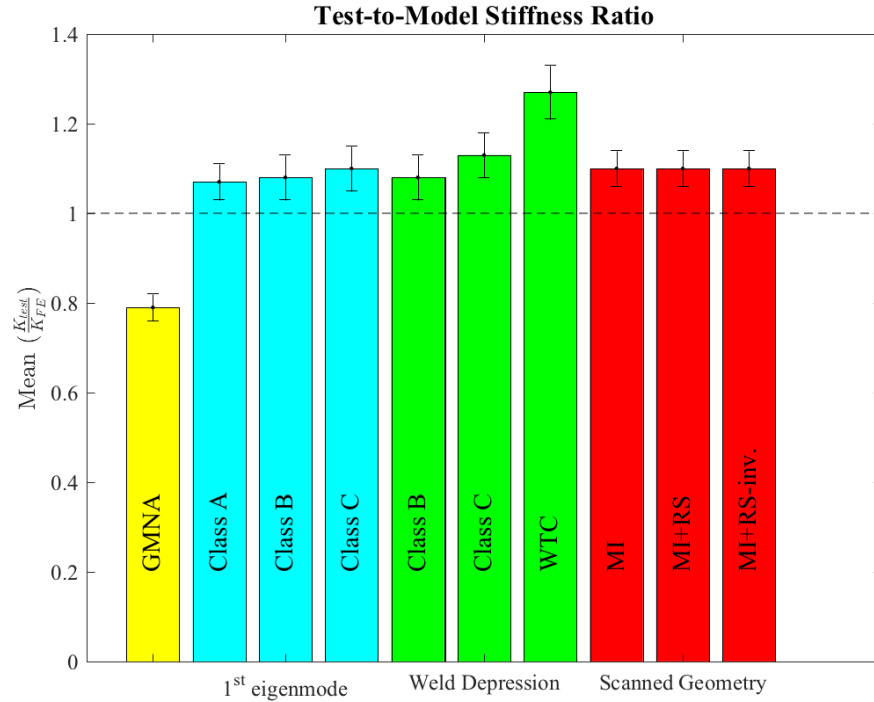


Figure 6.18 Summary of the test-to-predicted stiffness ratio mean GMNA and GMNIA models with all imperfections patterns discussed in this chapter.

The favorable agreement between the models and tests in this study is a promising sign of the potential of analysis-based design approaches such as GMNIA both generally and for the specific case studied here of thin-walled spirally welded tapered tubes. In addition, the amplitude of imperfections considered in the models with generated imperfections are tied to well-established EC3-1-6 fabrication tolerance quality classes, which are already widely used in the design of thin-walled shells. The usage of the weld depression along with EC3-1-6 recommendations for the amplitudes for each quality class is more nuanced. The results of Class C GMNIA models with both patterns of generated imperfections were quite reasonable compared to test data. The implementation of the real measured imperfections could be more accurate if treated carefully, considering the mesh density used and the orientation with respect to realistic loading and boundary conditions. However, it is not

always a feasible or practical method when dealing with real full-scale structure design. The implementation of the residual stresses in this case did not show much effect on the strength and the stiffness of model which confirms the original assumption that initial geometrical imperfections are more dominant in severing the shell strength and stiffness.

The GMNIA models are going to be used in Chapter 7, to build reference resistance design curves for SWTs, and for design of 3 MW archetype wind turbine tower in Chapter 8.

Chapter 7

Reference Resistance Design of Spirally Welded Tubes

7.1 Introduction

Shell buckling is known to be one of the most complicated problems in structures. Many factors can affect the post-buckling behavior, strength, and failure. Buckling of thin-shells is usually driven by initial geometric imperfections, as discussed in Chapters 3 and 6. As briefly described in Chapter 2, using numerical modeling to design shells is a growing trend, adopted by structural design guidelines in the world. However, building a reliable numerical model for a thin-walled shell is still a challenging process that requires a strong knowledge of numerical (finite element) modeling. Recent research by Rotter et al. proposed a new method called Reference Resistance Design (RRD). The RRD method is used to build generalized capacity curves for specific type of shells, the method has been adopted by Eurocode 1993-1-6:2007 for Strength and Stability of Metal Shells (EC3-1-6). EC3-1-6 was one of the first design codes in the world to formalize the use of advanced modeling in the design of shells. Two methods are described in detail in EC3-1-6 for the design of shells for buckling using numerical models, the first one (LBA-MNA) uses the perfect geometry of the shell to build the model and two numerical runs are required: 1- Linear Buckling Analysis (LBA), to get the critical loads and stresses, and 2- Material Nonlinear Analysis (MNA), to get the plastic loads. The second method is the Geometrical and Material Nonlinear Analysis with Imperfections implemented (GMNIA), which requires a set of linear and nonlinear analyses on both the perfect geometry and the geometry with initial imperfections, see Fig. 7.1. Design using global numerical GMNIA analyses is a sophisticated process that intends to use the full power of numerical modeling

tools in design. The procedure requires running a set of analyses on several steps increasing sophistication of your model in every step and then testing and calibrating your final model by another set of analyses. Rotter's RRD method performs this sophisticated GMNIA modeling in advance for a particular class of shells and then provides the output of those models as simplified capacity strength curves that the designer can utilize without performing their own analysis. RRD allows a designer to benefit from verified numerical analyses of a similar structure without going into the sophistication of building and verifying their own numerical models. To develop RRD, the procedure consists of running numerical models with varied slenderness ratio and imperfection amplitudes, verify the results with available test results or verified hand calculations, then building standardized strength curves using normalized results from numerical models. The argument of what type of imperfections to be implemented in the FE models to get reliable and distinct results is discussed in Chapter 5 and 6, and is critical in RRD. In this chapter, RRD curves are built for medium length SWT where the ovalization buckling mode is restricted and the local buckling is the critical limit state.

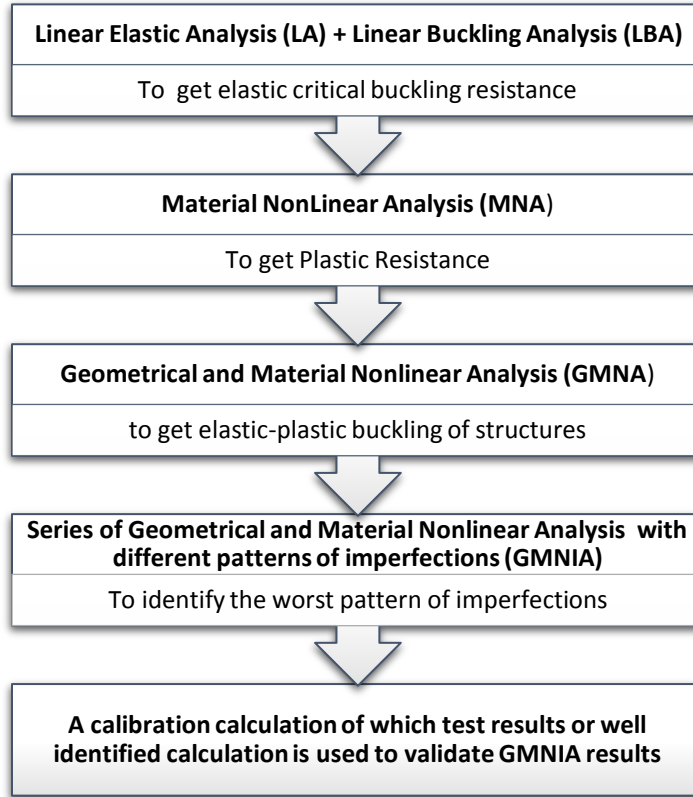


Figure 7.1 Design by GMNIA analyses according to EC3-1-6 (ECCS 2013).

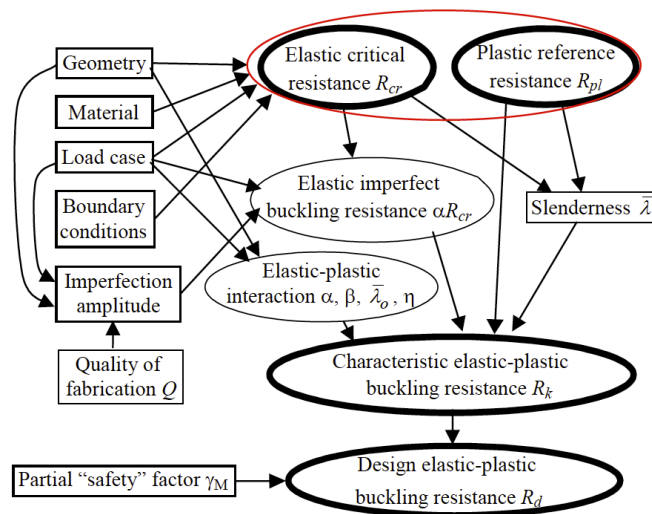


Figure 7.2 The processes of RRD method (Rotter 2016).

7.2 Building RRD curves

RRD curves are built to such that normalized GMNIA results, of a specific geometry of a shell under specific loading, can be used to predict the strength of a similar shell geometry. Due to the great variety of shapes and forms of shells structures, unique curves are built for each shell structure. Such curves can potentially save lots of time consumed by designer in building finite element models. EC3-1-6 section 8.5 provides guidelines for the buckling limit state in the design of shells using standardized capacity curves. Eq. 7.1-7.3 provides the capacity curves equations by calculating, the buckling reduction factor χ as the ratio of the GMNIA ultimate moment to the plastic moment ($\chi = \frac{M_k}{M_p}$) which is typically plotted against relative slenderness ($\lambda = \sqrt{\frac{M_p}{M_{cr}}}$) or relative strength ($\frac{M_k}{M_{cr}}$) as shown in Fig. 7.3. The elastic imperfection reduction factor (α), the interaction component (η), the plastic range factor (β), and the squash limit relative slenderness (λ_o), these parameters (RRD parameters) are left to designers to be computed for a specific structures RRD curves.

$$\chi = 1 \quad \text{when } \lambda \leq \lambda_o \quad (7.1)$$

$$\chi = 1 - \beta \left(\frac{\lambda - \lambda_o}{\lambda_p - \lambda_o} \right)^\eta \quad \text{when } \lambda_o < \lambda < \lambda_p \quad (7.2)$$

$$\chi = \frac{\alpha}{\lambda^2} \quad \text{when } \lambda_p \leq \lambda \quad (7.3)$$

where the plastic limit slenderness ($\bar{\lambda}_p = \sqrt{\frac{\alpha}{1-\beta}}$).

The RRD parameters (α , $1 - \beta$, and η) are represented in the form $\left(\frac{a}{[1+b(\delta_o/t)^c]} \right)$ where a , b , and c are the constants to be computed for every parameter from GMNIA models.

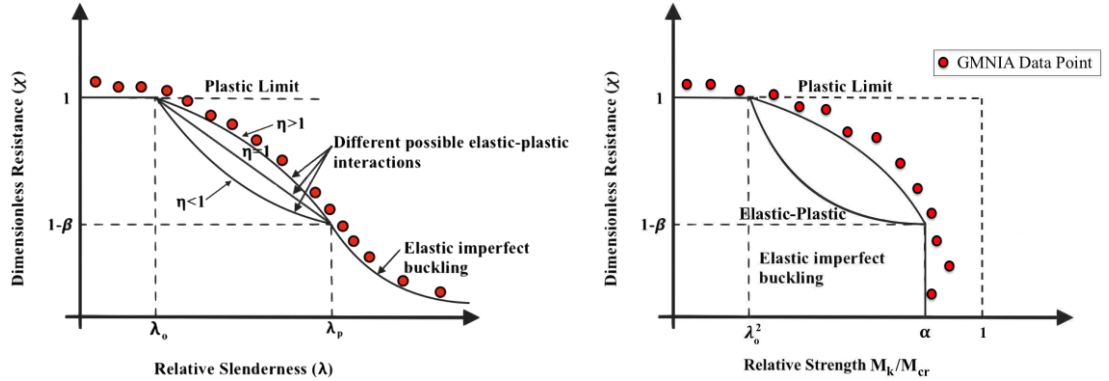


Figure 7.3 Typical shell strength curves.

Although providing these curves is relatively an easy process, a designer may still wonder on how to use these curves if they do not know which amplitude of imperfections to consider. One idea is to build these curves for the three quality classes from EC3-1-6. For SWT project, we have SWT test results and an assigned quality class for our specimens so if the curves are built with respect to Class A, B, and C, it is straight forward.

7.2.1 An example from literature (Chen et al. 2008)

Chen et al. (2008) used the RRD method to build flexural strength curves for cylindrical shells under global bending in the elastic-plastic range. Their parametric model was chosen to be for a prismatic shell under bending with a single circumferential weld depression imperfection at mid-length. The dimensions of the parametric model were carefully selected to make sure the ovalization mode did not affect the outcome. The diameter of the model was constant, and the thickness varies to get a wide range of slenderness. To build the design curves they ran 99 GMNIA models and they determined the RRD parameters to be:

$$\alpha = \frac{1}{(1+2(\delta_o/t)^{0.8})}, \quad 1 - \beta = \frac{0.77}{(1+1.2(\delta_o/t)^{0.8})}, \quad \text{and} \quad \eta = \frac{0.8}{(1+0.07(\delta_o/t)^2)}$$

Using these computed parameters and Eq. 7.1-7.3, and for a range for the amplitude of imperfections δ_o from $0.01t$ to $2t$, Chen et al. (2008) RRD curves were and SWT test results were indicated to the plots, see Fig. 7.4 (a) and (b). The same RRD curves were built again with EC3-1-6 three quality classes, see Fig. 7.4 (c) and (d).

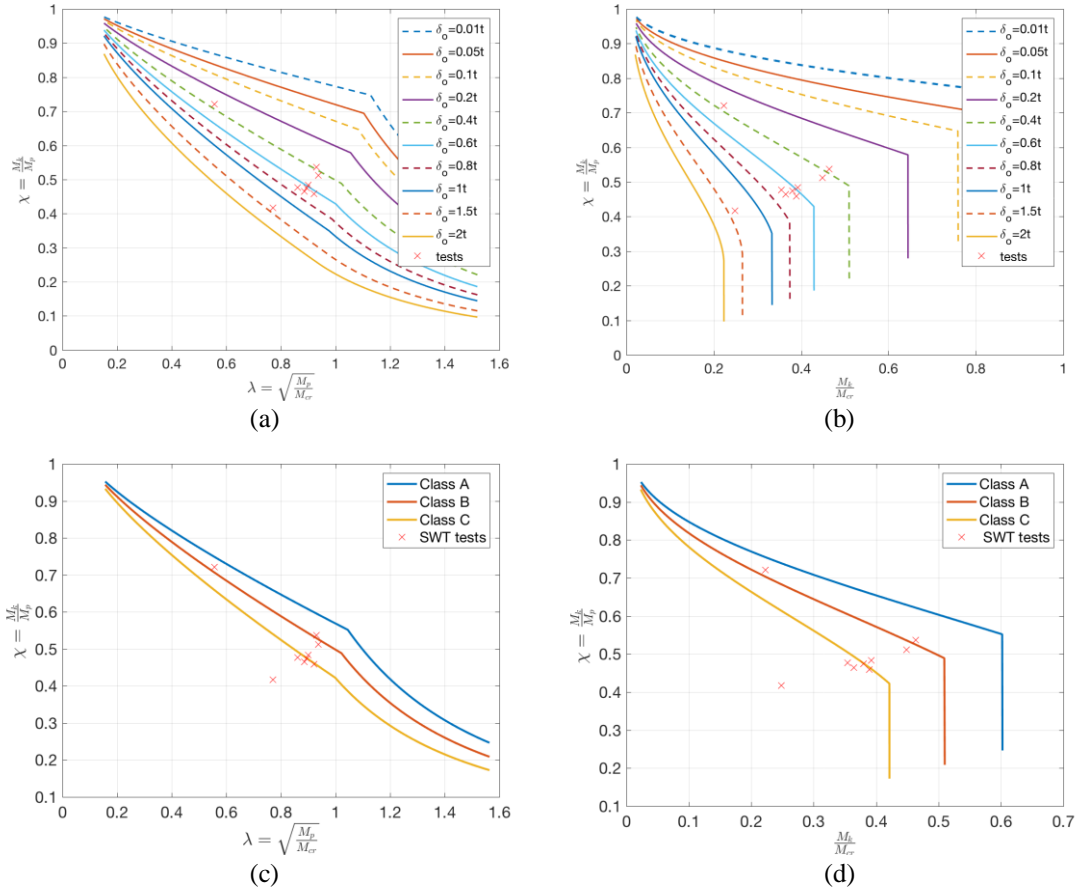


Figure 7.4 RRD capacity curves built with the $(\alpha, \beta,$ and $\eta)$ parameters computed by Chen et al. (2008) and SWT test results indicated.

For SWT specimens they were all classified as Class C except SW-230-0° (as described in Chapter 3) which is the outlier point far below Class C curve in Fig. 7.4 (c) and (d). The three points representing SWT tests results adjacent to Class B curve are specimens (SW-145-0°, SW-350-120°, and SW-350-240°) these specimens were classified as Class C according to one tolerance measurement only, but they were Classified as Class B or higher

according to other tolerance measurements. In general, RRD curves using Chen et al. (2008) parameters, overestimated the strength of the SWT. Of course, the design strength obtained from these curves is converted to a reliability basis using partial safety factor γ_{M1} of EC3-1-6 (Sec. 8.5.2(2)).

7.3 RRD for SWT models

Since SWTs have special geometric features and imperfection patterns the idea of building and calibrating RRD curves specifically for spirally welded tapered tubes could show better results and is pursued in this section. The analyses required to get the plastic resistance and elastic critical resistance could be substituted by theoretical solutions, to save computation time. As proved in Chapter 5, with the recommended meshing protocols carefully followed, the critical moments from LBA runs, and plastic moments from MNA runs, could be substituted with theoretical critical moment (Eq. 7.7) and plastic moments (Eq. 7.4). The theoretical plastic moment (Eq. 7.4) and theoretical critical moment (Eq. 7.7) are computed using equivalent section with radius R_{eq} , where ϕ is the angle of tapering and yielding stress is assumed to be ($\sigma_y = 450$ MPa).

$$\text{Plastic moment for thin-walled shells} \quad M_p = 4R_{eq}^2 t \sigma_y \quad (7.4)$$

$$\text{where equivalent} \quad R_{eq} = \left(\frac{R_{max}}{\cos \phi} \right) \quad (7.5)$$

$$\text{Yielding moment} \quad M_y = \pi R_{eq}^2 t \sigma_y \quad (7.6)$$

$$\text{Critical moment} \quad M_{cr} = \pi \left[\frac{ER_{min}t^2}{\sqrt{3(1-\nu^2)}} \right] \cos^2 \phi \quad (7.7)$$

7.3.1 Geometry of Parametric Model with Spiral Weld Depression Imperfection

For the scope of this study where the failure is controlled by local buckling and not the ovalization mode, a shell numerical parametric model was created for building the RRD curves. This parametric model was chosen to be close to the SWT specimens (Chapter 3) that will be used to verify the proposed RRD curves. A SWT model with maximum diameter ($D_{max} = 1000mm$), the minimum diameter ($D_{min} = 860mm$), and the length of the model is ($L = 4D_{max} = 4000mm$), as sketched in Fig. 7.5. The width of the plates that form the tube is 300 mm, which will result in a range of helical angles from 5.5° at the largest diameter to 6.3° at the smallest diameter, as the helical angle changes with the variation in diameter along the length, see Fig. 7.5.

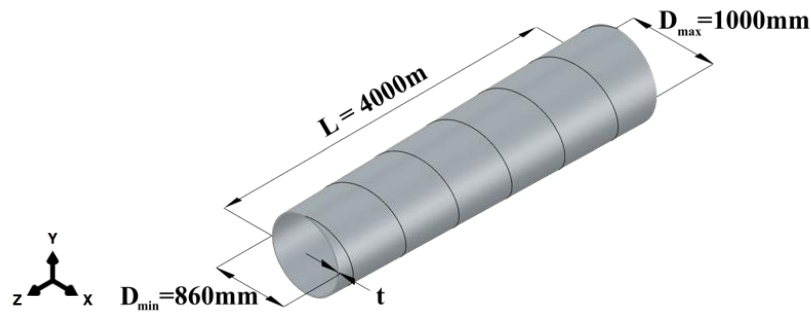


Figure 7.5 Spirally welded tube parametric model dimensions.

For the same geometry eleven models were created with thicknesses ranging from 20 mm to 1.42 mm, these thicknesses are selected to represent a range of maximum radius-to-thickness ratios varying from 25 to 2000, and correspondingly the relative slenderness changes from 0.35 to 3.1. The boundary conditions of the model are applied at two reference points at the center of cross sections at each end of the tube. The nodes at the large end are constrained to a single centroidal reference point, and nodes at the small end are constrained to a second centroidal reference point, using an ABAQUS beam-type

Multi-Point Constraint (MPC), which restricts displacement between nodes in the plane of the constraint such that the section remains circular, but permits the nodes to rotate as if there was an end plate at each end. The moments and boundary conditions are applied at the reference points. At the larger end, the model is permitted to rotate around the X and Y-axes, and to move along Z-axis, while at the small end the model is permitted to rotate around X and Y- axes only, see Fig. 7.5 for axes orientation. The material model used is an elastic perfectly plastic model with elastic modulus of 200 GPa, yield stress of 450 MPa, and ultimate strain of 0.15.

7.3.2 Imperfections

As mentioned before imperfections play a big role in predicting strength of a shell structure. The buckling behavior of slender tubes under bending is sensitive to imperfections, particularly where compressive stress is applied. The sensitivity to imperfections is mainly controlled by its pattern, amplitude, and its location relative to compressive stress. It is almost impossible for a designer to get the “real imperfections”, as the design process precedes manufacturing and imperfections occur during manufacturing, transportation, and construction. Studies have proposed several approaches of representing imperfections and the argument of which is more representative of the real imperfections and which is most deleterious or easier to generate numerically is a long one, see (e.g. Jansseune et al. 2016). A common example with a clear mathematical basis for the imperfections pattern is to use the 1st eigenmode-affine pattern generated by running a linear buckling analysis of the perfect model under the same loading. This approach is to be applied as recommended by EC3-1-6, if there is no reasonable or more realistic imperfection data available. Another common approach is to use what is referred to as “weld depression imperfections” which

has been proven by several practical studies to be more realistic for welded structures and more severe to strength and post-buckling behavior than the 1st eigenmode-affine pattern imperfections, (see Chapter 6). Rotter and Teng (1989) suggested several representative profiles for real weld depression imperfections, and their study proved that weld profile “Type A” is typically the most severe for strength degradation of structures.

7.3.3 Imperfections according to EC3-1-6

As described in Chapter 4, when the GMNIA models were built, the generated imperfection amplitude for dimples ($\delta_o = \Delta w_{eq,0} = U_n l_g$) were chosen to be as described in sec. 8.7.2 in EC3-1-6. The gauge length is used as ($l_g = l_{gx} = 4\sqrt{R_{avg}t}$) for the 1st eigenmode-affine imperfection pattern, and ($l_g = l_{gw} = \min(25t \text{ or } 500\text{mm})$) for weld depression imperfections. U_n is the dimple amplitude parameter and is computed as recommended in EC3-1-6 and listed in Table 7.1.

Table 7.1 Values of recommended dimple imperfections amplitude parameter.

Class A	Class B	Class C
$U_n = 0.01$	$U_n = 0.016$	$U_n = 0.025$

7.3.4 1st eigenmode-affine imperfections pattern

As an initial trial, we built GMNIA models with imperfections from 1st eigenmode-affine pattern. The imperfection pattern was scaled to meet quality Classes A, B, and C as recommended by EC3-1-6 (Table 7.1), see Fig. 7.6. Results are shown in Fig. 7.7, and as discussed in Chapter 6, the results of this type of GMNIA analysis with 1st eigenmode-affine pattern imperfections are less sensitive to imperfection amplitude. Although the tests results show reasonable agreement if compared to the Class C design curve, there is almost

no clear distinction between Classes A, B and C, especially at high slenderness, and the GMNIA results did not show consistent strength degradation when the amplitude of the imperfections increased, which is a requirement in EC3-1-6 (sec. 8.7.2) to use GMNIA models for design (e.g. at $\lambda = 1.38$, Class C GMNIA model shows more strength than Class A and Class B imperfections for the same model).

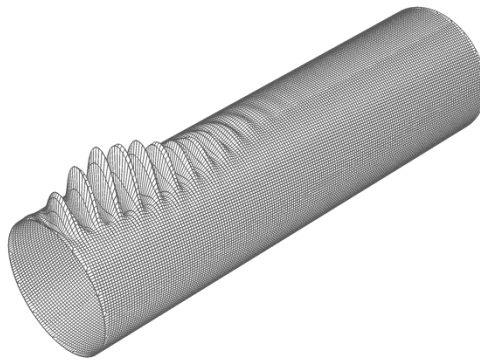


Figure 7.6 Typical imperfections from 1st eigenmode-affine pattern.

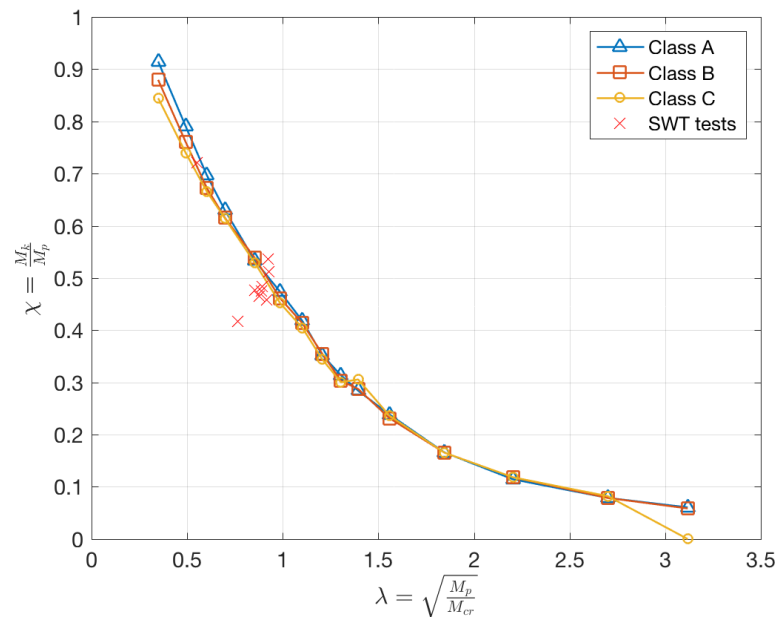


Figure 7.7 Capacity curve for GMNIA models with imperfections from 1st eigenmode-affine pattern.

7.3.5 Weld Depression imperfections

The second considered approach for building the GMNIA models necessary for RRD, is using a weld depression imperfections pattern of Rotter and Teng (1989), “Type A”. This weld depression profile is applied along the spiral seam welds on the parametric model. In this case, the imperfection profile amplitude is scaled to the thickness of each model: (0.05t, 0.1t, 0.2t, 0.4t, 0.6t, 0.8t, 1t, 1.5t, and 2t). In this set of the runs, we focused on the smaller range of radius to-thickness ratios from 25 to 350, to represent the relative slenderness (0.35 to 1.35), as the relative slenderness of SWT tests used for verification were between (0.54 and 0.93).

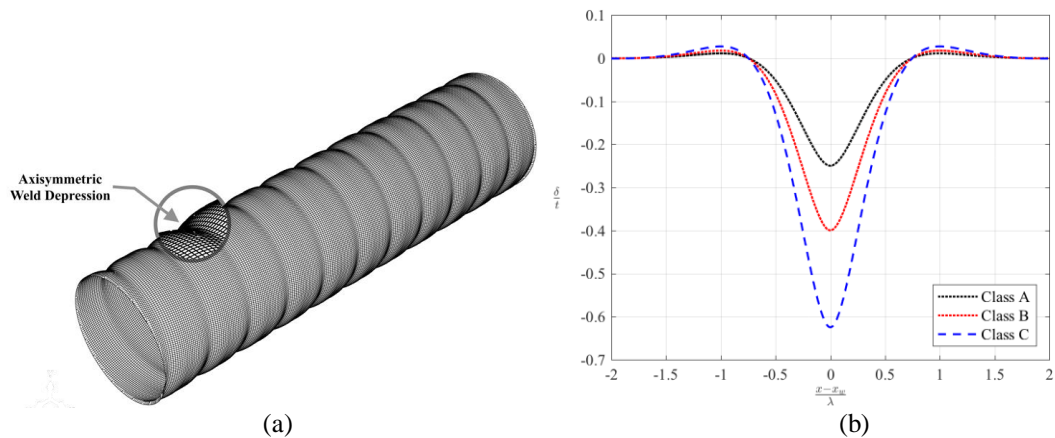


Figure 7.8. (a) Typical spirally welded tube with scaled weld depression imperfection along spiral seam weld, and (b) weld depression profiles as recommended by EC3-1-6 using Type A weld profile proposed by Rotter and Teng (1989).

The models were built with constant geometry (maximum diameter, minimum diameter and length), but with varied thickness to match the maximum radius-to-thickness ratios. The results are shown in Fig. 7.9 and 7.10, where each curve connects the same imperfection magnitude for all the models with different slenderness. Fig. 7.9 shows the results in terms of normalized moment and relative slenderness. Notice the strength of the

models with lowest slenderness ratio drops below the plastic moment. This drop gets more severe to models with higher slenderness and the same imperfection amplitude, as the imperfection amplitude for low slenderness tubes are large (in this case when $\frac{R}{t} = 25$, the thickness is 20 mm and the amplitude for imperfection profile range from 1 mm to 40 mm). Such an imperfection provides numerical convenience but is not practically important. In the models with high slenderness, where elastic buckling is the controlling limit state the effect of the imperfections decreases, and the strength curves get closer to each other. The slenderness of the SWT tests (reported in Chapter 3) lies in the elastic-plastic range, so the effect of low and high slenderness ratios is not as important for the scope of this study.

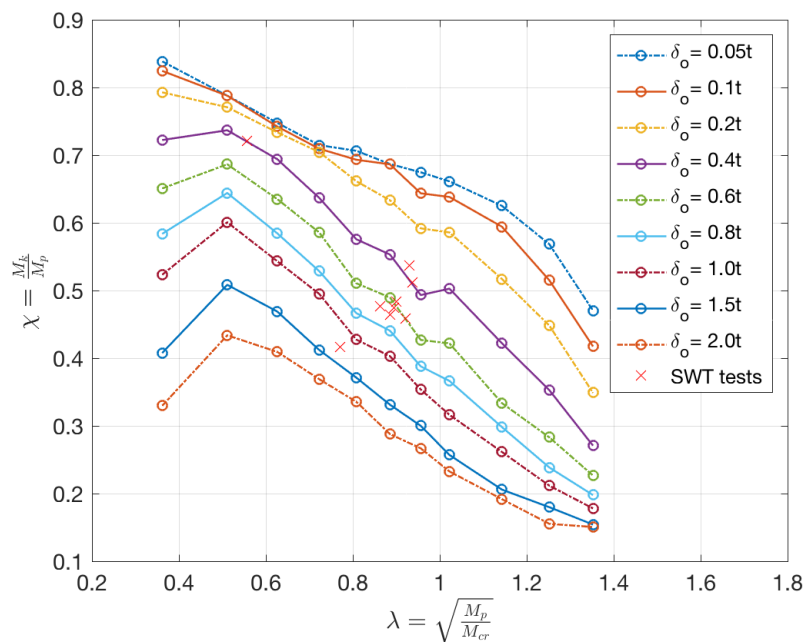


Figure 7.9 Capacity curves of normalized flexural strength of GMNIA models of spirally welded tapered tubes in terms of relative slenderness.

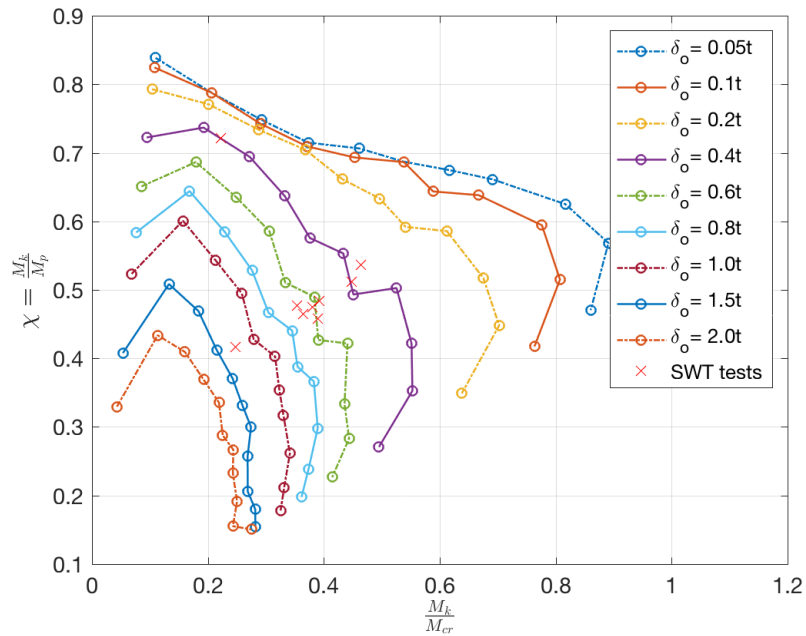


Figure 7.10 Capacity curves of normalized flexural strength of GMNIA models of spirally welded tapered tubes in terms of relative strength.

7.3.6 Validation of the methodology of choosing the parametric model dimensions

Up to this point all the GMNIA models were created with constant diameter, and length, but varied thicknesses to change the slenderness ratio, consequently the absolute value of the imperfection amplitude is not equal within the same curve. This variation of the imperfections amplitude shows some inconsistencies for the GMNIA models with low slenderness. A small test to study the effect of the absolute value of the imperfections amplitude was conducted. This test intended to eliminate the assumption that the curves shape would have changed if we used the same absolute value for the imperfection amplitude. So, within the same curve instead of having a constant diameter and length, and variable thicknesses. A new set of GMNIA models with a constant thickness and variable diameters and lengths, were created with the same slenderness ratio and geometric features as a scaled geometry of the parametric model used in building the RRD curves. The new

GMNIA models were created with constant thickness ($t = 3.2\text{mm}$) and for maximum radius to thickness ratios ($\frac{R_{max}}{t} = 25, 50, 75, 100, 125, 150, 175, 200, 250, 300, \text{ and } 350$), the maximum radius was calculated and the minimum radius was set equal to ($R_{min} = 0.86R_{max}$), and the length of the model was kept at ($L = 8R_{max}$). The new GMNIA models were built with weld depression imperfections, same as before, but only the imperfection amplitudes consistent with Class A, B, and C from EC3-1-6. The new amplitudes for the Classes A, B, and C are $0.25t$, $0.4t$, and $0.625t$ respectively. Fig. 7.11 shows the GMNIA analyses results for the new models with constant absolute value of the imperfections amplitude along each curve (referred to in the plots by δ_{o2}) and the closest curves from the previous GMNIA models with variable absolute value of the imperfections amplitude (referred to in the plot by δ_{o1}). The curve features of the new GMNIA models did not show significant changes although within the elastic-plastic range the results were quite consistent in slope compared to the results from the first set of runs.

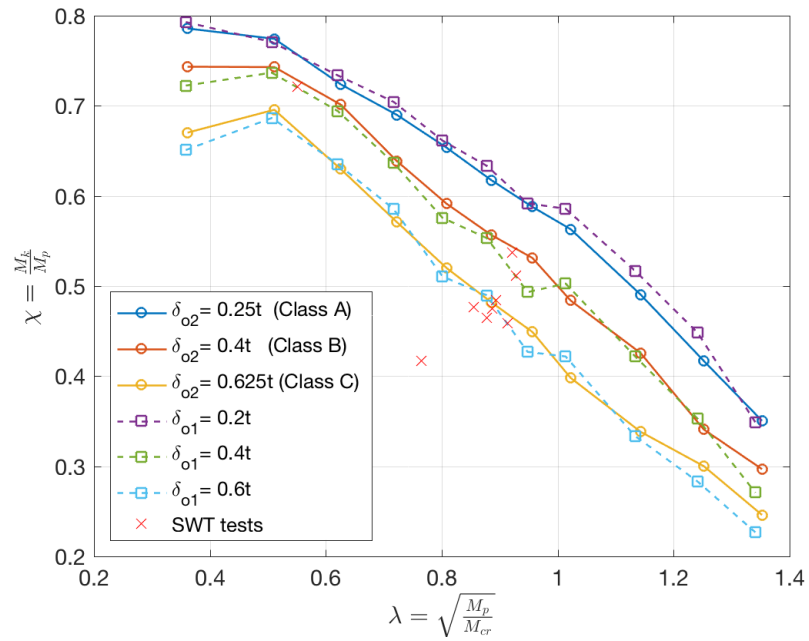


Figure 7.11 Capacity curves in terms of relative slenderness of Set 2 of GMNIA models with imperfections consistent with EC3-1-6 quality classes and the closest curves of Set 1 of GMNIA models and test results.

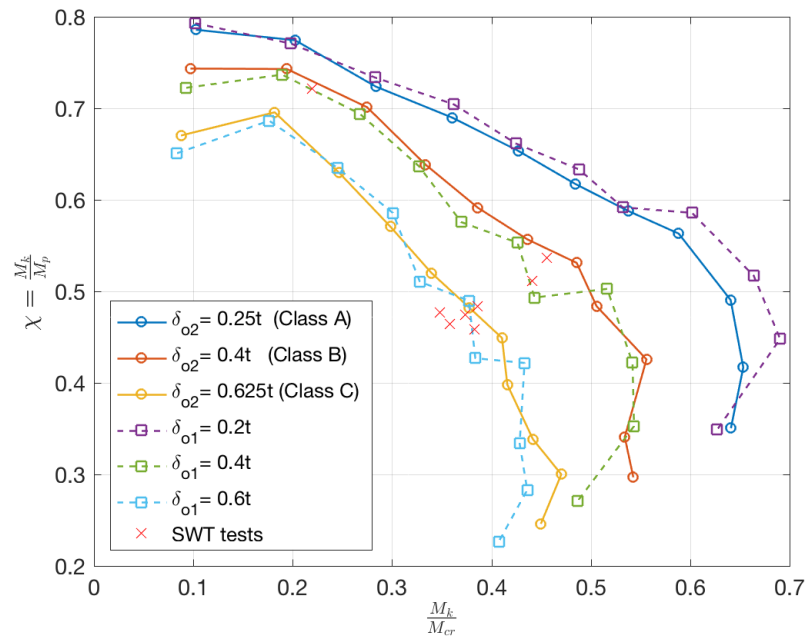


Figure 7.12 Capacity curves in terms of relative strength of Set 2 of GMNIA models with imperfections consistent with EC3-1-6 quality classes and the closest curves of Set 1 of GMNIA models and test results.

We therefore conclude that for a section with constant diameter and length, and varying thickness, or a section with constant length-to-diameter ratio and thickness, and varying diameter, even when imperfections are expressed as a function in thickness, the results are consistent with either approach.

7.4 Fitting RRD parameters for SWT sections

Using the analyses in sec 7.3.5 and 7.3.6, the RRD parameters (α , β , and η) are established to match the RRD curves built with GMNIA results of the SWT parametric models. A small modification to the previously established factors by Chen et al. (2008) to count for the tapering and the spiral weld imperfections, also these curves are lower bound to all test results, see Fig. 7.14.

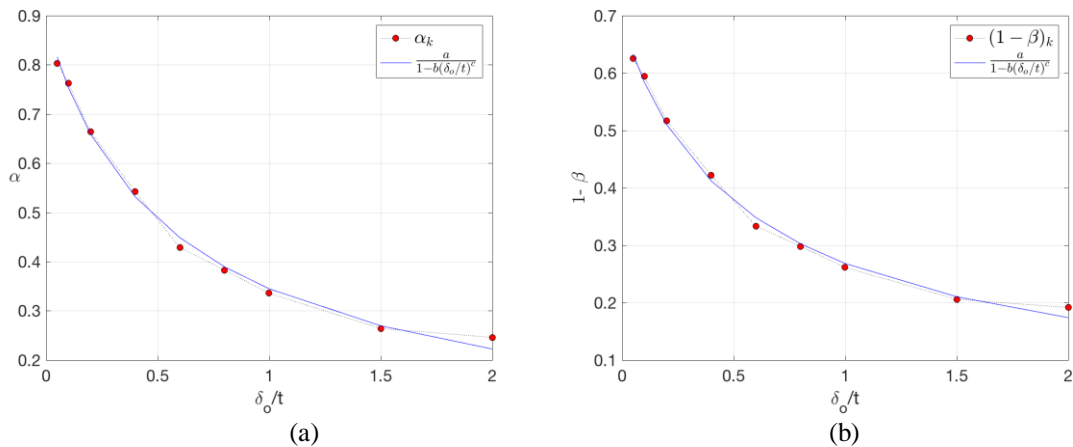


Figure 7.13 RRD curve parameters (a) elastic imperfection reduction factor, and (b) plastic range factor.

The fitted curves of the elastic imperfection reduction factor (α) and the plastic range factor (β), shown in Fig. 7.13 (a) and (b), and the should be computed as:

$$1 - \beta = \frac{0.70}{(1+1.6(\delta_o/t)^{0.92})}, \text{ and } \alpha = \frac{0.90}{(1+1.5(\delta_o/t)^{0.92})}$$

And the best fit to the interaction component to minimize the differences between GMNIA models and the curves, and is computes as:

$$\eta = \frac{0.60}{(1 + 0.1(\delta_o/t)^{2.5})}$$

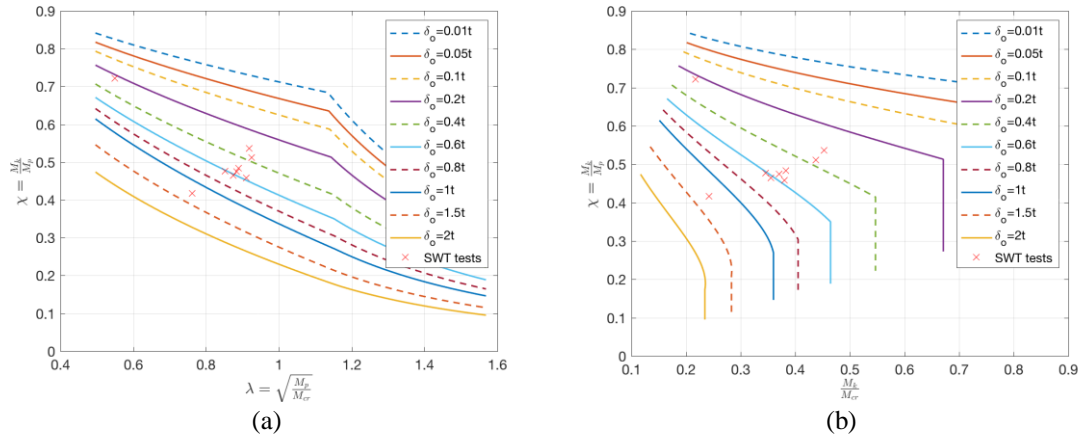


Figure 7.14 Capacity curves of SWT built with updated RRD parameters with SWT tests results against (a) relative slenderness, and (b) relative strength.

7.5 Summary and Conclusions

In this Chapter, the reference resistance design RRD method is discussed and used to create capacity strength curves for SWT sections under bending. An example from literature, Chen et al. (2008), for building the RRD capacity strength curves for prismatic cylindrical shells under bending, was described and checked if could be used for design of SWTs.

The effect of the imperfection patterns on the GMNIA models used in building RRD curves, was discussed and two patterns of imperfections were tested. A new RRD curves were created and verified with SWT tests results and the curve characteristic parameters were established specifically for SWT under bending.

For a specific shell structure under specific loading, RRD curves can be built based on results from verified GMNIA analyses. The RRD curves can be used for design of a shell structure, if the RRD curves were created for a similar shell structure under same loading and boundary conditions. RRD capacity strength curves, permit designers to benefit from the powerful numerical analyses (GMNIA) without going into the sophisticated process of building GMNIA models. Building the RRD curves for SWTs using GMNIA models with 1st eigenmode-affine pattern imperfections, did not show a clear distinction between curves with different amplitudes of this imperfection pattern, it is not recommended to be used for building RRD curves. The GMNIA models with weld depression imperfection pattern, showed consistent results. The GMNIA models with weld depression imperfections pattern, with constant diameter and length, and variable thickness showed consistent results as sections with constant thickness and length-to-diameter ratio, and variable diameter, even with the imperfection pattern is a function in thickness.

The RRD capacity strength curves are used in the design of a full archetype 3 MW wind turbine tower in Chapter 8.

Chapter 8

Design of Archetype 3 MW Wind Turbine Tower

8.1 Wind Turbines load cases

The structural components of the wind turbines (i.e. the tower, the foundation, the base connections and intermediate flanges) are usually designed according to several load cases. These load cases can occur during transportation, construction, normal operation (power production), maintenance, and extreme conditions. The safety factor and type of analysis varies according to the load case. The load cases are determined according to wind conditions in terms of: cut-in wind speed (V_{in}), cut-out wind speed (V_{out}), rated wind speed (V_r), reference wind speed (V_{ref}), and wind speed at hub height (V_{hub}). According to IEC 61400-1:2005 (Design requirement for wind turbines by International Electrotechnical Commission) which is adopted by ASCE/AWEA RP2011 (Recommended Practice for Compliance of Large Land-based Wind Turbine Support Structures), there are 21 load cases grouped into 8 design situations that should all be considered in design as described in Table 9.1.

Table 9.1 Design load cases (IEC 61400-1:2005)

Design Situation	DLC	Wind conditions	Type of analysis	Partial Safety Factor	Other conditions
1. Power production	1.1	NTM $V_{in} < V_{hub} < V_{out}$	U	N	For extrapolation of extreme events
	1.2	NTM $V_{in} < V_{hub} < V_{out}$	F	*	
	1.3	ETM $V_{in} < V_{hub} < V_{out}$	U	N	
	1.4	ECD $V_{hub} = V_r \pm 2.0m/s$ and = V_r	U	N	
	1.5	EWS $V_{in} < V_{hub} < V_{out}$	U	N	
2. Power production plus occurrence of fault	2.1	NTM $V_{in} < V_{hub} < V_{out}$	U	N	Control system fault or loss of electrical network
	2.2	NTM $V_{in} < V_{hub} < V_{out}$	U	A	Protection system or preceding internal electrical fault
	2.3	EOG $V_{hub} = V_r \pm 2.0m/s$ and = V_{out}	U	A	External or internal electrical fault including loss of electrical network
	2.4	NTM $V_{in} < V_{hub} < V_{out}$	F	*	Control, protection, or electrical system faults including loss of electrical network
3) Start up	3.1	NWP $V_{in} < V_{hub} < V_{out}$	F	*	
	3.2	EOG $V_{hub} = V_{in}$ $V_{hub} = V_r \pm 2.0m/s$ and = V_{out}	U	N	
	3.3	EDC $V_{hub} = V_{in}$ $V_{hub} = V_r \pm 2.0m/s$ and = V_{out}	U	N	
4. Normal shut down	4.1	NWP $V_{in} < V_{hub} < V_{out}$	F	*	
	4.2	EOG $V_{hub} = V_r \pm 2.0m/s$ and = V_{out}	U	N	
5. Emergency shut down	5.1	NTM $V_{hub} = V_r \pm 2.0m/s$ and = V_{out}	U	N	
6. Parked (standing still or idling)	6.1	EWM 50-year recurrence period	U	N	
	6.2	EWM 50-year recurrence period	U	A	Loss of electrical network connection
	6.3	EWM 1-year recurrence period	U	N	Extreme yaw misalignment
	6.4	NTM $V_{hub} < 0.7 V_{ref}$	F	*	
7. Parked and fault conditions	7.1	EWM 1-year recurrence period	U	A	
8. Transport, assembly, maintenance and repair	8.1	NTM V_{maint} to be stated by the manufacturer	U	T	
	8.2	EWM 1-year recurrence period	U	A	

where:

DLC	Design load case	$V_r \pm 2m/s$	Sensitivity to all wind speeds in the range should be analyzed
ECD	Extreme coherent gust with direction change		
EDC	Extreme direction change	F	Fatigue
EOG	Extreme operating gust	U	Ultimate strength
EWM	Extreme wind speed	N	Normal
EWS	Extreme wind shear	A	Abnormal
NTM	Normal turbulence model	T	Transport and erection
ETM	Extreme turbulence model	*	Partial safety for fatigue
NWP	Normal wind profile model		

8.2 3 MW 140 m archetype spirally welded wind turbine towers

In this chapter a 3 MW 140 m archetype wind turbine tower is designed using design guides, GMNIA models, and proposed reference resistance design for SWT (RRD-SWT). The tower was originally designed by design team of KTS, and the detailed geometry of the tower sections, sections thicknesses transitions and intermediate flanges were provided to run a design check. Only one load case was provided for design representing the envelope of several load cases for the purpose of design check, the full design of a wind turbine tower is much more complicated and extreme load cases should be considered such as: extreme wind load, seismic load combinations and fatigue loads (ASCE/AWEA 2011). The design assumptions considered are:

- KTS design was intended to meet EC3-1-6 quality Class B specifications.
- The full tower is composed of four SWT sections attached together by three intermediate flanges.
- The SWT sections are made of spirally welded steel plates with constant width 1.8 m and the maximum length of a plate 6 m, the plates thicknesses vary from 23 mm to 12 mm.
- Intermediate flanges are used for practical purposes in construction and they act as intermediate stiffeners, restraining the tower from ovalization buckling modes.
- Only one load case considered here representing an envelope of the operational load cases including weight of mechanical parts, blades, and tower's weight without

considering wind pressure on the body of the tower, the weight of intermediate flanges, and other nonstructural components.

- The yielding stress is taken 450 MPa and Young’s modulus is 200 GPa.

The design provided here is for local buckling due to axial compression and bending only. Fig. 8.1 (a) shows the local coordinate system of the tower where x is the meridional axis and y is the axis in leeward direction. of the loads applied, and their straining actions. The straining actions are shown in Fig. 8.1 (b). The available nominal strengths are calculated according to design guides and specifications, so the load cases considered in the envelope were not factored.

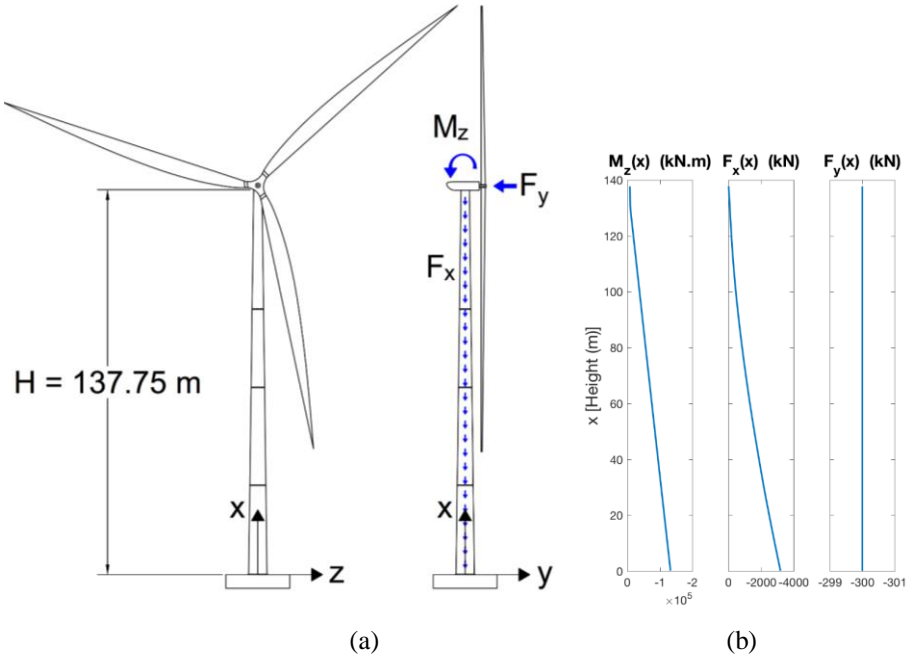


Figure 8.1 (a) Local coordinate system and operational forces directions, and (b) envelope of straining actions.

8.3 Tower geometry

The tower is designed to be composed of four tapered SWTs (SWT-1, SWT-2, SWT-3 and SWT-4) attached together with three intermediate flanges (FL-1, FL-2, and FL-3). The base diameter (maximum diameter) is 6.55m and the top diameter (minimum diameter) is 3 m, and the tapering angle is constant throughout the whole height of the tower 0.74° . The four sections vary in length from 27.91 m to 42.75 m, see Fig. 8.2 (a). The section thickness transitions are shown in Fig. 8.2 (b), two of the sections have only two plate thicknesses SWT-1 and SWT-2, SWT-3 has four plate thicknesses, and SWT-4 has seven plate thicknesses. Since these sections are built with helically oriented plates, there is a transition section where two thicknesses for the two plates are at the same cross section, the elevations provided in Fig. 8.2 (b) is considering the point where the cross section has all shifted to the new thickness (i.e. not counting for the transition sections). The slenderness, in terms of diameter-to-thickness ratio, varies within each section as the diameter and the thickness both change, the maximum slenderness ratio within the tower is 288.3 and the minimum is 214.3, see Fig. 8.2 (c). The geometry of the sections is summarized in Table 8.1 and the geometry of the intermediate flanges is summarized in Table 8.2.

Table 8.1 Summary of the sections geometry.

Section	D_{max} (mm)	D_{min} (mm)	L (m)	t_{max} (mm)	t_{min} (mm)	$\left(\frac{D}{t}\right)_{max}$	$\left(\frac{D}{t}\right)_{min}$
SWT-1	6550	5731	31.71	23	22	284.8	254.4
SWT-2	5731	4828	34.91	22	21	260.5	228.8
SWT-3	4828	4107	27.91	21	18	229.9	218.2
SWT-4	4107	3000	42.75	18	12	288.3	214.3

Table 8.2 Intermediate flanges dimensions.

Intermediate Flange	D (mm)	b (mm)	N_{bolts}
FL-1	5753.3	155	212
FL-2	4849.1	150	180
FL-3	4124.5	140	136

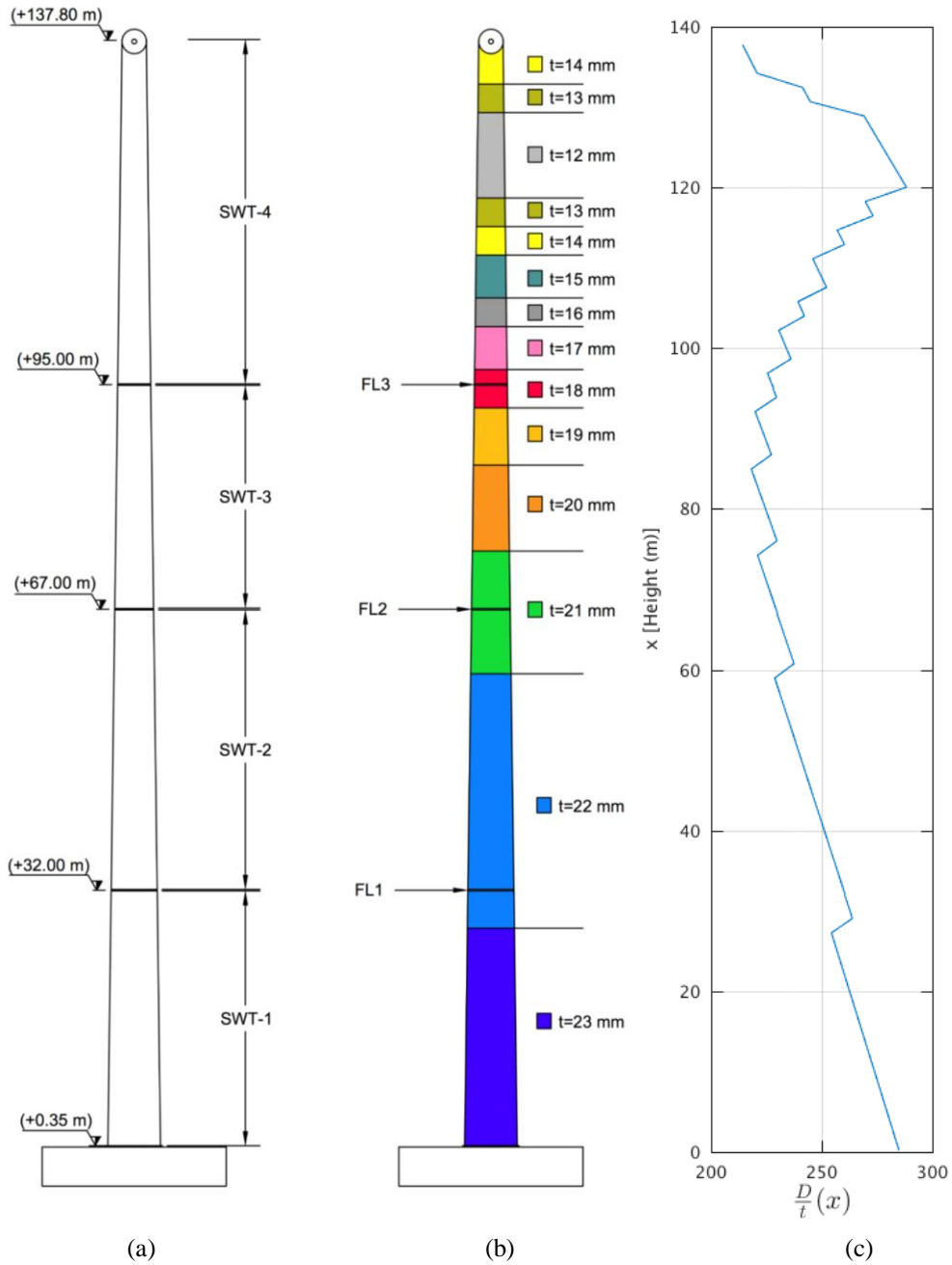
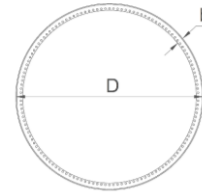


Figure 8.2 (a) SWT sections and elevations, (b) section transitions and location of flanges, and (c) slenderness ratio along the height.

Fig. 8.2 (c) shows that the maximum diameter-to-thickness ratio is located at $x = 120$ m, the same location where the lowest plate thickness is used $t(x = 120) = 12$ mm, although this location is assumed to observe low axial compressive stresses as the moment and axial compression forces are low if compared to thicker sections, the optimal design of the tower requires to have the most efficient section at every location, the applied-to-nominal stress ratios should be close at all locations.

8.4 Design of the sections using hand calculations

To reach optimal design, the designer should follow an iterative process, where his design gets more detailed and more complicated but more efficient with every iteration. For the archetype tower, the designer probably started from a constant thickness prismatic cylinder, then added tapering and checked the stresses along the height and then started varying the thicknesses accordingly. The behavior of tapered sections with variable thickness is much more sophisticated than the prismatic cylinders with constant thickness, and consequently its design is more complicated and predicting the location of critical stresses could be a tricky process. In the EC3-1-6 extended commentary, guidelines for design of truncated cones (tapered cylinders) under meridional compressive stress and for sections with thickness transitions, are provided. However, these guidelines are limited to some types of boundary conditions but does not cover all types. According to EC3-1-6, effective geometry of tapered cylindrical shell should be considered in calculations as follows:

$$R_e(x) = \frac{R(x)}{\cos \alpha} \quad (8.1)$$

$$L_e = \frac{L}{\cos \alpha} \quad (8.2)$$

where $R(x)$ is the radius and $R_e(x)$ is the effective radius at height x , α is the tapering angle, L_e is the effective height and L is the height of one section. The stress design using EC3-1-6 for tapered shells clearly states that the provisions should not be used where any of the boundary conditions is free (in EC3-1-6 this boundary condition is referred to as BC3). The boundary conditions are assumed to be pinned-pinned for all sections for the purpose of a simplified design check.

Using the effective geometry, design guides, and the proposed RRD-SWT, two checks were made for the nominal flexural strength and nominal compressive stresses. The design inputs are used as a function in the height (x) (i.e. $R(x)$ and $t(x)$) and the length is considered as the length of each of the four sections. The design using RRD-SWT curves is not completely valid here as it was only built for SWT sections with constant thickness under bending. As it was discussed in Chapter 7 the RRD curves are unique to a specific shell structure, in RRD-SWT case the thickness transitions were not considered and the combination of axial compression and bending also was not considered in the original study based on the assumption that was made in the beginning of the study.

The first check is for the nominal moments calculated according to the design guides and RRD-SWT and the ratio of the applied moment to nominal moments ($\frac{M_z}{M_n}$) is shown on Fig. 8.3 varying with the height. The check is conducted for EC3-1-6 and RRD-SWT with the three quality classes. For all design guides and RRD-SWT, the whole sections have more nominal flexural capacity than the applied moments except for EC3-1-6 quality Class C, as shown in Fig. 8.3, but that was expected as the tower was intended to be complying with EC3-1-6 Class B.

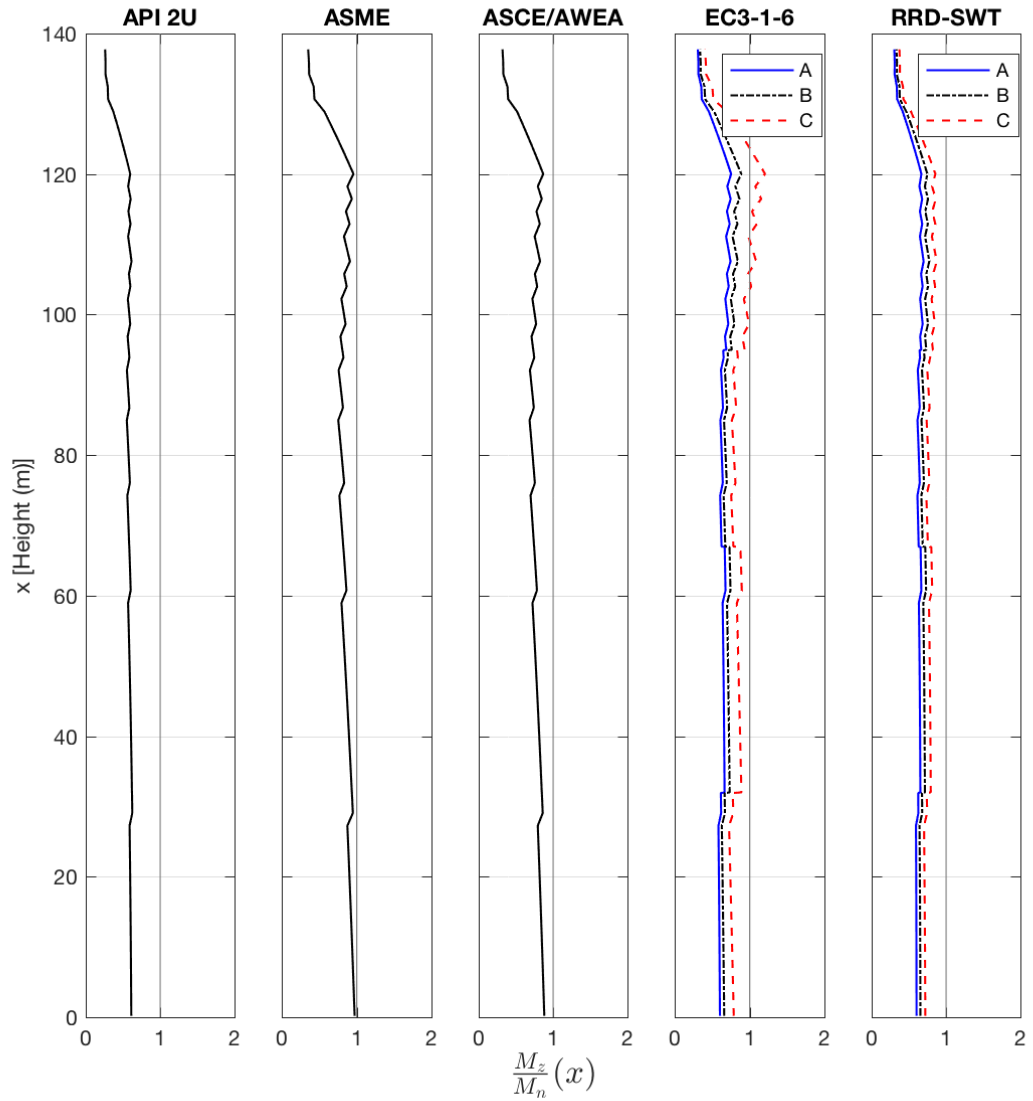


Figure 8.3 The ratio of unfactored applied moment to nominal moment obtained from design guides and proposed RRD-SWT.

The second check is for the nominal compressive stresses considering both the moment and the axial compression where the total stress is calculated:

$$\sigma_x(x) = \frac{F_x(x)}{A(x)} \pm \frac{M_z(x)}{S(x)} \quad (8.3)$$

where $A(x)$ is the cross-section area and $S(x)$ is the section modulus at location x .

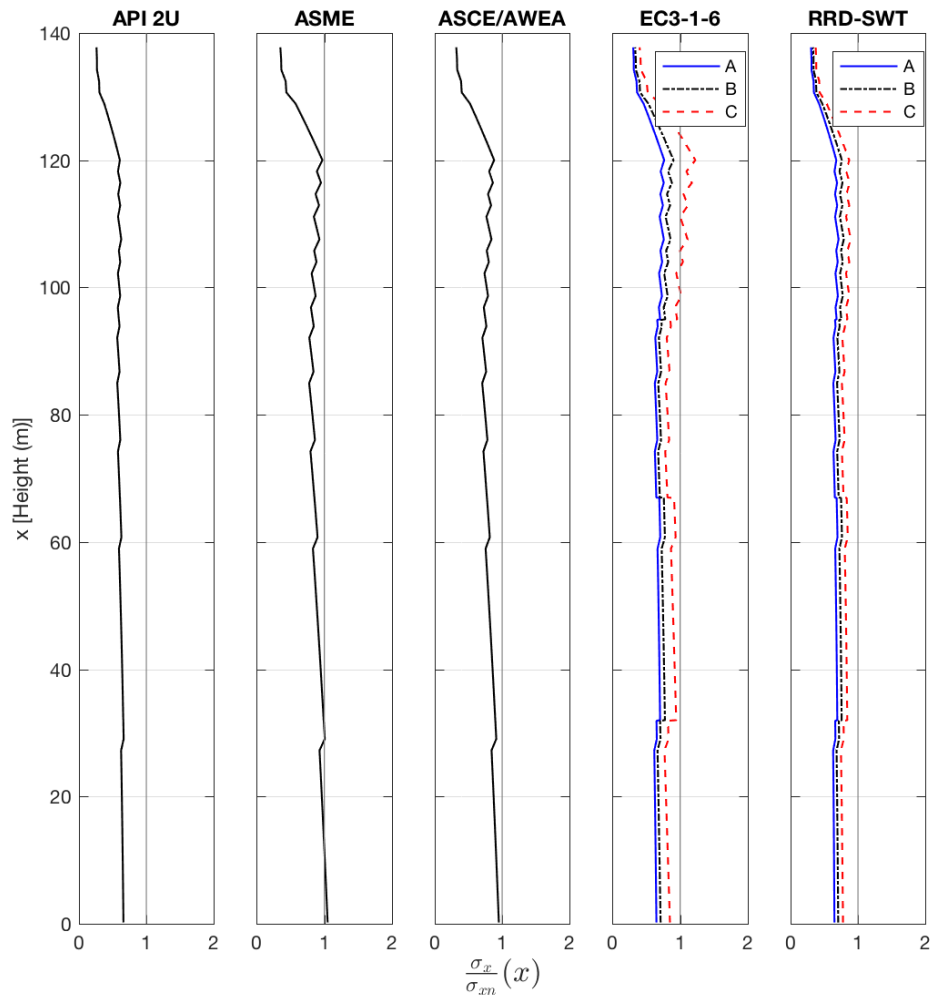


Figure 8.4 The ratio of compressive stress to allowable stress obtained from design guides and proposed RRD-SWT.

The ratio of the applied compressive stress to the nominal compressive stress ($\frac{\sigma_x}{\sigma_{xn}}$) is plotted against the height for design guides and RRD-SWT, see Fig. 8.4. In this case when the axial compression is considered, the required compressive stress was higher than the nominal compressive stress for ASME and EC3-1-6 Class C. However, the load case provided here was an envelope to several load cases which is not a real load case and it is not correct to be used in design from an engineering point of view.

Generally, the API 2U and the proposed RRD are less conservative than the ASME, ASCE/AWEA, and EC3-1-6.

8.5 Design using GMNIA models

Four GMNIA models were built with the exact geometry (maximum and minimum diameters, lengths, plate width, plate orientation, and thickness transitions) for SWT-1, SWT-2, SWT-3, and SWT-4. Equal moments were applied at both ends of the each SWT model to get a constant moment along the section, and the boundary conditions were assumed to be pinned-pinned. The imperfections pattern chosen is the weld depression “Type A” imperfections from Rotter and Teng (1989) and scaled to EC3-1-6 Class B, as described in detail in Chapter 4. It is not clear how to deal with the variable thicknesses in quality class classifications and imperfections implementation, as the imperfections amplitude is a function in thickness, and it is not possible to have the thickness as variable in the imperfection profile function as it will not fit at the plate-to-plate connections (if the two plates have different thicknesses), so a choice has to be made by the designer, one idea is to use the thickness of the thickest plate (as the worst imperfection) or an average thickness for each section, but in these cases the imperfections at the plates with lower thicknesses will be unacceptable according to tolerances and the results will underestimate the strength. Another idea is to use the minimum thickness within each section in the imperfection profile function for the whole section. In this case the tolerance measurement at any location will be complying quality class tolerance limits or higher, and the whole section will be classified as the worst quality from the whole section.

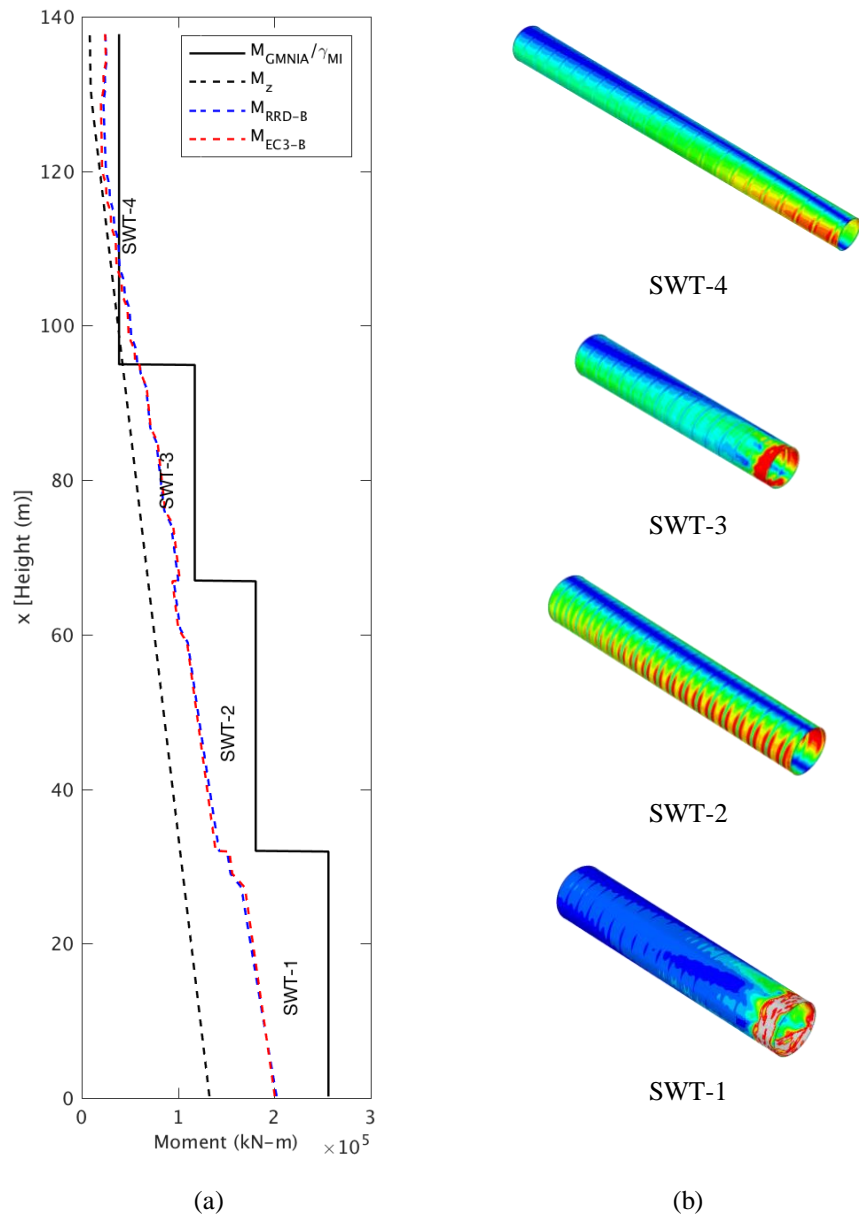


Figure 8.5 (a) Moment strength from GMNIA results vs applied moment, and nominal strengths calculated from EC3-1-6 and RRD Class, and (b) GMNIA von-Mises contour for each section.

The results of GMNIA models are shown in Fig. 8.5, and compared to allowable moments for Class B from RRD and EC3-1-6. The results show that the tower is safe for SWT-1, SWT-2, and SWT-3, but it is unsafe for SWT-4. It might be because the GMNIA models were subjected to equal moments at both ends, which is a rough assumption, but the models

were created to get the bending capacity of the sections the same method as it was done in the whole study. It must be noted that we are treating the section with thickness transitions with a simplified approach, and particularly for a SWT, where the plates are helically oriented, and the thickness is a function in the meridional and circumferential local axes.

8.6 Linear elastic analysis of Full tower model

The perfect geometry of the tower sections and the intermediate flanges were then used to build a full tower model. The SWT models were subjected to concentrated moments at both end and the full tower model was subjected to concentrated moment at the top of the tower, and the boundary conditions at both ends of the SWT models were as pinned-pinned and for the full tower model was fixed only at the bottom. In the full tower model, the sections were connected though the flanges. The results from numerical models for linear elastic analysis LBA(M_{cr-LBA}) the tower sections and compared to the theoretical critical moment ($M_{cr}(x)$), as provided in Eq. 9.4. The results show that the critical moment for the lowest eigen-buckling mode matched perfectly the theoretical analysis, see Fig. 8.6.

$$M_{cr}(x) = \frac{\pi E t^2(x) R(x) \cos(\beta)}{\sqrt{3(1-\nu^2)}} \quad (8.4)$$

The SWT sections were modeled with the exact orientation of the spirally welded plates, with thickness transitions, this could be the reason why the hand calculations do not match the numerical analysis results. Although the elastic flexural buckling strength exactly matched the hand calculations for the full tower model, the location of the buckling was different. In the full tower model, the buckling occurred at a location where a transition between sections with 13 mm and 12 mm thicknesses from the top of the tower side was

present, and again the hand calculations only consider the thickness transition when the full section has the same thickness.

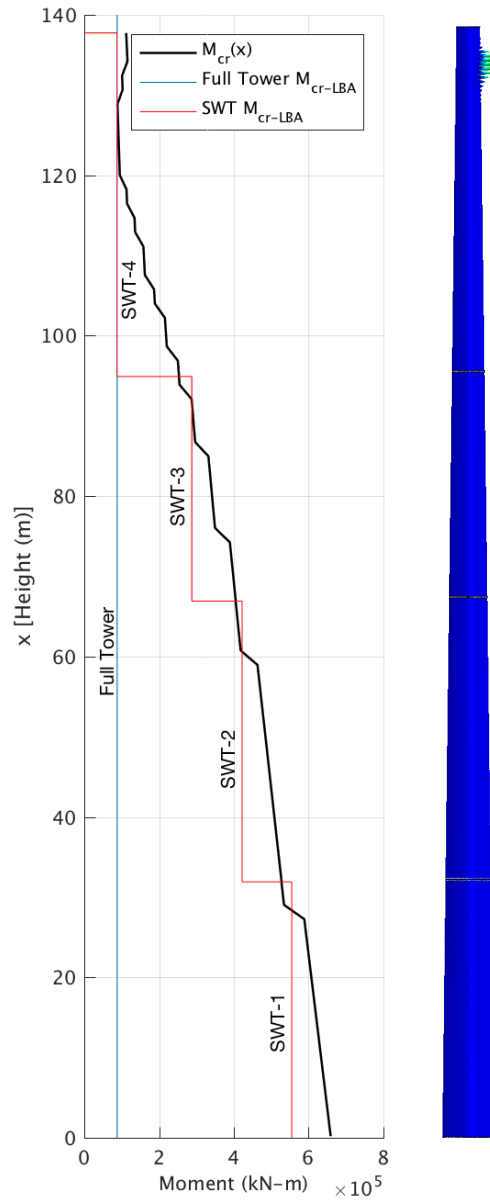


Figure 8.6 LBA results for the full tower and the SWT models compared to critical moment from theoretical calculation and 1st eigen-buckling mode for full tower model.

8.7 Summary and conclusions

Design check for a 3 MW archetype tower composed of four SWT sections with thickness transitions and intermediate stiffeners, was covered using four available design codes and

proposed reference resistance design described in Chapter 7. A comparison between the nominal moments and applied moments was made, where in this case the sections were all safe except for EC3-1-6 Class C. The same check was made for the compressive stress, but with applied axial loads and moments considered. The axial loads increased the compressive stress, such that the design became unsafe according to ASME and ASCE/AWEA, in addition to EC3-1-6 Class C.

Designing a real wind turbine tower require consideration of different load cases, from normal operational condition to extreme conditions. The design using GMNIA models (developed in Chapter 6) and design using RRD curves for SWT sections (developed in Chapter 7), were used for design of the 3 MW archetype wind turbine tower sections with the exact geometry and thickness transitions, and the results were reasonable compared to other design guides and specifications, although the design using GMNIA and RRD were oversimplified. The RRD-SWT design curves (built in Chapter 7) were used for a structure with more geometrical features than the structures they were built for and under combined loading. For the GMNIA design, although the models' boundary condition and loading did not match the real tower, the nominal moments obtained were reasonable for three out of four sections.

Specifications and design guides need to be updated to include the design of different geometries used in practice (in this case tapered shells, shells with thickness transitions) and the design should be related to the quality of the shell structure for more efficient design.

Chapter 9

Summary, Conclusions and Future Work

9.1 Summary

In this research, flexural strength of thin walled spirally welded tapered steel cylindrical shells (SWTs) was studied numerically, and verified against experimental work. Thin walled SWTs are potentially applicable to be used in construction of wind turbine towers to remove a constraint on the diameters used due to transportation limits and allow the industry to use wider range of diameters and thicknesses. The fabrication method was described, and the main geometric features were described for SWT. Classical theoretical solution for stability of thin walled cylindrical shells was summarized and the shifts from prismatic cylinders to tapered cylinders, and from short to long cylinders are discussed. A comparison between four of the available design guides that are applicable to thin walled cylindrical shells was covered. A summary of the experimental work done for cylindrical shells under axial compression and bending from literature was provided, and nine SWT tests conducted by Northeastern University research team and their results were described in detail. The measurements of the imperfections in the nine SWT specimens using high resolution laser scanner and the scans of the specimens during tests to track the development of buckling were described. The measured residual stresses and the proposed equivalent distribution was provided. A discussion was made on the two major approaches for implementing geometric imperfections measured imperfections and generated (or equivalent) imperfections, another implementation of residual stress in GMNIA models based on measurements were described. The effect of the mesh irregularities was studied to decrease their effect on the results of the numerical models, and a meshing guidance was

proposed. Following the mesh guidance and using three geometric imperfections patterns, and the residual stresses, GMNIA models were created for the nine SWT specimens and their results were verified against available test results. The new reference resistance design RRD method was used to build capacity curves for flexural strength of SWTs, using results the 121 GMNIA models with a range of imperfections amplitudes from 1% to 200% of the thickness. Lastly the proposed RRD curves and GMNIA design method were used in design check of an archetype 140 meters 3 MW wind turbine tower composed of four SWT sections.

9.2 Conclusions

The proposed method could efficiently resolve the transportation problem limiting the wind industry. The combination of several geometric aspects (tapering – section transitions - ...etc.) should not be ignored or oversimplified. SWTs have a unique geometry and accurate modeling of such sections requires representation of all geometric features.

It was found that the U.S. design guides are generally more conservative and less detailed if compared to Eurocode 3 (EC3-1-6), which is more descriptive and specific fabrication tolerances are provided to assess shells and assign quality class for the shell, where for each quality class there is a specific curve, we believe that this design method is generally more efficient.

From the SWT experimental work we concluded that the buckling in most of tests occurred at location closer to the smaller end of the SWT specimens, which agrees with theoretical solutions, in the other two specimens the test ended due to fracture in spiral seam weld in the tension side and the other buckled at location closer to larger end of the specimen.

Although the cross-to-spiral seam weld connections did not show a drastic effect on the ultimate strength of SWT specimens if compared to design moments for Class C per EC3-1-6 stress design method, the six specimens (SW-325 and SW-350) which were intended to study the effect of the cross weld location with respect to meridian of maximum compressive stress, it was noted that when the cross weld was placed at angles ($120^\circ - 240^\circ$) from the meridian of the maximum compressive stress the strength of the specimens with same diameter-to-thickness ratio increased.

The buckling was initiated at locations following spiral seam weld imperfections and the pattern of the buckling waves seems to follow the helical orientation of the plates.

Fatigue tests showed that the calculated detail category and CAFL recommended by EC3-1-9 for intersecting welds, is much lower than detail category and CAFL obtained from tests, and Jay (2017) recommended using at least DC=90 (as single double sided CJP butt weld).

Although thin-walled shells are extremely sensitive to imperfections, and the buckling and post buckling behavior are driven by initial geometric imperfections, for shells under bending, imperfections only matter in the compression side of the cross sections, but the buckling could be triggered by an imperfection that is less severe than the worst imperfection, if the compressive stress was higher at the less severe imperfection. Imperfections due to dimples usually control the design of circular shells under compressive stress (where failure occurs due to local buckling modes). There is no clear way on how to measure imperfections on tapered sections or sections with thickness

transitions, for the scope of this study (SWT project) thicknesses were constant and average radius was used for the gauge lengths.

High resolution scanners were used in measuring real imperfections and the analysis of the scanned geometry can be used for tolerances measurements and further investigation of the relation of imperfections and stresses to buckling. However, due to the way that the laser scanning rig was designed and the clamping, there was some influence on the scans, particularly in the early specimens. Since we only care for local buckling of medium length cylindrical shells under compressive stress, only the local dimples (with much shorter half-wavelengths than the imperfections caused by the scanning rig) affect the strength, the measured imperfections can be used as real imperfections to be implemented in GMNIA models. Generated imperfections in terms of chosen patterns and amplitudes, should be carefully chosen to get a good prediction of the shell strength.

The mesh sensitivity analyses for SWT models demonstrate that, for mesh inclination angles less than 10° , a model meshed with the S4R element with a 1:1 aspect ratio provided satisfactory performance if the mesh size is limited to $0.5\sqrt{R_{avg}t}$ and for inclination angles larger than 10° , a finer mesh ($\leq 0.25\sqrt{R_{avg}t}$) is needed for satisfactory performance.

The modeling protocol concluded from the mesh sensitivity analysis is also valid for nonlinear collapse analyses such as GMNIA models. The modeling protocol has been intentionally constructed to be convenient for designers to use, with meshing characteristics that are easily obtained in commercial finite element software such as ABAQUS and imperfection patterns, which are easily obtained and modeled.

The SWT GMNIA models were created with both generated measured imperfections and in general the results for all the GMNIA models with the same quality class imperfections as the tests or measured imperfections, were reasonable if compared with available SWT test results. It was noticed that the usage of the weld depression along with Eurocode 3 (EC3-1-6) recommendations for the amplitudes for each quality class is more nuanced than the 1st eigenmode-affine pattern.

The results of Class C GMNIA models with both patterns of generated imperfections were quite reasonable compared to test data.

The implementation of the real measured imperfections could be more accurate if treated carefully, considering the mesh density used and the orientation with respect to realistic loading and boundary conditions. However, it is not always a feasible or practical method when dealing with real full-scale structure design.

The implementation of the residual stresses in this case did not show much effect on the strength and the stiffness of model which confirms the original assumption that initial geometrical imperfections are more dominant in severing the shell strength and stiffness.

Using the validated GMNIA models and the available guidelines for building the capacity strength curves (RRD) for a specific shell structure under specific loading, RRD curves were built. RRD capacity strength curves, permit designers to benefit from the powerful numerical analyses (GMNIA) without going into the sophisticated process of building GMNIA models. Building the RRD curves for SWTs using GMNIA models with 1st eigenmode-affine pattern imperfections, did not show a clear distinction between curves with different amplitudes of this imperfection pattern, this form of imperfections is not

recommended to be used for building RRD curves. The GMNIA models with weld depression imperfection pattern, showed consistent results.

The GMNIA models with weld depression imperfections pattern, with constant diameter and length, and variable thickness showed consistent results as sections with constant thickness and length-to-diameter ratio, and variable diameter, even with the imperfection pattern is a function in thickness.

Designing a real wind turbine tower require consideration of different load cases, from normal operational condition to extreme conditions. The design using GMNIA models (developed in Chapter 6) and design using RRD curves for SWT sections (developed in Chapter 7), were used for design of the 3 MW archetype wind turbine tower sections with the exact geometry and thickness transitions, and the results were reasonable compared to other design guides and specifications, although the design using GMNIA and RRD were oversimplified. The RRD-SWT design curves (built in Chapter 7) were used for a structure with more geometrical features than the structures they were built for and under combined loading. For the GMNIA design, although the models' boundary condition and loading did not match the real tower, the nominal moments obtained were reasonable for three out of four sections.

Specifications and design guides need to be updated to include the design of different geometries used in practice (in this case tapered shells, shells with thickness transitions) and the design should be related to the quality of the shell structure for more efficient design.

9.3 Future Work

This dissertation provided numerical modeling and design guidelines for spirally welded tapered tube under flexural bending. Aiming to enable this technique to be used in construction of wind turbine towers; however, some of the points still need more investigations and some of the problems discussed in the thesis should be researched.

More SWT specimens should be scanned with careful handling of the clamping and a modification to the scanning rig need to be designed to support the specimens without influencing the imperfections to get more reliable data on the imperfections induced by the manufacturing process.

The error resulting from the mesh layout (models with helical meshes with angles larger than 10°), should be investigated in the future for ABAQUS and other finite element software packages.

KTS according to the findings of this research project decided to change their fabrication process to avoid having the 4-way cross-to-spiral seam weld connections, see Fig. 9.1, the new geometry introduce new imperfection patterns these patterns should be studied and investigated experimentally and analytically.

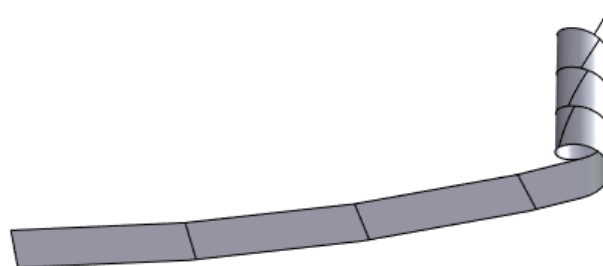


Figure 9.1 New fabrication method of SWT with staggered cross weld (provided by KTS).

The study should be expanded to full scale wind turbine towers with real load cases and the effect of other features should be studied such as: the intermediate flanges, openings, base connections, stiffeners.... etc.

The study of SWT sections under combined axial compression and bending and the effect of section transitions should be studied, and the design methods proposed in this thesis should be verified or modified to fit the new structures.

For future work a more focused study should be conducted on shell design guides and specifications and a detailed evaluation for designing wind turbine towers should be provided.

References

1. Abell, M. (2013) “Thin vs Thick shells”, CSI Knowledgebase.
2. Agbayani, N., Vega, R. E., Newell, J. (2011) “Unresolved US Code Compliance Issues for Wind Energy Structures: The Need for Research” Structure Congress 2011 Reston, VA.
3. Altenbach, H., Eremeyev, V. (2017) “Shell-like Structures: Advanced Theories and Applications” CISM International Centre for Mechanical Sciences.
4. Almroth, B.O. (1965) “Influence of Edge Conditions on the Stability of Axially Compressed Cylindrical Shells”, NASA CR-161.
5. American Bureau of Shipping (ABS) (2004) “Guide for Buckling and Ultimate Strength Assessment for Offshore Structures”.
6. American Petroleum Institute (API) (2004) “API-RP 2A: Recommended Practice for Planning, Designing, and Constructing Fixed Offshore Platforms”.
7. American Petroleum Institute (API) (2000) “API Bull. 2U: Bulletin on Stability Design of Cylindrical Shells”.
8. American Society for Civil Engineers and American Wind Energy Association ASCE/AWEA (2011) “Recommended Practice for Compliance of Large Land-based Wind Turbine Support Structures”.
9. American Society of Mechanical Engineers (ASME) “ASME STS-1: Steel Stacks”.
10. American Wind Energy Association AWEA (2017) “U.S. Wind Industry Second Quarter 2017 Market Report”. AWEA Data Services.
11. Apt, J., Jaramillo, P., Stine D. D. (2013) “Managing Variable Energy Resources to Increase Renewable Electricity’s Contribution to the Grid”, Scott Institute for energy innovation, Carnegie Mellon University.
12. Arbocz, J. (1968) “The effect of general imperfections on the buckling of cylindrical shells”. PhD thesis, California Institute of Technology.

13. Arbocz, J., Abramovich, H. (1979) "The initial imperfection data bank at the Delft University of Technology, Part I. Technical Report LR-290", Faculty of Aerospace Engineering, Delft University of Technology, Delft, The Netherlands.
14. Aslani, F., Uy, B., Hicks, S. J., Kang, W.H. (2015) "Spiral Welded Tubes – Imperfections, Residual Stresses, and Buckling Characteristics" Eighth International Conference on Advances in Steel Structures, Lisbon, Portugal.
15. Burton, T., Jenkins, N., Sharpe D., Bossanyi, E. (2011) "Wind Energy Handbook, Second Edition", John Wiley & Sons.
16. Calladine, C.R. (1983). "Theory of shell structures". Cambridge University Press.
17. Chen, L. (2011) "Buckling of Circular Steel Cylindrical Shells under Different Loading Conditions" PhD Thesis, The University of Edinburgh.
18. Chen, L., Doerich, C., Rotter, J. M. (2011) A study of cylindrical shells under global bending in the elastic-plastic range", *Steel Construction*, 1, 59–65.
19. Chen, L., Rotter, J. M., Doerich, C. (2011) "Buckling of Cylindrical Shells with Stepwise Variable Wall Thickness Under Uniform External Pressure", *Engineering Structures*, 33, 3570-3578.
20. Cotrell, J., Stehly, T., Johnson, J., Roberts, J. O., Parker, Z., Scott, G., Heimiller, D. (2014) "Analysis of Transportation and Logistics Challenges Affecting the Deployment of Larger Wind Turbines: Summary of Results". Technical Report NREL/TP-5000-61063.
21. Doerich, C. (2007) "Strength and Stability of Locally Supported Cylinders", Ph.D. Thesis, University of Edinburgh, Scotland.
22. European Committee for Standardization (CEN) (2007) "Eurocode 3 Design of steel structures Part 1-6: Strength and Stability of Shell Structures".
23. European Committee for Standardization (CEN) (2005) "Eurocode 3 Design of steel structures Part 1-9: Fatigue".
24. Gettel, M., Schneider, W. (2007) "Buckling strength verification of cantilevered cylindrical shells subjected to transverse load using Eurocode 3", *Journal of Constructional Steel Research*.
25. Guo, L., Yang, S., Jiao, H. (2013) "Behavior of Thin-walled Circular Hollow Section Tubes Subjected to Bending", *Thin-Walled Structures*, 73. 281-289.

26. Hallai, J., Kyriakides, S. (2011) "On the effect of Lüders bands on the bending of steel tubes. Part I: Experiments". *International Journal of Solids and Structures*, 48, 752-762.
27. Hanada, M, Takeda, H., Fukushima, H. (1986) "Development of High Speed Submerged Arc Welding in Spiral Pipe Mill" *Transactions of the Iron and Steel Institute of Japan* vol. 26
28. Harris, L. A., Suer, H. S., Skene, W. T., Benjamin, R. J. (1957) "The Stability of Thin-Walled Unstiffened Circular Cylinders Under Axial Compression Including the Effects of Internal Pressure," *J. Aeronaut. Sci.*, 24, 587-596.
29. Heyman, J. (1977) "Equilibrium of shell structures". Oxford University Press.
30. Hoff, N.J., Soong, T.C. (1965) "Buckling of Circular Cylindrical Shells in Axial Compression", *International Journal of Mechanical Sciences*, 7, 489-520.
31. Holst J.M., Rotter J.M., Calladine C. R. (2000) "Imperfections and buckling in cylindrical shells with consistent residual stresses" *Journal of Constructional Steel Research* 54, 265-282.
32. Hübner, A., Teng, J. G., Saal, H. (2006) "Buckling behaviour of large steel cylinders with patterned welds". *International Journal of Pressure Vessels and Piping* 83, 13-26.
33. Hutchinson, J. W. (1971) "Effect of a local axisymmetric imperfection on the buckling behavior of a circular cylindrical shell under axial compression", *AIAA journal* Vol. 9, 48-52
34. Jamal, M., Lahlou, L., Midani, M., Zahrouni, H., Limam, A., Damil, N., Potier-Ferry, M. (2003) "A semi-analytical buckling analysis of imperfect cylindrical shells under axial compression", *Int. J. Solids Struct.*, 40, 1311-1327.
35. Jansseune, A., De Corte, W., Belis, J. (2016) "Imperfection sensitivity of locally supported cylindrical Silos subjected to uniform axial compression" *International Journal of Solids and Structures* 96, 92-109
36. Jay, A., Myers, A. T. (2014) "Imperfection Analysis and Optimized Design of Tapered Spirally-welded Wind Turbine Towers". *Proceedings of the Annual Stability Conference SSRC'14*, Toronto-Canada.
37. Jay, A., Myers, A.T., Torabian, S., Mahmoud, A., Smith, E., Agbayani, N., Schafer, B.W. (2016a) "Spirally Welded Steel Wind Towers: Buckling Experiments, Analyses, and Research Needs". *J. Constructional Steel Research* 125, 218-226.

38. Jay, A., Myers, A.T., Mirzaie, F., Mahmoud, A., Torabian, S., Smith, E., Schafer, B.W. (2016b) "Large Scale Bending Tests of Slender, Tapered, Spirally Welded Steel Tubes", J. Structural Engineering. 142(12)
39. Jay, A., Torabian, S., Mahmoud, A., Myers, A. T., Schafer, B.W., Smith E. (2015) "Static Flexural Local Buckling Tests on Large Scale Spirally Welded Tubes for use as Wind Turbine Towers". Structures Congress 2015, Portland-Oregon, USA.
40. Jay, A. (2017) "Experimental Investigation of The Local Buckling and Fatigue Behavior of Slender and Tapered Spirally Welded Steel Tubes to Enable Taller Wind Towers", PhD thesis Northeastern University, Boston, Massachusetts.
1. Koiter, W.T. (1963) "The effect of axisymmetric imperfections on the buckling of cylindrical shells under axial compression". In Proceedings Koninklijke Ned. Akad. Wetenschap, volume 66.
41. Limam, A., El Bahaoui, J., Khamlichi, A., El Bakkali, L. (2011) "Effect of multiple localized geometric imperfections on stability of thin axisymmetric cylindrical shells under axial compression", Int. J. Solids Struct., 48, 1034-1043.
42. Linscott, S. B., Perkins, P., Dennett, J. (1984) "Large, Horizontal-Axis Wind Turbines" DOE/NASA 20320-58.
43. Mahmoud, A., Torabian, S., Jay, A., Myers, A. T., Smith, E., Schafer, B. W. (2015) "Modeling protocols for elastic buckling and collapse analysis of spirally welded circular hollow thin-walled sections" Proceedings of the Annual Stability conference, SSRC'15, Nashville-Tennessee, USA.
44. Mahmoud, A., Torabian, S., Jay, A., Mirzaie, F., Myers, A. T., Smith, E., Schafer, B. W. (2016) "Collapse Analyses on Spirally Welded Tapered Tubes using EC3 Generated Imperfections" Proceedings of the Annual Stability conference, SSRC'16, Orlando-Florida, USA.
45. Mahmoud, A., Mirzaie, F., Torabian, S., Jay, A., Myers, A. T., Smith, E., Schafer, B. W. (2016) "Collapse Analysis of Spirally Welded Tapered Tubes under Flexural Moments using Measured and Generated Imperfections". Proceedings of the 7th International Conference on Coupled Instabilities in Metal Structures. Baltimore-Maryland, USA.

46. Mahmoud, A., Torabian, S., Jay, A., Mirzaie, F., Myers, A. T., Smith, E., Schafer, B. W. (2017) "Modeling the Flexural Collapse of Thin-Walled Spirally Welded Tapered Tubes" J. Structural Engineering.
47. Nussbaumer, A., Borges, L., Davaine, L. (2011) "Fatigue Design of Steel and Composite Structures" ECCS - European Convention for Constructional Steelwork.
48. Pircher, M., Berry, P.A., Ding, X., Bridge, R. Q. (2001) "The shape of circumferential weld-induced imperfections in thin-walled steel silos and tanks" Thin-Walled Structures, 39. 999-1014.
49. Pueppke, N. B. (2014) "Buckling behaviour of spirally welded steel tubes" Master of Science Thesis TU Delft. Rotter, J. M., Teng, J. G. (1989) "Elastic Stability of Cylindrical Shells with Weld Depressions", Journal of Structural Engineering, 115(5). 1244-1263.
50. Righter, R. W. (1996) "Wind Energy in America: A History". University of Oklahoma Press.
51. Rotter J.M. (1996) "Elastic plastic buckling and collapse in internally pressurised axially compressed silo cylinders with measured axisymmetric imperfections: interactions between imperfections, residual stresses, and collapse. In: Proceedings of the International Workshop on Imperfections in Metal Silos: Measurement, Characterisation, and Strength Analysis" ECCS 1996.
52. Rotter, J. M. (1998) "Shell structures: the new European standard and current research needs" Thin-Walled Structures 31, 3-23.
53. Rotter, J. M., Schmidt, H. (2013) "Buckling of Steel Shells European Design Recommendations – 5th Edition" ECCS - European Convention for Constructional Steelwork.
54. Rotter, J.M. (2011) "The New Framework for Shell Buckling Design and the European Shell Buckling Recommendations Fifth Edition", Journal of Pressure Vessel Technology, Vol. 133, 011203-(1-9).
55. Rotter, J.M., Sadowski A.J., Chen L. (2014) "Nonlinear stability of thin elastic cylinders of different length under global bending". International journal of solids and structures, 51, 2826-2839.
56. Rotter, J.M., Al-Lawati, H. (2016) "Length effects in the buckling of imperfect axially compressed cylinders" The International Colloquium on Stability and Ductility of Steel Structures, Timisoara, Romania.

57. Rotter, J. M. (2016) "The New Method for Reference Resistance Design for Shell Structure" The International Colloquium on Stability and Ductility of Steel Structures, Timisoara, Romania.
58. Sadowski, A. J., Van Es, S.H.J., Reinke, T., Rotter, J. M., (Nol) Gresnigt, A. M., Ummenhofer, T. (2015) "Harmonic analysis of measured initial geometric imperfections in large spiral welded carbon steel tubes". *Engineering Structures*, vol. 85, 234-248.
59. Sadowski, A. J., Rotter, J. M. (2014) "Modeling and behaviour of cylindrical shell structures with helical features". *Computers and Structures*, 133. 90-102.
60. Sadowski, A. J., Rotter, J. M. (2014) "Solid or shell finite elements to model thick cylindrical tubes and shells under global bending". *International Journal of Mechanical Sciences*, 74. 143-153.
61. Sadowski, A. J., Rotter, J. M. (2013)". On the relationship between mesh and stress field orientations in linear stability analyses of thin plates and shells". *Finite Elements in Analysis and Design*, 73. 42-54.
62. Schmidt, H., Krysiak, R. (1994) "Static Strength of Transition Cones in Tubular Members under Axial Compression and Internal Pressure", *Proceedings of 6th International Symposium for Tubular Structures*, Melbourne, Australia.
63. Schafer, B.W., Li, Z., Moen, C.D. (2010) "Computational modeling of cold-formed steel"., *Thin-Walled Structures*, 48. 752-762.
64. Schneider, W., Brede, A. (2005) "Stimulating Equivalent Geometric Imperfections for the Numerical Buckling Strength Verification of Axially Compressed Cylindrical Steel Shells", *Thin-Walled Structures* vol. 37, issue 6, 530-536.
65. Schmidt, H. (2000) "Stability of steel shell structures: General Report", *J. Constr. Steel. Res.*, 55, 159-181.
66. Seide, P. (1956) "Axisymmetric Buckling of Circular Cones Under Axial Compression". *Journal of Applied Mechanics*, 23.625-628.
67. Seide, P., Weingarten, V.I. (1961) "On the Buckling of Circular Cylindrical Shells Under Pure Bending", *Journal of Applied Mechanics*, vol. 28-1, 112-116.

68. Sim H.B., Prowell I., Elgamal A., Uang C.M. (2014) "Flexural tests and associated study of a full-scale 65-kW wind turbine tower", *J. Struct. Eng.*, 140 (5).
69. Simulia (2014) "ABAQUS manual 6.14-5". Dassault Systèmes Simulia Corp.
70. Singer, J., Arbocz, J., & Weller, T. (2002). *Buckling Experiments: Experimental Methods in Buckling of Thin-Walled Structures Vol. 1 & 2*". New York: John Wiley & Sons, Inc.
71. Teng J.G., Rotter J.M. (1989) "Elastic-plastic large deflection analysis of axisymmetric shells" *Computers and Structures*, 31(2), 211-233.
72. Teng, J. G., Rotter J. M. (2004) "Buckling of Thin Metal Shells", Spon Press, London, pp. 42-87.
73. Timoshenko, S. (1953) "History of Strength of Materials", McGraw-Hill Book Company.
74. Timoshenko, S., Gere, J. M. (1961) "Theory of Elastic Stability. Second edition."
75. Van, Es S. H. J., Gresnigt, A. M., Vasilikis, D., Karamanos, S. A. (2016) "Ultimate bending capacity of spiral- welded steel tubes – Part I: Experiments". *Thin-Walled Structures* 102, 286-304.
76. Vasilikis, D., Karamanos, S., A., van Es, S. H. J., Gresnigt, A. M., (2016) "Ultimate bending capacity of spiral-welded steel tubes – Part II: Predictions". *Thin-Walled Structures*, 102. 305-319.
77. Vasilikis, D., Karamanos, S., van Es, S., & Gresnigt, A. (2015). *Ultimate Bending Capacity of Spirally-Welded Steel Tubes - Part II: Predictions*. *Thin-Walled Structures*.
78. Yamaki, N. (1984) "Elastic stability of Circular Cylindrical Shells", *North Holland Series in Applied Mathematics and Mechanics*, volume 27.
79. Yu, C.L., Chen, Z. P., Wang, J., Yan, S.J., Yang L. C. (2012) "Effect of weld reinforcement on axial plastic buckling of welded steel cylindrical shells", *Journal of Zhejiang University Science A*, 13-2, 79-90.

Appendix A

Geometry Builder

Note: Some of the functions are confidential and are property of KTS.

The geometry is built using a set of functions that creates the geometry of the trapezoidal plates and roll them into the full spirally welded tapered tube.

Inputs: (original-Code by KTS)

- 7- Base diameter
- 8- Top diameter
- 9- Thickness
- 10- Height
- 11- Maximum width of the plates (strip width)
- 12- Maximum length of the plates

Inputs: (added by JHU team)

- 1- Load (C: compression, M: moment)
- 2- Type of the run (buckling, static Riks-Lanczos, static Riks-subspace)
- 3- Element Type ('S4R', 'S4', 'S9R5', 'S8R')
- 4- Material Properties (True Stress- Strain curve)
- 5- Imperfection (out-of-roundness, dimple, accidental eccentricity, 1st eigenmode-affine pattern, weld depression)
- 6- For the MI models (point cloud data file)

ABAQUS input creator

```
function abaqus_inp_riks_res(jobname,ts,ETYPE,Load_type,mat,Data)
%UNTITLED Summary of this function goes here
% Detailed explanation goes here

E=mat.E;
Nu=mat.Nu;
PL=mat.PL;
number_of_int_points=31;
bending_stress_circ=5; %check zones in RSS3.DWG for residual stresses on
a trapezoidal
bending_stress_long=[20 2.5];
membrane_stress_circ=PL(1,1)*[0.25 0.5];
membrane_stress_long=[-5 10];
nodes=Data.Nodes;
elements=Data.Elements;
```



```

Dt=Data.Dtop;
Top_Nodes=Data.Top_Nodes;
phi=Data.phi;
Bottom_Nodes =Data.Bottom_Nodes;
EL_W=Data.EL_W;
RSS_elements=Data.RSS_elements;
h=Data.H;

cd(['INP_' date]);
%fileID=fopen([jobname, '_',AR, '.inp'],'w');
fileID=fopen([jobname, '.inp'],'w');
fprintf(fileID, '*Heading\n');
fprintf(fileID, ' %s\n', jobname);
fprintf(fileID, '** Job name: %s\n', jobname);
fprintf(fileID, '** Generated by: Abaqus/CAE 6.12-3\n');
fprintf(fileID, '*Preprint, echo=NO, model=NO, history=NO, contact=NO\n');
fprintf(fileID, '**\n');
fprintf(fileID, '** PARTS\n');
fprintf(fileID, '**\n');
fprintf(fileID, '*Part, name=Part1\n');

%% Node & Element Generation
fprintf(fileID, '*Node\n');
fprintf(fileID, '%7d, %12f, %12f, %12f\n', nodes');
if strcmp(ETYPE, 'S4R')==1
    fprintf(fileID, '*Element, type=%s\n', ETYPE);
    fprintf(fileID, '%7d, %7d, %7d, %7d, %7d\n', elements');
elseif strcmp(ETYPE, 'S9R5')==1
    fprintf(fileID, '*Element, type=%s\n', ETYPE);
    fprintf(fileID, '%7d, %7d, %7d, %7d, %7d, %7d, %7d, %7d, %7d,
%7d\n', elements');
elseif strcmp(ETYPE, 'S4')==1
    fprintf(fileID, '*Element, type=%s\n', ETYPE);
    fprintf(fileID, '%7d, %7d, %7d, %7d, %7d\n', elements');
elseif strcmp(ETYPE, 'S8R')==1
    fprintf(fileID, '*Element, type=%s\n', ETYPE);
    fprintf(fileID, '%7d, %7d, %7d, %7d, %7d, %7d, %7d, %7d,
%7d\n', elements');
end
%% Nodes Sets
NN = length(nodes);
fprintf(fileID, '*NSET, NSET=ALL_Nodes, GENERATE\n');
fprintf(fileID, '%7d, %7d, %7d\n', 1, NN, 1);
fprintf(fileID, '*Nset, nset=Cross_Weld_nodes\n');
fprintf(fileID, '%7d, %7d, %7d, %7d\n', Data.cross_w');
fprintf(fileID, '\n');
fprintf(fileID, '*Nset, nset=Spiral_Weld_nodes\n');
fprintf(fileID, '%7d, %7d, %7d, %7d\n', Data.spiral_w');
fprintf(fileID, '\n');
fprintf(fileID, '*Nset, nset=rest_of_the_nodes\n');
fprintf(fileID, '%7d, %7d, %7d, %7d\n', Data.rest_of_the_nodes');
fprintf(fileID, '\n');

%% Elements Sets
NE = length(elements);
fprintf(fileID, '*ELSET, ELSET=ALL_Elements, GENERATE\n');
fprintf(fileID, '%7d, %7d, %7d\n', 1, NE, 1);
fprintf(fileID, '*ELSET, elset=Weld_elements\n');
fprintf(fileID, '%7d, %7d, %7d, %7d\n', EL_W');
fprintf(fileID, '\n');
fprintf(fileID, '*ELSET, elset=weld_elements_1\n');
fprintf(fileID, '%7d, %7d, %7d, %7d\n', find(RSS_elements==1));

```

```

fprintf(fileID, '\n');
fprintf(fileID, '*ELSET, elset=weld_elements_2\n');
fprintf(fileID, '%7d, %7d, %7d, %7d\n', find(RSS_elements==2));
fprintf(fileID, '\n');
fprintf(fileID, '*ELSET, elset=Inplate_elements_3\n');
fprintf(fileID, '%7d, %7d, %7d, %7d\n', find(RSS_elements==3));
fprintf(fileID, '\n');
fprintf(fileID, '*ELSET, elset=weld_elements_4\n');
fprintf(fileID, '%7d, %7d, %7d, %7d\n', find(RSS_elements==4));
fprintf(fileID, '\n');
fprintf(fileID, '*ELSET, elset=weld_elements_5\n');
fprintf(fileID, '%7d, %7d, %7d, %7d\n', find(RSS_elements==5));
fprintf(fileID, '\n');
fprintf(fileID, '*ELSET, elset=weld_elements_6\n');
fprintf(fileID, '%7d, %7d, %7d, %7d\n', find(RSS_elements==6));
fprintf(fileID, '\n');
fprintf(fileID, '*ELSET, elset=rest_of_the_elements\n');
fprintf(fileID, '%7d, %7d, %7d, %7d\n', Data.rest_of_the_elements');
fprintf(fileID, '\n');

%% Shell Section
fprintf(fileID, '*Shell Section, elset=ALL_ELEMENTS, material=STEEL\n');
fprintf(fileID, '%7f, %7d\n', [ts number_of_int_points]);
%fprintf(fileID, '*NODAL THICKNESS\n');
fprintf(fileID, 'Weld_nodes, %12f, %12f\n', [ts+Hweld ts]);
fprintf(fileID, 'rest_of_the_nodes, %12f, %12f\n', [ts ts]);
fprintf(fileID, '*End Part\n');
fprintf(fileID, '**\n');
fprintf(fileID, '**\n');

%%Assembly
fprintf(fileID, '**ASSEMBLY\n');
fprintf(fileID, '**\n');
fprintf(fileID, '*Assembly, name=Assembly\n');
fprintf(fileID, '**\n');
fprintf(fileID, '*Instance, name=Tower, part=Part1\n');
fprintf(fileID, '*End Instance\n');
fprintf(fileID, '**\n');
fprintf(fileID, '*Node\n');
fprintf(fileID, '%7d, %7d, %7d, %7d\n', NN+1, 0, 0, 0);
fprintf(fileID, '%7d, %7d, %7d, %7d\n', NN+2, h, 0, 0);
fprintf(fileID, '*Nset, nset=RP1, internal\n');
fprintf(fileID, '%7d, \n', NN+1);
fprintf(fileID, '*Nset, nset=RP2, internal\n');
fprintf(fileID, '%7d, \n', NN+2);
fprintf(fileID, '*Nset, nset=Bottom_Nodes, instance=Tower\n');
fprintf(fileID, '%7d, %7d, %7d, %7d, %7d, \n', Bottom_Nodes');
fprintf(fileID, '\n');
fprintf(fileID, '*Nset, nset=Top_Nodes, instance=Tower\n');
fprintf(fileID, '%7d, %7d, %7d, %7d, %7d, \n', Top_Nodes');
fprintf(fileID, '\n');
fprintf(fileID, '** Constraint: Constraint-1\n');
fprintf(fileID, '*MPC\n');
fprintf(fileID, 'BEAM, Bottom_Nodes, RP1\n');
fprintf(fileID, '** Constraint: Constraint-2\n');
fprintf(fileID, '*MPC\n');
fprintf(fileID, 'BEAM, Top_Nodes, RP2\n');
fprintf(fileID, '*End Assembly\n');

%% Elastic Material

fprintf(fileID, '**\n');
fprintf(fileID, '** MATERIALS\n');

```

```

fprintf(fileID, '**\n');
fprintf(fileID, '*Material, name=STEEL\n');
fprintf(fileID, '*Elastic\n');
fprintf(fileID, '%d, %d\n', E, Nu);
%% Plastic Material
fprintf(fileID, '*Plastic\n');
fprintf(fileID, '%12f, %12f,\n', PL');
fprintf(fileID, '** -----\n');
-----\n');
fprintf(fileID, '**\n');
%% Residual Stresses
fprintf(fileID, '*INITIAL CONDITIONS, type=STRESS, SECTION POINTS\n');
%st1 longitudinal
%st2 circumferential
IP=[1:number_of_int_points];
%invert stresses
K=fliplr(IP);
%K=IP;
for ip=1:number_of_int_points
    k=K(ip);
    st2(ip)=0;
    st1(k)=bending_stress_long(1)-
bending_stress_long(1)*2/(number_of_int_points-1)*(ip-1);
end
fprintf(fileID, 'TOWER.Weld_elements_1, %7d, %12f, %12f\n', [IP; st1;
st2]);
for ip=1:number_of_int_points
    k=K(ip);
    st2(ip)=-
bending_stress_circ(1)+bending_stress_circ(1)*2/(number_of_int_points-1)*(ip-
1);
    st1(k)=(-
bending_stress_circ(1)+bending_stress_circ(1)*2/(number_of_int_points-1)*(ip-
1))/2;
end
fprintf(fileID, 'TOWER.Weld_elements_2, %7d, %12f, %12f\n', [IP ;st1;
st2]);
for ip=1:number_of_int_points
    k=K(ip);
    st2(ip)=0;
    st1(k)=-
bending_stress_long(2)+bending_stress_long(2)*2/(number_of_int_points-1)*(ip-
1);
end
fprintf(fileID, 'TOWER.Inplate_elements_3, %7d, %12f, %12f\n', [IP
;st1;st2]);
for ip=1:number_of_int_points
    k=K(ip);
    st2(ip)=-
bending_stress_circ(1)+bending_stress_circ(1)*2/(number_of_int_points-1)*(ip-
1)+membrane_stress_circ(2);
    st1(k)=bending_stress_long(1)-
bending_stress_long(1)*2/(number_of_int_points-1)*(ip-
1)+membrane_stress_long(2);
end
fprintf(fileID, 'TOWER.Weld_elements_4, %7d, %12f, %12f\n', [IP; st1;
st2]);

for ip=1:number_of_int_points
    k=K(ip);
    st2(ip)=-
bending_stress_circ(1)+bending_stress_circ(1)*2/(number_of_int_points-1)*(ip-
1)+membrane_stress_circ(1);

```

```

        st1(k)=-
bending_stress_long(2)+bending_stress_long(2)*2/(number_of_int_points-1)*(ip-
1)+membrane_stress_long(1);
        end
        fprintf(fileID,'TOWER.Weld_elements_5, %7d, %12f, %12f\n',[IP; st1;
st2]);
        for ip=1:number_of_int_points
            k=K(ip);
            st2(ip)=0;
            st1(k)=bending_stress_long(1)-
bending_stress_long(1)*2/(number_of_int_points-1)*(ip-
1)+membrane_stress_long(1);
        end
        fprintf(fileID,'TOWER.Weld_elements_6, %7d, %12f, %12f\n',[IP; st1;
st2]);
        fprintf(fileID,'**\n');

%% Boundary Conditions

        fprintf(fileID,'** BOUNDARY CONDITIONS\n');
        fprintf(fileID,'**\n');
        fprintf(fileID,'** Name: BC-1 Type: Displacement/Rotation\n');
        fprintf(fileID,'*Boundary\n');
        fprintf(fileID,'RP1, 2, 2\n');
        fprintf(fileID,'RP1, 3, 3\n');
        fprintf(fileID,'RP1, 4, 4\n');
        fprintf(fileID,'** Name: BC-2 Type: Displacement/Rotation\n');
        fprintf(fileID,'*Boundary\n');
        fprintf(fileID,'RP2, 1, 1\n');
        fprintf(fileID,'RP2, 2, 2\n');
        fprintf(fileID,'RP2, 3, 3\n');
        fprintf(fileID,'RP2, 4, 4\n');
        fprintf(fileID,'**\n');

%% Step
        fprintf(fileID,'** STEP: Step-1\n');
        fprintf(fileID,'**\n');
        if jobname(2)=='S'
            %% RIKS
            fprintf(fileID,'*Step, name=Step-1, nlgeom=YES, inc=350\n');
            fprintf(fileID,'*Static, riks\n');
            fprintf(fileID,'0.01, 1., 1e-10, 0.01, ,\n');
            %% Loads

            M = 0.7*pi*E*ts^2*(Dt/2)*cos(phi)^2/sqrt((3*(1-Nu^2)));
            P = 2*M/(Dt/2)*cos(phi)^2;

            fprintf(fileID,'** LOADS\n');
            fprintf(fileID,'**\n');
            if Load_type == 'M'
                fprintf(fileID,'** Name: Load-1 Type: Moment\n');
                fprintf(fileID,'*Cload\n');
                fprintf(fileID,'RP1, 5, %d\n',-M);
                fprintf(fileID,'** Name: Load-2 Type: Moment\n');
                fprintf(fileID,'*Cload\n');
                fprintf(fileID,'RP2, 5, %d\n',M);
            elseif Load_type=='C'
                fprintf(fileID,'** Name: Load-1 Type: Concentrated force\n');
                fprintf(fileID,'*Cload\n');
                fprintf(fileID,'RP1, 3, %d\n',P);
                fprintf(fileID,'** Name: Load-2 Type: Concentrated force\n');
                fprintf(fileID,'*Cload\n');
                fprintf(fileID,'RP2, 3, %d\n',-P);
            else

```

```

end
fprintf(fileID, '**\n');

elseif jobname(2)=='R'
%Step for initial stresses only

%% Static
fprintf(fileID, '*Step, name=Step-1, nlgeom=NO\n');
fprintf(fileID, '*Static\n');
fprintf(fileID, '0.1, 1., 1e-05, 1.\n');
fprintf(fileID, '**\n');
end
%% Output request

fprintf(fileID, '** OUTPUT REQUESTS\n');
fprintf(fileID, '**\n');
fprintf(fileID, '*Restart, write, frequency=0\n');
fprintf(fileID, '**\n');
fprintf(fileID, '** FIELD OUTPUT: F-Output-1\n');
fprintf(fileID, '**\n');
fprintf(fileID, '*Output, field\n');
fprintf(fileID, '*Node Output\n');
fprintf(fileID, 'CF, U, UR\n');
fprintf(fileID, '**\n');
fprintf(fileID, '*Output, field, freq=9999\n');
fprintf(fileID, '*Element Output\n');
fprintf(fileID, 'MISES\n');
fprintf(fileID, '**\n');
fprintf(fileID, '** HISTORY OUTPUT: H-Output-1\n');
fprintf(fileID, '**\n');
fprintf(fileID, '*Output, history, variable=PRESELECT\n');
fprintf(fileID, '*output, history, freq=9999\n');
fprintf(fileID, '*End Step\n');

fclose(fileID);
cd ..

end

```

Changing Element type

```

function Data=abaqus_data(ConePatch,H,Dtop,Dbase,Etype)
Data.H=H;
Data.Dtop=Dtop;
Data.Dbase=Dbase;
nn=numel(ConePatch.Vertices(:,1));
Data.Nodes = [(1:nn)', ConePatch.Vertices(:,1), ConePatch.Vertices(:,2),
ConePatch.Vertices(:,3)];
ne=numel(ConePatch.Faces(:,1));
if strcmp(Etype,'S9R5')==1
Data.Elements=[(1:ne)', ConePatch.Faces(:,1), ConePatch.Faces(:,2),
ConePatch.Faces(:,3), ConePatch.Faces(:,4), ConePatch.Faces(:,5),
ConePatch.Faces(:,6), ConePatch.Faces(:,7), ConePatch.Faces(:,8),
ConePatch.Faces(:,9)];
elseif strcmp(Etype,'S4R')==1
Data.Elements=[(1:ne)', ConePatch.Faces(:,1), ConePatch.Faces(:,2),
ConePatch.Faces(:,3), ConePatch.Faces(:,4)];
else end
l=1;
m=1;

```

```

for i=1:nn
    a=Data.Nodes(i,4);
    if a==H
        Data.Top_Nodes(l) = Data.Nodes(i,1);
        l=l+1;
    elseif a==0
        Data.Bottom_Nodes(m) = Data.Nodes(i,1);
        m=m+1;
    else
        l=l;
        m=m;
    end
end
end

```

Imperfections implementation:

```

if any(imp==5)==1
    %define weld profile on mesh Rotter and Teng 1989 type A
    d_o=Hweld;
    lambda=pi/(3*(1-0.3^2))^0.25;
    ind_x=0:lambda/100:lambda;
    zeta=1;%for type A imperfection in the paper
    d=d_o*exp(-
    pi*ind_x/lambda).*(cos(pi*ind_x/lambda)+zeta*sin(pi*ind_x/lambda));
    Nw=ceil(lambda/0.25);% how many nodes will be in the depression imperfection
    profile

    for i=1:Nw
        z([i end-i+1],:)=d(i+(i-1)*Nw); %raise the X-edges
        z(Nw:end-Nw,[i end-i+1])=d(i+(i-1)*Nw); %raise the Y-edges
    end
end

%accidental eccentricity
if any(imp==2)==1
    if any(plate_id(2,:)==id)==1
        for i=2:ny-1
            for j=2:nx-1
                z(i,j)=Hweld*(x(ny-1,1)-x(i,j))/(x(ny-1,1)-x(2,j));
            end
        end
    end
    figure()
    surf(z)
end
end

%Dimple imperfection
if any(imp==3)==1
    if any(plate_id(1,:)==id)==1
        if class=='A'
            Uo=0.006;
        elseif class=='B'
            Uo=0.01;
        elseif class=='C'
            Uo=0.016;
        end
    end

    wo=Uo*lgx;
    N=int64(ceil(lgx/mesh_dim));
    ind_x=randi((ny-N),1,1);
    ind_y=randi((nx-N),1,1);

```

```
for i=ind_x:ind_x+N
    for j=ind_y:ind_y+N
        x1=(x(i,j)-x(i,ind_y))*pi/(x(i,ind_y+N)-x(i,ind_y));
        y1=(y(i,j)-y(ind_x,j))*pi/(y(ind_x+N,j)-y(ind_x,j));
        z1= -wo*sin(x1)*sin(y1);
        z(i,j)=z(i,j)+z1;
    end
end
end
end
```

Appendix B

Vestas Technical Report

Notes:

- 1- Commercial finite element software ABAQUS was used.
- 2- Meshes are created for each tower using 4-noded S4R elements with aspect ratio 1:1 following the meshing protocol proposed by (Mahmoud et al. 2016).
- 3- Two kinds of geometric imperfections patterns used:
 - a. VS1: lowest eigenmode under bending moment
 - b. VS2: Puppeke's proposed imperfection pattern
- 4- One set of models with no geometric imperfections (VS0).
- 5- Amplitudes of scaled imperfections were considered per sec. 8.7 Eurocode 1993-1-6:2007 Class C.
- 6- Three types of analysis are done:
 - a. GMNA: Geometric and Material Nonlinear Analysis
 - b. GMNIA: Geometric and Material Nonlinear Analysis with Imperfections
 - c. GNIA: Geometric Nonlinear Analysis with Imperfections
- 7- Same material model was considered for all GMNIA and GMNA models (Fig. 1) with $F_y= 462$ Mpa, $E=210,000$ MPa and Poisson's ratio $\nu=0.3$.
- 8- For the GNIA a linear elastic material model was used with $E=210,000$ MPa and Poisson's ratio $\nu=0.3$.
- 9- The boundary conditions considered was representing a simple beam boundary conditions with equal moments applied at both ends.
- 10- The convergence of the models with higher ($R/t =300-500$) was not finalized in VS1_300 and VS1_500 in GMNIA models also for ($R/t=100-500$) in GMNA models.
- 11- The rotation considered in Fig. 2(a-f) is the total rotation from both ends of the models
- 12- Theoretical eigen-buckling moment is calculated as $M_{cr-th} = \frac{\pi E t^2 R}{3\sqrt{(1-\nu^2)}}$.

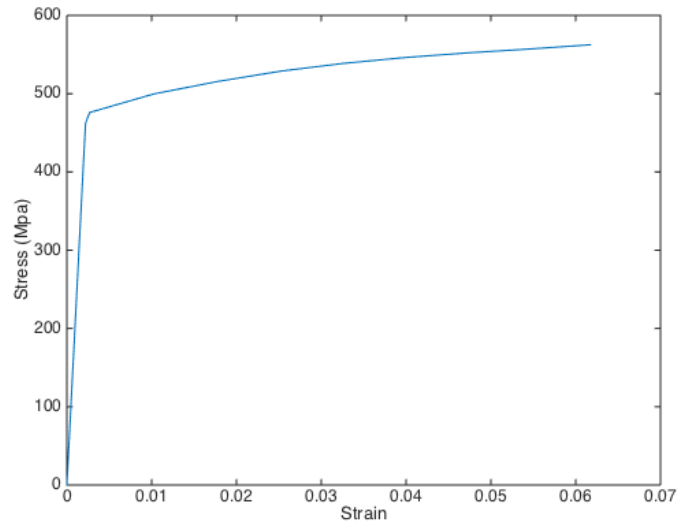


Figure B.1: Material stress strain curve used for GMNIA models.

Results Summary:

Table B.1 Dimensions and details of VS1 and VS2 models.

Model	r/t	r	t	h	l _g	U _n	d _w =w _{eq}	Mesh size	Imperfections pattern	Mu (MN-m)	
		(mm)	(mm)	(mm)	(mm)	(mm)	(mm)			GMNIA	GNIA
VS1_25	25	2000	80.00	25000	1600.00	0.025	50.00	200.0	Eigenmode	501.8	2358.4
VS1_50	50	2000	40.00	25000	1131.37	0.025	28.28	141.4	Eigenmode	215.7	627.3
VS1_75	75	2000	26.67	25000	923.76	0.025	23.09	115.5	Eigenmode	129.7	288.7
VS1_100	100	2000	20.00	25000	800.00	0.025	20.00	100.0	Eigenmode	90.2	165.5
VS1_300	300	2000	6.67	25000	461.88	0.025	11.55	57.7	Eigenmode	17.6	19.6
VS1_500	500	2000	4.00	25000	357.77	0.025	8.94	44.7	Eigenmode	7.5	7.5
VS2_25	25	2000	80.00	25000	1600.00	0.025	50.00	200.0	Puppeke	523.7	1925.8
VS2_50	50	2000	40.00	25000	1131.37	0.025	28.28	141.4	Puppeke	217.1	426.5
VS2_75	75	2000	26.67	25000	923.76	0.025	23.09	115.5	Puppeke	124.1	182.5
VS2_100	100	2000	20.00	25000	800.00	0.025	20.00	100.0	Puppeke	80.0	98.1
VS2_300	300	2000	6.67	25000	461.88	0.025	11.55	57.7	Puppeke	11.3	11.7
VS2_500	500	2000	4.00	25000	357.77	0.025	8.94	44.7	Puppeke	5.4	4.31

Table B.2 Dimensions and details of VS0 models.

Model	r/t	r	t	h	Mesh size	Mu (MN-m) GMNA
		(mm)	(mm)	(mm)		
VS0_25	25	2000	80.00	25000	200.0	601.6
VS0_50	50	2000	40.00	25000	141.4	281.2
VS0_75	75	2000	26.67	25000	115.5	163.4
VS0_100	100	2000	20.00	25000	100.0	113.4
VS0_300	300	2000	6.67	25000	57.7	35.46
VS0_500	500	2000	4.00	25000	44.7	13.2

Eigen-buckling critical moment for Linear Buckling Analyses (M_{cr-FE}) vs Theoretical solution (M_{cr-th})

Table B.3 Theoretical critical bending moment and lowest eigenbuckling moment

Model	M_{cr-th}	M_{cr-FE}
	(MN-m)	(MN-m)
VS_25	5213.1	5266.1
VS_50	1290.5	1308.9
VS_75	571.7	579.6
VS_100	321	325.2
VS_300	35.5	35.9
VS_500	12.8	12.9

Moment-Rotation curves:

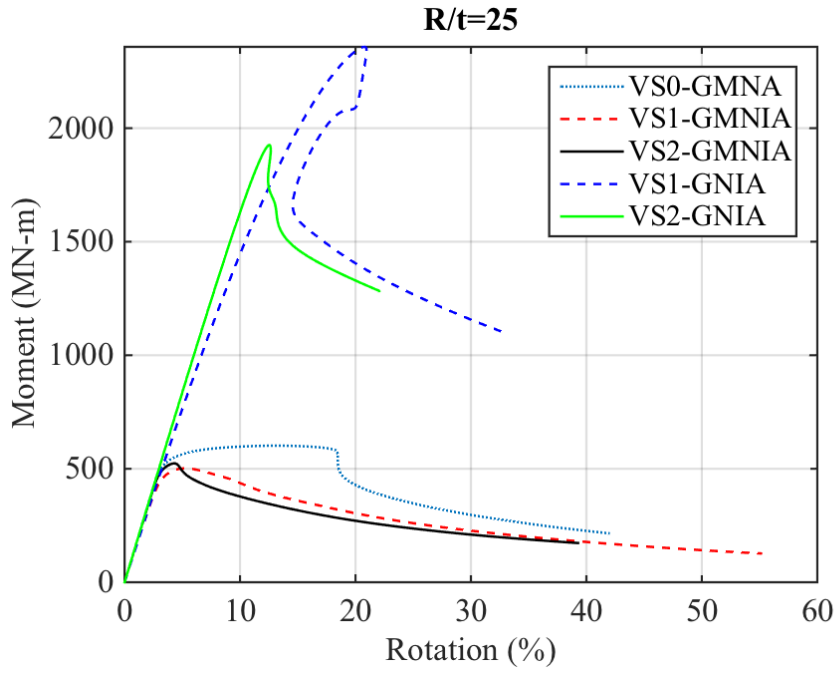


Figure B.2.a: Moment rotation curves of FE models for models with R/t=25

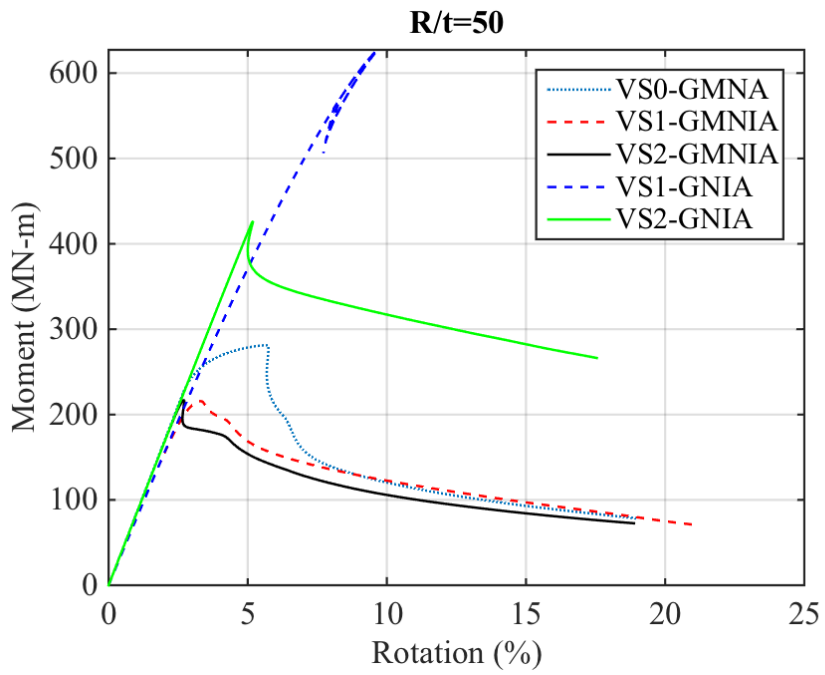


Figure B.2.b: Moment rotation curves of FE models for models with R/t=50

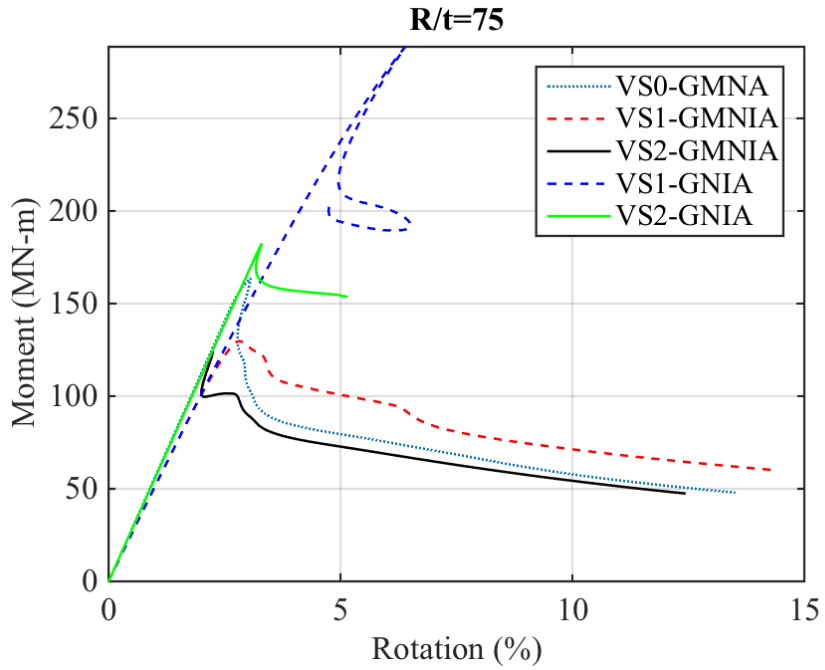


Figure B.2.c: Moment rotation curves of FE models for models with R/t=75

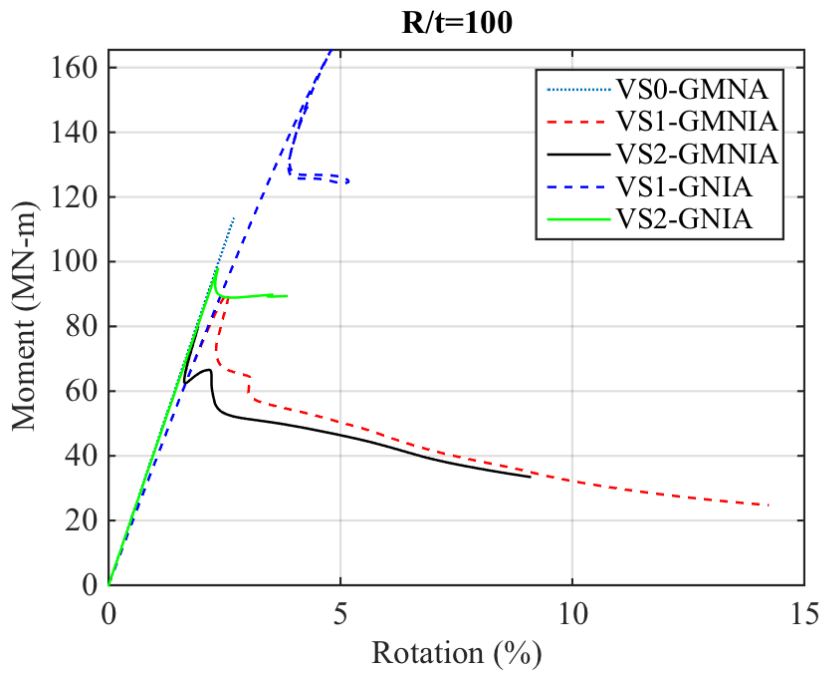


Figure B.2.d: Moment rotation curves of FE models for models with R/t=100

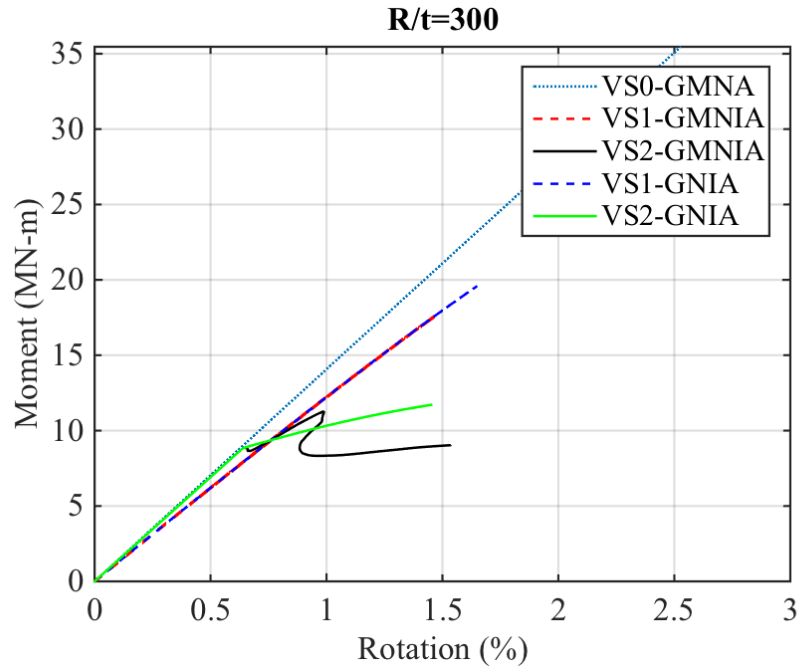


Figure B.2.e: Moment rotation curves of FE models for models with R/t=300

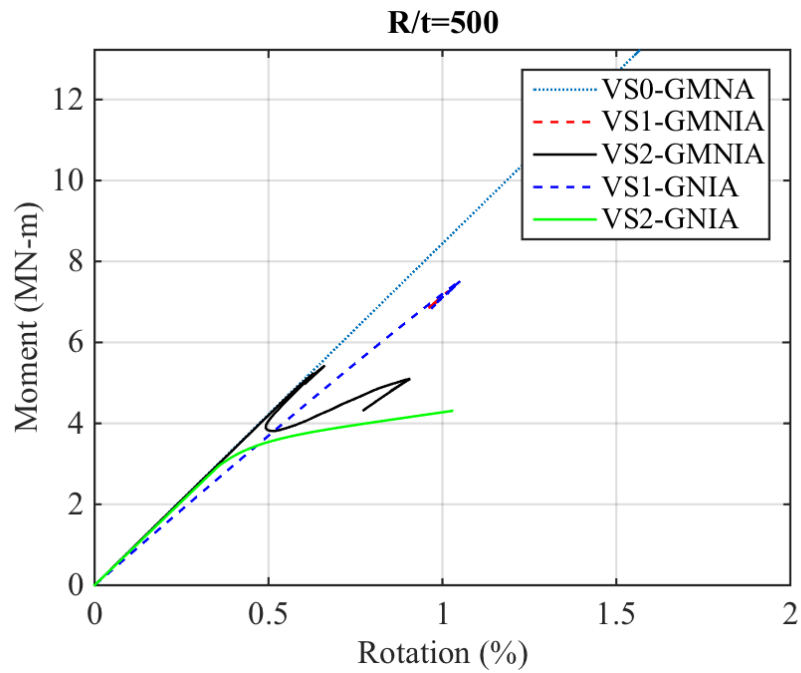


Figure B.2.f: Moment rotation curves of FE models for models with R/t=500

Failure modes:

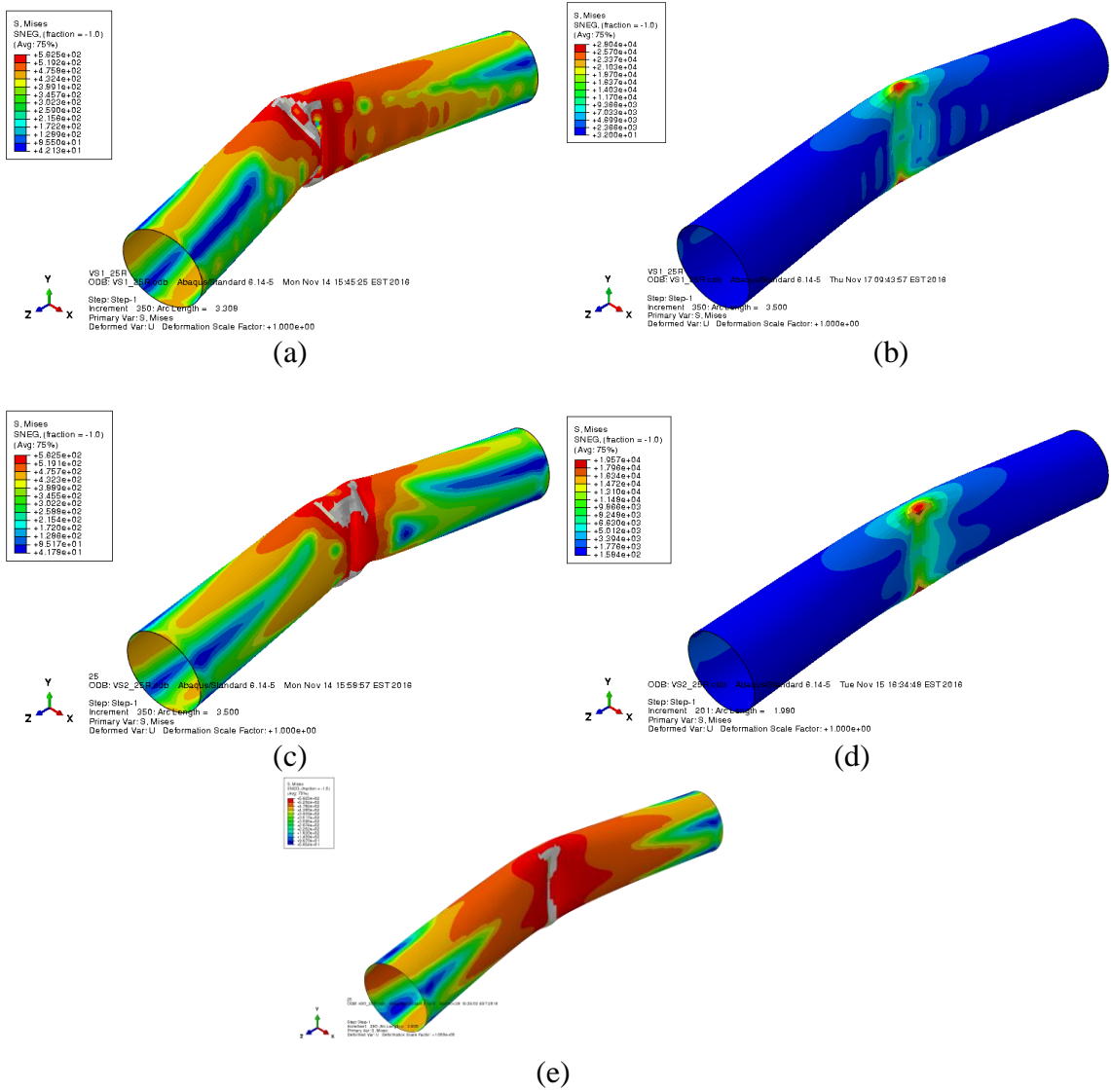


Figure B.3.a: Failure modes of models with $R/t=25$ (a)VS1-GMNA (b)VS-1 GNIA (c) VS2-GMNA (d) VS2-GNIA and (e) VS0-GMNA

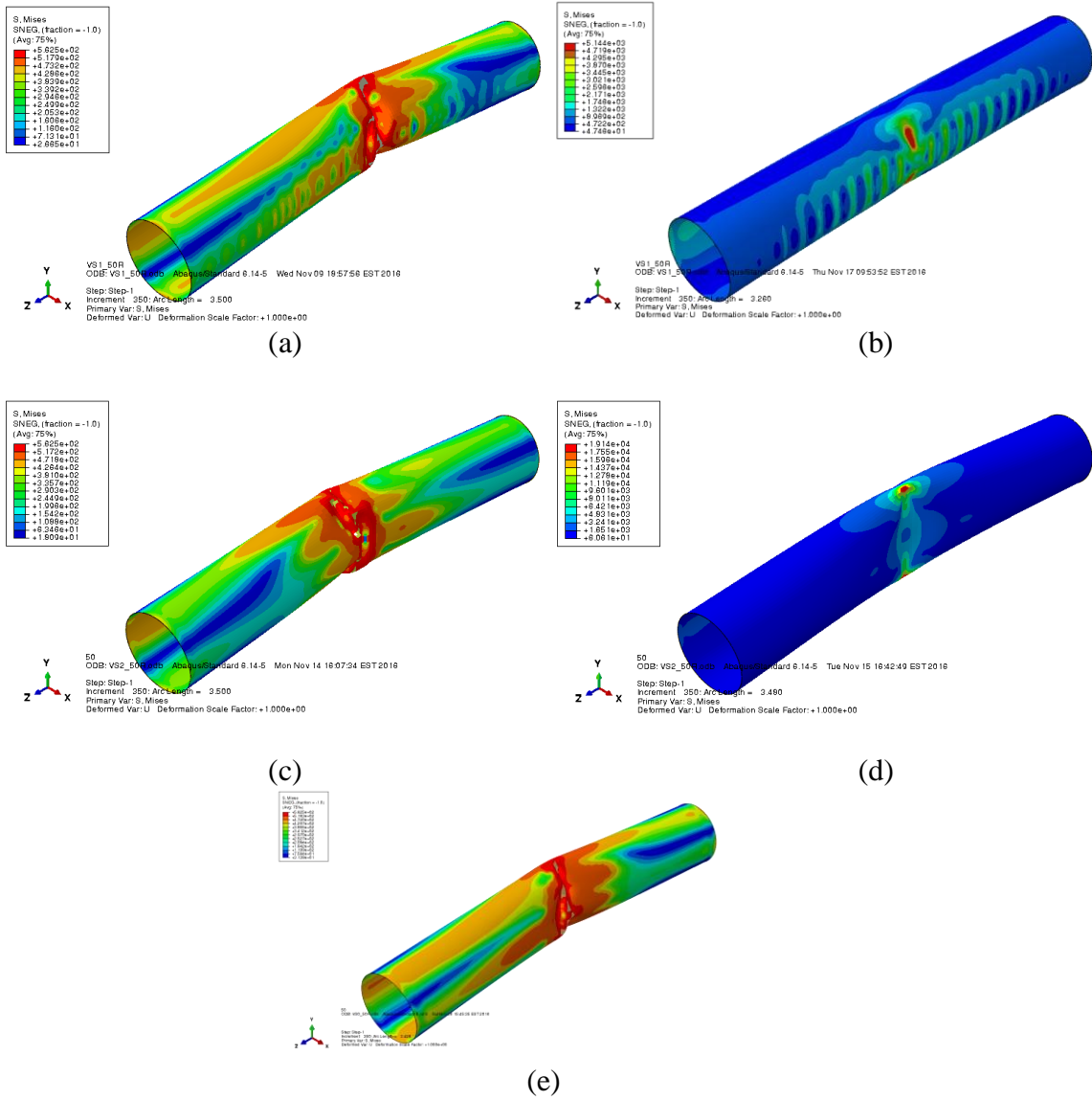


Figure B.3.b: Failure modes of models with $R/t=50$ (a)VS1-GMNA (b)VS-1 GNIA (c) VS2-GMNA (d) VS2-GNIA and (e) VS0-GMNA

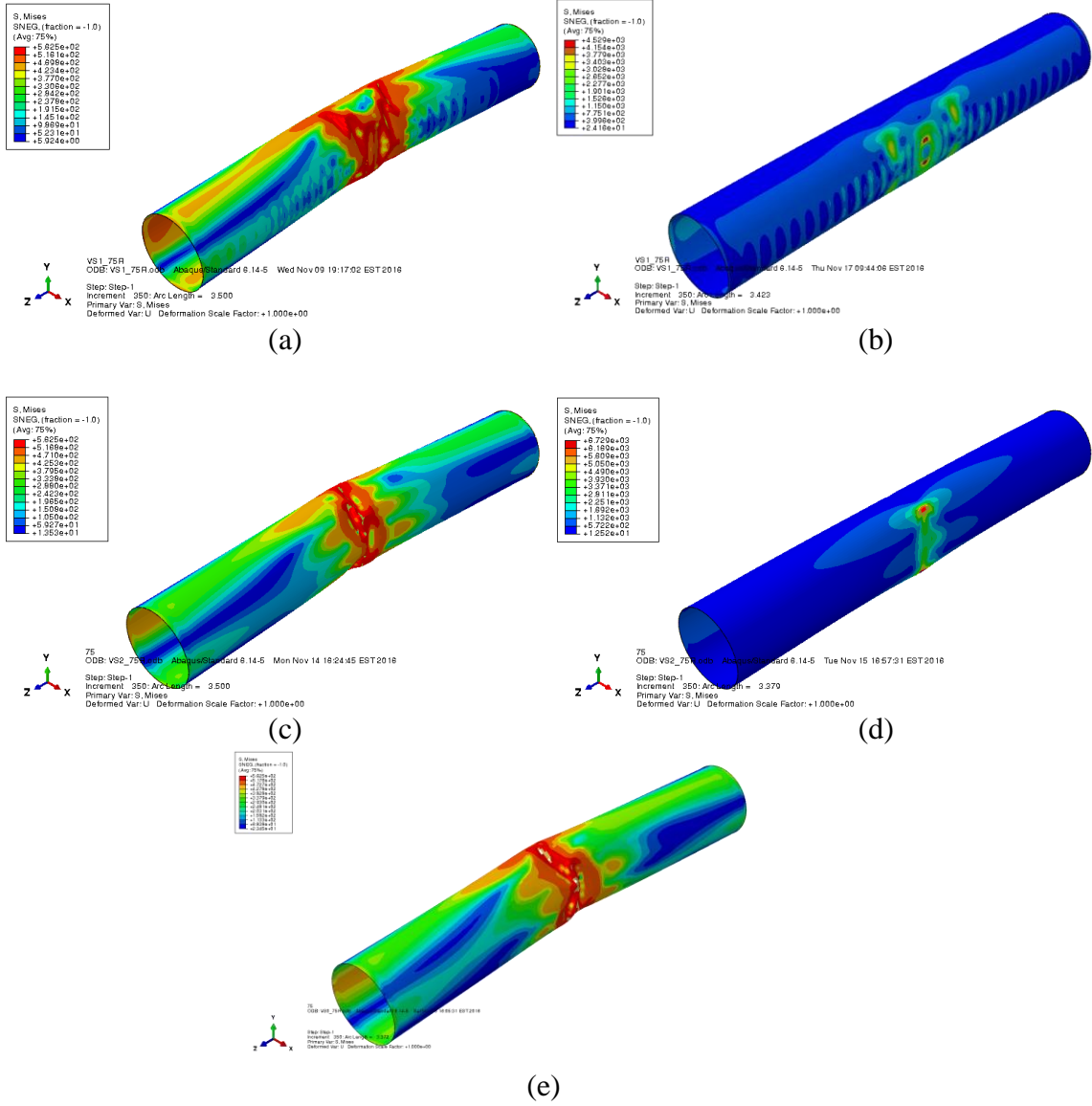


Figure B.3.c: Failure modes of models with $R/t=75$ (a)VS1-GMNA (b)VS-1 GNIA (c) VS2-GMNA (d) VS2-GNIA and (e) VS0-GMNA

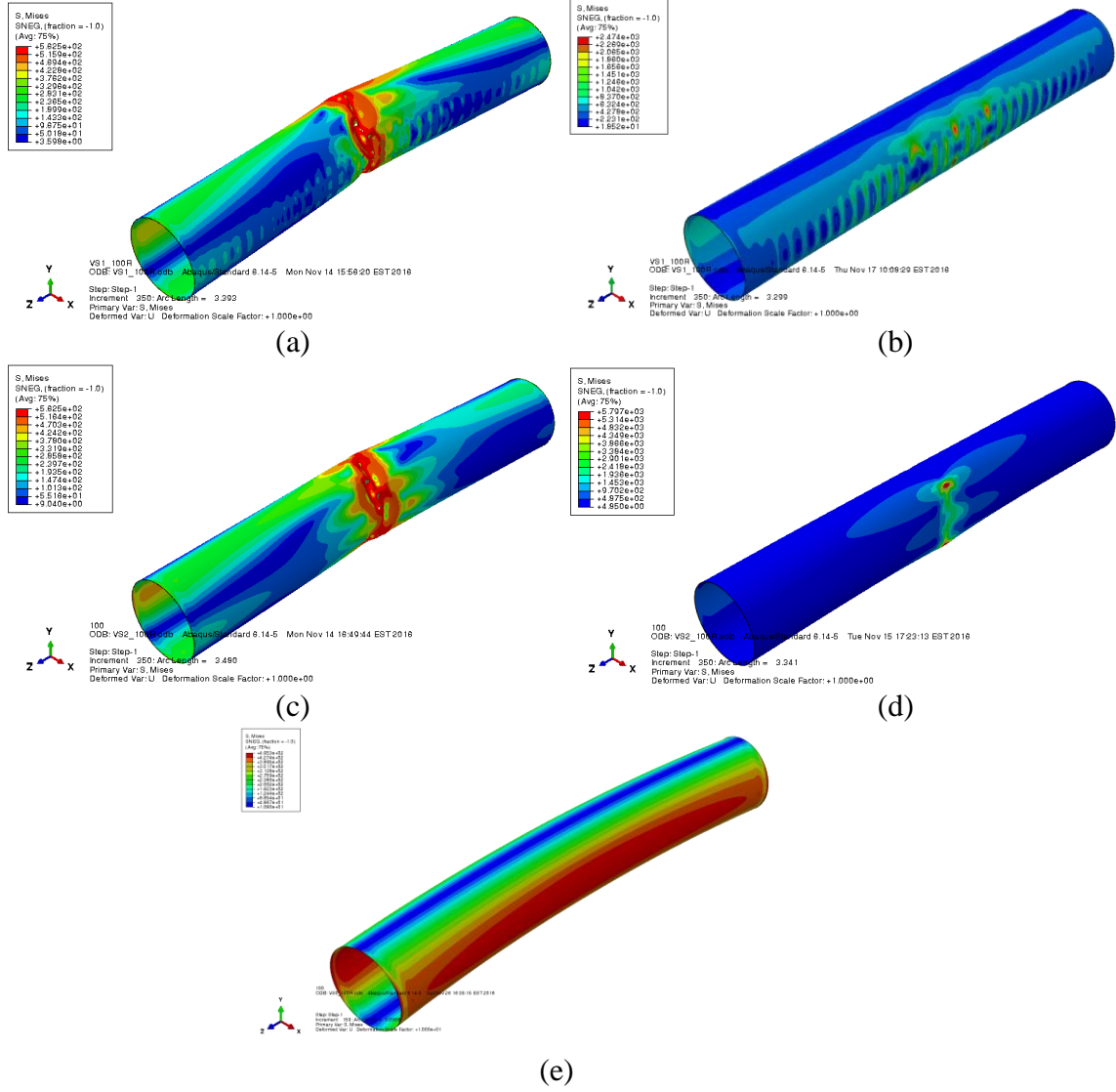


Figure B.3.d: Failure modes of models with $R/t = 100$ (a) VS1-GMNA (b) VS-1 GNIA (c) VS2-GMNA (d) VS2-GNIA and (e) VS0-GMNA

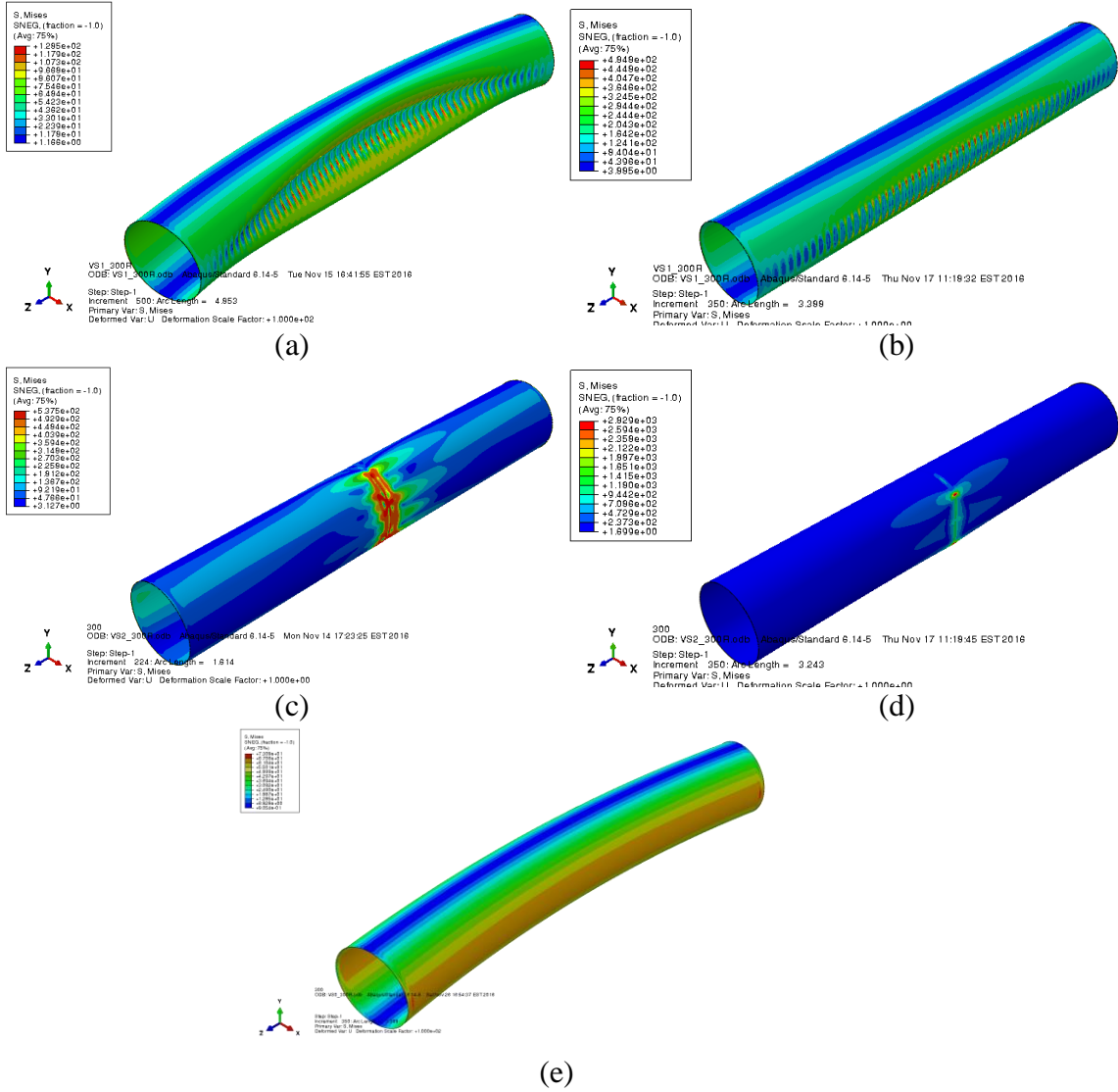


Figure B.3.e: Failure modes of models with R/t = 300 (a)VS1-GMNA (b)VS-1 GNIA (c) VS2-GMNA (d) VS2-GNIA and (e) VS0-GMNA

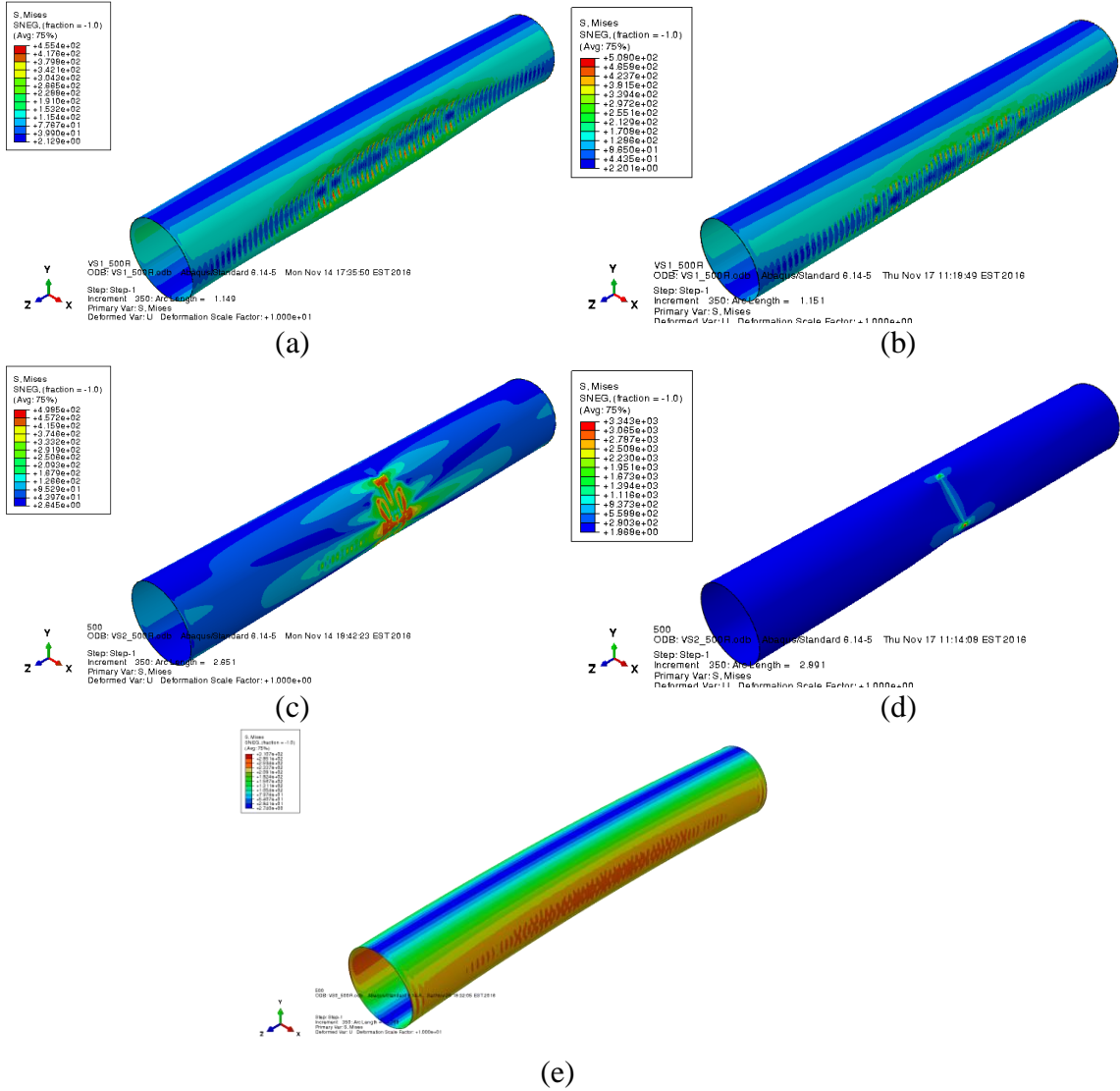


Figure B.3.f: Failure modes of models with $R/t = 500$ (a)VS1-GMNA (b)VS-1 GNIA (c) VS2-GMNA (d) VS2-GNIA and (e) VS0-GMNA

ABAQUS INPUT GENERATOR

```
%function nodes=Multi_Input(Db,Dt,h,ts,class)
    Db=4000;
    Dt=4000;
    h=25000;
    rb=Db/2;
    rt=Dt/2;
    C=6.89475908677537; %% for MPa=6.89475908677537 ### for ksi=1
    class='C';
    Load_type='M';
    ETYPE='S4R';
    aspect_ratio=1;
    addpath('Subs/');
    mat=load(['Material_prop.mat']);
    mat.Es =210000;
    mat.Nu = 0.3;
    mat.Fy =mat.Fy*C;
    mat.PL=mat.simp_mat;
    mat.PL(:,1)=mat.PL(:,1)*C;

    SL_ratio=[25, 50, 75, 100, 300, 500];

    mkdir(['Inputs_' datestr(now,'ddmmyyyy')])
    for i=1:length(SL_ratio)
        ts=rb/SL_ratio(i);
        jobname=num2str(SL_ratio(i));
        nth=round(Db*pi/(0.5*sqrt(rb*ts)));
        %Creating LBA
        num_el(i)=input_Tp_AR(jobname,rb,rt,h,ts,nth,aspect_ratio,'BL',ETYPE,Load_type,mat,class);
        %Creating GMNIA with eigenbuckling imperfection pattern
        num_el(i)=input_Tp_AR(jobname,rb,rt,h,ts,nth,aspect_ratio,'R',ETYPE,Load_type,mat,class);
        %Creating GMNIA with Puppeke imperfection pattern
        num_el(i)=input_Tp_AR_Puppeke_imperfections(jobname,rb,rt,h,ts,nth,aspect_ratio,'R',ETYPE,Load_type,mat,class);
    end
```

```
function
num_el=input_Tp_AR_Puppeke_imperfections(jobname,rb,rt,h,ts,nth,aspect_ratio,Run,ETYPE,Load_type,mat,class)
%ABAQUS input file for prismatic cylinder with ordinary mesh
%ETYPE = [ S4 - S4R - S8R - S9R5 ]
%w = imperfection percentage of buckling deformation
%Run = 'BL'- Buckling Lanczos
%      'BS'- Buckling Subspace
%      'R' - Riks Analysis
%Load_type = 'C'- compression
%           'M'- bending

    Db=2*rb;
    Dt=2*rt;
    phi=atan((rb-rt)/h);
```

```

l=pi*Db;
A=aspect_ratio;
mesh_size=l/nth;
nz=(h/A)/(1/nth);
nz=round(nz);
if mod(nz,2)==0
    nz=nz+1;
end
if mod(nth,2)~=0
    nth=nth+1;
end

nz
nth
num_el=nth*nz
AR=num2str(aspect_ratio*1000);

material = 'Steel';
Es=mat.Es;
Nu=mat.Nu;
Fy=mat.Fy;
PL=mat.PL;

%%%%%%%%%%%%%%%%%%%%%%%%%%%%%%%%%%%%%%%%%%%%%%%%%%%%%%%%%%%%%%%%%%%%%%%%%%Imperfections%%%%%%%%%%%%%%%%%%%%%%%%%%%%%%%%%%%%%%%%%%%%%%%%%%%%%%%%%%%%%%%%%%%%%%%%%%
if class=='A'
    Un=0.01;
elseif class=='B'
    Un=0.016;
elseif class=='C'
    Un=0.025;
end

lgx=4*sqrt(rb*ts);           % Gauge length, no weld (eq. 8.6)
lgw=min([25*ts 500]);       % Gauge length in weld (eq. 8.8)
lg=max([lgx lgw]);         % Choosing the maximum gauge length
w=max([lg*Un 25*ts*Un]);
%%%%%%%%%%%%%%%%%%%%%%%%%%%%%%%%%%%%%%%%%%%%%%%%%%%%%%%%%%%%%%%%%%%%%%%%%%

if strcmp(ETYPE,'S9R5')==1
    %nth=(nth+mod(nth,2))*2;
    %nz=(nz+mod(nz,2))*2;
    nth=nth*2;
    nz=nz*2;
elseif strcmp(ETYPE,'S4R')==1
elseif strcmp(ETYPE,'S4')==1
elseif strcmp(ETYPE,'S8R')==1
    nth=nth*2;
    nz=nz*2;
end

id=1;
%[r th z]-->[ID x y z] Nodal vertices
for i=0:nz
    Z=i*h/nz;
    rz=rb-(rb-rt)*Z/h;
    for j=0:nth-1
        th= j*2*pi/nth;
        [X,Y] = pol2cart(th,rz);
        x(id)=X;
        y(id)=Y;
        z(id)=Z;
        ID(id)=id;
        id =id+1;
    end
end

```

```

end
end

%%%%%%%%%%%%%%%%%%%%%%%%%%%%%%%%%%%%%%%%%%%%%%%%%%%%%%%%%%%%%%%%%%%%%%%%%%
[TH,R]=cart2pol(x',y');
ID_mat=reshape(ID,nth,nz+1);
R=reshape(R,nth,nz+1);
TH(TH<0)=TH(TH<0)+2*pi;
TH=reshape(TH,nth,nz+1);
Z=reshape(z,nth,nz+1);
d_r=zeros(nth,nz+1);
N=int64(round(lgx/2/mesh_size));
size_x=2*pi*rb/nth;
size_z=h/(nz+1);
ind_x=nth/2+1;
ind_z=(nz+1)/2;
n=2;
%%%%%%%%%%%%%%%%%%%%%%%%%%%%%%%%%%%%%%%%%%%%%%%%%%%%%%%%%%%%%%%%%%%%%%%%%%
%%%%%%%%%%%%%%%%%%%%%%%%%%%%%%%%%%%%%%%%%%%%%%%%%%%%%%%%%%%%%%%%%%%%%%%%%%
for localized dimple imperfections with Lg x Lg
% for i=ind_x-N:ind_x+N
%     for j=ind_z-N:ind_z+N
%         x2=(TH(i,j)-TH(ind_x,j))/(TH(ind_x,j)-TH(ind_x-N,j))*pi/2;
%         z2=(Z(i,j)-Z(ind_z))/(Z(ind_z)-Z(ind_z-N))*pi/2;
%         d_r(i,j)=-w*(cos(x2)^n)*(cos(z2)^n);
%     end
% end
% d_r2(1:N+1,:)=d_r(ind_x:ind_x+N,:);
% d_r2(nth-N:nth,:)=d_r(ind_x-N:ind_x,:);
% R=R+d_r2;
%%%%%%%%%%%%%%%%%%%%%%%%%%%%%%%%%%%%%%%%%%%%%%%%%%%%%%%%%%%%%%%%%%%%%%%%%%
%%%%%%%%%%%%%%%%%%%%%%%%%%%%%%%%%%%%%%%%%%%%%%%%%%%%%%%%%%%%%%%%%%%%%%%%%%
for full ring imperfection
for i=1:length(TH(:,1))
    for j=ind_z-N:ind_z+N
        z2=(Z(i,j)-Z(ind_z))/(Z(ind_z)-Z(ind_z-N))*pi/2;
        d_r(i,j)=-w*(cos(z2)^n);
    end
end
end
R=R+d_r;
%%%%%%%%%%%%%%%%%%%%%%%%%%%%%%%%%%%%%%%%%%%%%%%%%%%%%%%%%%%%%%%%%%%%%%%%%%
[x,y,z]=pol2cart(TH(:),R(:),Z(:));
nodes=[ID',x,y,z];
%elements
nn=length(nodes);
j=0;
k=0;
L=0;
if strcmp(ETYPE,'S9R5')==1
    for i=1:(nn-nth)/4
        B=nth*[1:nz]/2;
        b=any(B==i);
        L=k*nth;
        if b==1
            elements(i,:)=[i i+j+L i+j+L-nth+2 i+j+L+nth+2 i+j+L+2*nth
i+j+L+1 i+j+L+2 i+j+L+2*nth+1 i+j+L+nth i+j+L+nth+1];
            j=j+1;
            k=k+1;
        else
            elements(i,:)=[i i+j+L i+j+L+2 i+j+2*nth+L+2 i+j+2*nth+L i+j+L+1
i+j+nth+L+2 i+j+2*nth+L+1 i+j+nth+L i+j+nth+L+1 ];
            j=j+1;

```

```

        end
    end

elseif strcmp(ETYPE, 'S4R')==1
    for i=1:nn-nth
        B=nth*[1:nz];
        b=any(B==i);
        if b==1
            elements(i,:)=[i i i+nth i+1 i-nth+1];
        else
            elements(i,:)=[i i i+nth i+nth+1 i+1];
        end
    end
end
elseif strcmp(ETYPE, 'S4')==1
    for i=1:nn-nth
        B=nth*[1:nz];
        b=any(B==i);
        if b==1
            elements(i,:)=[i i i+nth i+1 i-nth+1];
        else
            elements(i,:)=[i i i+nth i+nth+1 i+1];
        end
    end
end
elseif strcmp(ETYPE, 'S8R')==1
    for i=1:(nn-nth)/4
        B=nth*[1:nz]/2;
        b=any(B==i);
        L=k*nth;
        if b==1
            elements(i,:)=[i i+j+L i+j+L-nth+2 i+j+L+nth+2 i+j+L+2*nth
i+j+L+1 i+j+L+2 i+j+L+2*nth+1 i+j+L+nth ];
            j=j+1;
            k=k+1;
        else
            elements(i,:)=[i i+j+L i+j+L+2 i+j+2*nth+L+2 i+j+2*nth+L i+j+L+1
i+j+nth+L+2 i+j+2*nth+L+1 i+j+nth+L ];
            j=j+1;
        end
    end
end
j=0;
ne=length(elements);
for i=1:nn
    b=find(elements(:,2:9)==i);
    a=length(b);
    if a==0
        k=i-j;
        nodes(k,:)=[];
        j=j+1;
    else
        end
end
else
end

Bottom_Nodes=[1:nth];
Top_Nodes =[nn-nth+1:nn];

cd(['Inputs_' datestr(now, 'ddmmyyyy')])
%fileID=fopen([jobname, '_', AR, '.inp'], 'w');
fileID=fopen(['VS2_' jobname 'R.inp'], 'w');
fprintf(fileID, '*Heading\n');
fprintf(fileID, ' %s\n', jobname);
fprintf(fileID, '** Job name: %s\n', jobname);

```

```

fprintf(fileID, '** Generated by: Abaqus/CAE 6.12-3\n');
fprintf(fileID, '*Preprint, echo=NO, model=NO, history=NO, contact=NO\n');
fprintf(fileID, '**\n');
fprintf(fileID, '** PARTS\n');
fprintf(fileID, '**\n');
fprintf(fileID, '*Part, name=Part1\n');

%% Node & Element Generation
fprintf(fileID, '*Node\n');
fprintf(fileID, '%7d, %12f, %12f, %12f\n', nodes');
if strcmp(ETYPE, 'S4R')==1
    fprintf(fileID, '*Element, type=%s\n', ETYPE);
    fprintf(fileID, '%7d, %7d, %7d, %7d, %7d\n', elements');
elseif strcmp(ETYPE, 'S9R5')==1
    fprintf(fileID, '*Element, type=%s\n', ETYPE);
    fprintf(fileID, '%7d, %7d, %7d, %7d, %7d, %7d, %7d, %7d, %7d,
%7d\n', elements');
elseif strcmp(ETYPE, 'S4')==1
    fprintf(fileID, '*Element, type=%s\n', ETYPE);
    fprintf(fileID, '%7d, %7d, %7d, %7d, %7d\n', elements');
elseif strcmp(ETYPE, 'S8R')==1
    fprintf(fileID, '*Element, type=%s\n', ETYPE);
    fprintf(fileID, '%7d, %7d, %7d, %7d, %7d, %7d, %7d, %7d,
%7d\n', elements');
end

%% Nodes Sets
NN = length(nodes);
fprintf(fileID, '*NSET, NSET=ALL_Nodes, GENERATE\n');
fprintf(fileID, '%7d, %7d, %7d\n', 1, NN, 1);

%% Elements Sets
NE = length(elements);
fprintf(fileID, '*ELSET, ELSET=ALL_Elements, GENERATE\n');
fprintf(fileID, '%7d, %7d, %7d\n', 1, NE, 1);

%% Shell Section

fprintf(fileID, '*Shell Section, elset=ALL_Elements,
material=%s\n', material);
fprintf(fileID, '%7f\n', ts);
fprintf(fileID, '*End Part\n');
fprintf(fileID, '**\n');
fprintf(fileID, '**\n');

%% Assembly
fprintf(fileID, '**ASSEMBLY\n');
fprintf(fileID, '**\n');
fprintf(fileID, '*Assembly, name=Assembly\n');
fprintf(fileID, '**\n');
fprintf(fileID, '*Instance, name=Tower, part=Part1\n');
fprintf(fileID, '*End Instance\n');
fprintf(fileID, '**\n');
fprintf(fileID, '*Node\n');
fprintf(fileID, '%7d, %7d, %7d, %7d\n', NN+1, 0, 0, 0);
fprintf(fileID, '%7d, %7d, %7d, %7d\n', NN+2, 0, 0, h);
fprintf(fileID, '*Nset, nset=RP1, internal\n');
fprintf(fileID, '%7d, \n', NN+1);
fprintf(fileID, '*Nset, nset=RP2, internal\n');
fprintf(fileID, '%7d, \n', NN+2);

fprintf(fileID, '*Nset, nset=Bottom_Nodes, instance=Tower\n');
fprintf(fileID, '%7d, %7d, %7d, %7d, %7d, \n', Bottom_Nodes);

```



```

fprintf(fileID, '\n');
fprintf(fileID, '*Nset, nset=Top_Nodes, instance=Tower\n');
fprintf(fileID, '%7d, %7d, %7d, %7d, %7d\n', Top_Nodes);
fprintf(fileID, '\n');
fprintf(fileID, '** Constraint: Constraint-1\n');
fprintf(fileID, '*MPC\n');
fprintf(fileID, 'BEAM, Bottom_Nodes, RP1\n');
fprintf(fileID, '** Constraint: Constraint-2\n');
fprintf(fileID, '*MPC\n');
fprintf(fileID, 'BEAM, Top_Nodes, RP2\n');
fprintf(fileID, '*End Assembly\n');

%% Elastic Material

fprintf(fileID, '**\n');
fprintf(fileID, '** MATERIALS\n');
fprintf(fileID, '**\n');
fprintf(fileID, '*Material, name=%s\n', material);
fprintf(fileID, '*Elastic\n');
fprintf(fileID, '%d, %d\n', Es, Nu);
%% Plastic Material
%PL=[50 0; 51 0.001724; 65 0.15; 65 0.25];

fprintf(fileID, '*Plastic\n');
fprintf(fileID, '%12f, %12f, \n', PL);
%% Step
fprintf(fileID, '** -----
-----\n');
fprintf(fileID, '**\n');
fprintf(fileID, '** STEP: Step-1\n');
fprintf(fileID, '**\n');
if Run=='BS'

%Buckling
fprintf(fileID, '*Step, name=Step-1, perturbation\n');
fprintf(fileID, '*Buckle\n');
fprintf(fileID, '10, , 10, 3000\n');
elseif Run=='BL'
fprintf(fileID, '*Step, name=Step-1, nlgeom=NO, perturbation\n');
fprintf(fileID, '*Buckle, eigensolver=lanczos\n');
fprintf(fileID, '10, , , \n');
elseif Run=='R'
%Riks
fprintf(fileID, '*Step, name=Step-1, nlgeom=YES, inc=350\n');
fprintf(fileID, '*Static, riks\n');
fprintf(fileID, '0.01, 1., 1e-010, 0.01, , \n');
end
fprintf(fileID, '**\n');

%% Boundary Conditions

fprintf(fileID, '** BOUNDARY CONDITIONS\n');
fprintf(fileID, '**\n');
fprintf(fileID, '** Name: BC-1 Type: Displacement/Rotation\n');
fprintf(fileID, '*Boundary\n');
fprintf(fileID, 'RP1, 1, 1\n');
fprintf(fileID, 'RP1, 2, 2\n');
fprintf(fileID, 'RP1, 6, 6\n');
fprintf(fileID, '** Name: BC-2 Type: Displacement/Rotation\n');
fprintf(fileID, '*Boundary\n');
fprintf(fileID, 'RP2, 1, 1\n');
fprintf(fileID, 'Rp2, 2, 2\n');
fprintf(fileID, 'RP2, 3, 3\n');

```

```

fprintf(fileID,'Rp2, 6, 6\n');
fprintf(fileID,'**\n');

%% Loads
if Run == 'R'
    M = pi*Es*ts^2*rb/(3*(1-Nu^2));
    P = 2*M/rb;
else
    M = 1;
    P = 1;
end
fprintf(fileID,'** LOADS\n');
fprintf(fileID,'**\n');
if Load_type == 'M'
fprintf(fileID,'** Name: Load-1   Type: Moment\n');
fprintf(fileID,'*Cload\n');
fprintf(fileID,'RP1, 5, %d\n',-M);
fprintf(fileID,'** Name: Load-2   Type: Moment\n');
fprintf(fileID,'*Cload\n');
fprintf(fileID,'RP2, 5, %d\n',M);
elseif Load_type=='C'
    fprintf(fileID,'** Name: Load-1   Type: Concentrated force\n');
fprintf(fileID,'*Cload\n');
fprintf(fileID,'RP1, 3, %d\n',P);
fprintf(fileID,'** Name: Load-2   Type: Concentrated force\n');
fprintf(fileID,'*Cload\n');
fprintf(fileID,'RP2, 3, %d\n',-P);
else
end
fprintf(fileID,'**\n');

%% Output request

fprintf(fileID,'** OUTPUT REQUESTS\n');
fprintf(fileID,'**\n');
fprintf(fileID,'*Restart, write, frequency=0\n');
fprintf(fileID,'**\n');
fprintf(fileID,'** FIELD OUTPUT: F-Output-1\n');
fprintf(fileID,'**\n');
fprintf(fileID,'*Output, field, variable=PRESELECT\n');

if Run=='BS'
fprintf(fileID,'*output,field\n');
fprintf(fileID,'*node output\n');
fprintf(fileID,'u,\n');
fprintf(fileID,'*node file,global=yes\n');
fprintf(fileID,'u,\n');
elseif Run=='BL'
fprintf(fileID,'*output,field\n');
fprintf(fileID,'*node output\n');
fprintf(fileID,'u,\n');
fprintf(fileID,'*node file,global=yes\n');
fprintf(fileID,'u,\n');
else
fprintf(fileID,'**\n');
fprintf(fileID,'** HISTORY OUTPUT: H-Output-1\n');
fprintf(fileID,'**\n');
fprintf(fileID,'*Output, history, variable=PRESELECT\n');
fprintf(fileID,'*output, history, freq=1\n');
end
fprintf(fileID,'*End Step\n');

```

```
fclose(fileID);  
cd ..  
end
```

Appendix C

Mesh Sensitivity Analyses – Extra Data

Full Moment-Rotation Curves for Nonlinear Collapse Models

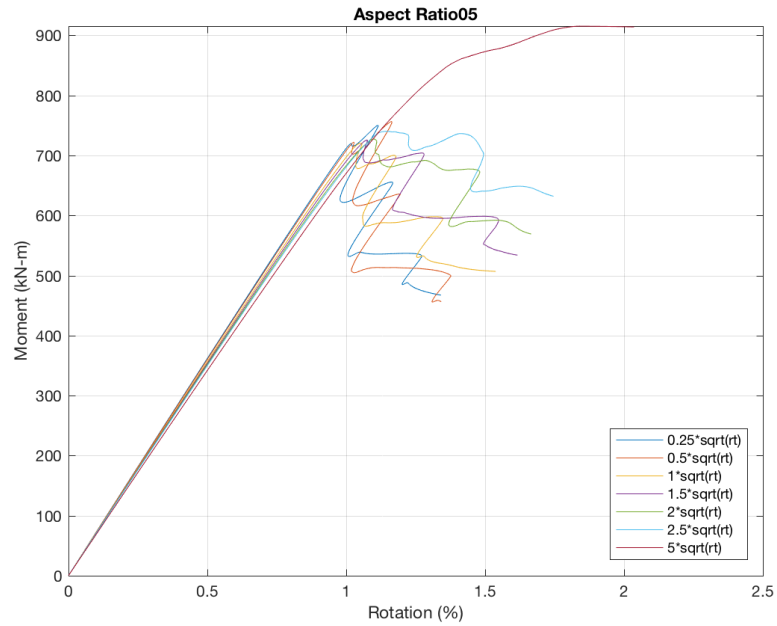


Figure C.1: Mesh sensitivity analysis for nonlinear collapse models with aspect ratio 1:2.

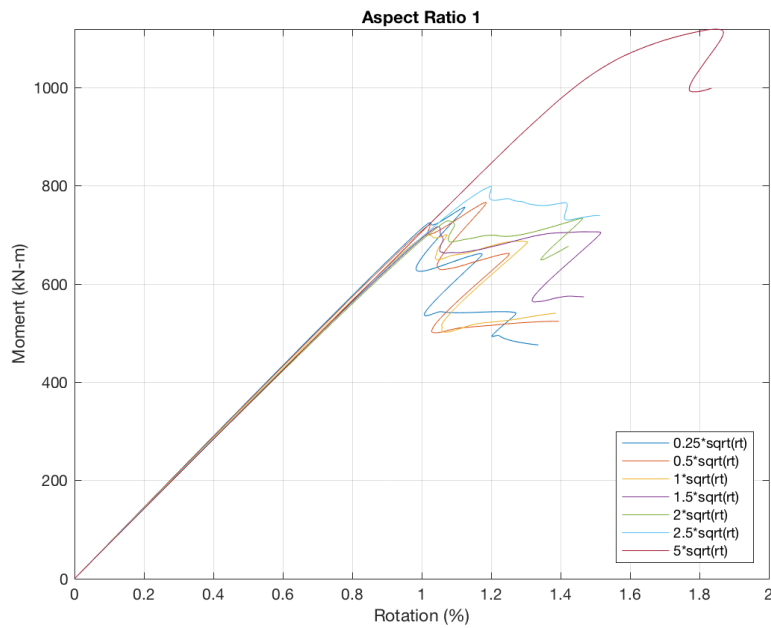


Figure C.2: Mesh sensitivity analysis for nonlinear collapse models with aspect ratio 1:1.

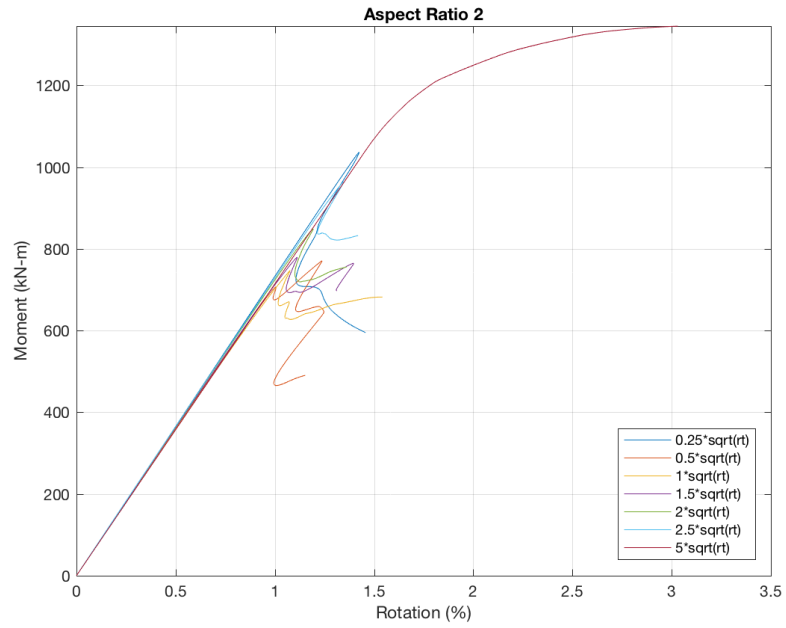


Figure C.3: Mesh sensitivity analysis for nonlinear collapse models with aspect ratio 2:1.

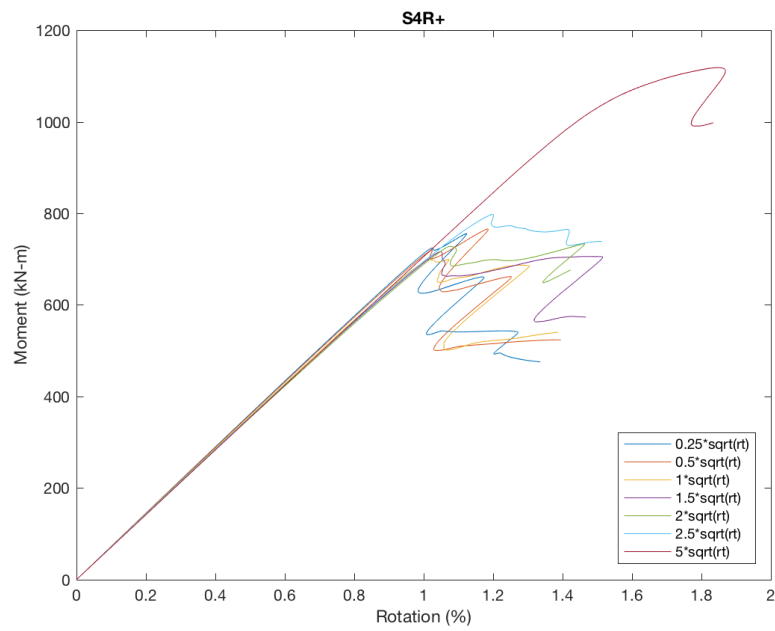


Figure C.4: Mesh sensitivity analysis for nonlinear collapse models for element S4R.

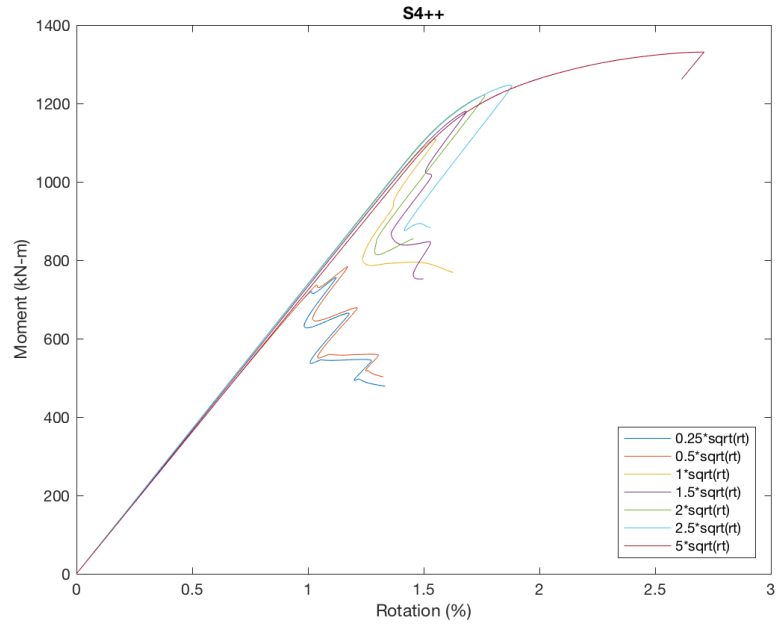


Figure C.5: Mesh sensitivity analysis for nonlinear collapse models for element S4.

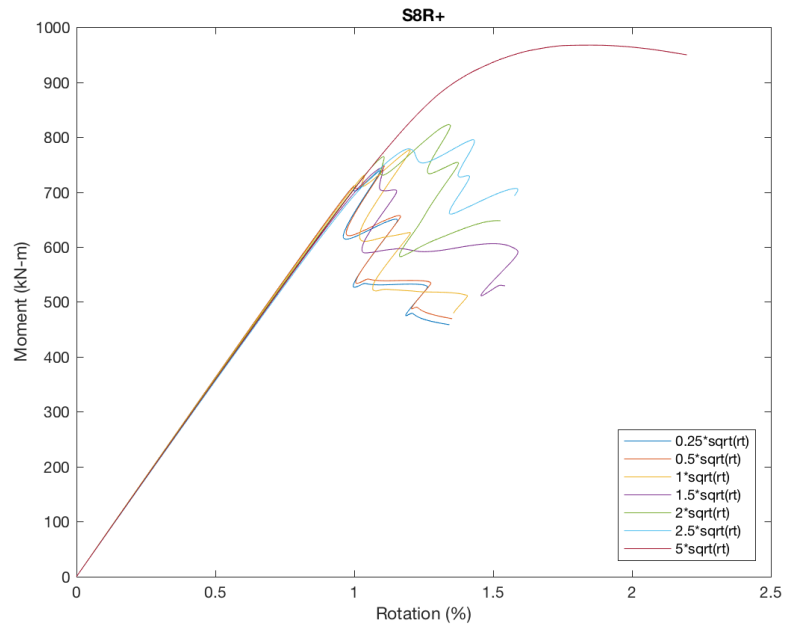


Figure C.6: Mesh sensitivity analysis for nonlinear collapse models for element S8R.

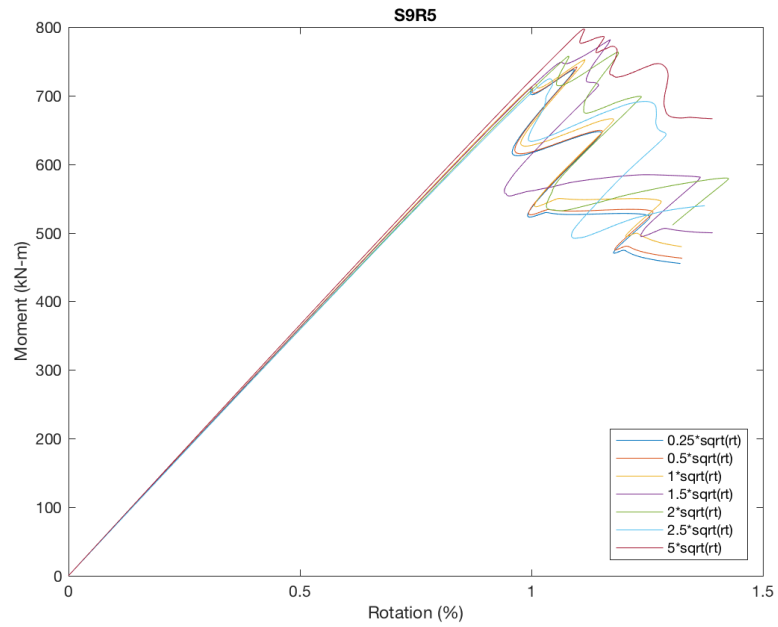


Figure C.7: Mesh sensitivity analysis for nonlinear collapse models for element S9R5.

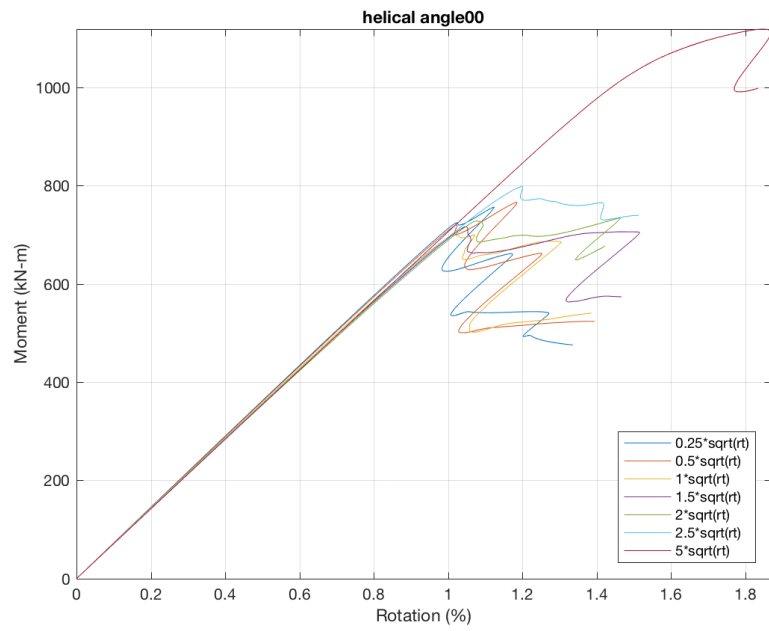


Figure C.8: Mesh sensitivity analysis for nonlinear collapse models for helical angle 0° .

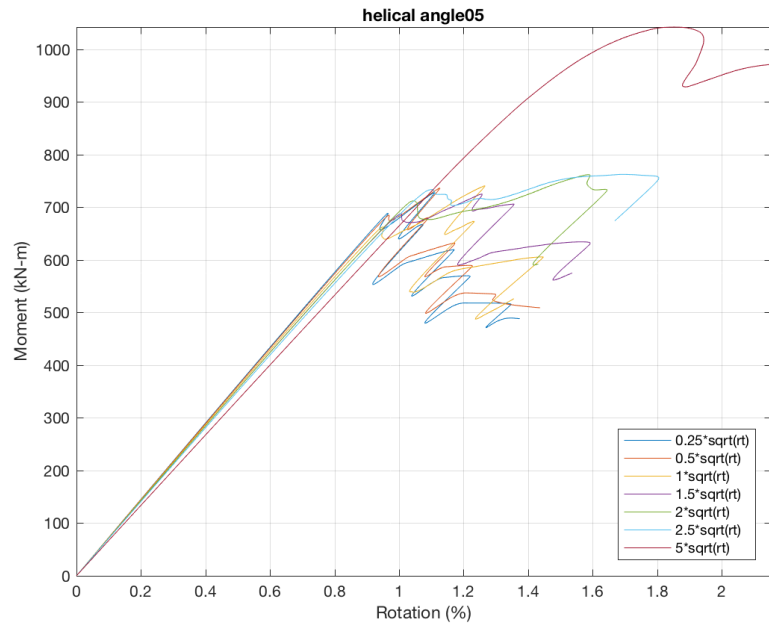


Figure C.9: Mesh sensitivity analysis for nonlinear collapse models for helical angle 5° .

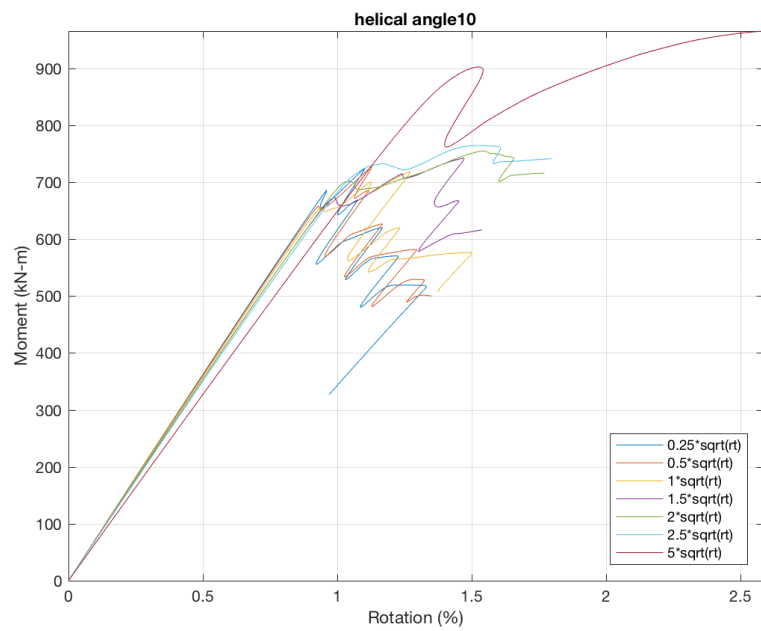


Figure C.10: Mesh sensitivity analysis for nonlinear collapse models for helical angle 10° .

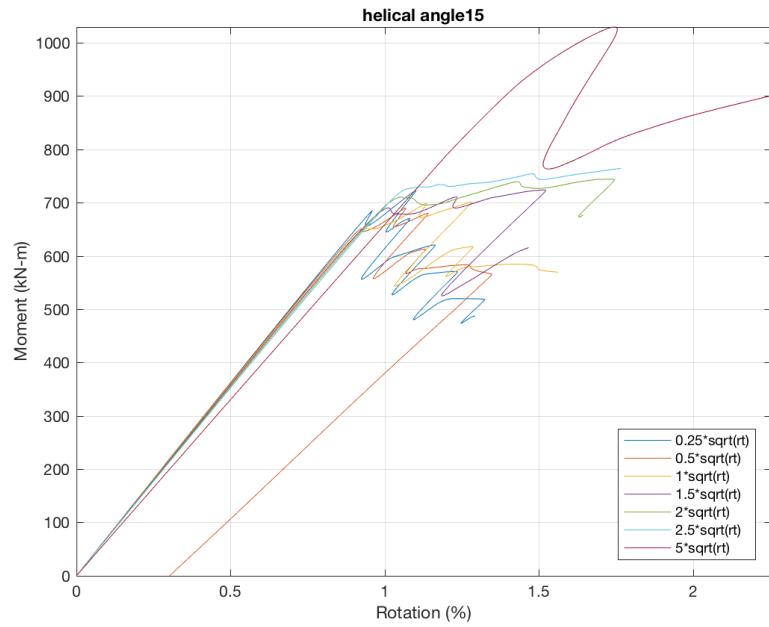


Figure C.11: Mesh sensitivity analysis for nonlinear collapse models for helical angle 15°.

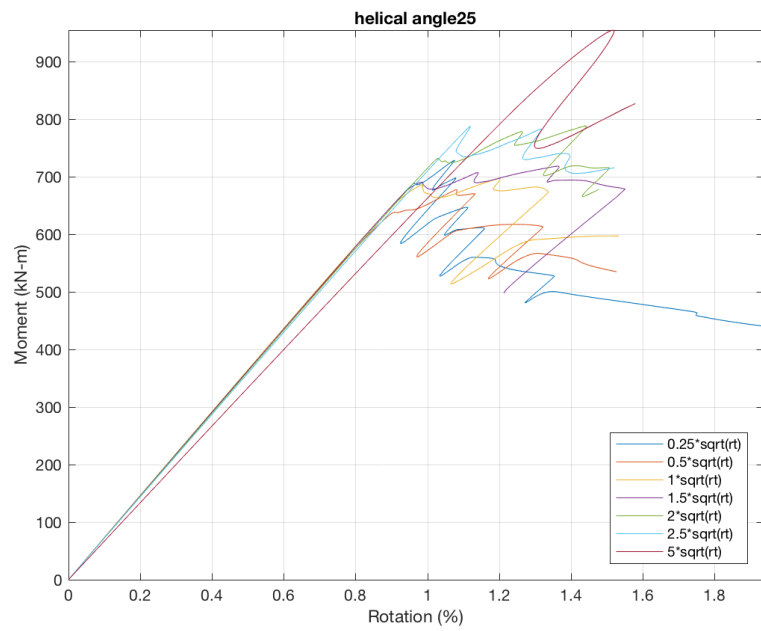
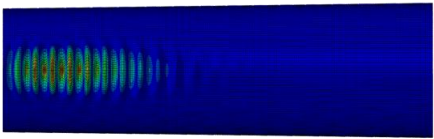
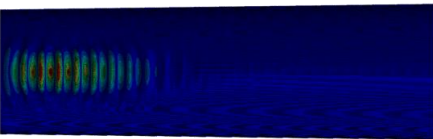
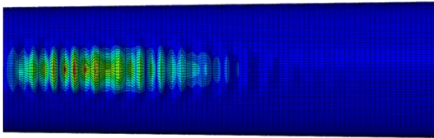
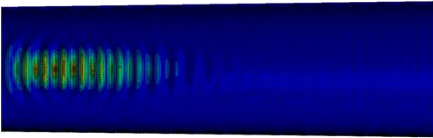
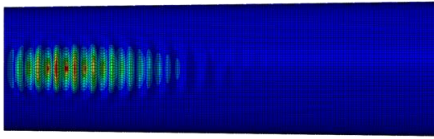
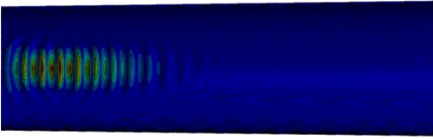
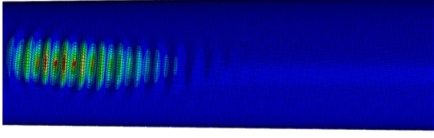
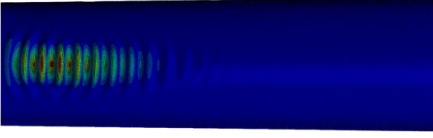
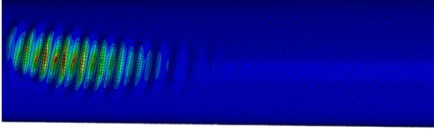
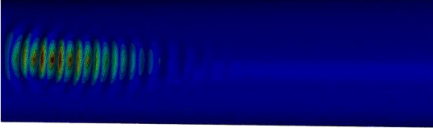
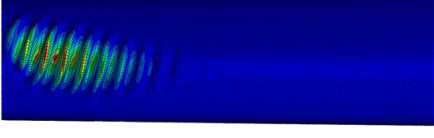


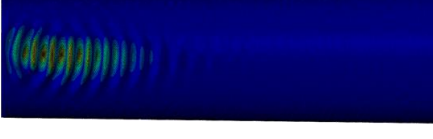


Figure C.12: Mesh sensitivity analysis for nonlinear collapse models for helical angle 25°.

Mesh size effect on buckled shape of LBA

Parameter	Mesh Size	
	$0.5 \sqrt{R_{avg} t}$	$0.25 \sqrt{R_{avg} t}$
Aspect Ratio 1:2		
Aspect Ratio 2:1		
Aspect Ratio 1:1 Inclination Angle = 0°		
Inclination angle=5°		
Inclination angle=10°		
Inclination angle=15°		
Inclination angle=25°		

Appendix D

Moment-Rotation Curves of the RRD-SWT GMNIA models

RRD Set I: GMNIA-weld depression models with constant diameter and varied thickness

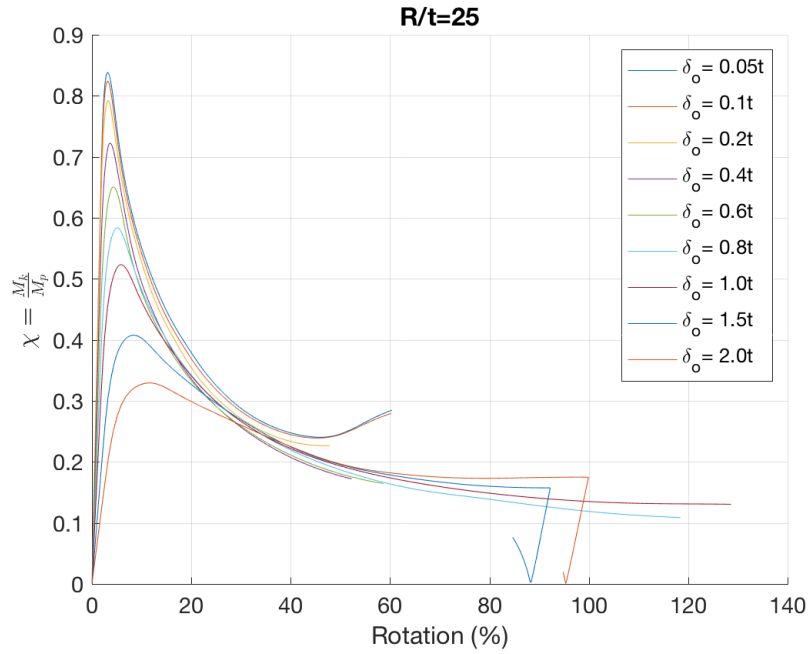


Figure D.1: GMNIA-WD moment-rotation curves for RRD curves for sections with $R/t=25$.

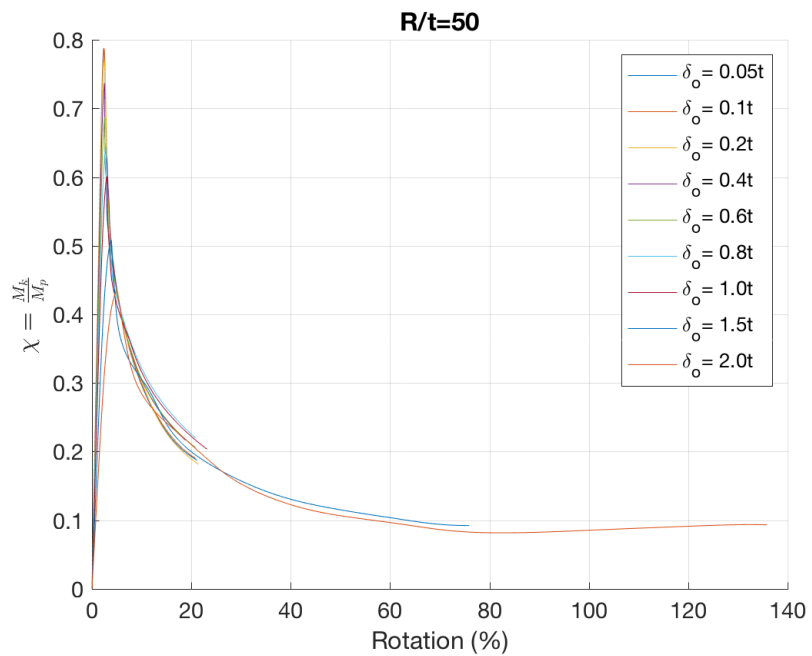


Figure D.2: GMNIA-WD moment-rotation curves for RRD curves for sections with $R/t=50$.

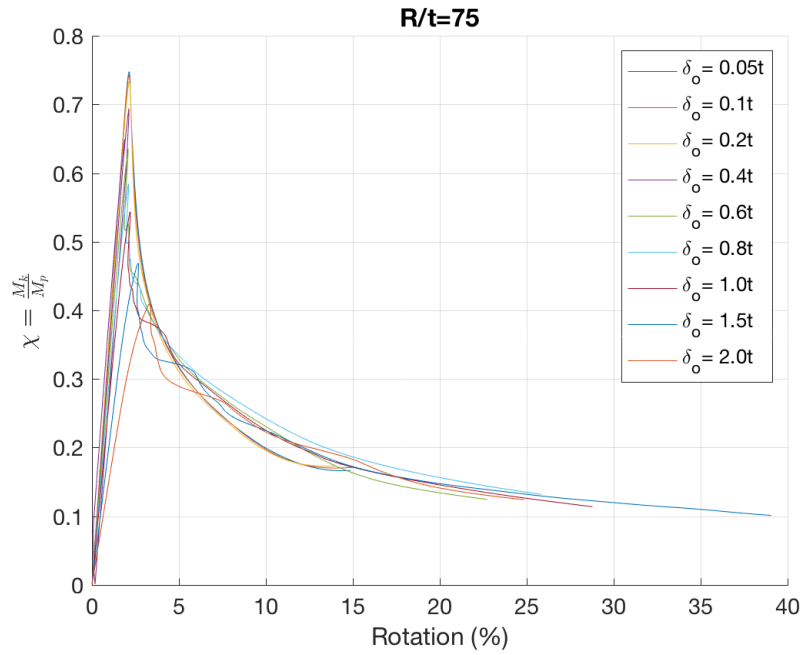


Figure D.3: GMNIA-WD moment-rotation curves for RRD curves for sections with $R/t=75$.

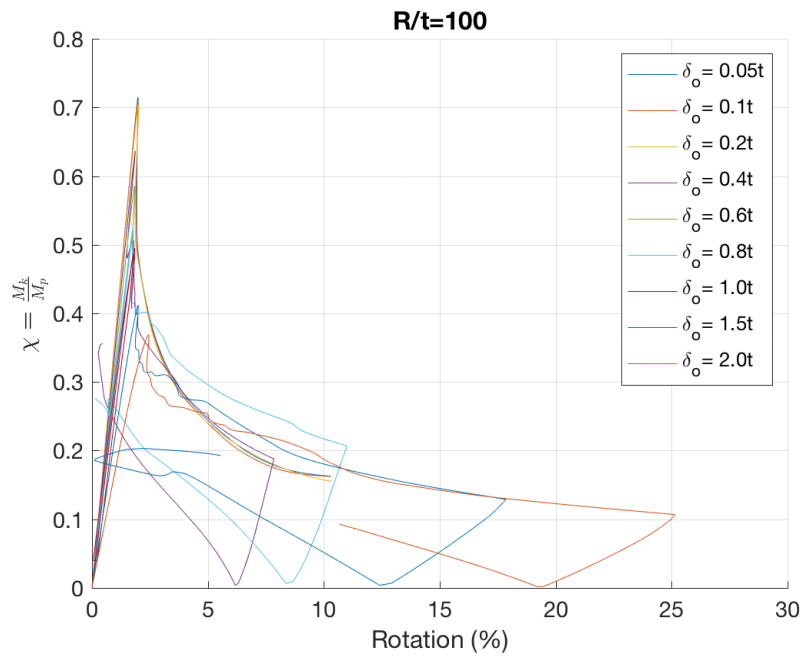


Figure D.4: GMNIA-WD moment-rotation curves for RRD curves for sections with $R/t=100$.

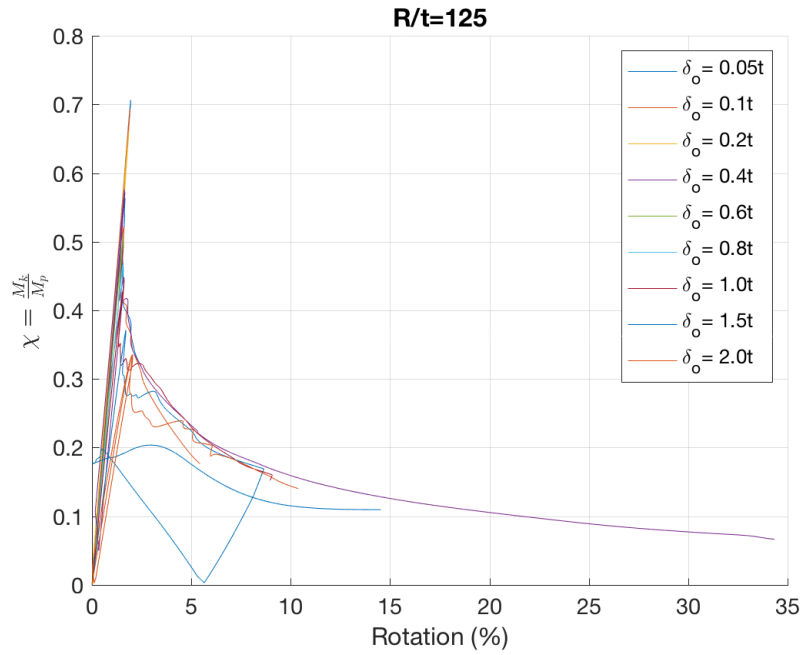


Figure D.5: GMNIA-WD moment-rotation curves for RRD curves for sections with $R/t=125$.

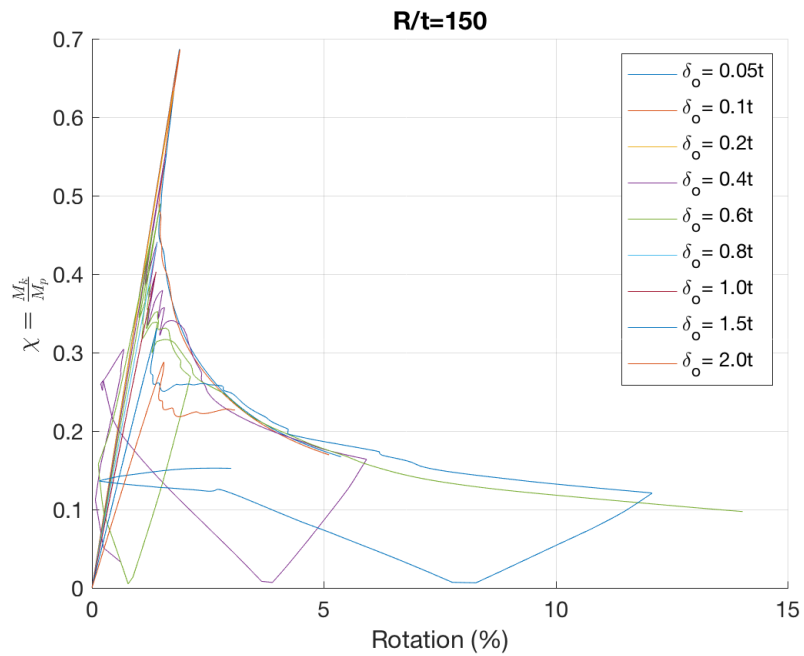


Figure D.6: GMNIA-WD moment-rotation curves for RRD curves for sections with $R/t=150$.

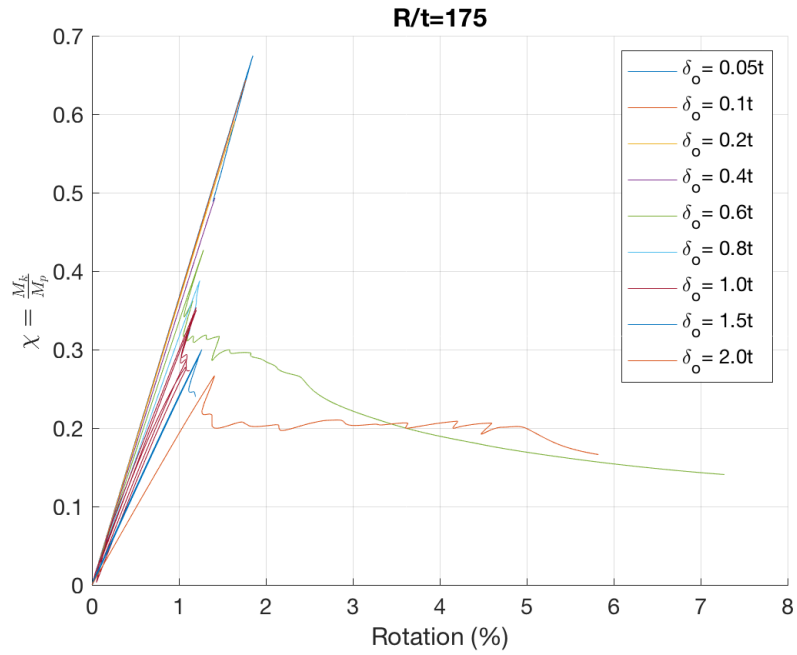


Figure D.7: GMNIA-WD moment-rotation curves for RRD curves for sections with $R/t=175$.

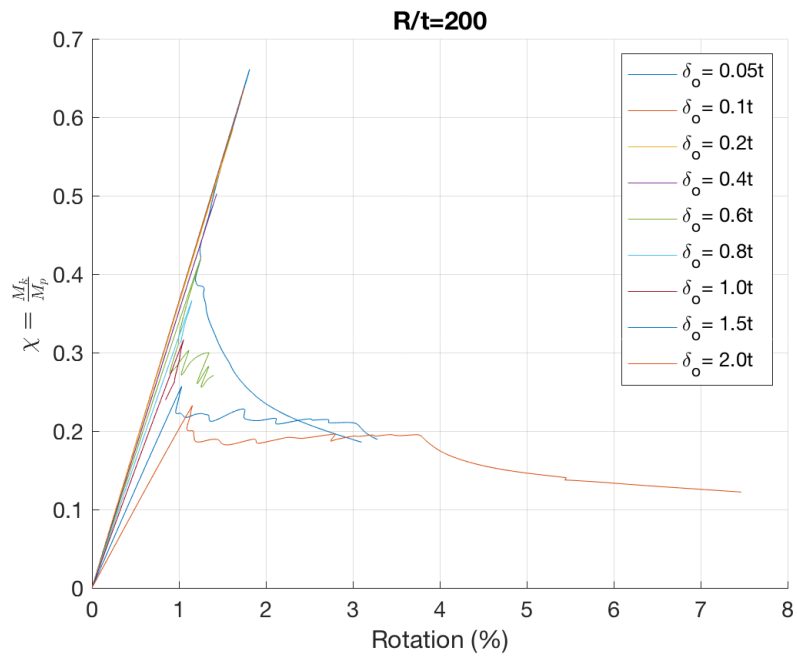


Figure D.8: GMNIA-WD moment-rotation curves for RRD curves for sections with $R/t=200$.

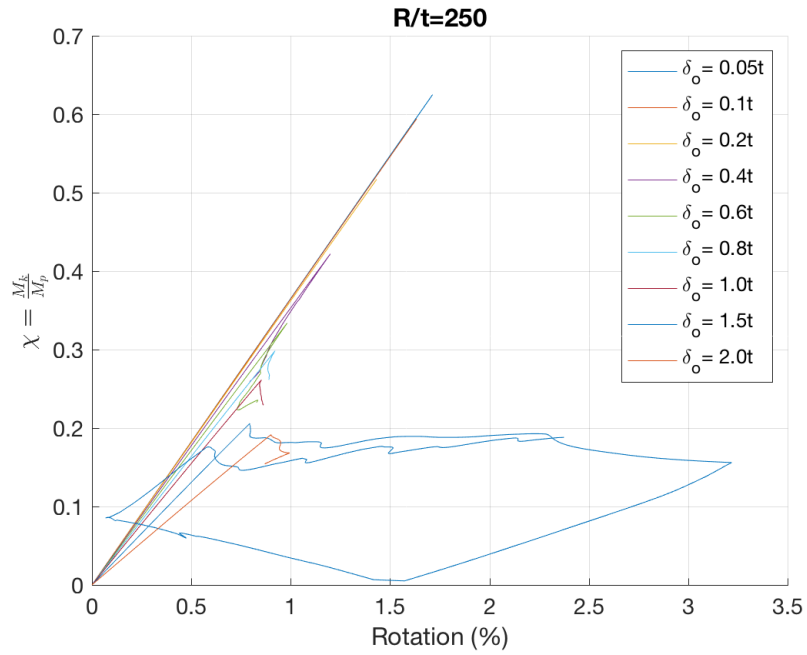


Figure D.9: GMNIA-WD moment-rotation curves for RRD curves for sections with $R/t=250$.

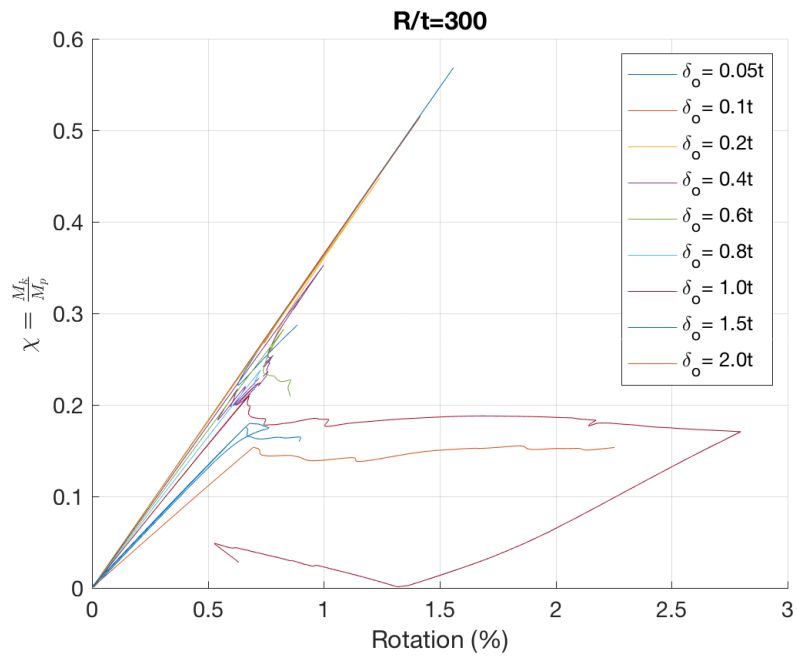


Figure D.10: GMNIA-WD moment-rotation curves for RRD curves for sections with $R/t=300$.

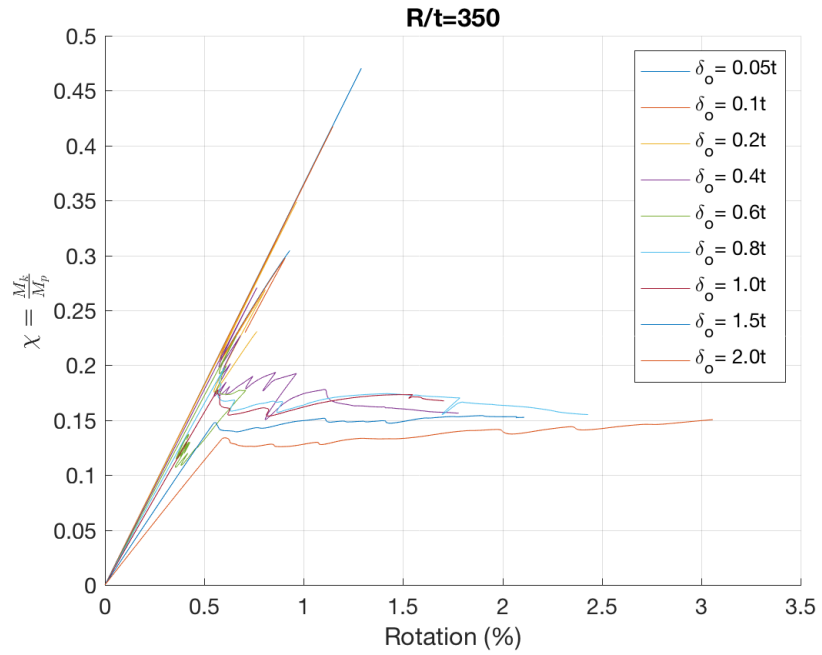


Figure D.11: GMNIA-WD moment-rotation curves for RRD curves for sections with $R/t=350$.

RRD Set II: GMNIA-weld depression models with constant thickness and varied diameter

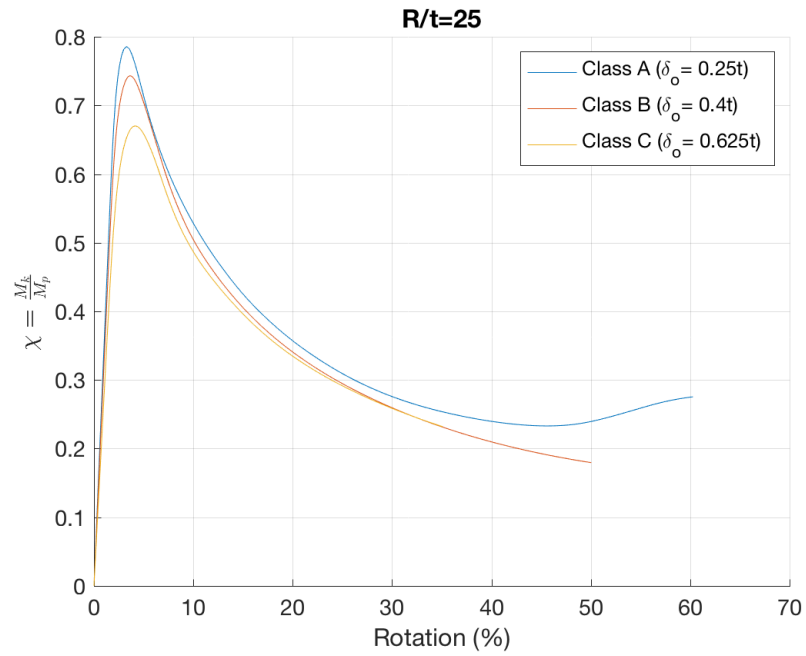


Figure D.12: GMNIA-WD moment-rotation curves for RRD curves for sections with R/t=25.

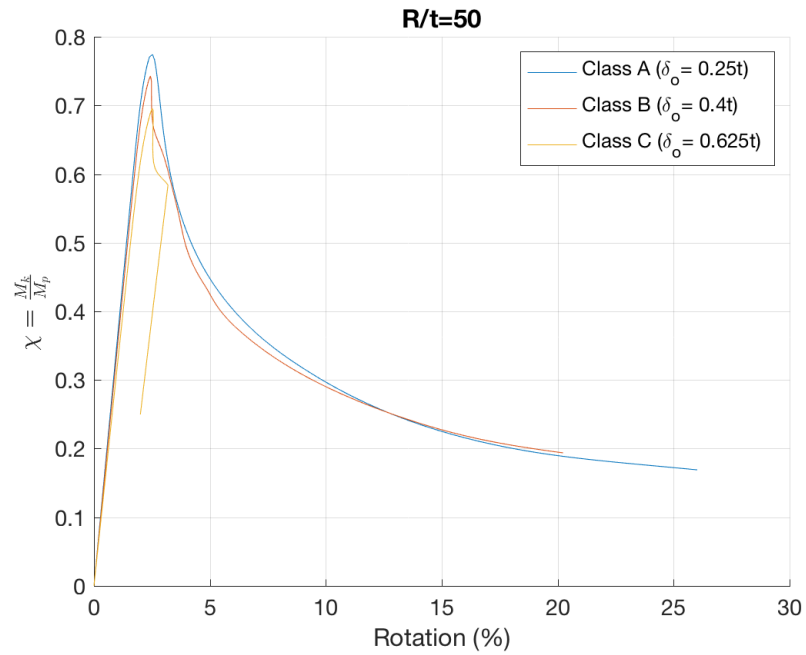


Figure D.13: GMNIA-WD moment-rotation curves for RRD curves for sections with R/t=50.

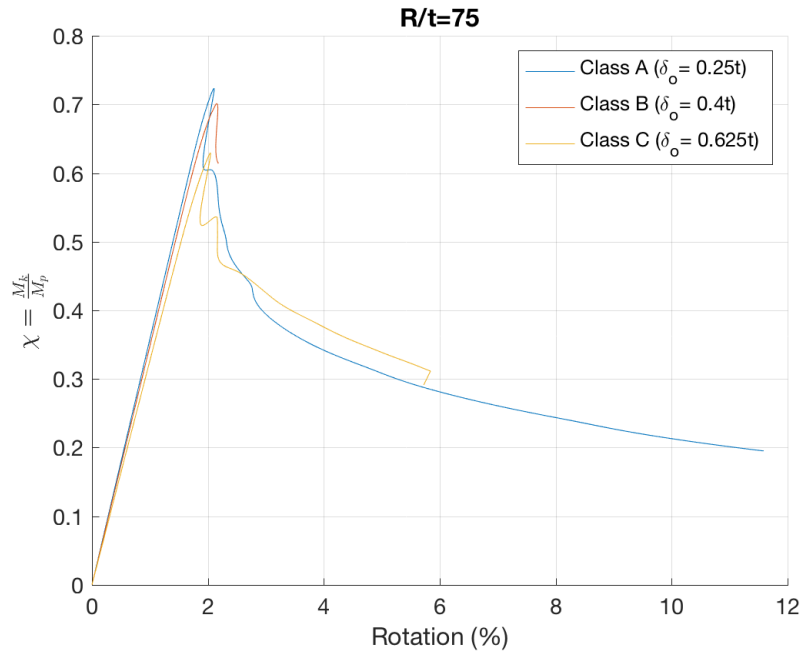


Figure D.14: GMNIA-WD moment-rotation curves for RRD curves for sections with R/t=75.

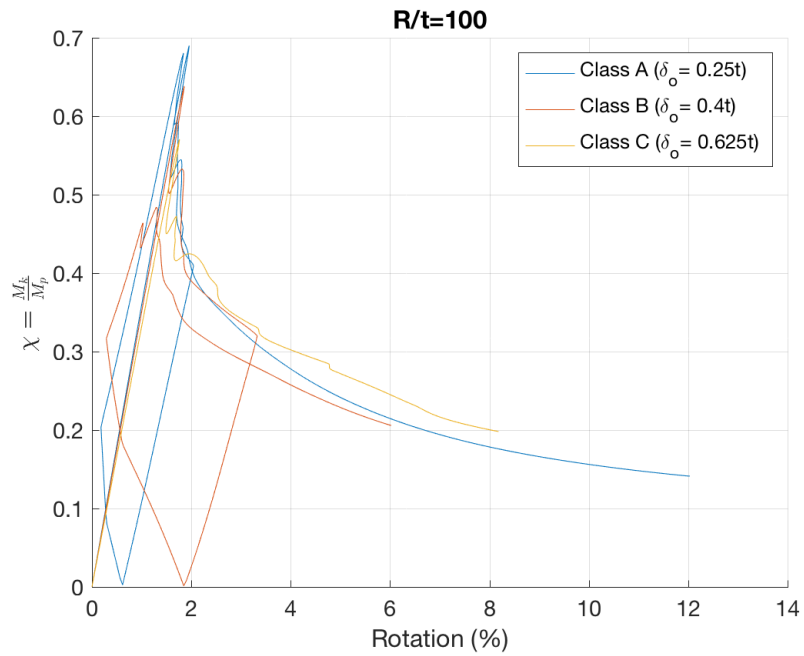


Figure D.15: GMNIA-WD moment-rotation curves for RRD curves for sections with R/t=100.

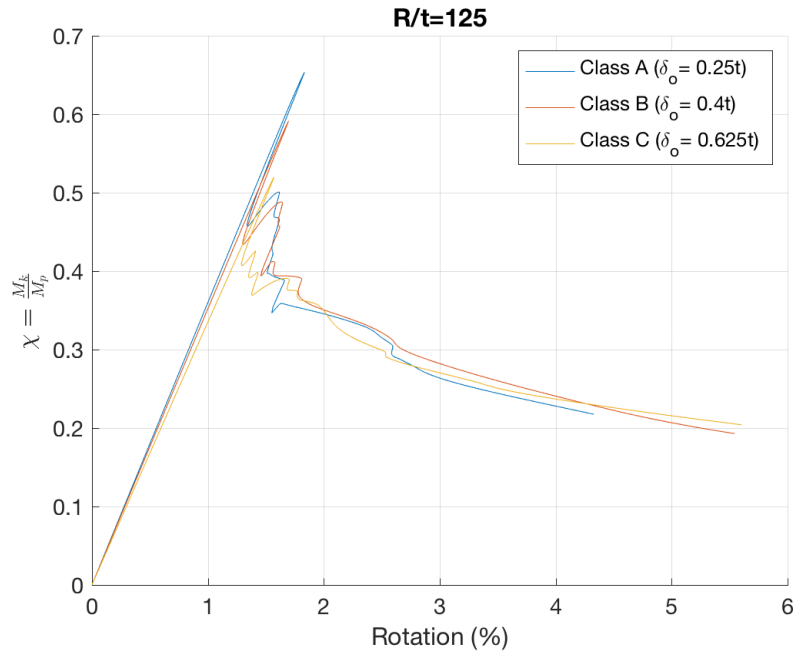


Figure D.16: GMNIA-WD moment-rotation curves for RRD curves for sections with $R/t=125$.

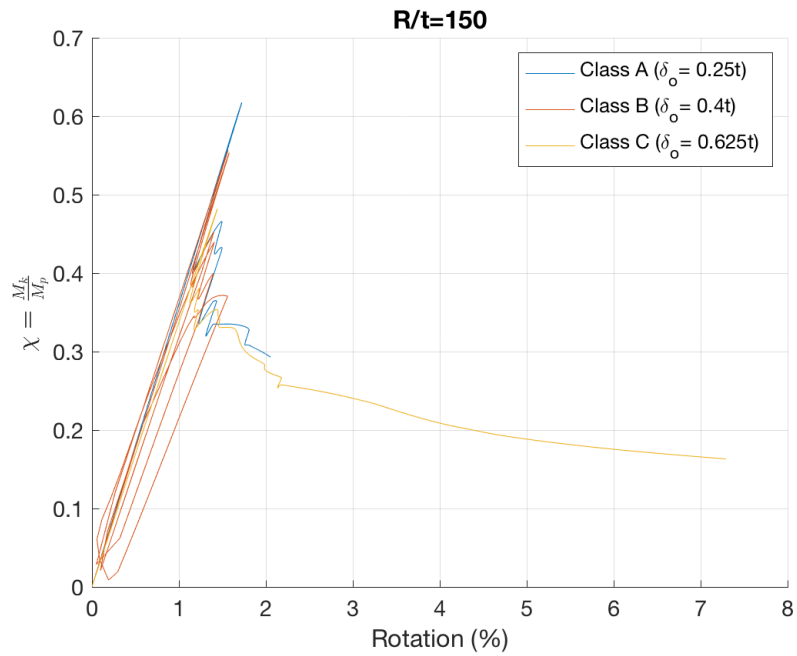


Figure D.17: GMNIA-WD moment-rotation curves for RRD curves for sections with $R/t=150$.

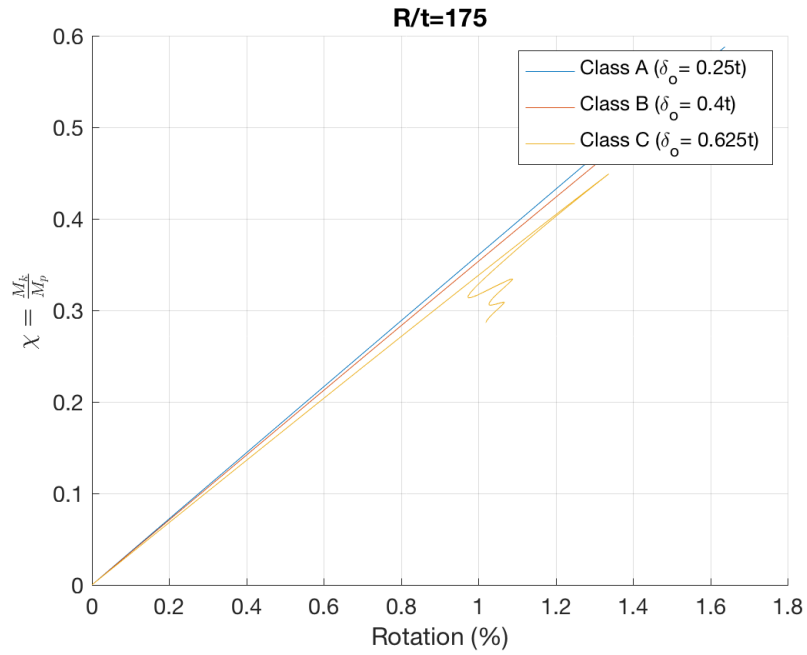


Figure D.18: GMNIA-WD moment-rotation curves for RRD curves for sections with $R/t=175$.

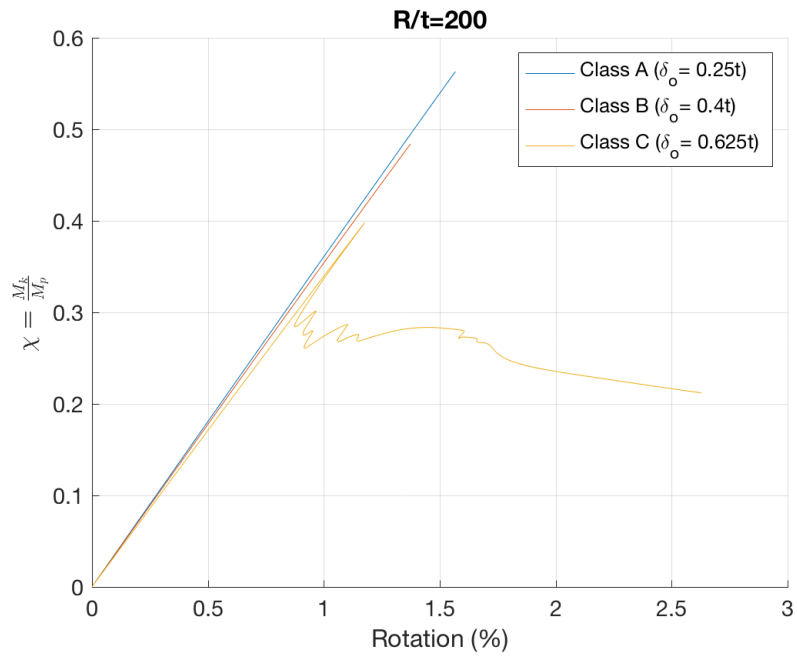


Figure D.19: GMNIA-WD moment-rotation curves for RRD curves for sections with $R/t=200$.

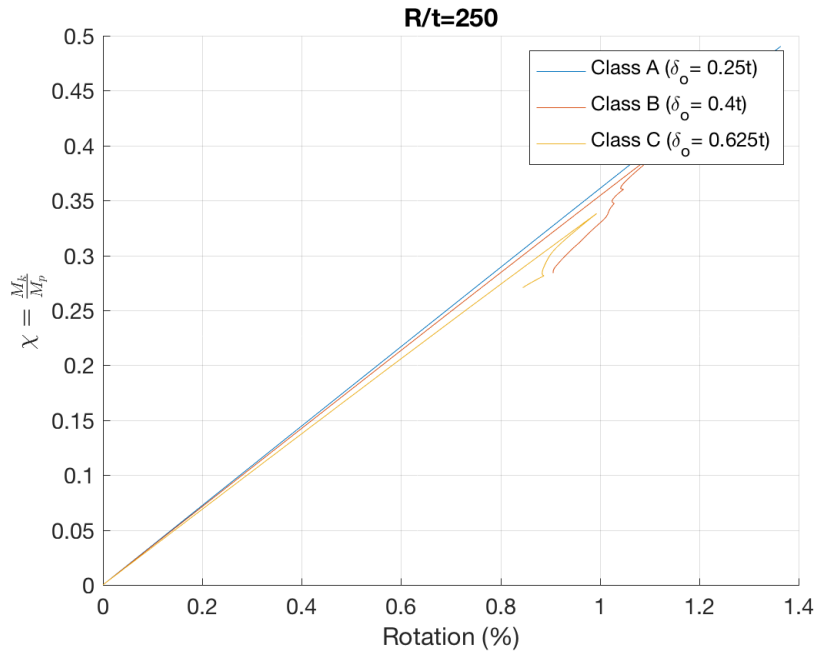


Figure D.20: GMNIA-WD moment-rotation curves for RRD curves for sections with R/t=250.

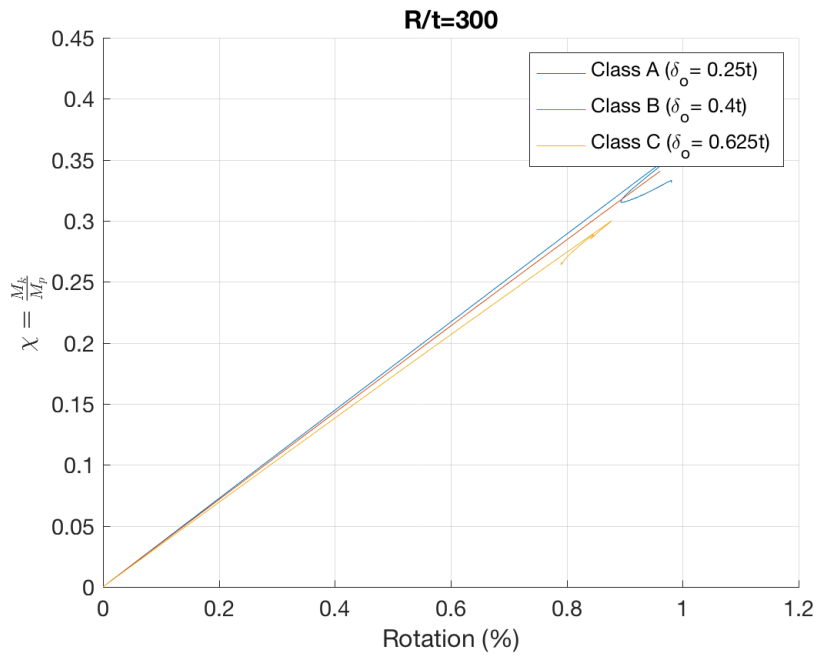


Figure D.21: GMNIA-WD moment-rotation curves for RRD curves for sections with R/t=300.

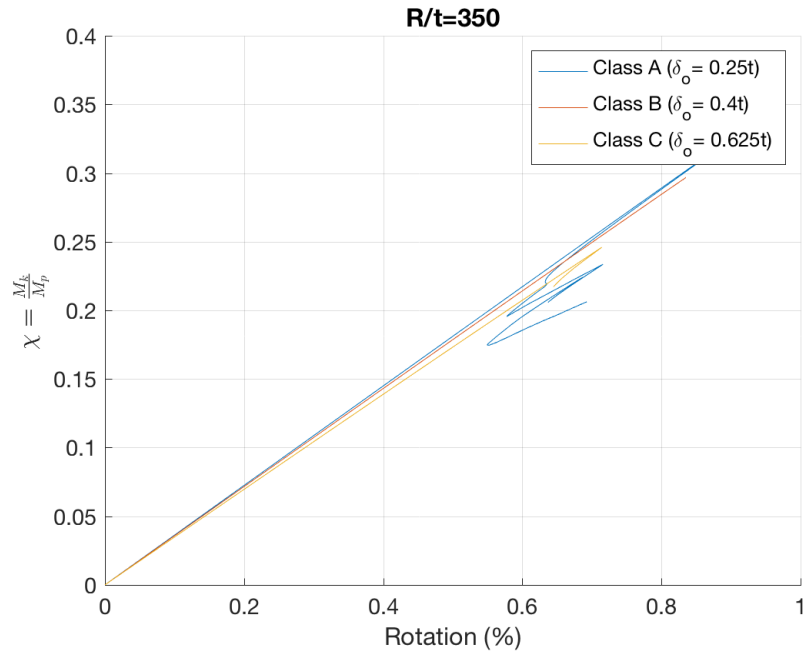


Figure D.22: GMNIA-WD moment-rotation curves for RRD curves for sections with $R/t=350$.

Appendix E

Detailed Design Calculations for Two Sections of the 3MW Archetype Tower

Design Inputs:

1- Section Properties:

Property	Section 1 (under highest bending moment)	Section 2 (the highest D/t)
Diameter (D)	6503.45 mm	3459.9 mm
Thickness (t)	23 mm	12 mm
Radius (R)	3251.7 mm	1730 mm
Height of this section of the tower (L)	31.71 m	42.745 m
Area (A)	234959 mm ²	65217.6 mm ²
Section modulus (S)	764021972.7 mm ³	112823123.7 mm ³
Slenderness ratio (D/t)	282.76	288.325
Yield stress (F_y)	450 MPa	450 MPa
Modulus of Elasticity (E)	200 GPa	200 GPa

2- Straining Actions (unfactored loads):

Forces	Section 1 (under highest bending moment)	Section 2 (the highest D/t)
Axial (F_x)	4778 kN	1825 kN
Moment (M_z)	130638 kN-m	18732 kN-m
Stresses		
Axial ($\sigma_{x-axial} = \frac{F_x}{A}$)	22.7 MPa	30.78 MPa
Moment ($\sigma_{x-bending} = \frac{M_z}{S}$)	188.1 MPa	182.63 MPa
Combined ($\sigma_x = \frac{F_x}{A} + \frac{M_z}{S}$)	210.45 MPa	213.42 MPa

3- Design for nominal strengths:

a. API Bull. 2U

Calculation	Section 1 (under highest bending moment)	Section 2 (the highest D/t)
$M_x = \frac{L_r}{\sqrt{Rt}}$	115.95	296.7
C_x	0.605	0.605
\bar{c}	1	1
$\alpha_{xL} = \frac{169\bar{c}}{195 + 0.5(D/t)} < 0.9$	0.502	0.498
$F_{xeL} = \alpha_{xL}\sigma_{xeL} = \alpha_{xL}C_x2E\left(\frac{t}{D}\right)$	430 MPa	418.22 MPa
$F_{xcl1} = \frac{233F_y}{166 + 0.5(D/t)} \leq F_y$	341.1 MPa	338 MPa.
$\Delta = \frac{F_{xeL}}{F_y}$	0.95	0.929
$\eta = \frac{0.45}{\Delta} + 0.18$	0.651	0.6642
$F_{xcl2} = \eta F_{xeL}$	284.70 MPa	277.78 MPa
$\sigma_{x-nominal} = F_b = \min(F_{xcl1}, F_{xcl2})$	279.89 MPa	277.78 MPa
Check Moment only		
$M_n = \sigma_{xn} \times S$	213850 kN-m	31340 kN-m
$\frac{M_z}{M_n}$	0.611	0.6
Check Combined Stresses		
$\frac{\sigma_x}{\sigma_{xn}}$	0.647	0.648

b. ASME STS-1

Calculation	Section 1 (under highest bending moment)	Section 2 (the highest D/t)
$K_s = \left(\frac{10F_y/E - t/D}{7.2F_y/E} \right)^2$	1.37	1.38
Y	1	1
$\sigma_{xn} = S_{bl} = \frac{EtY}{4D}$	176.8 MPa	173.4 MPa
Moment Ratio		
$M_n = \sigma_{xn} \times S$	135100 kN-m	19565 kN-m
$\frac{M_z}{M_n}$	0.97	0.957
Combined Stresses Ratio		
$\frac{\sigma_x}{\sigma_{xn}}$	1.02	1.04

c. ASCE/AWEA RP2011

Calculation	Section 1 (under highest bending moment)	Section 2 (the highest D/t)
$\sigma_{xn} = F_{cr} = 0.276 \frac{E}{(D/t)}$	195.22 MPa	191.45 MPa
Moment Ratio		
$M_n = \sigma_{xn} \times S$	149150 kN-m	21600 kN-m
$\frac{M_z}{M_n}$	0.876	0.867
Combined Stresses Ratio		
$\frac{\sigma_x}{\sigma_{xn}}$	0.928	0.94

d. EC3-1-6 (Class B)

Calculation	Section 1 (under highest bending moment)	Section 2 (the highest D/t)
γ_{MI}	1.1	1.1
$\omega = \frac{l}{\sqrt{rt}}$	115.95	296.7
C_{xb}	3	1
$C_x = 1 + \frac{0.2}{C_{x,b}} \left[1 - 2\omega \frac{t}{r} \right]$	0.957	0.6
$\sigma_{X,Rcr} = 0.605EC_x \frac{t}{r}$	819.32 MPa	503.6
$\lambda = \sqrt{\frac{f_{yk}}{\sigma_{X,Rcr}}}$	0.74	0.94
λ_0	0.2	0.2
β	0.6	0.6
η	1	1
Q	Class B = 25	Class B = 25
$\Delta w_k = \frac{1}{Q} \sqrt{\frac{r}{t}} \cdot t$	10.93	5.76
$\alpha_x = \frac{0.62}{1 + 1.92(\Delta w_k/t)^{1.44}}$	0.3738	0.3717
$\lambda_p = \sqrt{\frac{\alpha_x}{1 - \beta}}$	0.967	0.964
$\chi_x = 1 - \beta \left(\frac{\lambda - \lambda_0}{\lambda_p - \lambda_0} \right)^\eta$	0.576	0.4147
$\sigma_{xn} = \sigma_{X,Rk} = \chi_x f_{yk}$	259.45 MPa	186.6 MPa
Moment Ratio		
$M_n = \sigma_{xn} \times S$	198230 kN-m	21056 kN-m
$\frac{M_z}{M_n}$	0.66	0.89
Combined Stresses Ratio		
$\frac{\sigma_x}{\sigma_{xn}}$	0.698	0.964

e. RRD-SWT Class B

Calculation	Section 1 (under highest bending moment)	Section 2 (the highest D/t)
$\omega = \frac{\ell}{\sqrt{rt}}$	115.95	296.7
C_{xb}	3	1
$C_x = 1 + \frac{0.2}{C_{x,b}} \left[1 - 2\omega \frac{t}{r} \right]$	0.957	0.6
$\sigma_{X,Rcr} = 0.605EC_x \frac{t}{r}$	819.32 MPa	503.6
$\lambda = \sqrt{\frac{f_{yk}}{\sigma_{X,Rcr}}}$	0.74	0.94
λ_0	0.2	0.2
$\frac{\Delta w_k}{t}$	Class B = 0.4	Class B = 0.4
$\beta = 1 - \frac{0.90}{1 + 1.6(\Delta w_k/t)^{0.92}}$	0.585	0.585
$\eta = \frac{0.60}{1 + 0.1(\Delta w_k/t)^{2.5}}$	0.594	0.594
$\alpha_x = \frac{0.90}{1 + 1.5(\Delta w_k/t)^{0.92}}$	0.547	0.547
$\lambda_p = \sqrt{\frac{\alpha_x}{1 - \beta}}$	0.967	1.14
$\chi_x = 1 - \beta \left(\frac{\lambda - \lambda_0}{\lambda_p - \lambda_0} \right)^\eta$	0.581	0.4927
$\sigma_{xn} = \sigma_{X,Rk} = \chi_x f_{yk}$	261.24 MPa	221.71 MPa
Moment Ratio		
$M_n = \sigma_{xn} \times S$	199600 kN-m	25014 kN-m
$\frac{M_z}{M_n}$	0.654	0.75
Combined Stresses Ratio		
$\frac{\sigma_x}{\sigma_{xn}}$	0.693	0.81

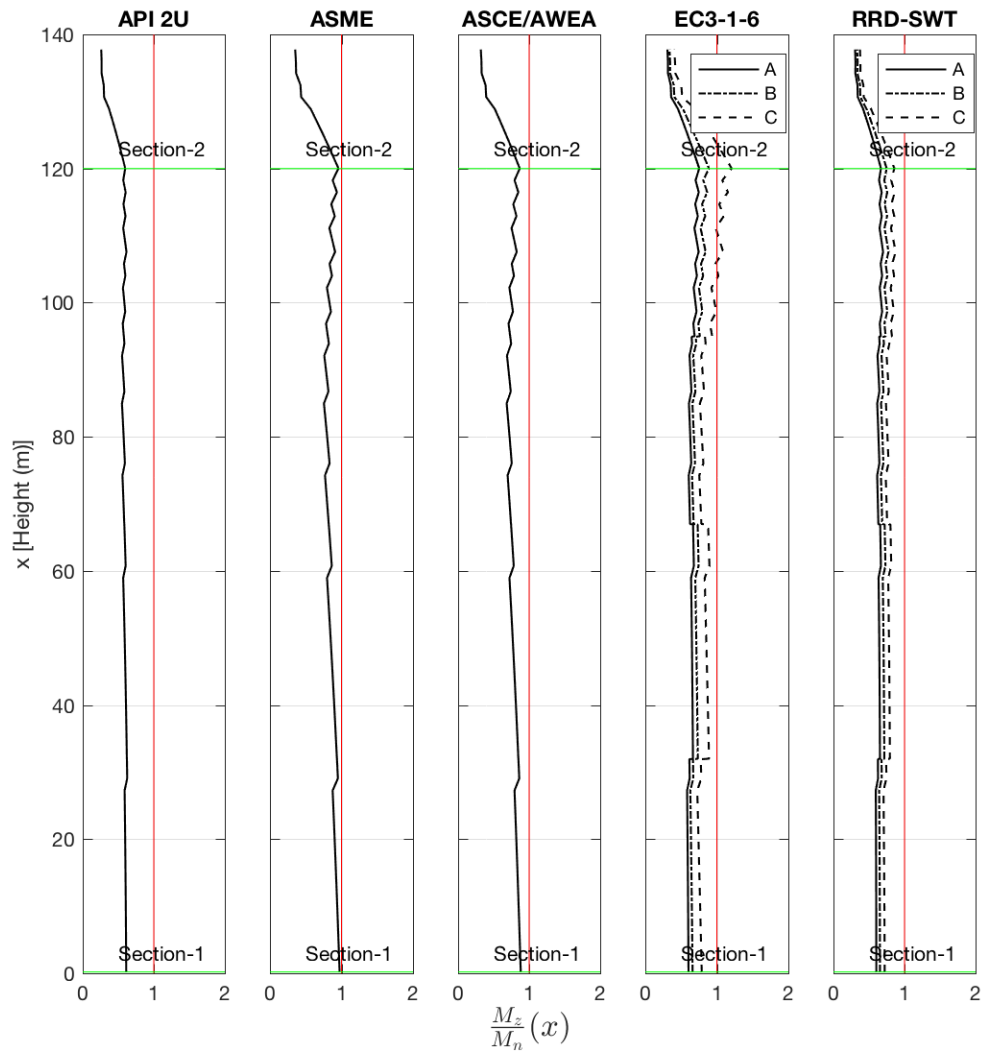


Figure E.1 The ratio of applied moment to nominal moments obtained from design guides and proposed RRD-SWT.

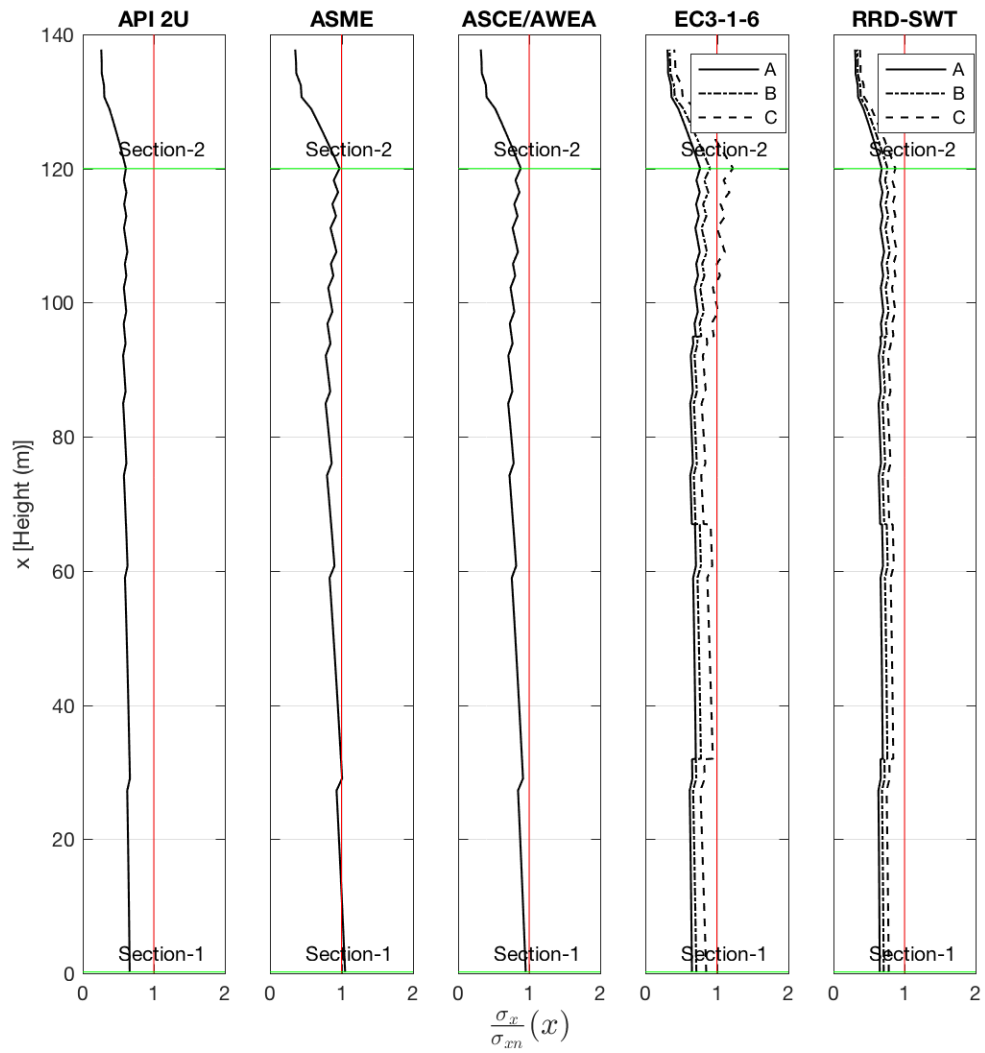


Figure E.2 The ratio of applied compressive stress to nominal compressive stress obtained from design guides and proposed RRD-SWT.

Curriculum Vitae

Abdullah Mahmoud

2924 N Calvert St Apt. 3, Baltimore, MD 21218

Phone: +1(443) 527-5655

Email: abdullah@jhu.edu

(or abdullahnabil85@gmail.com)

- Education**
- 2017 Ph.D. Civil Engineering**
Johns Hopkins University, Baltimore, Maryland, USA
Thesis title: “Analysis and Design of Spirally Welded Thin-Walled Steel Tapered Cylindrical Shells Under Bending with Application to Wind Turbine Towers”
- 2016 M.S.E. Civil Engineering**
Johns Hopkins University, Baltimore, Maryland, USA
- 2012 M.Sc. Structural Engineering**
Cairo University, Giza, Egypt
Thesis title: “Experimental and Analytical Studies on Failure Modes of Structure Steel Scaffolds”
- 2008 B.Sc. Civil Engineering**
Cairo University, Giza, Egypt
- Work Experience**
- 2013 (Thin-Walled Structures [Lab](#)) Johns Hopkins University, Whiting School of Engineering**
- 2017** Graduate Research Assistant-Ph.D. student
I studied stability of shelled structures in a project aiming to enable spiral welding technique to be used in fabrication and construction of tall slender wind turbine towers. The research is divided into experimental testing and numerical analysis. I studied the effect of imperfections’ patterns and magnitudes on thin shells strength and stiffness. I used numerical finite element models with material and geometric nonlinearities and imperfections (aka: GMNIA) in predicting strength of shells and verified against test results and conducting a parametric study and reliability analysis to develop design recommendations to be adopted for such structures.
- 2011 Applied Science International ([ASI](#)) - The Steel Network ([TSN](#)) USA-Egypt**
to Structural Engineer
- 2013** Designing cold formed steel structures along with helping to develop a software for analysis and design of cold formed steel structures using Eurocode 3, ASCE 7-10, IBC 2012
Main projects:
Steel Smart System (SSS v6.2-v6.5) (2011-2013)
Condo apartments, Kazakhstan (2012)
Residential building, Congo (2013)

Work Experience	<p>2009 ACE Consulting Engineers (Moharram-Bakhoum) (ACE), Egypt to Structural Engineer</p> <p>2011 Providing analysis, design and detailed drawings for new heavy industrial structures (mostly army ammunition factories some was designed with blast proof features) and retrofit of existing structures.</p> <p><u>Main projects:</u> Egyptian Company for Ferro-silicon Alloys (2009) National Authority for Military Production (2010-2011) Abu Za'abal Company for Chemical Industries 18 (2010) Redeployment Project of Weapons and Ammunition Factories (2010-2011) Egyptian Company for Fertilizers (2011)</p> <p>2008 NSM Engineering Consulting Office (NSMECO) to Structural Designer</p> <p>2009 Providing structural designs /drawings for construction. Work in accordance with the planning and scheduling of the structural design stages for the project in coordination with Structural Manager. Reviews the Structural drawings done by draftsman and ensure its accuracy and provides guidance where necessary. Co-ordinate with other departments during the various stages of the production cycle. Belkas Sugar Factory second line –Kaliobiya (2009) Nile Sugar Company – Alexandria (2008) Mashhour mosque – Alsharqiya (2008) Pyramids stock exchange building – Giza (2007-internship)</p>
Standards Experience	<ul style="list-style-type: none"> ▪ American Iron and Steel Institute Standard (AISI 2001/04-2007) ▪ American Institute of Steel Construction (AISC 360-10) ▪ American Society of Civil Engineers Standard (ASCE/SEI 7-10) ▪ American Association of State Highway and Transportation Officials (AASHTO) ▪ Eurocode 3: Design of Steel Structures (EN 1993-1-1, EN 1993-1-3, EN 1993-1-6) ▪ International Building Code (IBC 2012) ▪ International Existing Building code (IEBC 2012) ▪ The Recommended Practice for Compliance of Large Land-based Wind Turbine Support Structures, American Wind Energy Association (AWEA/ASCE RP2011) ▪ Egyptian Code of Practice (ECP 2008)
Teaching	<p>Johns Hopkins University, Whiting School of Engineering</p> <p>Teaching Assistant:</p> <ul style="list-style-type: none"> ▪ Spring 2014: Perspectives on the Evolution of Structures (EN.560.141.01) ▪ Fall 2016: Statics and Mechanics of Materials (EN.560.141.01) ▪ Spring 2014: Perspectives on the Evolution of Structures (EN.560.141.01) <p>2016-2017 Mentoring High School Researchers in the Thin-Walled Structures Lab</p>

- Graduate Courses**
- Structural Stability
 - Bridge Design and Evaluation
 - Investigation, Diagnosis and Rehabilitation
 - Advanced Steel Design
 - Structural Dynamics
 - Special Topics in Steel Structures
 - Selected Topics in Earthquake Engineering
 - Cold-Formed Steel Structures
 - High Rise Steel Buildings
 - Analysis of Bridge Decks
 - Prestressed Concrete
 - Solid Mechanics for Structures
 - Applied Mathematics for Engineers
 - Probability and Statistics in Civil Engineering
 - Risk and Decision Analysis
 - Wind Engineering (Audit)
 - Preservation Engineering (Audit)
 - Probabilistic Methods in Civil Engineering and Mechanics (Audit)

- Skills**
- | | | |
|---|--|---|
| <p>Technical</p> <ul style="list-style-type: none"> ▪ Structure dynamics ▪ Light-gauge steel ▪ Tall buildings ▪ Shell stability and design ▪ Structural forensics ▪ Retrofit of Structures ▪ Finite Element Analysis ▪ Lab experience ▪ Non-destructive testing | <p>Software</p> <ul style="list-style-type: none"> ▪ SAP2000, ETABS 8 ▪ Autocad 2D/3D ▪ Revit ▪ Steel Smart System ▪ MS Office ▪ Visual Basic for MS office ▪ ABAQUS, ANSYS ▪ CUFSM ▪ Matlab | <p>Personal</p> <ul style="list-style-type: none"> ▪ Critical thinking ▪ Researchability ▪ Multi-tasking ▪ Interpretation and analysis ▪ Time management ▪ Negotiation Skills ▪ Communication Skills ▪ Attention to details ▪ Documentation |
|---|--|---|
- Language Proficiency**
- | | | |
|-----------------|----------------|---------------|
| English: Fluent | Arabic: Fluent | French: Basic |
|-----------------|----------------|---------------|

- Activities & Hobbies**
- Volunteer at STEM Achievement in Baltimore Elementary Schools (SABES) 2014-2016
 - Academic Coordinator, Civil Engineering Graduate Association (CEGA-JHU) 2014-2015
 - Head of Life Makers Family in Cairo University 2004-2006
 - Member in SAHWA charity organization activities since summer 2007
 - Member of International Association for Civil Engineering Students (IACES)

Publications

- Mahmoud, A., Abdelghaffar, M. E. (2013) “*Experimental and Analytical Study Failure Modes of Structural Steel Scaffolds*” SSRC proceedings, Saint Louis-MO, USA.
- Mahmoud, A., Torabian, S., Jay, A., Myers, A. T., Smith, E., Schafer, B. W. (2015) “*Modeling protocols for elastic buckling and collapse analysis of spirally welded circular hollow thin-walled sections*” Proceedings of the Annual Stability conference, SSRC’15, Nashville-Tennessee, USA.
- Jay, A., Torabian, S., Mahmoud, A., Myers, A. T., Schafer, B.W., Smith E. (2015) “*Static Flexural Local Buckling Tests on Large Scale Spirally Welded Tubes for use as Wind Turbine Towers*” Structures Congress 2015, Portland-Oregon, USA
- Mahmoud, A., Torabian, S., Jay, A., Mirzaie, F., Myers, A. T., Smith, E., Schafer, B. W. (2016) “*Collapse Analyses on Spirally Welded Tapered Tubes using EC3 Generated Imperfections*” Proceedings of the Annual Stability conference, SSRC’16, Orlando-Florida, USA
- Mahmoud, A. N., Mirzaie, F., Torabian, S., Jay, A., Myers, A. T., Smith, E., Schafer, B. W. (2016) “*Collapse Analysis of Spirally Welded Tapered Tubes under Flexural Moments using Measured and Generated Imperfections*” Proceedings of the 7th International Conference on Coupled Instabilities in Metal Structures. Baltimore-Maryland, USA.
- Jay, A., Myers, A.T., Torabian, S., Mahmoud, A., Smith, E., Agbayani, N., Schafer, B.W. (2016) “*Spirally Welded Steel Wind Towers: Buckling Experiments, Analyses, and Research Needs*” J. Constructional Steel Research 125.
- Jay, A., Myers, A.T., Mirzaie, F., Mahmoud, A., Torabian, S., Smith, E., Schafer, B.W. (2016) “*Large Scale Bending Tests of Slender, Tapered, Spirally Welded Steel Tubes*” J. Structural Engineering.
- Mahmoud, A., Torabian, S., Jay, A., Mirzaie, F., Myers, A. T., Smith, E., Schafer, B. W. (2017) “*Modeling the Flexural Collapse of Thin-Walled Spirally Welded Tapered Tubes*”, J. Structural Engineering.